Simultaneous Measurement of Acoustic Fields and Flow Fields using Optical Methods

David Brian Hann

A thesis submitted in fulfilment of the requirements
for the degree of Doctor of Philosophy
The University of Edinburgh
1995

Abstract

Two different optical techniques are applied to the measurement of the acoustic particle velocity in velocity fields. Firstly, the measurement of both the acoustic particle velocity and the mean flow velocity using Laser Doppler Anemometry is described. Secondly, the Particle Image Velocimetry method is investigated to determine the possibility of measuring the acoustic particle velocity and then both the acoustic particle velocity and the mean flow velocity.

For the first case, consideration is given to the conditions necessary to obtain both of these parameters. The theory was then developed to allow the analysis of the Laser Doppler Anemometry signal. Experiments are then described which test the technique and some successful measurements are made.

In the second case, the conditions for the use of Particle Image Velocimetry is discussed and the theory is developed. The theory is compared against computationally constructed images in order to test the range and accuracy of the possible ways of doing the measurement. Experiments are then done which show that the measured values agree well with the theory.

Declaration

This thesis has been composed by myself and it has not been submitted in any previous application for a degree. The work reported within was executed by myself, unless otherwise stated.

Acknowledgements

Thanks to all in the department for their help. Thanks to Will Hossack for his help with the image processing routines. Thanks to the Southsider and Addleston's for their support on the difficult days. A special special thanks to Katy for keeping me sane over the last year and for listening even if she did not understand much of what I was saying.

Table of Contents

List of Tables

List of Figures

Chapter 1

Introduction

This thesis is concerned with constructing the theory underlying, and demonstrating the use of, optical techniques which permit measurements to be made of the acoustic particle velocity (the velocity amplitude of a sinusoidal oscillation) and the measurement of the mean flow velocity of the air simultaneously.

We shall confine ourselves to the study of sound fields of the order of 1kHz and intensity of the order of 120dB and higher, but acoustics, which is defined in Kinsler *et. al.*([36]) as the generation, transmission and reception of energy in the form of vibrational waves, covers a large range of topics open to physical investigations. In this regime, the non-linear effects in the sound field produce a mean flow field (usually called acoustic streaming) which is dependent on the sound field. The measurement of the sound field by probe microphones will upset this balance, and so a non-intrusive method of measuring the acoustic particle velocity is necessary, and if it can also measure the mean flow as well it will be very useful.

It is the topic of flow-sound field interactions that we are interested in. The presence of an intense sound field will produce a flow field[41], just as the presence of a flow field can produce a sound field(e.g. organ, whistle, etc.). A flow can also increase the attenuation, or amplification, of a sound propagating through a duct [8,51].

The measurement of the acoustic particle velocity separately from the pressure measurements allows the acoustic impedance to be measured rather than assumed [57]. This has many applications in acoustics, where the impedance measurement is needed to determine the intensity at a point.

The two optical techniques in which we are interested are Laser Doppler Anemometry (LDA) and Particle Image Velocimetry (PIV). In order to deal with these the thesis is split into two parts, the first is concerned with the Laser Doppler Anemometry method of measuring flow, and the second is concerned with the Particle Image Velocimetry method of flow measurement.

We begin in Chapter 2 with a discussion of the basics of acoustics, for example acoustic intensity and impedance, before developing the acoustic relationships which will be of use in later experimental work. Current methods of measuring the acoustic particle velocity are reviewed, providing some indication for the motivation of the work undertaken in this thesis. The basics of acoustic streaming are discussed.

LDA is discussed in Chapters 3,4 and 5. LDA is a point measuring technique which has been used to measure flow velocity [1] and the absolute acoustic particle velocity non-intrusively, and it has been used to calibrate microphones[62]. The measurement of sound fields using LDA is not new since several techniques of signal processing have been used to measure the acoustic particle velocity (frequency tracking [15], frequency analysis [61,66] and Photon Correlation [55,25,56]). Taylor [61] showed that the presence of a flow in the interrogation area made it difficult to determine the acoustic particle velocity, so it was not possible to use this processing method to find both the acoustic particle velocity and the mean flow velocity simultaneously from the area of interest. Work done by Greated et al. [25,7] however showed that the photon correlation signal could be used to measure the acoustic particle velocity and the mean flow velocity simultaneously for a mean flow velocity very much larger than the acoustic particle velocity.

Our aims in this Thesis are to:

- develop the stochastic model of Laser Doppler anemometry using the Photon Correlation method to include the case for a sinusoidal oscillation superimposed on a mean flow. This will allow the acoustic particle velocity and the mean flow velocity to be retrieved from the experimental information.

- show that the theoretical function agrees with experimentally measured function.

- use the method to investigate the flow and sound field in a situation in which both are linked (e.g. in an organ pipe).

This will allow the study of areas such as acoustic streaming where flow and sound fields affect one another.

In the second section of the Thesis, we are interested in the possibility of the use of PIV for the measurement of the acoustic particle velocity and mean flow velocity. PIV is another non-intrusive optical method of measurement which is used extensively in fluid dynamics. PIV provides an almost instantaneous measurement of the Eulerian velocity vectors over a large plane of the flow[2].

The main aims in the PIV sections are to:

- develop the theory of Particle Image Velocimetry to show the form of the power spectrum and the autocorrelation plane for the case where the particle images are formed by the oscillation of the seeding particles.
- show that this would still allow the measurement of the flow velocity.
- investigate different methods for the measurement of the amplitude of oscillation from the power spectrum or the autocorrelation plane. The desired method has to work independent of the user and to give consistently accurate results.
- investigate the effect of different parameters on the measured value using computationally generated simulated images.
- show that the results obtained using simulated images are also valid for real images.
- use the method in an experiment and compare the experimental results with the expected results.

To fulfil these aims, the second section is broken down into the following chapters. The principles of PIV are discussed in chapter 6, the theory of PIV is studied in chapter 7 showing that it might be possible to measure the amplitude of the oscillation from the power spectrum and the autocorrelation plane. These possibilities are investigated

using simulated images in chapter 8 and various parameters such as the particle image size and the interrogation area size are investigated to see how they affect the measurements. The best method is determined using these simulated images.

The simulated images are compared with the experimental images in Chapter 9 to determine if the conclusions arrived at for simulated images are valid. The best method of analysing the negatives is then used on images from an experiment involving a standing wave in a tube. The amplitude and the flow velocity are measured from pictures obtained from the experiment.

The conclusions are in Chapter 10, which will discuss the two methods and compare them to determine the validity of each method.

The Appendices contain the mathematics of the stochastic model, the program listing for the analysis program and the papers submitted to journals.

Chapter 2

Acoustic background.

2.1 Introduction

In this chapter we will define the various acoustic quantities which are used to parameterise and describe sound fields. Expressions relating the velocity and pressure are developed and the theory of acoustic streaming is discussed.

2.2 Intensity and impedance:- the relationship between acoustic velocity and pressure

To completely define a sound field both the pressure, p, and the acoustic velocity, v, at any point must be determined, where p is the difference between the instantaneous and the equilibrium pressures, while v is the particle velocity or instantaneous velocity of a small element or particle of fluid. Both of these quantities are required for the evaluation of the impedance and the intensity but, although pressure is easily measured using small, cheap and accurate microphones, the measurement of acoustic particle velocity is more difficult [57].

The acoustic intensity which quantifies the transport of energy by the sound field is defined as

$$\mathbf{I} = < p\mathbf{u} > = \frac{1}{T}\int_0^T p\mathbf{u}dt \tag{2.1}$$

where the angled brackets indicate time averaging and the integral is taken over one cycle of the acoustic disturbance. The intensity is useful in applications such as deter-

mining the location of noise sources or sinks in industrial machinery (Bruel & Kjaer 1982b)[10].

The specific acoustic impedance, z , is defined as the ratio of the pressure to the acoustic particle velocity

$$z = \frac{p}{u} \tag{2.2}$$

When dealing with sound in pipes or horns however, it is more convenient to use the acoustic impedance which is defined, for a fluid acting on a surface of area S perpendicular to the direction of the acoustic particle velocity, as the complex quotient of the pressure at the surface divided by the volume velocity at the surface [36]

$$Z = \frac{p}{U} \tag{2.3}$$

where

$$U = Su \tag{2.4}$$

Equation (2.3) can also be written as

$$Z = |Z|e^{i\phi} \tag{2.5}$$

where $|Z|$ is the impedance amplitude and ϕ is the phase difference between the velocity and pressure. Acoustic impedance is closely analogous to electrical impedance with pressure and volume velocity corresponding to voltage and current respectively.

For a plane standing wave in a tube the particle velocity and pressure are out of phase and are simply related through

$$p = \mathbf{i}\rho_0 cu \tag{2.6}$$

where ρ_0 and c are the characteristic impedance of the medium and speed of sound in the medium respectively and $\mathbf{i}\rho_0 c$ is the specific acoustic impedance for a standing wave in a tube. For air at standard temperature and pressure $\rho_0 c$ takes the value 415 Pa.s/m. The acoustic pressure is not usually quoted as a pressure, but rather in terms

of sound pressure levels or intensities relating to some arbitrary reference level (usually the limit of hearing for the ear at 1kHz, 10^{-12}W/m^2, equivalent to 20.4 μPa).

For intensity levels measured in decibels

$$IL(db) = Intensity\ \ level = 10\log\left(\frac{I}{I_{ref}}\right) \tag{2.7}$$

Then, since the intensity and effective (r.m.s.) pressure for a standing wave are related through [36]

$$I = \frac{p_{rms}^2}{\rho_0 c} \tag{2.8}$$

we get

$$SOUND\ \ PRESSURE\ \ LEVEL(SPL) = 20\log\left(\frac{p_{rms}}{p_{ref}}\right) \tag{2.9}$$

If we note that $p_{ref}$is defined as 20μPa and that for a standing wave

$$p_{rms} = zu_{rms} \tag{2.10}$$

where u_{rms} is the r.m.s. velocity and z=415 Pa.s/m and both are imaginary since the pressure and the velocity are out of phase, then we can write (2.9) as

$$SPL = 20\log\left(\frac{zu_{rms}}{20\text{x}10^{-6}}\right) \tag{2.11}$$

or

$$u_{rms} = \frac{20\text{x}10^{-6}}{415}10^{\frac{SPL}{20}} \tag{2.12}$$

Since the velocity amplitude a_m is related to u_{rms} through $a_m = \sqrt{2}u_{rms}$ we can get

$$a_m = 0.0694\text{x}10^{0.05\,SPL-6} \tag{2.13}$$

It is thus possible for the SPL to be deduced from the acoustic particle velocity if the impedance of the system is known.

2.3 Sound intensity measurement when a flow is present.

As we noted before, the intensity can only be properly defined if we know the pressure and velocity at a point, or by controlling the sound field so that a simple known relationship exists between the them in which case pressure or velocity measurements alone become sufficient. Velocity measurements can be made either directly or indirectly. An indirect method involves the use of pressure gradient microphones, while direct methods include the use of Rayleigh Discs and Hot Wire Anemometry.

The indirect measurement of the acoustic intensity, which became feasible with the advent of cheap high speed digital signal processors, involves the use of two closely spaced microphones from which the pressure gradient can be estimated and transformed to a velocity using the equations of motion for the sound field [21,11]. This technique can also be extended to direct measurement of impedance and absorption [47]. This technique however suffers from a variety of drawbacks ranging from calibration difficulties, the need for empirical frequency corrections, directivity effects and assumptions which need to be made about the field under investigation. The introduction of a microphone can also upset the field under investigation.

The direct measurement of the velocity using Rayleigh Discs [53] involves the use of a thin disc, typically made of mica or brass of about 1cm diameter. This is suspended in the sound field and the acoustic velocity field acts on the disc to produce measurable torques of magnitude proportional to the mean square velocity. Such a device is, however, rather difficult to use and has a host of empirical correction factors and assumptions which have to be applied and accounted for [34,52,40]. Also, since the torque is proportional to the disc diameter, the disc cannot be arbitrarily small and will, therefore, produce significant distortions in the sound field.

The Hot-Wire Anemometer (HWA) is a common fluid velocity measuring device which relies on the cooling effect of a flow upon a thin electrically heated wire. The resistance of the wire varies with temperature and since a certain velocity of air flow over

the wire will cool it down by a distinct amount, the resistance of the wire will be related to the air velocity. The HWA has been successfully applied to the measurement of acoustic velocities to obtain some good results in the measurement of brass instrument input impedances (Pratt[50] and Elliot[20]). The experiments that Pratt and Elliott carried out showed that there was a small flow within the brass instruments (possibly due to the acoustic streaming caused by the high intensities needed to get reliable results from the HWA). The presence of this small flow is necessary for the measurement of the acoustic velocities using the HWA, since it is not possible for the probe to measure in zero-mean flows. The HWA also suffers from the drawbacks of calibration difficulties and, like all material probes, disturbance of the sound field.

2.4 Acoustic streaming

It is well known that a sound wave does not in general propagate unchanged, even in the case of an infinite plane wave. Firstly, energy will be dissipated due to diffusion (viscosity, thermal conductivity and other relaxation effects), so that the plane wave becomes attenuated, and secondly a sound wave of finite amplitude will be deformed as energy will be transferred, as the wave is convected, to higher harmonics as the wave propagates. In the linear case, where diffusion and convection are neglected, the plane wave will be unchanged. To a first approximation, where convection is neglected, the wave becomes attenuated only, and a monochromatic wave preserves its form. At a higher approximation the wave will be both attenuated and deformed as it propagates; convection leads to an energy transfer from lower to higher harmonics and diffusion gives rise to a damping which is more pronounced at the higher frequencies. So in a weak sound field, the maximum of energy is to be found at lower and lower frequency as the sound propagates through the medium, and for a strong sound field, where the convection affects the sound field more than the diffusion, we would expect the energy to be transferred to higher frequencies as we travel away from the source. In monochromatic sources the importance of convection is determined by the Mach number ($M = \frac{a_m}{c}$, where c is the isotropic speed of sound and a_m is the velocity

amplitude (acoustic particle velocity)) compared with unity. If $M << 1$ the effect of convection is negligible. The importance of diffusion is determined by the Stokes number ($S = \frac{\mu\omega}{\rho c^2}$, where μ is the coefficient of shear viscosity, ω is the angular frequency and ρ is the density of the fluid) compared with unity. For $S << 1$ the diffusion effects are in most cases negligible.

It is also well established experimentally that in addition to the to-and-fro motion of the fluid elements in a sound field, a pattern of time-independent circulation of the fluid traversed by the sound can be set-up. This circulation is referred to as acoustic streaming. There are two kinds of such streaming, one occurring near solid boundaries with which a sound wave is allowed to interact, or near solid boundaries which are oscillating, the other produced by the interaction of a free progressing beam of sound waves with the surrounding fluid. In the first case the linearised motion will be vortical in the vicinity of the solid boundaries (i.e. within the "acoustic boundary layer" defined as being of the order of magnitude $\delta = \sqrt{\frac{2\mu}{\rho\omega}}$. Outside this boundary layer the motion is irrotational to the first order. In the case of a sound beam, we are usually justified in assuming that the motion is also irrotational to the first order. The acoustic streaming cannot be explained using only linear terms, since all first order quantities are periodic with time and cannot produce a mean motion. The explanation for acoustic streaming is therefore found from the higher approximations of the Navier Stokes equation.

Acoustic streaming of the first kind was observed by Faraday and Dvorak (discussed in Rayleigh's book[53]) in the last century, and theoretical studies of these streaming phenomena were first undertaken by Rayleigh who applied the method of successive approximations in the solving of the differential equations governing the motion of the fluid. The linearised equations of motion were used as the first approximation and by solving the equations to the second approximation Rayleigh was able to explain some of the effects observed in the boundary layers near solid bodies. Thus the streaming pattern of Kundt's tube, indicated by observations of Dvorak, was predicted. This was later confirmed experimentally by Andrade [5]. When introducing small solid obstacles in the form of cylinders and spheres in a sound field, Andrade also observed a flow of air in the vicinity of these obstacles.

Westervelt and Nyborg [68,48] introduced new forms of the theory which took into account discrepancies with Rayleigh's work, and Schlichting [54] developed the forms of the acoustic boundary layer.

Acoustic streaming accompanying a beam of sound, or the "Quartz wind" as it was called for a long time, is a time independent circulation of the fluid frequently observed near a high intensity beam of sound. Meissener [45] observed such streaming near quartz oscillators, and explained it as due to a "pumping action" by the quartz crystal. Later however, it was observed that the streaming took place near the beam of sound even if the sound source was screened by thin films transparent to the radiation, but preventing fluid near the source entering the region. The measured force varied greatly with the distance and it became clear that the streaming had to be ascribed to forces acting directly on the fluid and it was likely to be associated with the mechanism of radiation pressure.

The first theoretical analysis of the streaming associated with a beam of sound was given by Eckart [19]. He used the method of successive approximations to solve the equations of motion and showed that the streaming caused by sound waves could be regarded as formed by generation of steady vortices of the second order. The vortices were generated, due to viscous forces, by a transfer of angular momentum from the wave motions to the fluid by viscous force. In the analysis by Eckart it is presupposed that the motion is isentropic and he also neglects, a priori, the effect on the streaming due to the variation of the coefficients of viscosity μ, μ' and $\xi = \mu' + \frac{2}{3}\mu$, with the density changes due to the sound waves. It was found that the forces which generate the vortices depend on both the coefficient of the shear and bulk viscosity, while the forces resisting the vortical motion depend on the coefficient of shear viscosity only. It was suggested that a study of the streaming phenomena could provide a method for determining the ratio of the bulk and shear coefficients of viscosity. Liebermann [40] following this suggestion, studied experimentally the streaming caused by a collimated sound beam, and determined the ratio of the second coefficient of viscosity (μ')to the coefficient of shear viscosity for water and a number of organic liquids. The result was

that the viscous number $V = 2 + \frac{\mu'}{\mu} = \frac{4}{3} + \frac{\xi}{\mu}$ is larger than 4/3 and consequently $\xi > 0$ for the liquids studied.

The works by Eckart and Liebermann have been followed by similar studies by several investigators. Markham [43] extended the theory to take into account the relaxation processes. The equation of state $\nabla p = c_0^2 \nabla \rho$ used by Eckart was replaced by the relation $p_1 = c_0^2 \rho_1 + R.\frac{\delta \rho_1}{\delta t}$ where R is defined as a relaxation factor, generally a function of frequency. Thus the influence of the quartz wind on the thermal conductivity in the sound wave could be accounted for by considering the conductivity as a relaxation phenomenon. It was concluded [48,68,44,13] that the streaming velocity is determined by the coefficient of sound absorption rather than by the two coefficients of viscosity only. With this modification Medwin[44] studied streaming in gases and found, especially for the monotonic gas argon, that the shear viscosity and thermal conductivity alone accounted for the observed streaming velocity within an error of four percent, the frequency being 185kHz. This leads to the result that the coefficient of bulk viscosity (ξ) is equal to zero within the error mentioned.

It was Stuart [60] who pioneered the idea that, when the Reynolds number R_s, given by $\rho_0 U_s l/\mu$, is large, we can, and indeed must, use the full equation of motion, including the important inertia term. Lighthill [41] refers to "Stuart streaming" to describe streaming motions calculated using the full equation.

It is hardly an exaggeration to say that all really noticeable streaming motions especially those generated by ultrasonic sources, are Stuart streaming. Acoustic streaming is Rayleigh Nyborg Westervelt streaming at low intensities, but as the power increases Stuart streaming develops.

We shall mainly be interested in RNW streaming and it is hoped that the methods developed within this thesis will be used to measure these phenomena.

Chapter 3

Considerations when using Laser Doppler Anemometry for acoustic measurement

3.1 Introduction

As we saw in chapter 2, conventional techniques for measuring superimposed flow velocity and acoustic particle velocity suffer from a variety of drawbacks. Consequently we shall look to direct optical techniques which will perhaps surmount these difficulties. The Laser Doppler Anemometry technique (LDA) provides a non-intrusive method of measuring the absolute value of the velocities. The direction of the velocity will be in the direction perpendicular to the fringes formed by the crossed laser beams, but the sense of the direction has to be deduced from the knowledge of the flow unless a technique such as frequency shifting is used. There are two main disadvantages to LDA, firstly we need optical access to the flow and secondly, we need scattering centres seeded into the flow and it is the velocity of these seeded particles which is measured. In some cases the dust particles naturally present in the air will be sufficient, but in most cases the flow has to be seeded.

In this chapter, the techniques and various configurations for LDA will be discussed to explain our choice of the photon correlation method. The measurement accuracy,

speed and ease of method will be considered before we move on to derive the form of the anemometer output signal function for the velocity distribution in order that the correlation function will be understood.

3.2 Principle of the LDA technique.

The principle of LDA is relatively simple: laser light is projected into the flow under investigation, it is scattered from small particles which are either introduced, or already present in the flow and which follow the flow faithfully. The Doppler shift imposed on the light is then analysed to reveal the fluid velocity. The technique has been used since Yeh in 1964 [69] so there has been considerable work done on both optical design and signal processing. There are several books available which give excellent introductions to this work Durst et al., Watrasiewicz et al., Drain and Durrani and Greated [18,67, 17,14] in particular will be referenced frequently.

LDA systems fall into two types - reference beam heterodyne mode and crossed beam mode (Figure(3–1)). In the heterodyne mode the light scattered from the moving particles undergoes a Doppler shift which combines with the reference beam frequency, and the resultant beat frequency is analysed to deduce the flow velocity. In the crossed beam, or differential Doppler, mode both beams interfere forming an area of fringes. As the seeding particle pass through this, the particles scatter the light and this is detected by a photomultiplier.

The Laser Doppler technique has many applications in fluid dynamics where the great advantages are that there is no obstruction to the flow and spatial resolution is very high. Nothing but light is needed to be positioned at the point of interest and the light from a laser can be focussed to a very small volume where the velocity is to be measured. Typical resolution is 20-100μm which exceeds that obtainable by any other method.

Since Yeh and Cummins's initial work, there have been many developments of the optical configurations and signal processing, so it would take a long time to cover them

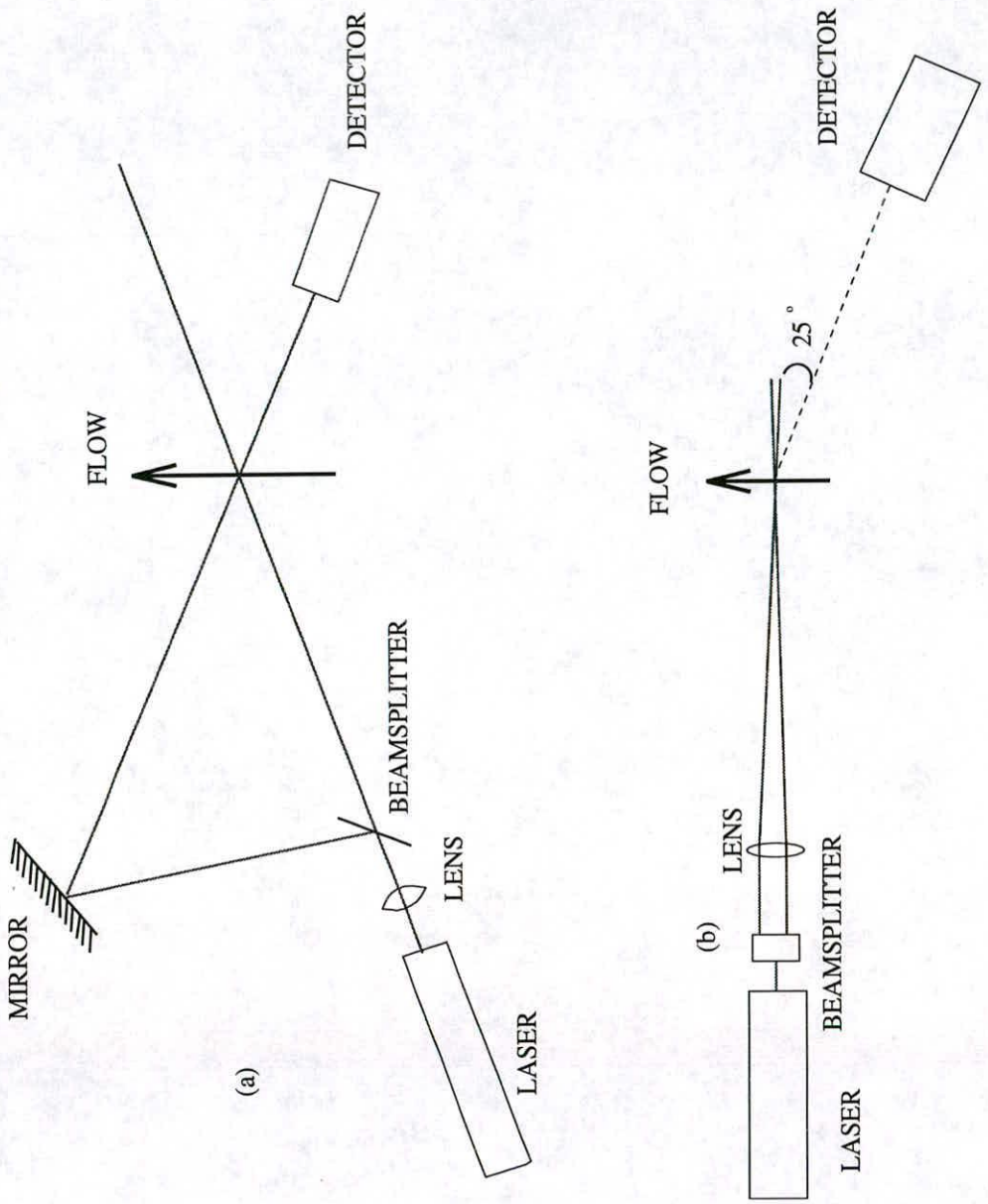

Figure 3–1: LDA configurations. (a) Heterodyne mode. (b) Crossed beam mode.

all here, so we will only mention some of the arrangements. The references [18,67,14, 17] will give a good background of other arrangements and methods.

3.3 Optical considerations

Of the two arrangements mentioned in the previous section, we are interested more in the Differential Doppler system for several reasons.

Firstly, this configuration is more suited to low concentration flows, since it has a higher signal to noise ratio. We do not wish to seed the flow heavily, since the presence of large seeding concentrations affects the flows [42,63], so a high signal to noise ratio is an advantage. Secondly we can use large collection optics which can increase the sensitivity when we have a low seeding density. Thirdly, the optics are much easier to align. The Doppler signal can be detected at any angle so the photomultiplier can be positioned to avoid the flare from the ends of the tube.

As noted before, the measuring volume can be very small which means that, to a good approximation, the flow velocity changes little over the area of measuring. We do have some turbulence in our measurements, but this is quite a small factor as long as we are well outside the boundary layer.

The range of velocities that can be measured depends in part on the fringe spacing. For the flow velocity, a large spacing will be good for measuring a slow velocity, while a small spacing will be good for the measurement of a fast velocity. For sound fields, the displacements of the particles during the oscillation should ideally be of the order of a half of the fringe spacing. This gives a higher than actual measuring limit, since the technique can work at smaller displacement, but it does give a useful rule of thumb estimate for the lower limit of the technique.

In a crossed beam system the fringe spacing can easily be shown to be that shown in equation (3.1)

$$d = \frac{\lambda}{2 \sin \theta} \tag{3.1}$$

where λ is the laser light wavelength and θ the half angle between the beams. If a particle is passing through the fringe pattern with velocity U, the frequency of the

scattered light pulses is

$$\omega = \frac{4\pi U \sin\theta}{\lambda} = DU \tag{3.2}$$

where D is known as the velocity to frequency conversion factor. This means that if we can determine the frequency of the light pulses scattered by the seeding particles as they pass through the fringes, we can calculate the velocity if the wavelength of the light and the intersection angle of the beams is known.

3.4 Signal processing considerations

The signal from a Laser Doppler Anemometer can be analysed in the frequency or the time domains. The various methods are frequency tracking, frequency analysis and photon correlation spectroscopy.

Frequency analysis is a commonly used LDA technique which involves amplifying the photomultiplier signal,mixing it with an oscillator frequency, f_{os}, and viewing it using a filter of centre frequency, f_{os}, and bandwidth Δf_o. The frequency f_{os} is changed with time according to a prearranged sweep time. The analyser sweeps many times to build up a signal which is proportional to the square root of the velocity density distribution.

Taylor [61,62] however showed, that the signal obtained from the frequency analysis for flow and sound fields superimposed is very complicated and it is also known that because of the stochastic nature of the scattering process a swept frequency measurement device could have no particles in the fringe pattern when any particular frequency range was being observed. This is called "Drop-out"and will cause some problems in the analysis and so the concentration of the seeding has to be dense enough so that there is a very low probability of there being no seeding particles in the interrogation area.

Frequency tracking is based on the principle shown in Figure (3–2). The Voltage Controlled Oscillator (VCO) provides a continuous signal which is mixed with the Doppler signal and passed through a narrow band filter which is normally pre-set to a

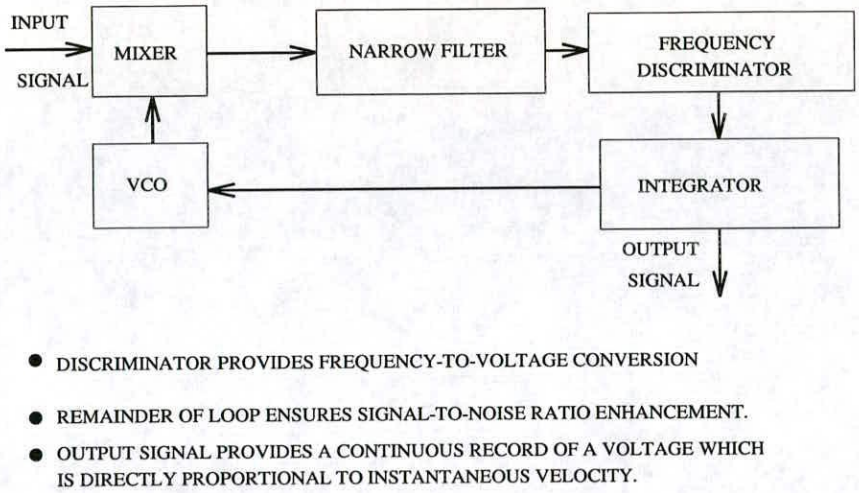

Figure 3–2: Principles of frequency tracking

specific value. Variations in the frequency of the Doppler signal are compensated by the VCO and the output signal, provided the loop has been properly designed, is proportional to the instantaneous Doppler frequency and, therefore to the instantaneous velocity.

A near–continuous input signal is normally required and, if this is not available, a drop-out mechanism is employed to hold the last signal until a new signal arrives. However, this can lead to erroneous signals, and so a large particle concentration is desired.

In cases where the intensity of the scattered light and/or the signal to noise ratio is very low, photon correlation spectroscopy offers particular advantages. The photomultiplier amplifies each photoelectron leaving the cathode material. The average number of these pulses is linearly related to the intensity of the scattered light. If the intensity is low, the average number of photons reaching the photocathode can be such that single pulses reach the anode at times which are well separated. A statistically viable sample of these signals will show a sinusoidal variation in the photon arrival rate due to the intensity variation across the fringe pattern in the measuring volume.

As the scattered light intensity increases, the average photon arrival rate at the cathode increases yielding overlapping of the electron pulses at the anode. The contributions from single pulses will add and, at the anode, only the resultant signal will

be detected: this will be essentially a continuous current at high light intensities. If this current is fed through the load resistor of the photodetector, a voltage signal is obtained which is proportional to the instantaneous anode current. Intensity variations in the scattered light yield voltage variations at the photomultiplier output. The output is autocorrelated and this produces an output which can be analysed to give the flow velocity.

We will choose to use the photon counter correlator which computes the correlation function from the individual photons scattered from the fringe pattern. This type of processing is better at the low light levels than frequency techniques and can deal with smaller signal to noise ratios.

3.5 Tracking of particles suspended in an acoustic field

For LDA and later for PIV we have to understand the characteristics and behaviour of particles suspended in fluids with regards to their suitability for use as seeding particles. Earlier we have made it clear that LDA depends on signals from particles suspended in the flow, rather than signals from the fluid itself. Since the experimenter wishes to know the velocity of the fluid rather than the velocity of the suspended particles, it is important to know how well the motion of the suspended particles represents the motion of the fluid.

Hjelmfelt and Mockros [32] and Hinze [30] showed that the ratio of the velocity of a seeding particle to the local velocity of the fluid is determined by the density ratio $s = \frac{\rho_p}{\rho_f}$ and the Stokes number $N_s = \frac{\mu}{\rho_f \omega d_p}^{1/2}$, thus the response of a particle of diameter d_p and density ρ_p to the fluid fluctuations of angular frequency ω is determined by these parameters only.

Brandt et al [9] showed that for spherical particles with the force exerted on the particles by the vibrating medium obeying the Stokes-Cunningham Law, then the ratio

of the velocities will be

$$\frac{V_p}{V_m} = \left[\left(\frac{4\pi r^2 \rho \omega F}{9\eta}\right) + 1\right]^{\frac{1}{2}} \tag{3.3}$$

for a sinusoidal vibration, where V_p and V_m are the velocity amplitudes of the particles and the medium respectively, r is the radius of the particles and ρ their density, ω the frequency of the sound, η the viscosity of the medium, and F the Cunningham correction factor. This allows us to predict what the limiting size for particles of a particular density is, so that the seeding particles can be chosen so that they are smaller than this in order that they will follow the medium at that particular frequency.

For smoke particles of density 1000kg/m^3 and size 1μm in air, the particles will follow the air to within 1% up to approximately 8kHz, well within the range of frequencies used in this Thesis. Even at 2μm the particles will follow the field to 5% up to 4kHz.

Particle sizes below 1μm can in fact be easily generated. Tobacco smoke, which is what we used, typically has particle diameters of less than 0.4μm, if the smoke is less than about 4 minutes old [35]. Particles of this size will allow sound fields of up to 10kHz to be investigated.

It is also possible, when using the very sensitive photon correlation technique, to dispense with seeding particles altogether and just use the naturally occurring "dust" particles in the air. These are typically submicron, which can be advantageous if it is inconvenient to introduce artificial seeding, and should be borne in mind when deciding on the optical system. The effect of "drop-out" is not relevant because it is an intermittent process which will be averaged out over the relatively long time period of the photon correlation measurement.

3.6 Conclusion

We have discussed some of the methods used in LDA and decided that the photon correlation method will be the best one to pursue since the signal-to-noise ratio is high, so that heavy seeding is not required, drop-out is no longer a problem because we are averaging over a long time, and the combined field can be measured more easily.

Chapter 4

The Derivation of the theoretical correlation function for the time averaged sound and velocity fields.

4.1 Introduction

We shall now deduce the form of the output signal and correlation function appropriate to the Differential Doppler system and the photon correlation method of signal analysis.

The flow is of the form

$$U = a_0 + a_m \sin \omega\tau \tag{4.1}$$

and we wish to be able to find the mean flow velocity (a_0) and the acoustic particle velocity (a_m, the velocity amplitude of the sinusoidal oscillation) from the correlation function.

The approach will be that used by Sharpe et al. [56] involving the integration of the probability density function over the velocity dependent autocorrelation function for the fringe geometry under investigation. This well known stochastic method follows the method of Durrani and Greated (1977) [17] and is strictly only applicable to quasi-steady flows in which the velocity does not change "too much" as it travels over the fringe pattern. Sharpe used the method to derive the correlation function for the sound field only, which should be a special case of this more general form.

We should also expect the form to be similar to the correlation function derived by Durrani and Greated (1977) and Barnes et al. [7] on the assumption that the flow velocity was much greater than the oscillatory velocity(Equation (4.2)).

$$R(\tau) \propto J_0(Da_m\tau)\cos(Da_0\tau) \tag{4.2}$$

D is the velocity to frequency conversion factor defined in equation (3.2). This is also the form of the function if some velocity shifting is done on a system with a sound field only.

This can be analysed by consideration of the peaks and turning points of the flow, or by transforming into the Fourier plane where this will form two peaks at frequencies proportional to $a_0 + a_m$ and $a_0 - a_m$, in which $a_0 >> a_m$.

4.2 Time averaged correlation functions for sinusoidal oscillations superimposed on a mean flow.

As we have stated before, the aim is to develop a stochastic model for the correlation function so that its form, when there is a mean flow superimposed on a sinusoidal oscillation, can be understood for all cases of a_0 and a_m.

Let us write the output from the detector associated with any p^{th} particle in the observation volume as that given in equation (4.3) [17].

$$x_p(t) = \kappa K_p W(\beta\xi_p(t))(M + \cos D\xi_p(t)). \tag{4.3}$$

κ is a constant associated with the optical power and detector sensitivity, K_p characterises the particle scattering cross section, M is a constant introduced if the beams are not of equal strength and $\xi_p(t)$ is the particle position at time t and $W(\beta\xi_p(t))$ is the spatial weight function which represents the envelope on the fringes due to the Gaussian cross section of the laser beams (equation (4.4)).

$$W(\beta\xi_p(t)) = \exp(-\beta^2\xi_p^2(t)) \tag{4.4}$$

The total output is then

$$x(t) = \kappa \sum_p K_p W(\beta \xi_p(t))(M + \cos D\xi_p(t)) \tag{4.5}$$

where

$$\beta = \frac{\cos\theta}{r_0}.$$

and

$$D = \frac{4\pi \sin\theta}{\lambda}$$

Here r_0 is the radius at the e^{-2} intensity points of the beam waist. In order to understand the scales of this a little better we could put some numbers into these equations. Using the values used in the experiment in Chapter 5, r_0 is of the order of 0.1mm, and this can be compared to the fringe spacing used which is of the order of 4μm . For the 675Hz standing wave at 129.77dB as in the experiment set up, the amplitude of the oscillation is of the order of 20μm, so the oscillating particle passes through many fringes in one cycle.

In equation (4.5) the low-frequency term has been retained. This can be filtered out since it is not necessary, but for this derivation it will be retained.

To determine the autocorrelation function for $x(t)$ we write ξ_p as the initial particle position (at time $t = 0$) and ζ_p as its position at time τ later (equation (4.6)).

$$\zeta_p = \xi_p + \int_0^\tau v_p(z)dz = \xi_p + \eta_p(\tau) \tag{4.6}$$

$v_p(z)$ is the instantaneous velocity of the p^{th} particle which in this case is

$$v_p(z) = a_0 + a_m \sin(\omega_m z + \psi). \tag{4.7}$$

ψ is a random phase. We are interested in recovering the velocity amplitude a_m and the mean flow velocity a_0.

Following the derivation of Durrani and Greated(1977)[17, section 3.3] in which it was assumed that ζ and ξ are independent random variables, since the position of a particle depends only on its own previous position and its instantaneous velocity (i.e.we assume there are no collisions in the measuring volume) we find that the autocorrelation function of the output voltage of the photomultiplier is

$$\begin{aligned} R(\tau) &= E[x(t)x(t+\tau)] \\ &= [\kappa C_0 g_0 \int_{-\infty}^{\infty} W(\beta y)(M+\cos Dy)dy]^2 \\ &\quad + \frac{\kappa^2 C_1 g_0}{2} \int_{-\infty}^{\infty} p_\eta(y;\tau) R_w(\beta y)(M+\cos Dy)dy \end{aligned} \tag{4.8}$$

where $E[\,]$ is the expectation operator, $C_0 = E[K_p], C_1 = E[K_p^2], g_0$ is the average number of particles per unit length of the measuring volume and $R_w(\beta y)$ is the autocorrelation of the spatial weighting function of a Gaussian beam system, given by

$$R_w(\beta y) = \sqrt{\frac{\pi}{2\beta^2}} \exp(-\frac{\beta^2 y^2}{2}).$$

Here $p_\eta(y;t)$ is the probability density function of the variable $\eta(t)$ which must be determined in order to evaluate the autocorrelation function. This is done below, but first we note that the first term in equation (4.8) is the square of the mean value of the Doppler signal. This will be ignored since it is time independent and so will only contribute a constant or pedestal to the correlation function.

From equations (4.6) and (4.7) we have

$$\eta_p(\tau) = a_0\tau + a_m \int_0^\tau \sin(\omega_m z + \psi)dz = a_0\tau + \frac{2a_m}{\omega_m}\left[\sin(\frac{\omega_m \tau}{2})\sin(\frac{\omega_m \tau}{2} + \psi)\right] \tag{4.9}$$

where ψ is a random variable uniformly distributed over the interval $0 - 2\pi$:

$$p(\psi) = \frac{1}{2\pi}, \qquad 0 < \psi < 2\pi.$$

We can use the relationship for a function of random variables to obtain

$$p_\eta(y;\tau) = \frac{1}{\pi\sqrt{A_m^2 - (y - a_0\tau)^2}}, \qquad -y + a_0\tau \le A_m \le y - a_0\tau$$

$$A_m = \frac{2a_m}{\omega_m}\sin(\frac{\omega_m \tau}{2}).$$

If we ignore the constant term then equation (4.8) takes the form

$$R(\tau) = \sqrt{\frac{\pi\kappa^4 C_1^2 g_0^2}{8\beta^2}} \int_{a_0\tau - A_m}^{a_0\tau + A_m} \frac{dy}{\pi\sqrt{A_m^2 - (y - a_0\tau)^2}} \exp\left(\frac{-\beta^2 y^2}{2}\right)(M + \cos Dy). \tag{4.10}$$

If we proceed to evaluate by substitution of $y = a_0\tau + A_m \sin\omega\tau$ and solve (See Appendix A), we get:

$$\begin{aligned}
R(\tau) &= \frac{\kappa^2 C_1 g_0}{2}\sqrt{\frac{\pi}{2\beta^2}}\exp\left(-\frac{\beta^2 A_m^2}{4}\right)\exp\left(-\frac{\beta^2 a_0^2\tau^2}{2}\right) \\
&\Big[M\left\{I_0\left(\frac{\beta^2 A_m^2}{4}\right)I_0(\beta^2 A_m a_0\tau) + 2\sum_{n=1}^{\infty}(-1)^n I_n\left(\frac{\beta^2 A_m^2}{4}\right)I_{2n}(\beta^2 A_m a_0\tau)\right\} \\
&+I_0\left(\frac{\beta^2 A_m^2}{4}\right)\cos(Da_0\tau)J_0\left(A_m\sqrt{D^2-\beta^4 a_0^2\tau^2}\right) \\
&+2\cos(Da_0\tau)\sum_{k=1}^{\infty}J_{2k}(DA_m)\sum_{n=1}^{\infty}I_n\left(\frac{\beta^2 A_m^2}{4}\right)(-1)^{n-k}I_{2(n-k)}(\beta^2 A_m a_0\tau) \\
&+2\cos(Da_0\tau)\sum_{k=1}^{\infty}J_{2k}(DA_m)\sum_{n=1}^{\infty}I_n\left(\frac{\beta^2 A_m^2}{4}\right)(-1)^{n+k}I_{2(n+k)}(\beta^2 A_m a_0\tau) \\
&+2\sin(Da_0\tau)\sum_{k=0}^{\infty}J_{2k+1}(DA_m)\sum_{n=1}^{\infty}I_n\left(\frac{\beta^2 A_m^2}{4}\right)(-1)^{n+k}I_{2n+2k+1}(\beta^2 a_0 A_m\tau) \\
&+2\sin(Da_0\tau)\sum_{k=0}^{\infty}J_{2k+1}(DA_m)\sum_{n=1}^{\infty}I_n\left(\frac{\beta^2 A_m^2}{4}\right)(-1)^{n-k}I_{2n-2k+1}(\beta^2 a_0 A_m\tau)\Big] \quad (4.11)
\end{aligned}$$

This is the full expression for the time-dependent part of the autocorrelation function. From this three important limiting cases can be seen.

If we consider a situation with zero mean flow,i.e. $a_0 = 0$, then the expression becomes

$$\begin{aligned}
R(\tau) &= \frac{\kappa^2 C_1 g_0}{2}\sqrt{\frac{\pi}{2\beta^2}}\exp\left(-\frac{\beta^2 A_m^2}{4}\right) \\
&\left[I_0\left(\frac{\beta^2 A_m^2}{4}\right)(M + J_0(DA_m)) + 2\sum_{k=1}^{\infty}I_k\left(\frac{\beta^2 A_m^2}{4}\right)J_{2k}(DA_m)\right]. \quad (4.12)
\end{aligned}$$

This is exactly the expression calculated in Sharpe and Greated (1989) [56] for a periodic acoustic field. The equation can be simplified by taking typical values of β and a_m . For example, for a laser beam of unfocussed e^{-1} width 0.5mm focussed from 2cm separation using a 20cm focal length lens, β takes the value 25000. If this is put into the equation above and we consider the behaviour of $e^{-x}I_n(x)$ [65] for small values of x, this approximates to

$$R(\tau) \propto J_0(DA_m). \quad (4.13)$$

Since we generally are concerned with cases where $\omega_m\tau$ is small we can approximate

$$A_m = \frac{2a_m}{\omega_m}\sin\left(\frac{\omega_m\tau}{2}\right) \approx a_m\tau \quad .$$

This allows Equation (4.13) to become

$$R(\tau) \propto J_0(Da_m\tau). \tag{4.14}$$

If there is no acoustic field present, i.e. $a_m = 0$,then the equation (4.11) becomes

$$R(\tau) = \frac{\kappa^2 C_1 g_0}{2}\sqrt{\frac{\pi}{2\beta^2}}\exp\left(-\frac{\beta^2 a_0^2\tau^2}{2}\right)(M + \cos(Da_0\tau)) \tag{4.15}$$

This is the correlation function for a non-turbulent flow [1,17].

If we now consider a combined flow with typical magnitudes for β, a_m and a_0 then again the expression can be simplified. If we consider the behaviour of $e^{-x}I_n(x)$ for small values of x [65] and note the $\omega_m\tau$ is also small we can show that the correlation function $R(\tau)$ approximates to ;

$$\begin{aligned} R(\tau) &= \frac{\kappa^2 C_1 g_0}{2}\sqrt{\frac{\pi}{2\beta^2}}\exp\left(-\frac{\beta^2\tau^2(a_0^2 + \frac{a_m^2}{2})}{2}\right) \\ &\quad \left[M + cos(Da_0\tau)J_0\left(a_m\tau\sqrt{D^2 - \beta^4 a_0^2\tau^2}\right)\right] \end{aligned} \tag{4.16}$$

This is very close to equation (4.2) with the only difference being the extra term in the Bessel function which is dependent on the velocity of the flow. This extra term is much smaller than the other term ($D^2 \sim 10^{12}$, $\beta^4 a_0^2\tau^2 \sim 10^8$ for typical values of β, D, τ and a_0 that were used in our experiments), although it could be comparable for certain arrangements where β is large and D is smaller. This equation shows the form of the theoretical correlation function for all values of a_0 and a_m.

Chapter 5

Experiments to verify the theoretical model

5.1 Introduction

In this chapter we shall compare the results of experiments with the theoretical results developed in the previous chapter. We shall look at several cases of flow and sound field interaction. Firstly we shall consider the case in which the flow and sound field are generated separately, and we shall show that the model holds for a non-zero mean flow which is much larger than the acoustic particle velocity, as was shown by Barnes et al. [7]. Then, we shall consider the case were the mean flow velocity is smaller than the acoustic particle velocity.

We shall then briefly use the technique for the measurement of the mean flow and acoustic particle velocities in an organ pipe to show the changes that the sound field produces on the expected flow through the pipe.

5.2 Experiment to compare the theoretical expression with the measured expression

5.2.1 Experimental details

The validity of Equation (4.16) was tested in a series of experiments in which the flow and sound field were introduced independently into the tube. The correlation function of the combined field was measured and compared to the theoretical expression obtained in the previous chapter.

Figure (5–1) shows a schematic diagram of the apparatus used to produce the combined flow. The loudspeaker is positioned at the end of a brass branching section, with one of the branches leading along a 2 meter tube to a air pump which could blow or suck air and had a clamp which would allow the velocity of the flow to be adjusted. The other branch leads to a 70cm long glass tube of diameter 2.5cm which was open at the other end. A standing wave of frequency 675 Hz was measured using a probe microphone and the frequency was not changed for the rest of the experiment.

For the optical measuring system a 15 mW He-Ne laser was used as a light source, its beam being split into two parallel components 26mm apart which were then focused into the tube by a lens of focal length 153mm.

The LDA setup that we used here only measures the component of the velocity along the tube, so the point of focus was positioned on the axis where the velocity would be purely along the tube. Since the acoustic particle velocity is zero at a velocity node the cross over point was positioned at a velocity anti-node, about 5cm from the end of the tube, where the acoustic particle velocity would be maximum.

The photomultiplier was aligned at approximately 25° to the optical axis and then focussed onto the cross-over point. The signal from the photomultiplier was sent to a photon correlator where the signal was processed to produce the correlograms.

We shall use the separate nature of the sound and flow production to set up two cases, the first has the acoustic particle velocity less than the mean flow velocity, and

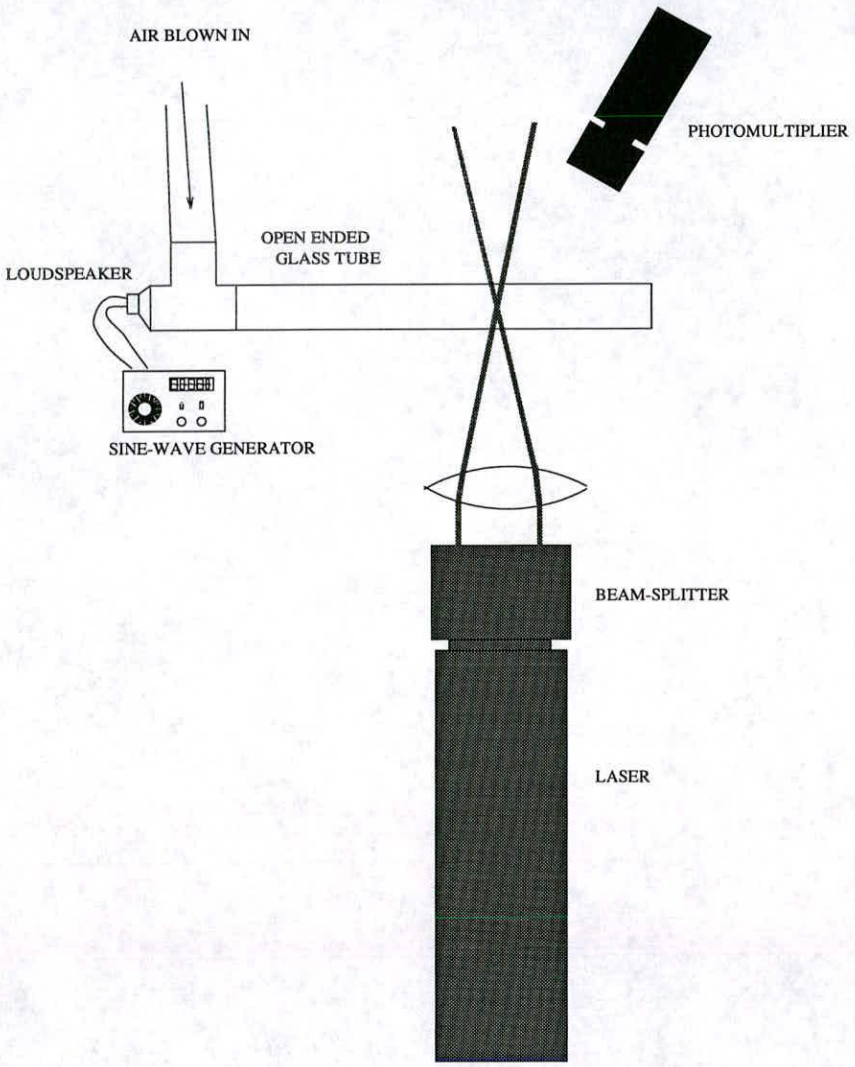

Figure 5–1: Schematic diagram of the apparatus used

the second has the mean flow velocity much less than the acoustic particle velocity. The flow will effect the standing wave to some extent, but this is not the object of this simple experiment, and so will not be taken into account.

The correlation functions for these cases were measured and compared to the theoretical curves expected, and then the correlograms were Fourier transformed into the frequency domain to allow easier analysis.

5.2.2 Results

$$D = \frac{4\pi \sin\theta}{\lambda} = 1.69\text{x}10^{6} m^{-1} \tag{5.1}$$

The correlograms measured were entered into a computer and these are shown in Figures (5–2 and 5–3). In order to analyse these graphs it is necessary to know whether the acoustic particle velocity is greater than the mean flow velocity or vice versa. Usually this can be determined from our knowledge of the flow as in this experiment, but it should be noted that it is also possible to determine this from consideration of the turning points of the two different types of correlation function. Table (5–1) shows how the position of the peaks and zeros of Bessel and cosine functions area related to one another. The Bessel function peaks and the cosine peaks are spaced evenly, with the positions between successive peaks being of the order of 1:2:3. The zeros of the Bessel function are positioned at a ratio of 1:2:3 to each other, while the zeros of the cosine are placed at a ratio of 1:3:5. Thus if the Bessel function argument is smaller ($a_m < a_0$) then the turning points are evenly spaced (see Figure (5–2) where the turning points are at 21:45). If the cosine function argument is smaller ($a_0 < a_m$) then the turning points are spaced at a ratio of 1:3:5 (see Figure (5–3) where first two turning points are at 20:60). This allows us to determine the type of flow we are looking at if we do not know whether the flow or acoustic particle velocity is the larger. So we can determine which function is which, by analysing the positions of the turning points and then relating them to an argument of the Bessel function or the cosine function. Another possible way of analysing them is to Fourier transform them into the frequency domain. This utilises all the data in the correlogram and produces two peaks (Figures (5–4) and (5–5)) at frequencies directly proportional to either $a_m + a_0$

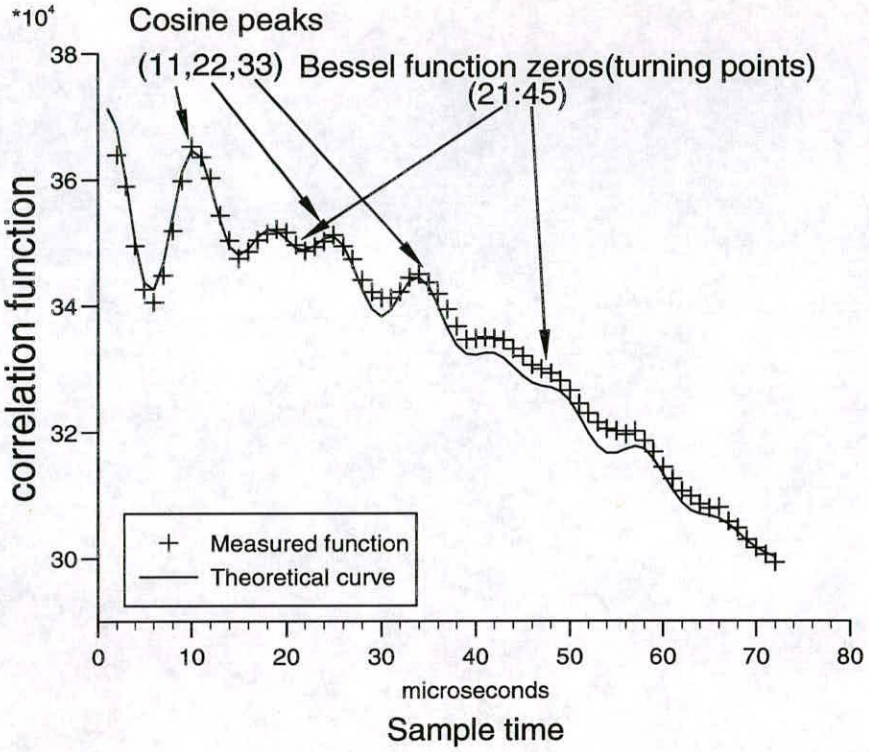

Figure 5–2: Theoretical and experimental correlation functions for combined flow when the acoustic particle velocity is smaller than mean flow velocity. Theoretical function with a_0=0.39ms^{-1}, a_m = 0.075ms^{-1}

Bessel fn peaks $J_0'(x)=0$	cosine peaks cos'(x)=0	Bessel zeros $J_0(x)=0$	cosine zeros cos(x)=0
3.8317	3.14159	2.4048	1.57079
7.0156	6.28319	5.5201	4.71239
10.1735	9.42478	8.6537	7.85398

Table 5–1: The zeros of the zero order Bessel function and the cosine function and their first derivatives

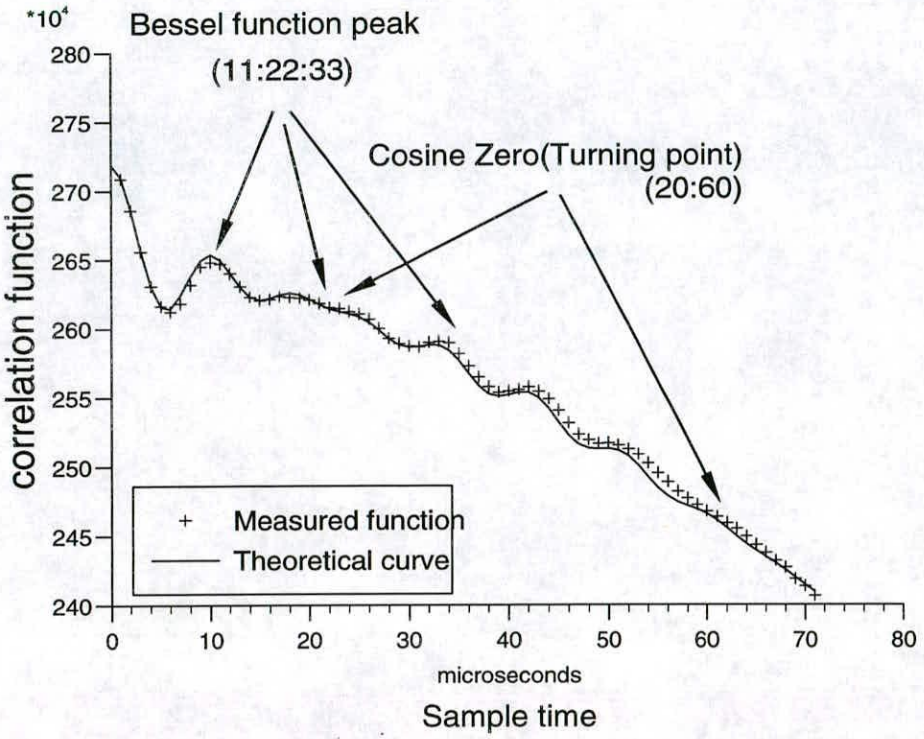

Figure 5–3: Theoretical and experimental correlation functions for combined flow when acoustic particle velocity is larger than mean flow velocity. Theoretical function with a_0=0.042ms^{-1}, a_m = 0.40ms^{-1}

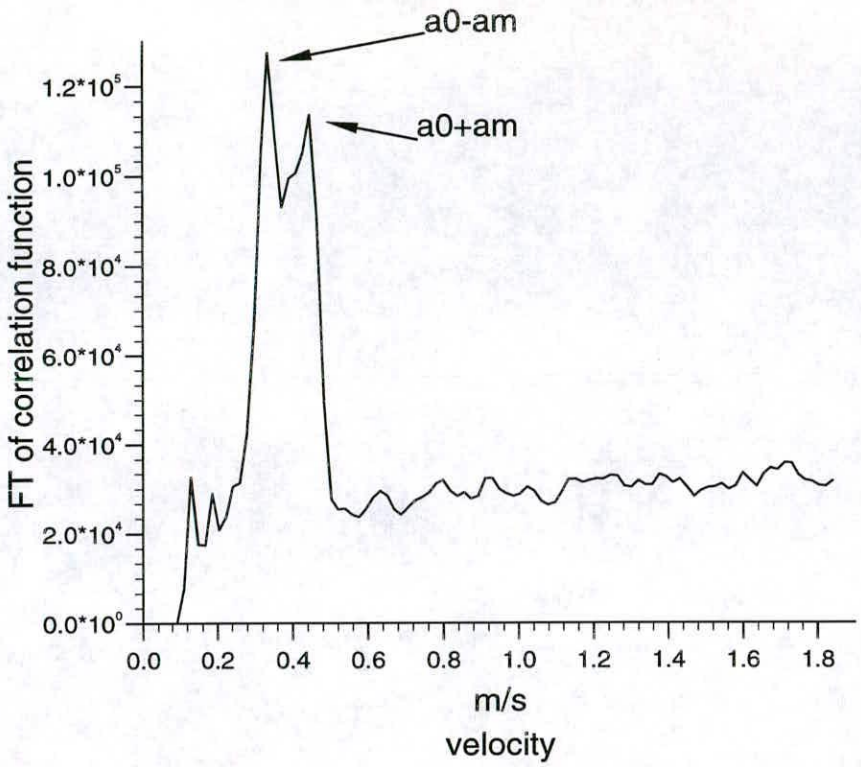

Figure 5–4: Fourier Transform of case where acoustic particle velocity is smaller than mean flow velocity. $a_0 = 0.39 \pm 0.009 \mathrm{ms}^{-1}$, $a_m = 0.065 \pm 0.009 \mathrm{ms}^{-1}$. **X-axis divided by D to give velocity.**

and $a_m - a_0$ or $a_0 + a_m$ and $a_0 - a_m$ depending on whether the acoustic particle velocity is greater than, or less than, the mean flow velocity respectively.

The expected Fourier transform is dependent on the second term of the Bessel function in equation (4.16) being much smaller than the first term so that it can be neglected. If this is not so then both the correlograms and their Fourier Transforms become too difficult to analyse.

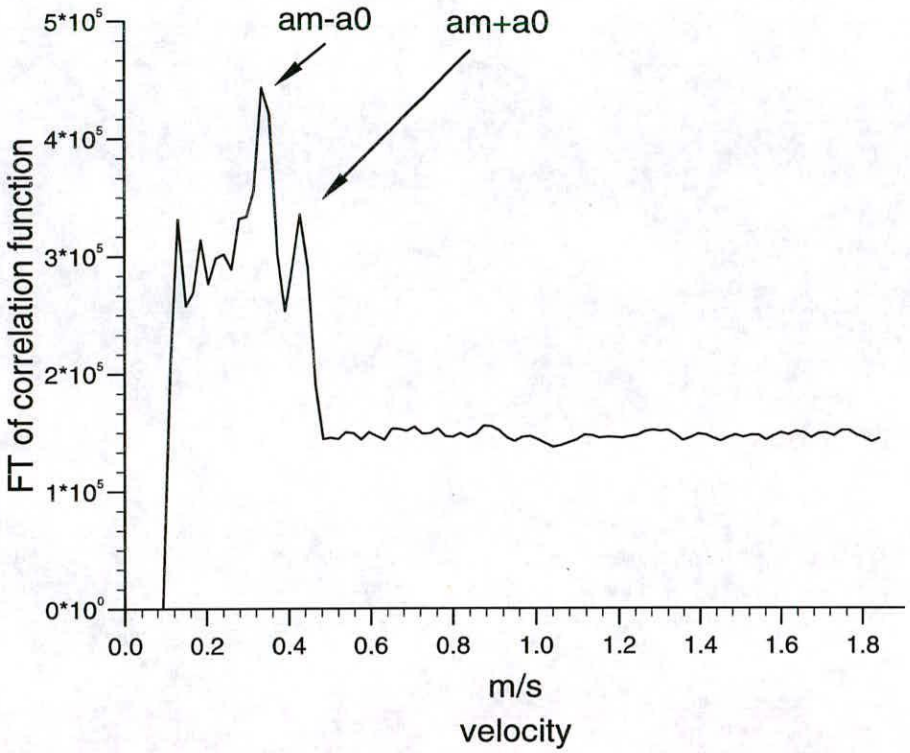

Figure 5–5: Fourier Transform of the case where acoustic particle velocity is larger than mean flow velocity. Values measured $a_0 = 0.043 \pm 0.009\text{ms}^{-1}$, $a_m = 0.38 \pm 0.009\text{ms}^{-1}$. X-axis divided by D to give velocity.

5.2.3 Conclusions

As can be seen the theoretical curve constructed using values measured from the correlogram, the experimental curve and the Fourier transforms are all in good agreement. It should be noted that there is a tendency for the value of the amplitude measured from the Fourier transform to be slightly small when $a_m << a_0$, due to the discontinuous nature of the Fourier transformed Bessel function, since this will mean that the expected peaks will be at the left and right sides of the pixel element for the peaks at the left and right of the mean flow respectively, while the peak found is at the centre of the pixel element. Consideration of this factor when the separation of the two peaks in the Fourier transform is small must be noted, but can be included in the errors. This means that the theoretical expression calculated fits the measured correlograms to a very good degree for both the cases of $a_m << a_0$ and $a_m >> a_0$

We can choose whether to analyse the correlation function or the Fourier plane. The Fourier plane gives an easy reading to measure, and uses all the information in the correlation function, but the presence of turbulence in the measured correlation function can produce a Fourier Plane where the acoustic particle velocity peaks are swamped out to produce a single very broad peak. This will also happen if the two peaks in the Fourier Plane are very close together.

The correlation function will become damped much faster if there is turbulence present in the flow, but it will still be possible to measure the parameters if the zeros and turning points are present, although there will be a greater error. The Fourier plane is easier to interpret, except when the two peaks become unresolvable, but the correlation function can still be analysed in these situations.

There is a limit on the difference between the two velocities using this technique. We wish at least one period of both the Bessel function and cosine function to be present, and the maximum number of periods that are possible in say a 70 channel correlator is 15 (since we wish at least 4 points to describe a period of the functions). This means that we can only measure the acoustic particle velocity and the mean flow velocity if they are within the range

$$\frac{1}{15} < \frac{a_m}{a_0} < 15. \tag{5.2}$$

This seriously limits the type of flow and sound fields that can be measured. However, this range can be extended significantly if a frequency shifting technique is used. This involves altering the phase difference between the beams repeatedly to make the fringe pattern at the interrogation spot shift in a particular direction. This effectively imposes a fixed, known velocity onto the flow so that the acoustic particle velocity to mean flow velocity ratio can be adjusted until it is within the limit set in equation (5.2).

5.3 Measurement across an organ pipe.

The method was used to measure the mean flow velocity and acoustic particle velocity profile across an organ pipe. In an organ pipe a steady sound field is created by a steady flow. The flow from the nozzle impinges on a knife edge which forces the air to either side. The instability of the jet has periodicities which are either amplified or damped by the sound box attached.

The measuring point is not far enough away from the jet for the flow to have a parabolic profile, but the flow profile can be determined. The measuring technique is strictly only valid for single frequency flows, but in this case there are a set of resonances in which the fundamental resonance was about 15dB louder than the first harmonic, which was the next loudest. The wooden sides and bottom of the pipe had been replaced by perspex to allow optical access, but the knife edge and jet were not changed in any way (Figure (5–6)).

5.3.1 Preliminary experiments

Before starting on the measurement of the profile, some introductory experiments were carried out in order to understand the flow a little better. Firstly, the active and passive resonances were found. The passive resonance for the open and closed tube were used to find the end correction due to the jet and knife edge, while the active resonances were used to show how the resonance frequency changes with the flow speed of the impinging jet.

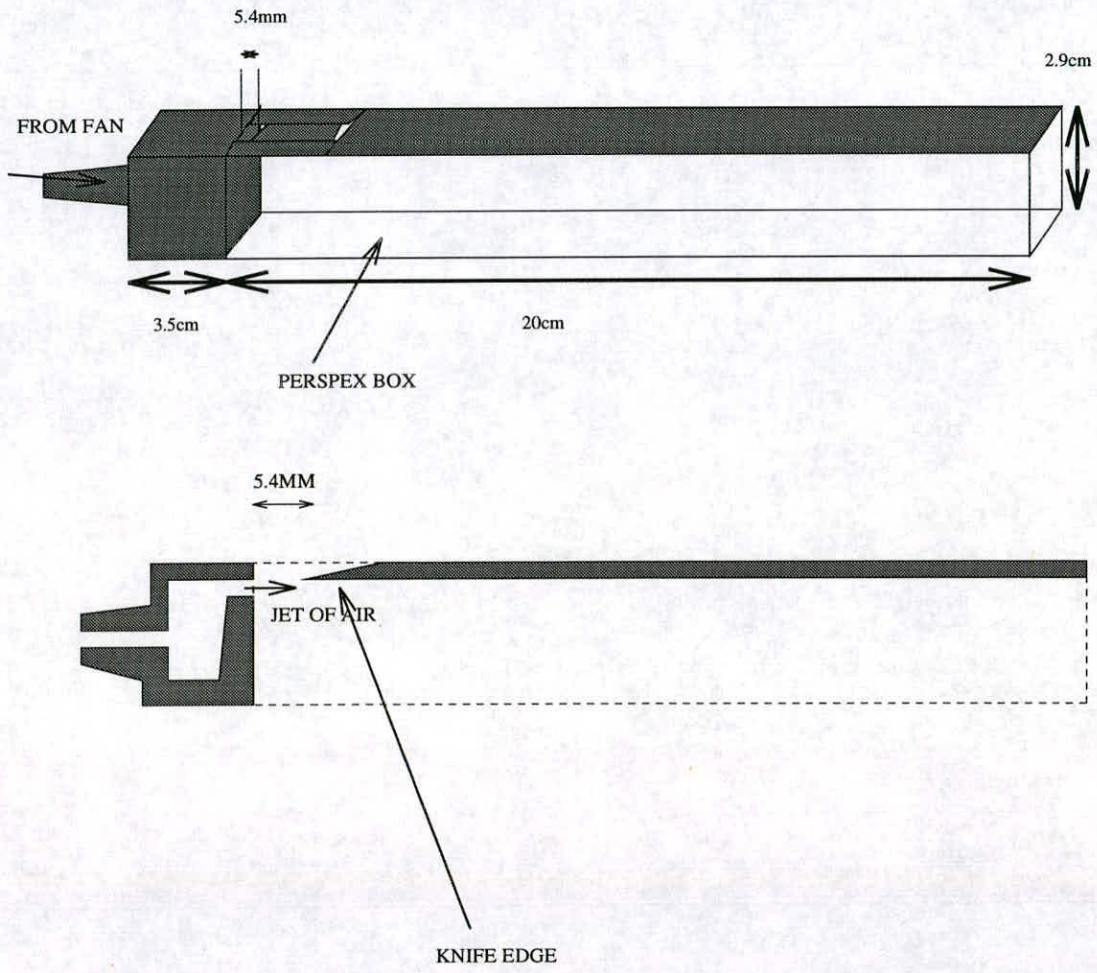

Figure 5–6: A diagram showing the dimensions of the organ pipe.

Resonances in air filled cavities

When the length of pipe is comparable with the wavelength of the sound, standing waves can be set up in the pipe. For a cylindrical pipe with one end closed and the other open, the resonance frequencies are

$$f_n = \frac{(2n-1)c}{4l'} \tag{5.3}$$

For a pipe open at both ends, the resonance frequencies are

$$f_n = \frac{nc}{2l'} \tag{5.4}$$

In both cases l' is greater than the geometrical tube length l, and is given by

$$l' = l + (\alpha_{open} r) + \alpha_{mouth} r \tag{5.5}$$

where r is half the width of the box, and α_{open} and α_{mouth} are constants. For an organ flue pipe, the end correction of the open end should be independent of frequency, and the end correction for the mouth end of the pipe has a dependency. In the next section we shall find that dependency.

End correction of a passively resonating organ pipe

A small microphone was inserted into the open end of the organ pipe which was connected to an oscilloscope (Figure(5–7)). The organ pipe was placed next to a loud speaker connected to a signal generator and the amplitude of the sound within the tube was observed to change when the frequency of the signal generator was adjusted. The frequencies, when the amplitude of the signal of the microphone was at a maximum were noted. The microphone position had to be adjusted at times to ensure that it was not at a pressure node in order to find all the resonance frequencies. The frequency was measured using a frequency meter. This was done firstly with the organ pipe open ended, and secondly with the open end of the organ pipe sealed. This allowed the end corrections of the open end and the mouth piece end to be calculated.

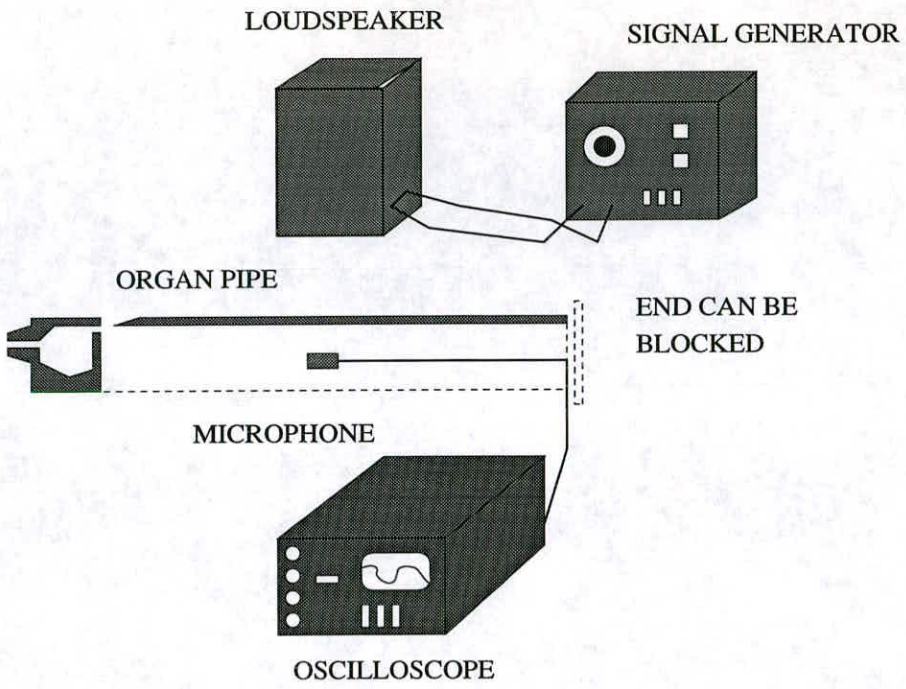

Figure 5–7: Apparatus used to measure the end corrections of passively resonating pipe

Results

We shall calculate the end corrections due to the open end and the mouth end, and for the mouth end only using the resonance frequencies shown in Table (5–2).

A graph of the end corrections versus the inverse of the frequency should be a constant if the end correction for the jet end is independent of frequency, but as we can see in Figure (5–8) the graph is a curve. The value for α_{open} was found to be a constant 0.775 , and this value is added to the closed ended end correction values in Figure (5–8) to show that α_{mouth} is the same for the end open or closed.

Conclusions

The end correction for the open end of the pipe is a constant, while the end-correction of the jet end varies with frequency, but tends towards 7 for high frequencies. This means that the resonance frequencies are not exact multiples of each other.

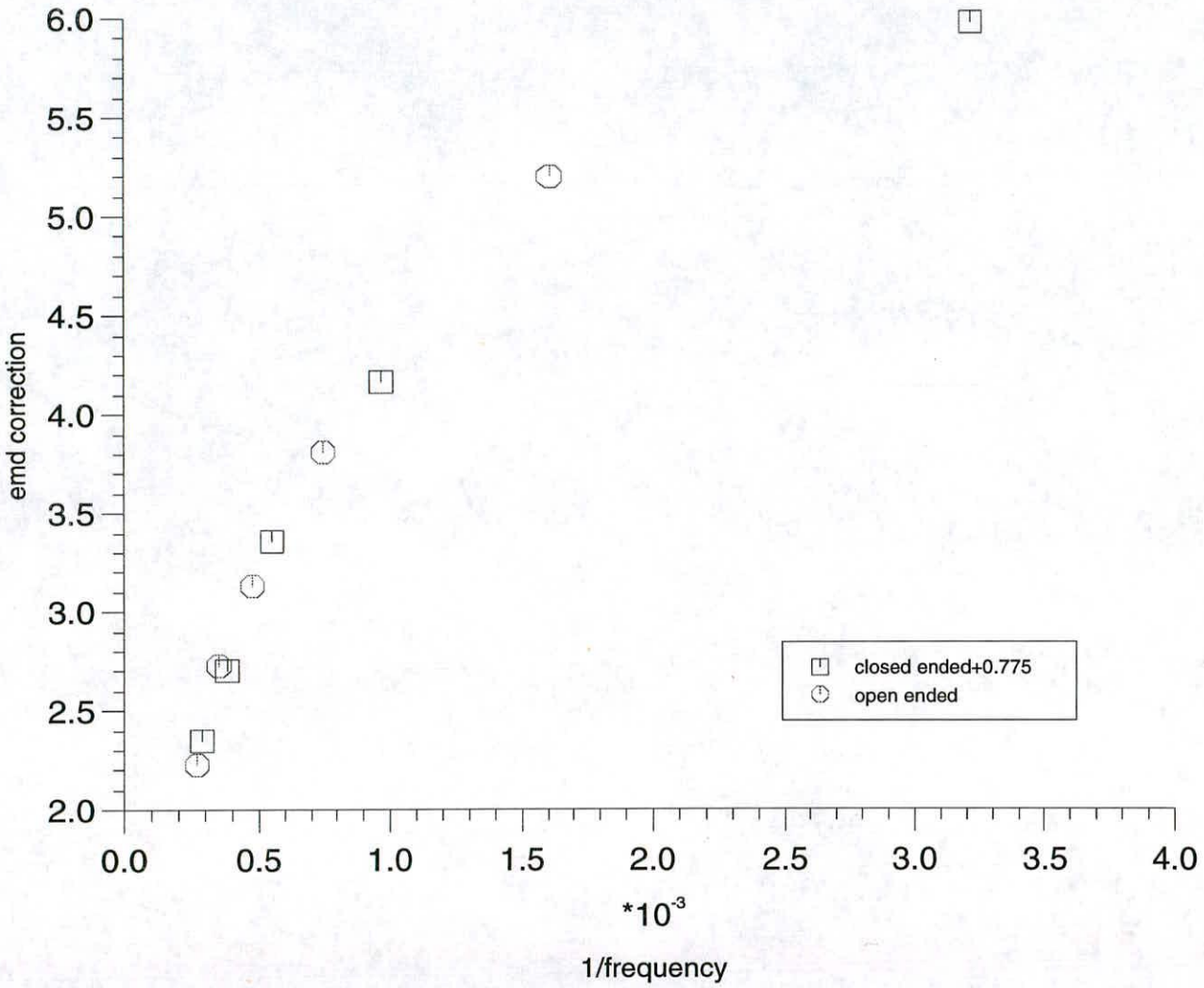

Figure 5–8: A Graph showing how end corrections for pipes with the end open and the end covered, vary with inverse of the frequency. The results for when the end is closed have a constant of 0.775 added.

closed end order of resonance	frequency (Hz)	α_{mouth}	Open ended frequency (Hz)	$\alpha_{mouth} + \alpha_{open}$
n=1	311.01	5.19	621.91	5.19
n=2	1033.3	3.39	1344.1	3.81
n=3	1810.0	2.58	2099.6	3.13
n=4	2643.2	1.93	2870.0	2.73
n=5	3480.0	1.57	3703.0	2.23

Table 5–2: The passive resonance frequencies of an organ pipe with the air temperature at 23.5°C.

5.3.2 Active resonance frequencies of an organ pipe

The frequency that the organ pipe will resonate at is called the active resonance frequency and will depend on several factors. One of these factors is the geometry of the resonance box, but another is the speed of the jet of air. We shall investigate here the effect that this latter factor has on the resonance frequency.

Apparatus and Method

The flow velocity of the air is controlled by a clamp and the speed of the flow is measured using a u-bend tube filled with water with one end of the tube connected to the pipe from the fan to the organ pipe Figure (5–9). The velocity of the air was slowly increased and the sound produced by the pipe was analysed using a frequency analyser to determine the fundamental frequency of oscillation. This was done over a range of velocities in order that the dependence of the end correction on the flow velocity could be found.

This was then done again for the case where the open end of the tube was blocked so that the only end correction is that for the jet end.

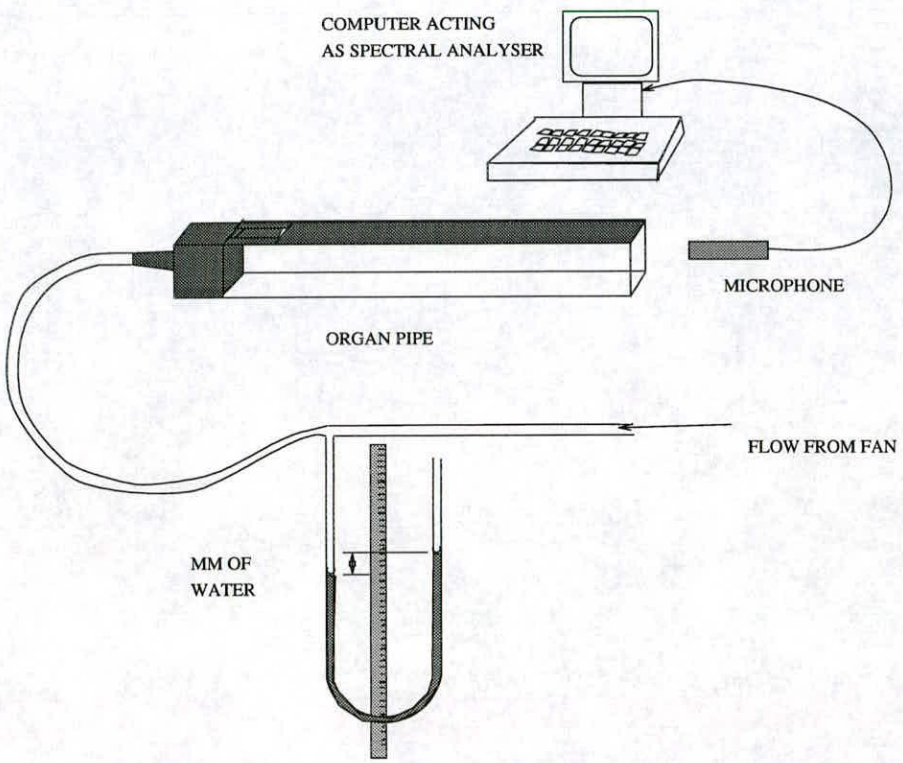

Figure 5–9: Apparatus used to measure active resonance frequencies of organ pipe.

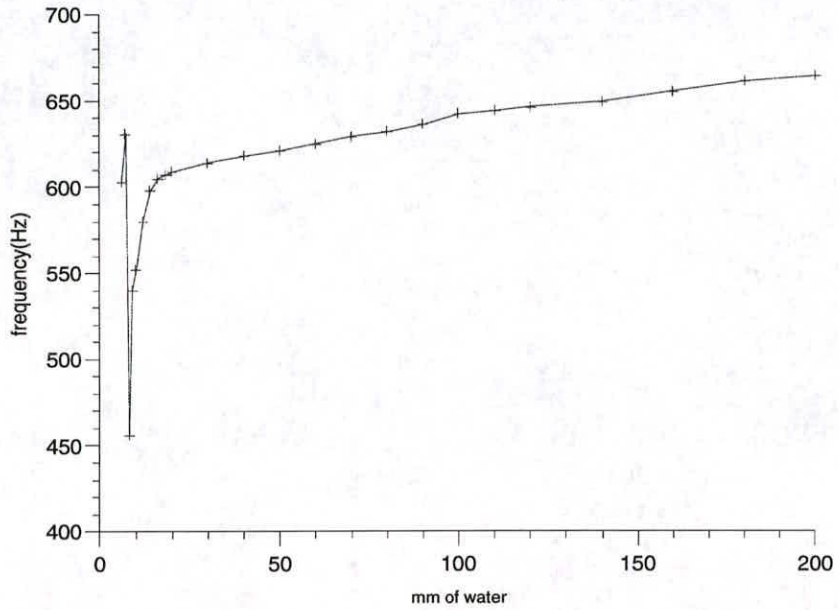

Figure 5–10: Variation of active resonance frequency with millimetres of water.

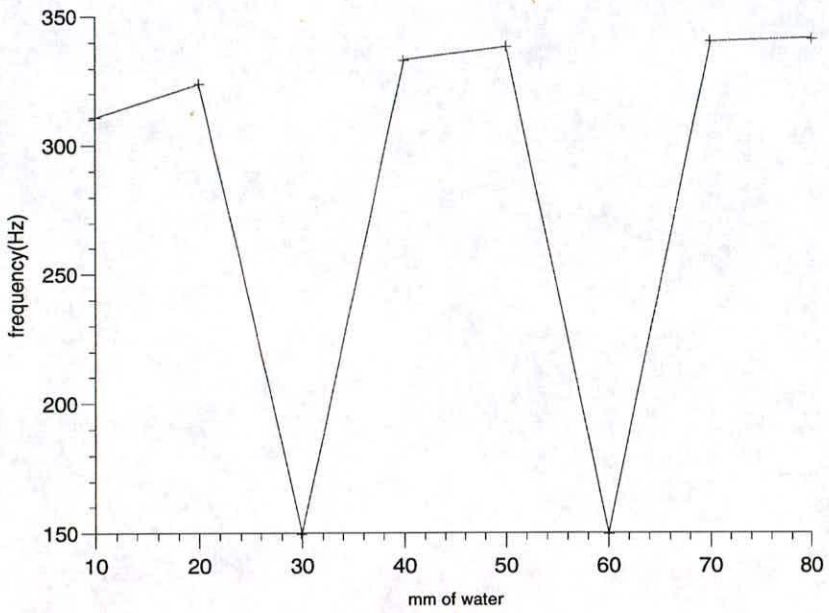

Figure 5–11: Variation of active resonance frequency with millimetres of water for an organ pipe with the end covered.

Results

Figure (5–10) shows the change of the resonance frequency as the velocity of the incoming air increases in an open ended organ pipe, and Figure (5–11) shows the frequency when the end of the pipe is covered. As the air velocity is increased, the frequency increases in general about the passive resonance frequency. When the frequency becomes much higher than the passive resonance frequency, the frequency drops or more likely becomes unreadable as there is a warbling coming from the organ pipe as the frequency tries to increase to the second resonance, but instead oscillates between the first resonance and the second resonance. The clearest sound could be heard when the active resonance was at the passive resonance frequency as all the energy of the system is forcing oscillation at the one frequency.

Conclusions

It is important for the LDA method to use an air speed which gives an active resonance near the passive resonance, since this give a clearer and louder signal. It also means that the signal is very close to being sinusoidal since the fundamental resonance frequency is of the order of 15db louder than the other resonance frequencies.

5.3.3 The measurement of the velocity profile of the tube using LDA

In this section a description is given of the use of LDA with photon correlation to measure the mean velocity and acoustic particle velocity profiles across the organ pipe. The profiles were measured 15mm from the end of the organ pipe and measurements were done at a resonance frequency of 615± 2 Hz.

The flow at this position will not be fully developed. An estimate of the distance for the central flow velocity to be 95% of the developed flow central velocity if the flow was constant over the width of the tube is given by [59]

$$X = \frac{dRe}{30}. \tag{5.6}$$

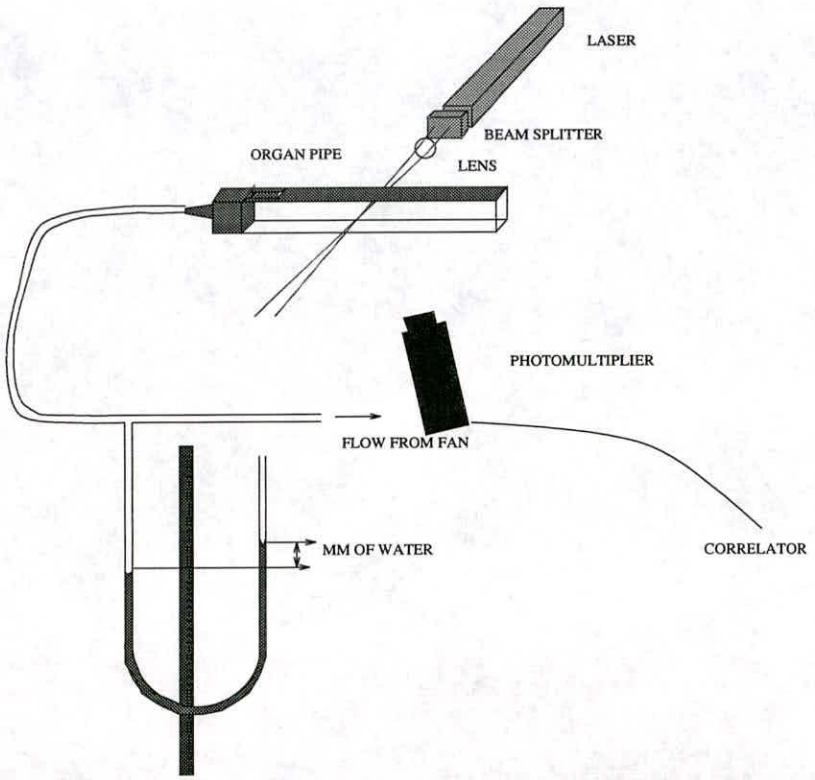

Figure 5–12: Apparatus used to measure the profile of the organ pipe

In the flow situation that we will be looking at (mean velocity, $\bar{u}$=0.15ms^{-1}, tube width, d =0.03m) the entrance length will be at least 30cm. Since the pipe is 20cm in length the profile will be flat up to a distance of 0.25 d from the centre. Since the flow is not constant over the width of the tube, There is also the distance for the flow to expand to become constant over the tube to add on to this distance. This will make the distance much further, and so the flow will never be fully developed in the organ pipe we used in this experiment.

Apparatus and method

The apparatus used is shown in Figure (5–12). The flow was seeded by using an incense stick which was placed at the intake of the fan. The speed of the flow was adjusted using a clamp which closed off the rubber tube. The flow speed was monitored using a u-tube with one end connected to the inlet pipe of the organ pipe. The displacement of the water from its average level was noted and used to keep the flow velocity constant over the time of the experiment. The measuring point chosen was 15mm from the end of the tube, which was the furthest along the tube that we could go and still neglect the effects due to the end.

The correlation function at millimetre intervals across the tube was measured and then analysed to give the mean flow velocity and the acoustic particle velocity components along the tube.

Results

Figure (5–13) shows a graph of the velocities versus the distance across the tube. The acoustic particle velocity is not constant across the tube, but is somewhat larger at the top of the tube than at the bottom of the tube. A possible reason for this could be that the sound wave generated on the knife edge has not had enough time to expand out to give a plane wave. This will have ramifications at the open end of the tube since this will mean that we will not have a perfect standing wave and this, possibly, is one of the reasons that we get a spectrum of sound instead of a clear single tone from the organ pipe.

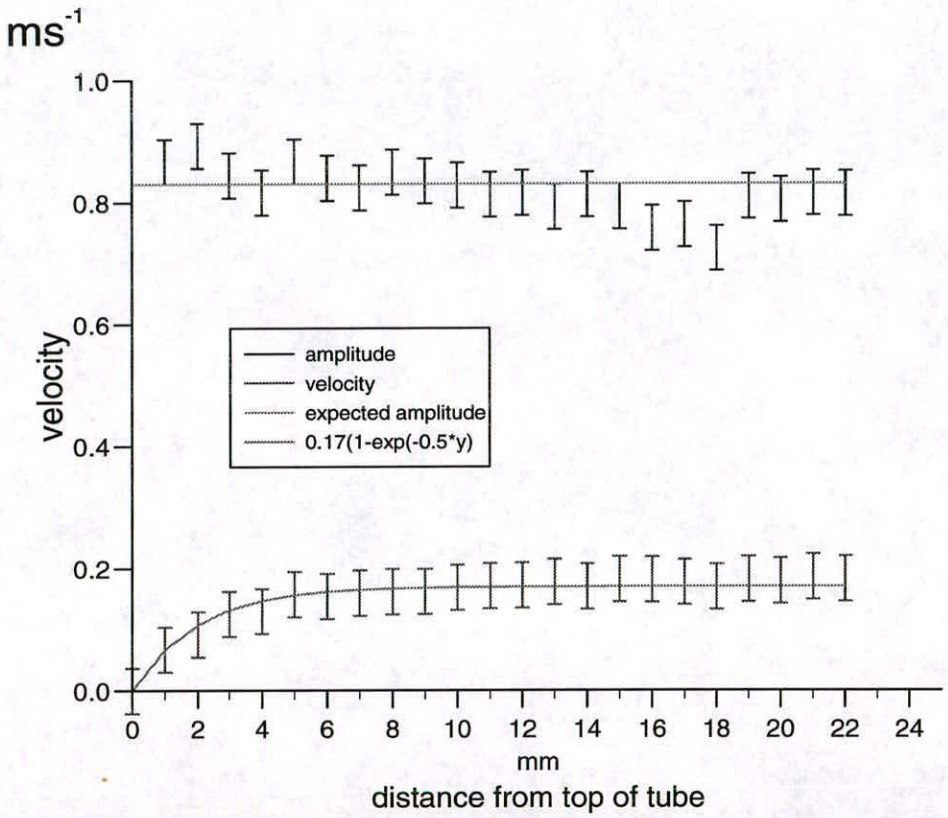

Figure 5–13: Measured profile of the organ tube.

The flow velocity along the tube has the profile which is consistent with the profile of a non-developed Poiseuille flow. The flat central flow is the expected shape for a non-developed flow, although we would have to compare the profile with the developed flow to make any more conclusions.

Conclusions

The flow velocity and the acoustic particle velocity measured show that the sound field envisaged in the organ pipe was an ideal case and did not occur at a point 15mm from the open end of the organ pipe. The flow field was not fully developed at this point of the tube, but showed the characteristics of an undeveloped Poiseuille flow.

5.4 General conclusions

In this first section of the thesis we considered the use of LDA in the measurement of combined flow and sound fields. The photon correlation method was singled out as being the best method to measure both the flow velocity and the acoustic particle velocity, since the frequency tracking and frequency analysis methods produced outputs too complicated to analyse. The photon correlation method also gave the best signal-to-noise ratio and so needed the least seeding.

The stochastic model of the correlation function was developed and was shown to be a more general case of the correlation function for a sound field only, and the correlation function of a flow field only. An extra term was discovered which was not present in the model used by Barnes *et al.* [7], which was not significant in the experiments that were done in this Thesis, but which could prove significant in other measurements.

The model was compared to measurements made in a flow and sound field, and the theoretical function compared well with the measured correlation function. The analysis of these correlation functions in the Fourier planes was discussed.

The technique was used in a case where the flow caused a sound. The intensity and velocity profile of an organ pipe were considered and shown to have some interesting characteristics worthy of further study.

5.4.1 Further work

This model and set-up could only measure one component of the velocity. LDA has successfully been set up to measure two or even three dimensions using lasers of different wavelength. The theory would be the same for this case, but we would need much more analysis hardware to implement this.

The technique has the condition that the acoustic particle velocity and the mean flow velocity must be in a smaller ratio than 1:15 since we need the two functions to be adequately resolved within the correlogram, although it is expected that frequency shifting can be used to satisfy this condition in the future.

As was also noted, turbulence was present in the measurements. The presence of turbulence in the correlograms damps the correlogram at a faster rate than for a non-turbulent case correlogram, but is not included in the model. A stochastic model could be developed to also include a turbulence term to make the model even more general. The turbulence will not affect the values measured using this technique as long as the correlation function is not damped so much that the peaks and turning points are no longer visible. The effect of turbulence on the Fourier plane would be to broaden the peaks, and this would introduce a lower limit to ratio between the acoustic particle velocity and the flow velocity if we analyse in the Fourier plane.

Chapter 6

Measurement using Particle Image Velocimetry

6.1 Introduction

Particle Image Displacement Velocimetry (PIDV) is a relatively recent photographic method of measuring many fluid velocity vectors simultaneously over extended regions of a flow domain. It is one of several techniques aimed at measuring accurately velocities at thousand of points in two, or three, dimensional regions. These methods have been made possible by significant advances in image processing technology based on improved computer hardware and improved video imaging technology. In principle these techniques record optical images of flow tracers (seeding particles) and deduce velocity from the displacements of the flow tracers during known short time intervals.

The related image processing techniques include tomographic interferometry (Hesselink [28]) and planar laser-induced fluorescence for scalars (Hassa et al. [27]), and nuclear–magnetic–resonance imaging (Lee et al [39]), laser speckle velocimetry, particle tracking velocimetry, molecular tracking velocimetry (Miles et al [46]) and particle image velocimetry for velocity fields. Reviews of these methods can be found in articles by Lauterborn and Vogel [38], Adrian [2,3], Hesselink [28] and Dudderar et al [16].

Imaging techniques are obviously useful in cases where the flow is not steady. When the flow is steady the entire flow can be investigated using a series of single point measurements done by a method such as LDA. However, when the flow is not steady, multi-point measurement techniques are capable of creating instantaneous pictures of the flow field that are unavailable from single-point measurements. Such information

is much needed in studies of turbulent flow, where it is now widely recognised that the instantaneous realisations of the flow may bear little resemblance to the averaged structure.

The field of multi-point measurement is still undergoing rapid evolution, and there are many alternative methods of producing and analysing images. We shall briefly discuss here the various methods and indicate their advantages and disadvantages. We will then go on to discuss the extra difficulties involved in determining the acoustic particle velocity from the images recorded, before deriving the equations necessary for the understanding of the power spectrum and the autocorrelation plane of the images.

In this section of the thesis, the principles of PIV will be considered, before the theory showing the form of the power spectrum and autocorrelation plane is evolved, which will allow us to measure the acoustic particle velocity (Chapter 7). The results of the theory will be tested using computationally simulated PIV images (Chapter 8) before, finally, experimental images are investigated (Chapter 9).

6.2 Principles of PIV

The determination of the fluid velocity involves the measurement of the fluid displacement over a known time interval, as embodied in the defining relationship

$$\begin{aligned} u &= \lim_{t_2 \to t_1} \frac{(x_2 - x_1)}{(t_2 - t_1)} \\ &= \lim_{\Delta t \to 0} \frac{\Delta x}{\Delta t}. \end{aligned} \tag{6.1}$$

The displacement $\Delta x = x_2 - x_1$ is formed by monitoring the motion of a marker that presumably follows the flow. Typically, this marker is a solid particle, or liquid particle, in a gaseous flow and whose typical dimension is of the order of a micrometer.

In PIV the times t_1 and t_2 are fixed, and one measures the separation of x_1 and x_2 in the image. The general method for this involves producing a pulsed light sheet, with time between pulses $t_2 - t_1$, which illuminates a flow which is being recorded. There

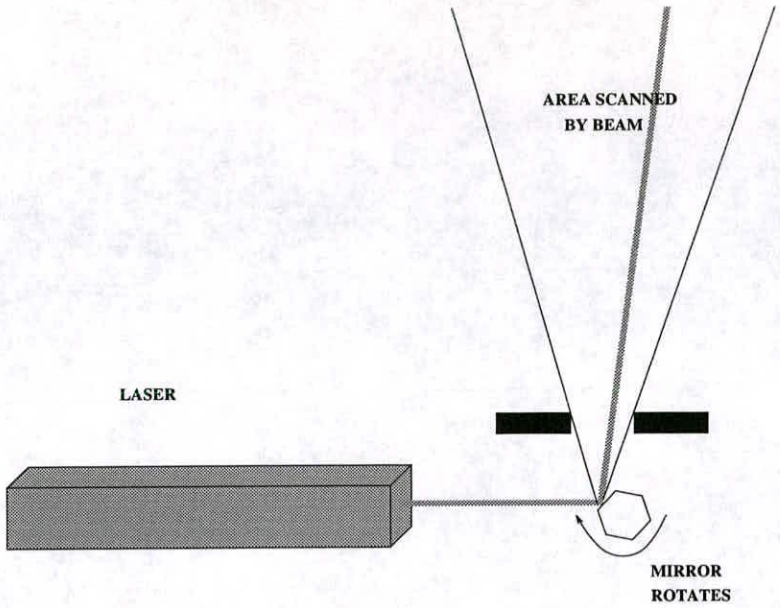

Figure 6–1: Apparatus needed to produce a light sheet using a scanning mirror

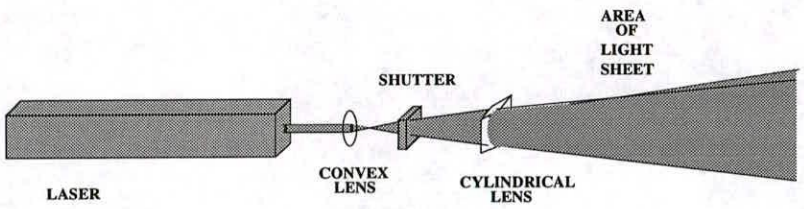

Figure 6–2: Apparatus needed to produce a light sheet using the shutter.

are several ways of producing this sheet, the simplest being the use of photographic flash lamps, but the most often used method employs an expanded laser beam which is interrupted by an electronic shutter or a rotating chopper (Figure (6–2)). Instead of a chopping the beam, a pulsed laser could be used, and this has the advantage that it is much more powerful than a continuous beam laser, but the minimum separation between the pulses is constrained by the recharge and relaxation times of the laser. Also, the expanded beam does not utilise the full power of the laser. One method which does utilise the full power of the laser is the rotating mirror method, which is widely used here in Edinburgh (Figure (6–1))[24].

In the rotating mirror method, the beam scans across the area as a face of the multi-

faceted mirror rotates across the laser beam (see Figure(6–1)), so the time between exposures can be varied by adjusting the rotational speed of the mirror. The full strength of the unexpanded beam is therefore reflected off the seeding particles every time the beam scans across them and this produces much brighter images on the negative for the same power laser than the chopped beam method and is very useful in cases where the medium attenuates the beam to a great extent as in the measurement of water waves in a wave tank.

6.2.1 Discussion of various methods of recording images

Once the required illumination has been produced, it is necessary to find a method of recording the images so that they can be analysed later. There are many ways of doing this. They can be recorded in two or three dimensions. Two dimensional records can be made using standard photographic film, photographic plates, video cameras and thermoplastic films.

Video cameras are available in various types e.g. solid state devices in which sensing is performed by large arrays of small photodetectors or scanning by an electron beam. A typical resolution is 512x512 detector elements in solid state cameras [31].

For photographic film there is a well known, roughly inverse relationship between the sensitivity of a film and the film resolution, and a compromise has to be made between adequate sensitivity and adequate resolution. Typical resolution is 400 lines/mm for 400ASA film.

Thermoplastic films offer a form of electronic photography in which the film images can be developed and erased electronically for repeated use. Stereographic imaging uses traditional photographic techniques with two cameras to obtain the third component of the velocity [6]. Holographic imaging may also be used to record the displacement of the particles in three dimensions. The hologram may be viewed afterwards in planar slices, so that the examination of the recording is similar to the examination of the photographic plate [23].

The photographic method will be used to record the images for later analysis since this gives adequate resolution and is more cost effective than video recording.

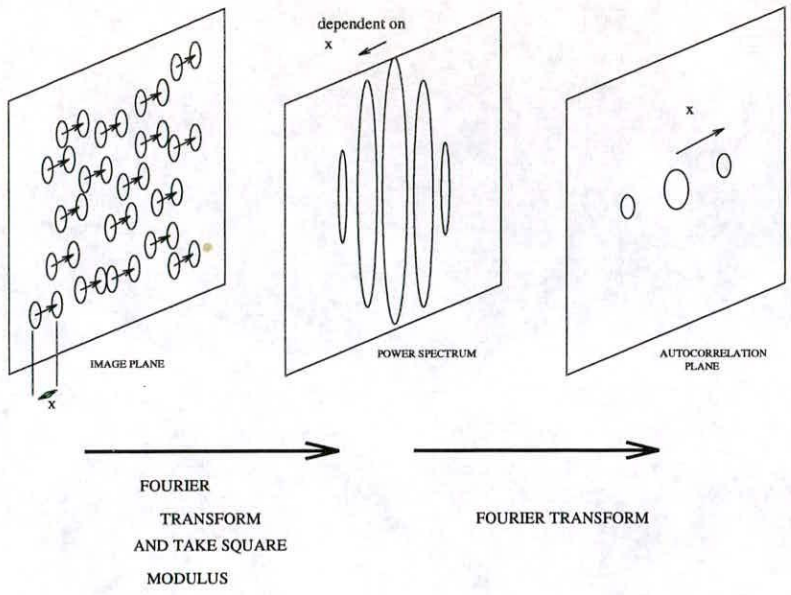

Figure 6–3: Theory behind PIV

6.2.2 Discussion of the various methods of analysis

We will assume here that the images were recorded on photographic film and will discuss ways of analysing these images in order to obtain the velocity displacements for the small interrogation areas.

One method is to use a travelling microscope to measure the displacements, but a much better and faster way is to use statistical techniques, such as the calculation of the autocorrelation plane of small areas of the image. The average displacement of the seeding images will form significant peaks in the autocorrelation plane, whose position relative to the central point can be calculated (Figure(6–3)).

The autocorrelation plane can be calculated using the Wiener-Kinchine method which utilises several Fourier Transforms(Equation(6.3))[1].

$$\text{Power Spectrum} = FT[\text{Image}]FT[\text{Image}]^* \tag{6.2}$$

$$\text{Autocorrelation Plane} = FT[\text{Power Spectrum}] \tag{6.3}$$

---

[1] $*$ denotes complex conjugate

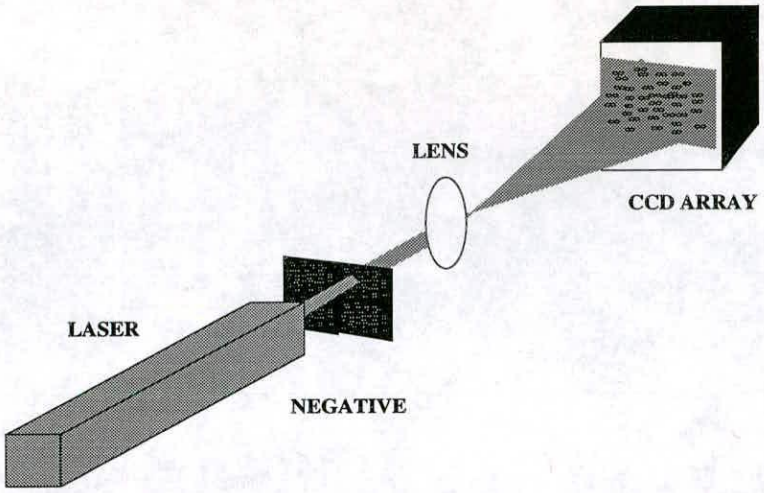

Figure 6–4: The recording of interrogation areas.

There are several ways of calculating the autocorrelation plane which depend on computational FT and optical FT. The method which we shall use involves scanning the image onto a computer and doing both FT's computationally. There are two ways of doing this. The first, and most accurate, is to probe the negative with an interrogating beam from a laser and then record the expanded image of the spot using a CCD array. Once the image is recorded, the Autocorrelation plane is calculated and the position of the relevant peaks noted before the interrogation spot is moved on to the next point(Figure(6–4)).

The second way involves scanning in the whole image using a desk-scanner [29]. The negative will be up to about a4 size first and this will help to increase the resolution of the image recorded.

Several other methods used to calculate the autocorrelation plane from the negative involves the use of optical Fourier Transforms. These have the advantage that they are practically instantaneous compared to computed FT's which can take a few seconds or less depending on the computer. This increase in speed becomes significant when we consider that an image will contain, say 100x100 interrogations, so there will be 10000 FT performed at least. If these take 1 second each computationally, then this will take 2hrs 45mins to do the entire negative.

Figure (6–5) shows the Young's Fringes method[22], where the negative is inter-

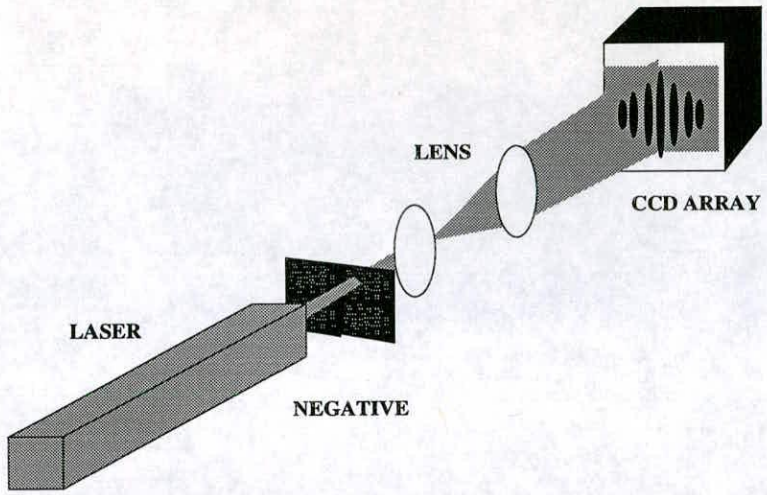

Figure 6–5: Young's fringes method of finding autocorrelation.

rogated by a laser beam and then a lens performs the first FT. The power spectrum is then recorded on a CCD array and the second FT is computed. This will half the number of FT computed and so will half the time taken to analyse the image.

The last way involves doing both the FT optically using lenses, with the power spectrum being recorded on some photorefractive crystals or a spatial light modulator which will be erased for each interrogation area [12,33]. This provides an almost instantaneous autocorrelation function which can be captured with a CCD array and analysed using a computer to give the velocity displacement.

Chapter 7

Theory of PIV

7.1 Considerations for the recording of images for the measurement of the Acoustic Particle Velocity

We are interested in extending the PIV technique so that, in addition to a mean velocity, the amplitude of a sinusoidally varying velocity component can be measured. This would allow the acoustic particle velocity (APV), and hence the intensity of the sound, to be measured. To do this, however, will put constraints on the recording of the images.

The constraints on recording images in PIV for flow velocity measurement are firstly that the seeding particles follow the flow faithfully, secondly that the distance that the seeding travels while the film is being exposed is negligible, and thirdly that the distance that the seeding travels between the exposures is larger than the image radius of the seeding particle and smaller than the interrogation area size.

The first constraint is obvious since we are really interested in the air movements that the seeding particles follow, so it is necessary that they follow the flow to a good degree of accuracy. The second constraint will allow us to pinpoint the position of the image with greater accuracy since a clear image will have a smaller image halo than a blurred image. The third constraint is necessary in order to be able to resolve the displacement peaks in the autocorrelation plane. If the separation is too small, then the displacement peak will be swallowed by the central peak. If it is too big, of the

order of the size of the interrogation area, there will be no significant displacement peak in the autocorrelation plane since correlated pairs will not exist in the area.

The seeding considerations for a PIV picture are almost the same as those for LDA (see section (3.5)). We still wish the particles to follow the oscillations, and so they have to be submicron in size, but we also wish the particles to scatter sufficient light into the camera. We have found that new tobacco smoke is ideal since it is typically 0.5μm in size for the first 10 minutes and is a very good scatterer.

The second consideration is modified slightly in that we wish to record the seeding particles over a whole oscillation. This gives a lower limit to the exposure time of $\frac{1}{frequency}$ since this is the period of the oscillation. If the mean flow component of the flow is small enough, however, so that the particles do not shift significantly over the period, we can use an exposure time which is several periods long. The criteria here is that the image of the oscillating particle will not move over the exposure time.

The third constraint becomes more rigid. Since the image formed by the oscillatory particle will be a streak and since it is necessary that the second image is not superimposed over the previous one, we will need large displacements of the image to make certain that there is no overlap. This, however, means that there is a restriction on how small the interrogation area can be. There is also the problem that we wish the interrogation area to be as small as possible for the APV and flow velocity not to change significantly over the interrogation area. Yet we wish to have enough particle pairs within the interrogation area to give much more prominent peaks for the velocity peaks than for the random correlations.

If we consider an square area which has an edge 3x the size of the streak length and a velocity displacement of comparable size to the streaks, for example, then only particles which have one of their images in the centre third will have a complete image pair within the area. This would mean that there were large numbers of single images within the area compared to the number of image pairs, and since the PIV method relies on there being more images pairs than random images, the method would produce small velocity peaks which will not be significantly larger than the noise peaks.

Thus we desire an interrogation area whose side is of the order of 5 or 6 streak

lengths in order that there are a much higher proportion of pairs than single images and this will also mean that there are a larger proportion of complete particle images present.

7.2 A mathematical derivation of the form of the power spectrum and the autocorrelation plane

In order that we can properly analyse the power spectrum and autocorrelation plane we need to have a theoretical model to compare with those computed. We shall therefore try to construct a model to show their approximate forms.

The image is formed by the oscillating particle. This has a probability that the particle will be at any point in its cycle of

$$P(\Phi) = \frac{\Pi(A_m)}{A_m\sqrt{(A_m^2 - x^2)}} \tag{7.1}$$

where $\Pi(A_m)$ is the box function which is 1 when $-A_m < x < A_m$ and 0 when $x \leq -A_m$ and $x \geq A_m$.

We will make two assumptions about the image thus formed, firstly we will assume that the image will be a convolution of the probability density function of a sine wave (shown in Equation (7.1)) and the image which would have been formed by the seeding particle if it had been at rest[64]. The image formed by this convolution has the form of a streak with magnified discs at either end, with the distance between the ends equal to twice the amplitude of vibration (A_m) (Figure (7–1)).

Secondly we assume that the image will be recorded linearly and accurately with enough resolution. This is important since if the image is not linearly recorded, or has inadequate resolution, then the image seen will no longer be of the shape envisaged. For the moment we shall assume that the image is recorded accurately. This will be discussed further in the conclusions at the end of this chapter.

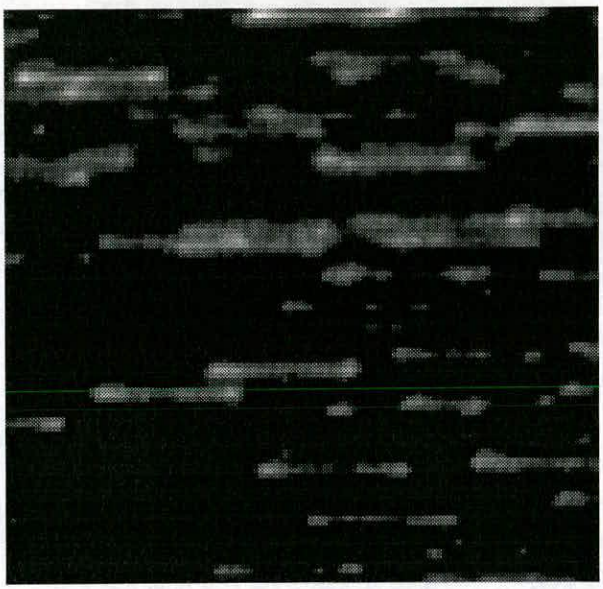

Figure 7–1: An interrogation area showing form of the images formed in a flow which is oscillating

For ease of mathematics, we will assume that the oscillation is in the x direction. This means that the image of a single particle recorded on the film using a camera whose aperture is open for the period of the oscillation will be of the form

$$\mathrm{I_n(x,y)} = \frac{\Pi(A_n)\delta(y)}{A_n\sqrt{A_n^2 - x^2}} \otimes \Psi(x,y). \tag{7.2}$$

The image of a seeding particle $\Psi(x,y)$ will be of the form of an Airy disc with a width of a say and this can further be approximated by a Gaussian of width $\frac{a}{\pi}$ in order to simplify the mathematics slightly as was done by Adrian (1988)[2] (see Figure (7–2)). The intensity of the interrogation area can be considered to be a summation of these images randomly placed. This can be expressed mathematically by the expression in equation (7.3).

$$\begin{aligned} \mathrm{I(x,y)} &= \Pi(T,T)\sum_n B_n \mathrm{I_n(x,y)} \\ &= \sum_n \frac{B_n\Pi(A_n)\delta(y-y_n)}{A_n\sqrt{A_n^2-(x-x_n)^2}} \otimes \exp^{\frac{\pi}{\sigma^2}(x^2+y^2)} \end{aligned} \tag{7.3}$$

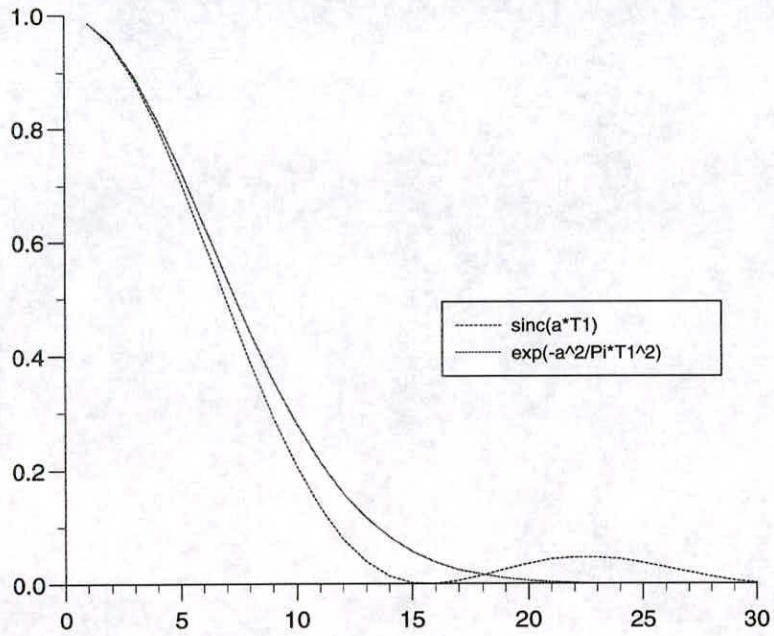

Figure 7–2: Comparison of an Airy function of width a with an exponential of width $\frac{a}{\pi}$

This is only an approximate expression for intensity over the interrogation area since we are neglecting any noise and also making three assumptions.

Firstly, we are assuming that all the seeding particle images are the same. This assumes that all the seeding particles are the same size and shape and for smoke particles this is usually only true for fresh smoke. Brandt [9] discusses the coagulation of smoke particles in a strong acoustic field and shows that after 10 minutes the smoke has formed ropes of particles of indeterminate length and shape. Since we are taking measurements in the regime where the smoke is still relatively fresh, the particles will still be small enough to follow the flow.

Secondly, we are assuming that all particles are in focus. Since the depth of focus of the camera is very small, the particles which are out of focus in the interrogation area will generally cause a constant background illumination across the negative and this will not significantly alter the expression.

Thirdly, we are assuming that all the images are contained by the window. This assumption, which was made in the flow only case, is not generally true in this case however. The images have a length which is sometimes of the order of 1/5th of the size of the interrogation area and so there is a large number of images which are clipped by the window. The large number of incomplete particle images will produce a low frequency component in the power spectrum which will translate into a larger central peak in the autocorrelation plane.

Using the Wiener-Kinchine method of producing the autocorrelation plane means that the power spectrum is defined as;

$$\mathrm{PS(k,l)} = FT[\mathrm{I(x,y)}]FT[\mathrm{I(x,y)}]^* \tag{7.4}$$

and the autocorrelation plane is defined as

$$\mathrm{R(x,y)} = FT[\mathrm{PS(k,l)}]. \tag{7.5}$$

The Fourier transform of the image can be shown to be,

$$\begin{aligned} FT[\mathrm{I(x,y)}] &= \sum_n \frac{C_n}{A_n} J_0(2\pi A_n k) e^{-\pi\sigma^2(k^2+l^2)} \\ &\quad (\cos[2\pi(kx_n + ly_n)] + \mathbf{i}\sin[2\pi(kx_n + ly_n)]) \end{aligned} \tag{7.6}$$

Therefore the power spectrum is

$$\begin{aligned} \mathrm{PS(k,l)} &= \sum_n \sum_m \frac{C_m C_n}{A_n A_m} J_0(2\pi A_n k) J_0(2\pi A_m k) e^{-2\pi\sigma^2(k^2+l^2)} \\ &\quad \cos\left[2\pi\left(k(x_n - x_m) + l(y_n - y_m)\right)\right] \end{aligned} \tag{7.7}$$

If we assume that the streak length is constant over the area under investigation, say $2A_m$, then the expression can be simplified to Equation (7.8)

$$\begin{aligned} \mathrm{PS} &= \frac{1}{A_m^2} J_0^2(2\pi A_m k) e^{-2\pi\sigma^2(k^2+l^2)} \\ &\quad \sum_n \sum_m C_m C_n \cos\left[2\pi\left(k(x_n - x_m) + l(y_n - y_m)\right)\right] \end{aligned} \tag{7.8}$$

Looking at Figure (7–3) which is the power spectrum of Figure (7–1), we can see that there are two parts to the equation of significance, the $J_0^2()e^{-2\pi\sigma^2(k^2+l^2)}$ term and the summation. The summation term causes the speckled effect which we will ignore since the random size and orientation of the terms will make this term approximateable by a constant.

The $J_0^2()e^{-2\pi\sigma^2(k^2+l^2)}$ term determines the shape of the halo. The Bessel function produces fringes which are perpendicular to the direction of the streak. It might be possible then to measure the streak length from the power spectrum and this is investigated in section (8.2.1).

The Fourier transform of equation (7.8) ignoring the summation term is;

$$\begin{aligned} \mathrm{R(x,y)} &= \frac{2}{\pi^2 A_m \sqrt{|2 - \frac{x^2}{A_m}|}} \; K\left(\frac{2}{\sqrt{|2 - \frac{x^2}{A_m}|}}\right) \otimes e^{-\frac{\pi}{2\sigma^2}(x^2+y^2)} \\ &\quad \otimes \sum_n \sum_m D_m D_n \delta(x_n - x_m).\delta(y_n, y_m) \end{aligned} \tag{7.9}$$

and this is shown in Figure (7–4).

The K() function is the elliptical integral of the first kind and has no simpler definition than

$$K(m) = \int_0^{\pi/2} [(1 - t^2)(1 - mt^2)]^{-1/2} dt \tag{7.10}$$

and has the form shown in figure (7–5) which was numerically solved.

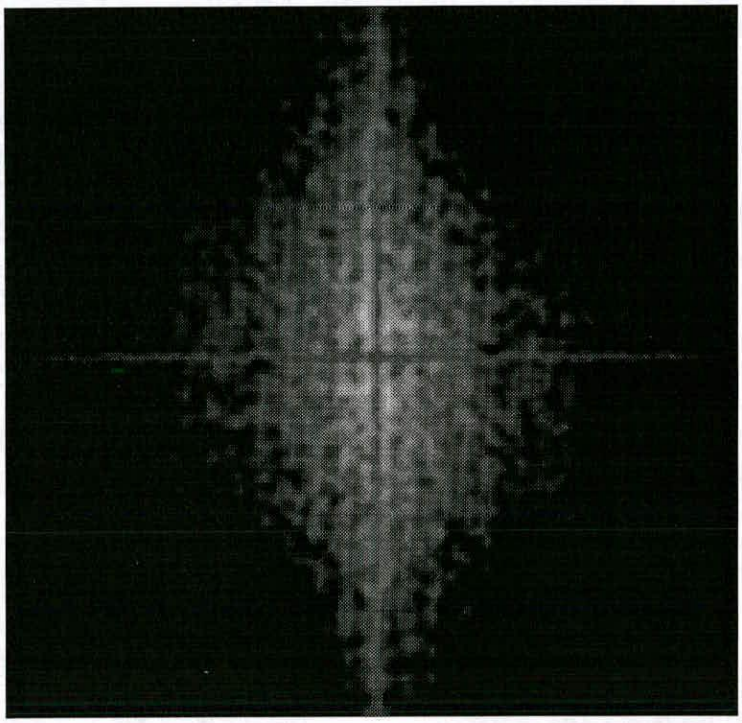

Figure 7–3: Power spectrum showing vertical fringes formed by shape of the image.

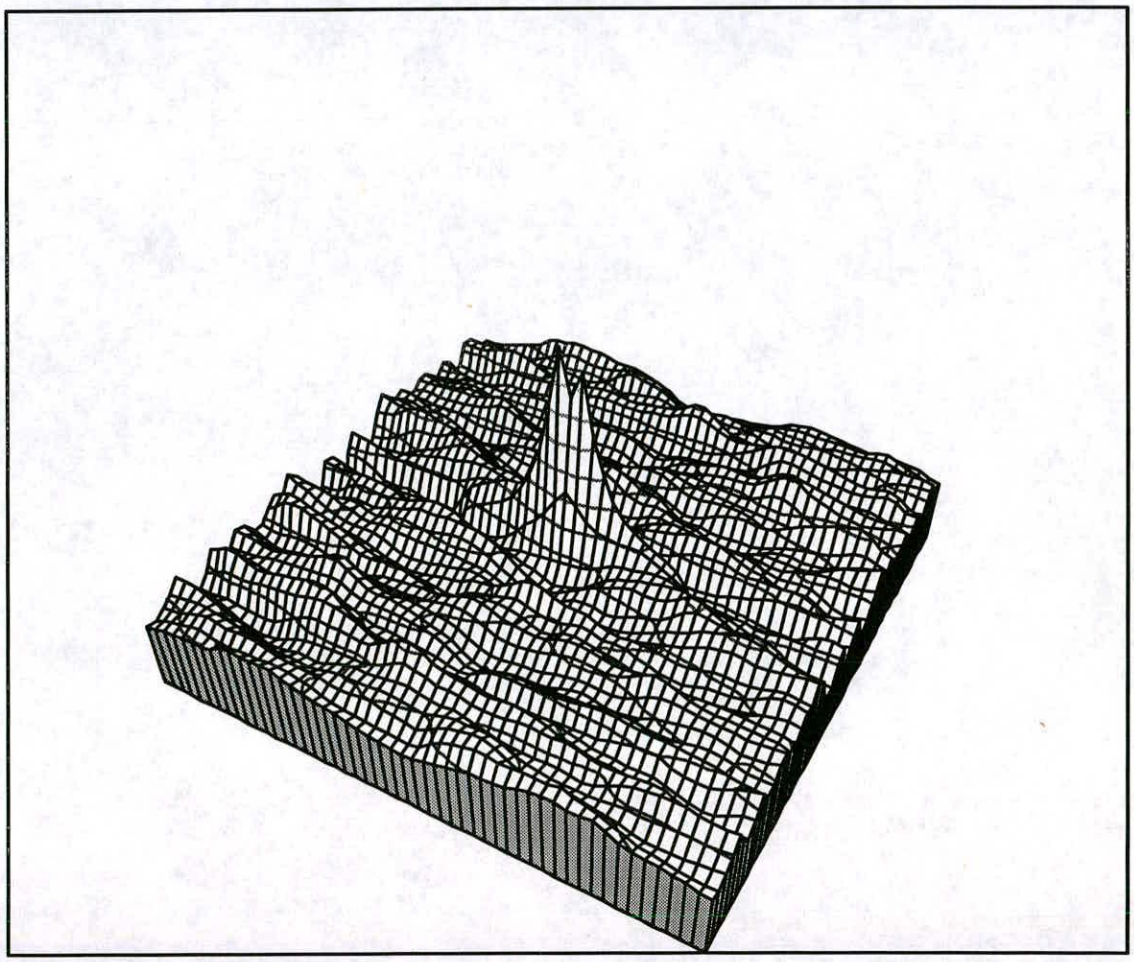

Figure 7–4: Autocorrelation plane of interrogation area showing the broad central peak caused by the shape of the images.

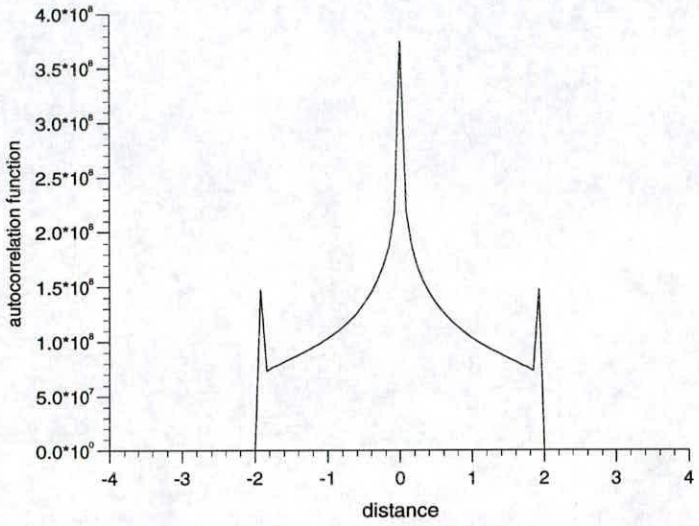

Figure 7–5: Form of elliptical integral function of the first kind for streak of length 2 distance units

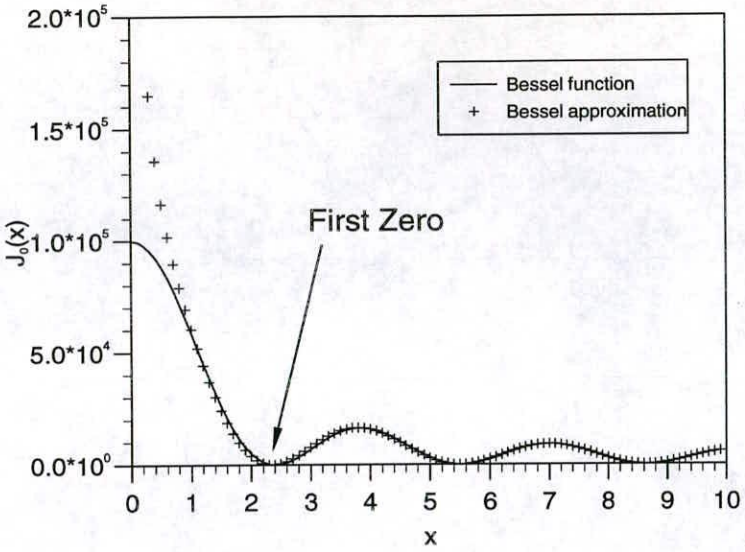

Figure 7–6: A graph showing a Bessel function (solid line)and its approximation (marked line) showing that past the first zero they coincide.

We can approximate the Bessel function term in the power spectrum in order to get an analytical form of the autocorrelation function[65]. If we note that for $2\pi A_m k >> 2.5$ (see Figure (7–6)

$$J_0(2\pi A_m k) \approx \frac{1}{\sqrt{2\pi A_m k}} \cos(2\pi A_m k - \frac{\pi}{4}) \tag{7.11}$$

then equation (7.8) can, if we consider the summation term as being a constant, be approximated as

$$\mathrm{PS} = \frac{1}{4\pi A_m^2 k} e^{-2\pi\sigma^2(k^2+l^2)} (1 + \sin(4\pi A_m k)) \tag{7.12}$$

The Fourier transform of this will be

$$\mathrm{AP} = e^{-\frac{\pi}{2\sigma^2}(x^2+y^2)} \otimes (\Pi(2A_m) + \frac{1}{\sqrt{4\pi A_m^2 k}} \otimes \frac{1}{\sqrt{4\pi A_m^2 k}}) \tag{7.13}$$

This function is more similar to that shown in Figure (7–4) than the K() function (see Figure (7–7) which shows the right hand part of the function), and this means that in general the end peak is not produced in the Fourier Transform possibly due to the averaging of the central portion of the Power spectrum. The portion of the power spectrum within the first minimum is the only different part of the function and it must

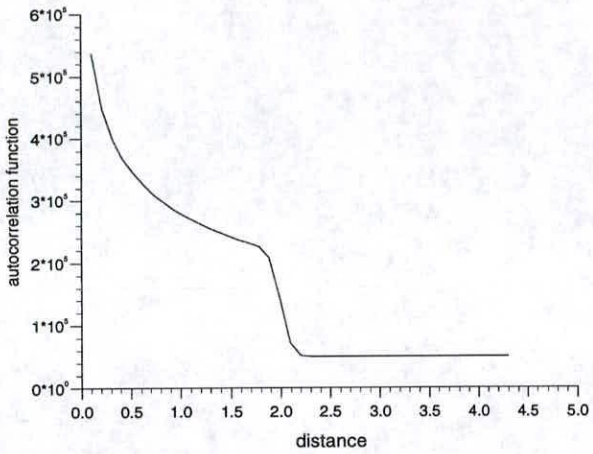

Figure 7–7: Form of the approximation to the elliptical integral. Showing only positive distance. Streak length was 2 distance units.

be this part which produces the side peaks at $\pm A_m$ in Figure (7–5). This part is spread over only a few pixels, and has other contributions to its size, such as a spike due to background illumination in the interrogation area, so it would be more likely to take on the attributes of the approximation than the exact form of the Power Spectrum.

7.2.1 When a Flow is also present

If a flow is also present in the interrogation area and if we make a multiple exposure photograph of the area, then we can also measure the average velocity over the area. If we define the velocity displacement as being $(\Delta x, \Delta y)$, so that a particle pair will occur at $(\frac{\Delta x}{2}, \frac{\Delta y}{2})$ and $(-\frac{\Delta x}{2}, -\frac{\Delta y}{2})$, then equation (7.14) showing the intensity across the interrogation area, will now become

$$\begin{aligned} \mathrm{I(x,y)} &= \Pi(T,T)\sum_n \frac{B_n \Pi(A_n)\delta(y-y_n)}{A_n\sqrt{A_n^2-(x-x_n)^2}} \otimes e^{-\frac{\pi}{\sigma^2}(x^2+y^2)} \\ &\quad \otimes \left[\delta(x-\frac{\Delta x}{2}, y-\frac{\Delta y}{2}) + \delta(x+\frac{\Delta x}{2}, y+\frac{\Delta y}{2})\right] \end{aligned} \tag{7.14}$$

We will have to make a further assumption here that most of the particle pairs are present within the interrogation. If a significant number of the particles have their

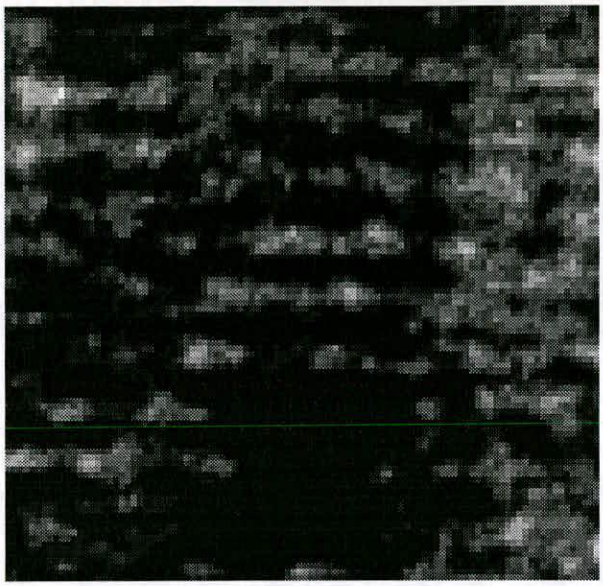

Figure 7–8: An interrogation area showing the form of the interrogation area when a flow displacement is also present between exposures

associated images outside the interrogation area, then this will tend to produce less prominent velocity peaks and it is even possible that the random correlation peaks will be larger than the velocity peaks.

$$\begin{aligned} \mathrm{PS} &= \frac{1}{A_m^2} J_0^2(2\pi A_m k) e^{-2\pi\sigma^2(k^2+l^2)} (1 + \cos(2\pi(\Delta x k + \Delta y l))) \\ &\quad \sum_n \sum_m C_m C_n \cos(2\pi(k(x_n - x_m) + l(y_n - y_m))) \end{aligned} \tag{7.15}$$

The power spectrum of an interrogation area of the type shown in equation (7.14) will be of the form shown in Equation (7.15) and Figure (7–9) and this is similar to that for the sound field except that there is an extra cosine term present which will form fringes superimposed on the $J_0^2() \exp^{2\pi\sigma^2(k^2+l^2)}$ halo. Here we have made the same assumption as for the streak length in that we assume that the velocity displacement does not change over the interrogation area.

The separation of these fringes will be related to the velocity displacement, but it will be easier to measure this in the autocorrelation plane. This will consist of images

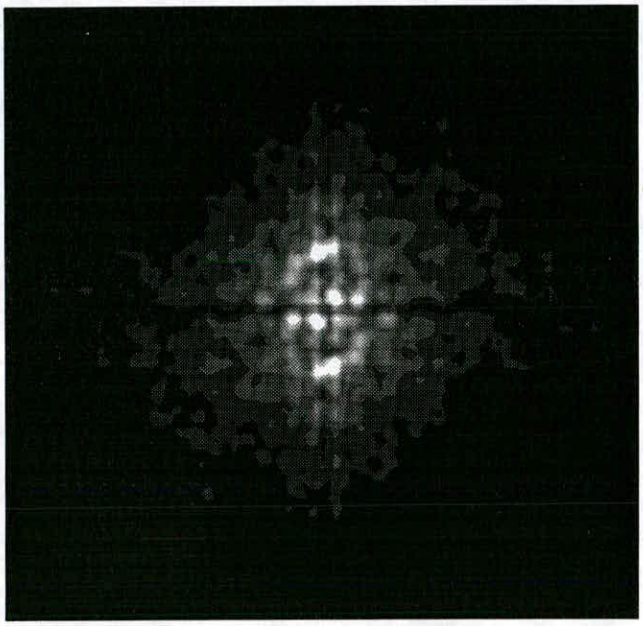

Figure 7–9: Power spectrum for case where there is a displacement between exposures, showing cosine fringes (at 45° to horizontal) superimposed on the vertical fringes due to the image shape.

similar to those formed for the single image case centred on the positive and negative velocity displacements (see Figure (7–10) and Equation (7.16)).

$$\begin{aligned} \mathrm{R(x,y)} &= \frac{2}{\pi^2 A_m \sqrt{|2-\frac{x^2}{A_m}|}} K\left(\frac{2}{\sqrt{|2-\frac{x^2}{A_m}|}}\right) \otimes \exp^{\frac{2\pi}{\sigma^2}(x^2+y^2)} \\ &\otimes\left(1+\frac{1}{2}\delta(x-\Delta x, y-\Delta y)+\frac{1}{2}\delta(x+\Delta x, y+\Delta y)\right. \end{aligned} \tag{7.16}$$

Again we have the K() function and it is also possible to approximate this with the same term as shown in equation (7.13). In this case (see Figure(7–10)) we do have side peaks on the central peaks due to the length of the streak, but they are shifted towards the centre and are not very prominent.

7.3 Conclusions

We now have a form for the power spectrum and the autocorrelation plane of the image area which we can analyse to find both the flow velocity and the acoustic particle velocity.

Firstly we shall note some of the assumptions which were made in the derivation of the theory.

- We assumed that the images are the convolution of the probability density function for a sine wave and the image of the seeding particle at rest and that they are recorded linearly.
- We assumed that the oscillation was strictly in a direction parallel with the pixel grid.
- We assumed that there were no images concatenated by the edges of the interrogation area.
- We assumed that the seeding particles images were all the same size and shape (i.e. they were all in focus, and the seeding particles were all the same shape and same order of size).

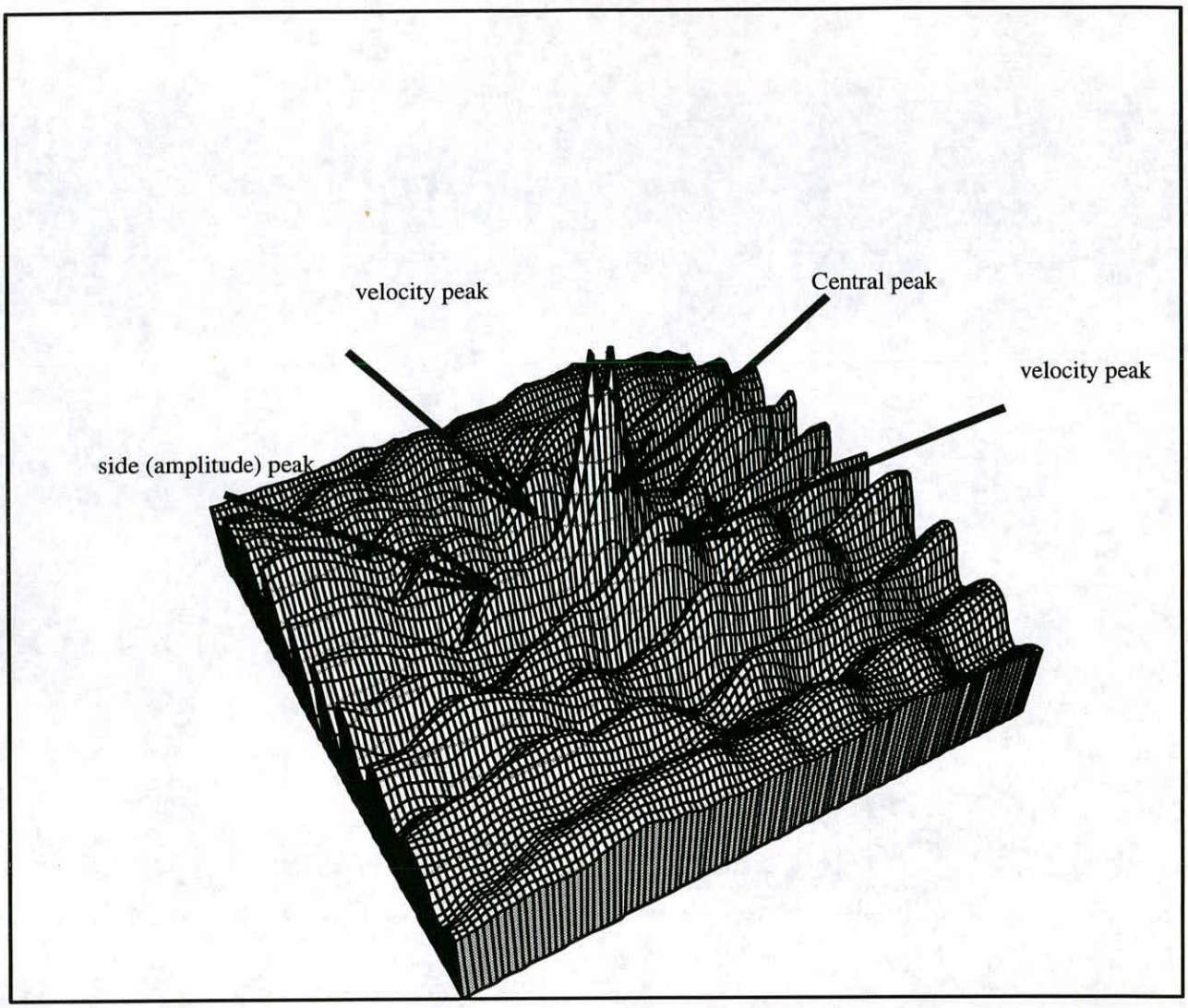

Figure 7–10: Autocorrelation plane of image which has been multiply exposed showing the velocity displacement peaks.The shape of the peaks is similar to that when we have only a single exposure

- We assume that images do not overlap.
- We assumed that the summation term in Equation(7.8) approximated to a constant.

We shall try here to justify some of these assumptions. If we consider them in order. The images are, to a good approximation, the convolution of the seeding particle images and the probability density function. The pixelation of the images (when they are scanned in, the scanner averages over the area of a pixel) will not be a problem as long as the image has enough resolution, and the image can be linearly recorded if we make sure that the image is not over-exposed. In fact, a small background illumination could be beneficial, in that this will allow us to use shorter exposure times. The image would then always be brighter than the threshold light level of the film, meaning that we could adjust the exposure time with more freedom, allowing us to use the linear area of the film. This background illumination would, however, make the negative noisier.

The orientation of the fringes was taken as horizontal to simplify the mathematics. This is not essential, and they can be oriented in any direction.

The effect of the images which overlap the edge of the interrogation area is not fully known, but will be discussed on page 82

A quick look at an image will show that the seeding particles are not all exactly the same shape and size, and they are not all sharply in focus. The average over the interrogation area will average out these different sizes to produce a halo with an averaged width. This point is covered in general PIV theory (see Adrian (1988)[2] for example).

The overlapping of images can be a problem, because this will push the brightest part into the non-linear area of the film unless this is taken into account and the exposure time of the images set so that even overlapping images will be within the linear area of the film.

The summation term is difficult to quantify in that it depends on the distribution of the images within the interrogation area. If the images are randomly positioned, then the summation term will be evenly distribution across the area. Various researchers have considered this term and the usual convention is to assume it is a constant.

A mathematical model has been determined which will allow us to find the amplitude of the oscillation and the flow velocity from PIV negatives. The model shall be tested using simulated PIV pictures in which the various parameters are known before the method chosen to analyse the negatives is used on real pictures of the case of acoustic streaming.

Chapter 8

Analysing Simulated PIV images

We can see from equations (7.15) and (7.16) that the value of the amplitude of fluctuation can be determined from the power spectrum and the autocorrelation plane. Also, we note that several assumptions were made to derive these equations, notably that only complete images are found within the interrogation area. We are also interested in how the ratio of the seeding particle image size and the streak length affects the values obtained.

In order to investigate these factors it is necessary to have images in which the values are known. It was for this reason that we determined to produce simulated images.

8.1 Production of the Images

Equation (7.2) assumes that the image is made from the convolution of the probability density function of the sine wave and the seeding particle image.

An artificial image can therefore be made up using this expression. When this image is scanned into the computer, however, the scanner averages over the area of a pixel. If this is done to the equation then the pixelated image can be approximated by

$$\begin{aligned} \mathrm{I_n(x,y)} &\approx \sum_{n=-T}^{T} \int_{n-0.5}^{n+0.5} \left(\frac{\Pi(A_m)}{\sqrt{A_m^2 - x^2}} \otimes e^{-\frac{\Pi(x^2+y^2)}{\sigma}} \otimes \delta(x-n) \right) dx \qquad (8.1) \\ &\approx \sum_{n=-T}^{T} \delta(x-n) \left(\sin^{-1}\left(\frac{n+0.5}{A_m}\right) - \sin^{-1}\left(\frac{n-0.5}{A_m}\right) \right) \otimes e^{-\frac{\Pi(x^2+y^2)}{\sigma}} \end{aligned}$$

This would involve doing a convolution in a generating program, but has the disadvantage that we are looking at the average of the pixels in a function which is changing very rapidly over that pixel and is discontinuous at the ends of the function. A function which changes very quickly in the image plane, changes slowly in the Fourier plane, and since it was easier to make image streaks of non-integer length in the Fourier plane, we chose to construct the images in the Fourier plane. The information is spread over the whole Fourier plane instead of being contained in a few pixels which have been averaged over, so it is easier to vary parameters in the Fourier plane.

The form of the constructed Fourier Transform will be

$$FT[I_n(x,y)] = J_0(\pi A_m k) e^{-\frac{\sigma(k^2+l^2)}{\pi}} \tag{8.2}$$

The image formed from this Fourier transform is placed randomly in a blank image file with as many particle pairs as desired, and the displacement due to the the velocity and the amplitude of the streak are varied with the position of the image in the file according to the expected streaming equations(Equation (8.3)- (8.5)).

$$A_m = 8\cos\left(\frac{2\pi x}{\lambda}\right) \tag{8.3}$$

$$U_x = 10\left(1 - 3\frac{(y_1 - y)^2}{y_1^2}\right)\sin\left(\frac{4\pi x}{\lambda}\right) \tag{8.4}$$

$$U_y = \frac{40\pi}{\lambda}(y_1 - y)\left(1 - \frac{(y_1 - y)^2}{y_1^2}\right)\cos\left(\frac{4\pi x}{\lambda}\right) \tag{8.5}$$

These are the equations of streaming in a square duct pipe with the wavelength in our examples being $\lambda = 8000$ pixels, and the width of the pipe being $y_1 = 901$ pixels.

The position of the images was pseudo-random, and this meant that for the same initial number in the random number generator, and same file size, the images were positioned in the same places in the blank file allowing us to construct identical photographs with different halo-widths on the images. The initial number of images and the size of the halo-widths could be altered to obtain images similar to those obtained experimentally. The listing for the generating program is shown in Appendix B.

8.2 Measurement of the streak length from the power spectrum and autocorrelation plane

There are two obvious methods of measuring the streak length from the data presented in the interrogation area, from the power spectrum and from the autocorrelation plane. In this section we will consider them both, showing examples constructed computationally, and showing the various factors which affect the results and the considerations which have to be made in order to get meaningful results.

8.2.1 The Power Spectrum

Equation(7.8) implies that the fringes caused by the streak length will be proportional to $J_0^2(\pi A_m k)$ in the x-direction of the power spectrum. If we consider Figure (8–2), the power spectrum of Figure (8–1), then we can see the vertical fringes due to the streak length, and the other fringes superimposed at an angle due to the displacement between image pairs. The measurement of the Bessel fringe spacing directly from this power spectrum would be affected by the noisy background and the cosine fringes, meaning that it would not be possible to accurately find the spacing between the fringes directly from the power spectrum. If we average the spectrum along the direction of the fringes however, this will produce a function which is proportional to $J_0^2(\pi A_m k)$ and so the peaks in the function will occur when $\pi A_m k = 3.8317$, 7.0159, 10.174, etc. This provides an easy relationship from which to obtain the length of the streak (Equation (8.6)). Since the power spectrum has symmetry, we will only consider the right hand side of the profile.

$$A_m = \frac{1}{2\pi k_n} * (3.8317 \text{ifn} = 1, 7.0156 \text{ifn} = 2, \text{or} 10.174 \text{ifn} = 3) \tag{8.6}$$

Figure (8–3) shows the square root of the averaged power spectrum (Figure (8–2)) and this can easily be compared to the form of the theoretical equation (equation (7.8)) with a Bessel function of the same argument to show that it compares favourably.

Figure 8–1: Sample interrogation area with $\sigma = 0.1414$,$A_m \approx 7.72$ pixels, $\underline{u}$=(-11.61,5.87)

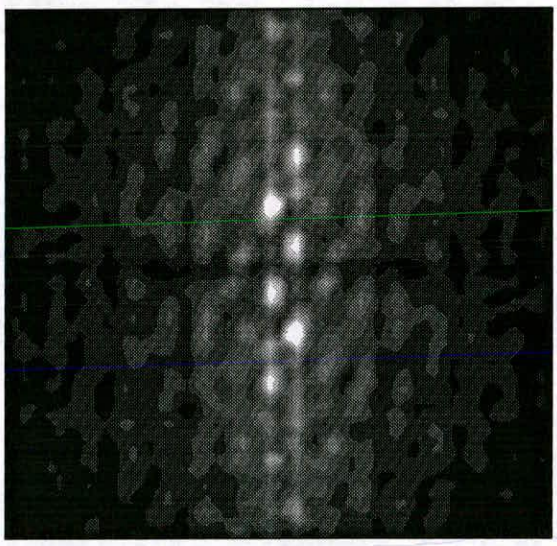

Figure 8–2: Power spectrum of Figure(8-1)

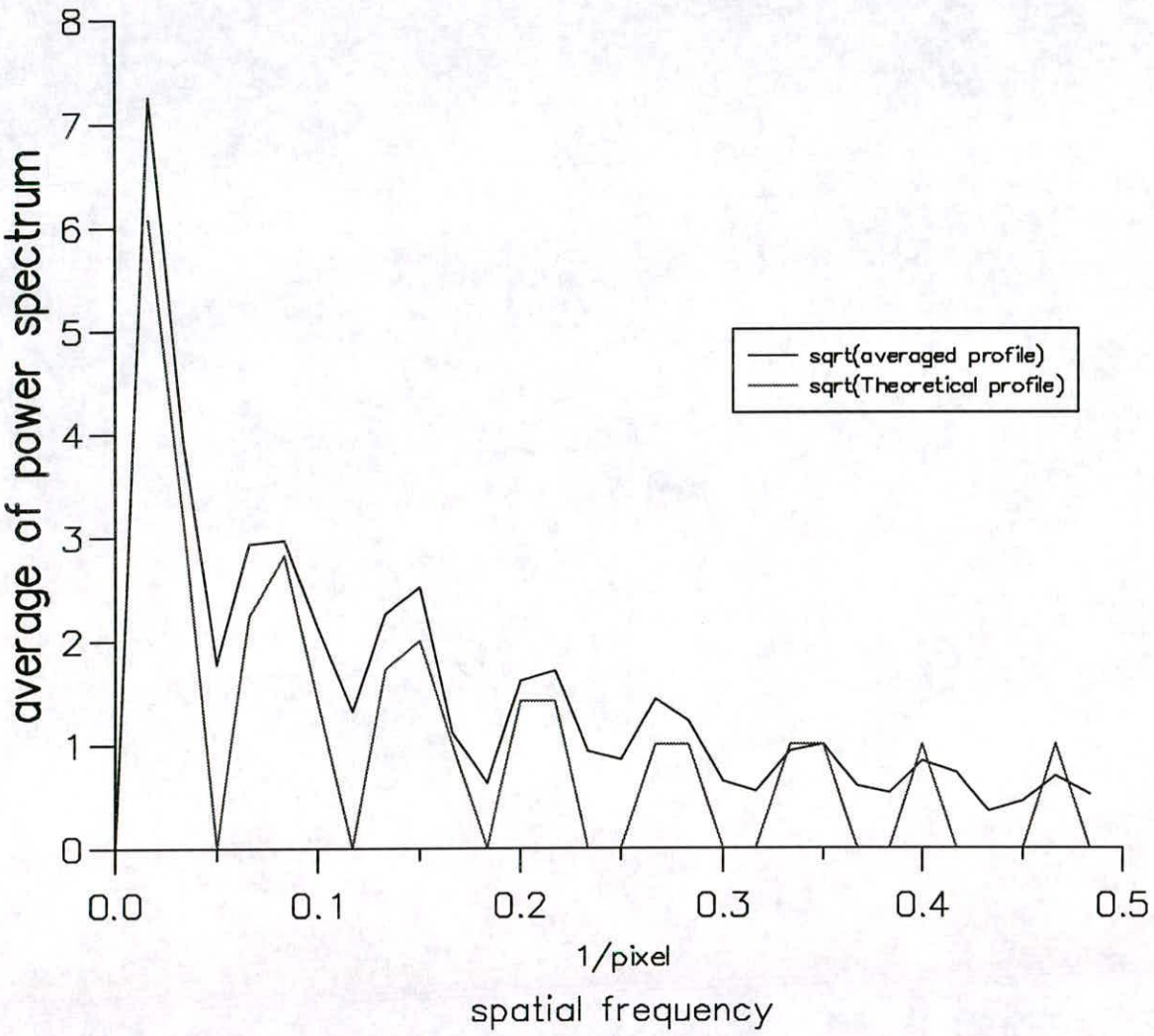

Figure 8–3: Graph showing profile of the power spectrum when averaged along the fringes compared to theoretical form .

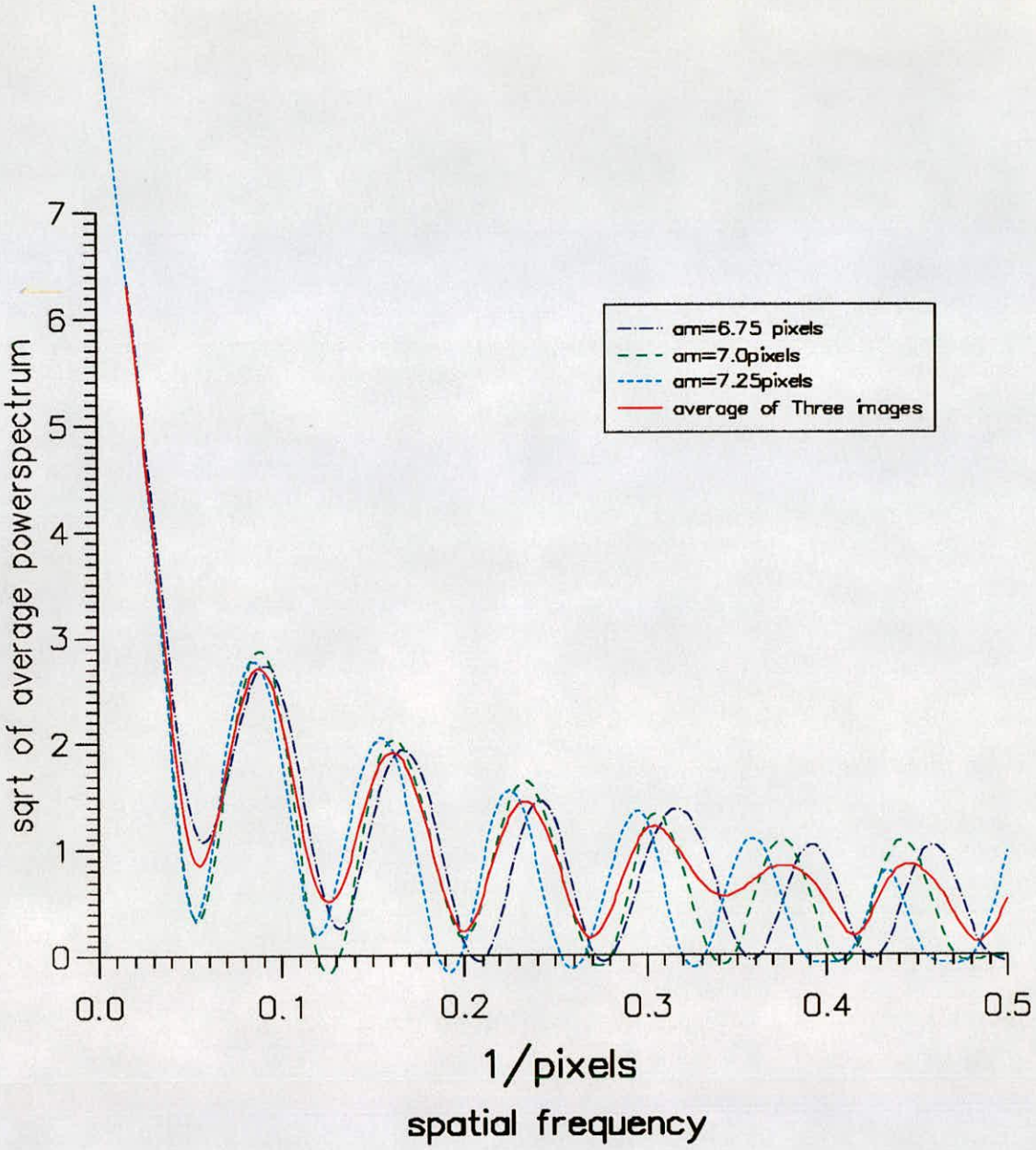

Figure 8–4: Profile of three images with amplitude 6.75,7.0 and 7.25 pixels and their average. This shows that the sum of three profiles with different amplitudes (in red) is similar to the profile of the average profile (in green)

Table (8–1) shows the amplitude measured from the various peaks of the profile of the power spectrum (the profile is found by averaging the power spectrum along the fringe direction). As can be seen, all the expected values are within the error bound of the measured value. There is a low frequency component added on to the Bessel function, but that will be expected from the summation which was ignored in equation (7.8) which will be a constant which is then multiplied by the halo-shape due to the seeding particle image. It can also be seen that it is inherently more inaccurate to measure from the first peak than from the second peak,because the error decreases inversely as the spatial frequency increases. This is because the spatial frequency is inversely related to the amplitude of the vibration. The first peak also gives a higher value due to the shift imposed on it be the central peak. There are two factors which

No. of Peak	Bessel function turning point	k $(\text{pixels})^{-1}$	A_m (pixels)	ΔA_m (pixels)
1st	3.8317	0.076	8.07	0.89
2nd	7.0156	0.145	7.70	0.44
3rd	10.174	0.210	7.69	0.30
4th	13.324	0.270	7.84	0.24
5th	16.471	0.344	7.61	0.18
6th	19.616	0.400	7.81	0.16
7th	22.760	0.467	7.76	0.14

Table 8–1: A table to show the amplitude measured from the various peaks in the averaged power spectrum. Expected value was 7.74 pixels.

can affect the profile of the power spectrum. The first is the incomplete (or clipped) images, the second is the variation of the amplitude over the area.

The first factor, the clipped images, was a factor which was not included in the initial theory in Equation (7.8). If we say that the n^{th} incomplete image will have the Fourier Transform $\Theta_n(k,l)$ then ignoring the summation we would add on to the power spectrum a factor

$$+2\sum_n\sum_m \quad \frac{C_m}{A_n}J_0(2\pi A_n k)\Theta_m(k,l)\exp^{2\pi\sigma^2(k^2+l^2)} + \sum_m\sum_n \Theta_m(k,l)\Theta_n(k,l)\exp^{2\pi\sigma^2(k^2+l^2)} \tag{8.7}$$

The second term will add a term which is almost constant to the power spectrum, and the first term will add a factor which is proportional to $J_0(2\pi A_n k)$. The effect of these incomplete images cannot be taken into account since it will depend not only on how many incomplete images there are, but also on how much of each image is missing. This effect can be suppressed if we have a much larger number of images completely contained within the interrogation area than are clipped, and so a larger interrogation area will be better.

The second factor, the variation of the amplitude was investigated by constructing a test case. In the situation stated here the amplitude varies from 7.716 - 7.807 pixels at the edges of the area, with the average being 7.763 pixels . This is not a very large variation across the area being about a 0.5 % variation. PIV will generally allow a 5 % variation of the mean velocity displacement across the interrogation area and it will have to be determined what the allowable variation for the amplitude will be.

If we consider Figure (8–4) which shows three profiles and the average of these three profiles, we can see that this averaging still produces the peaks and troughs of the function in the same places as the average profile.

Conclusions

The measurement of the amplitude is therefore possible from the profile of the power spectrum. The first peak of the profile is not the best position to take the measurement, however, since it is usually shifted by the central peak, and the error associated with the frequency is relatively higher than for the further peaks. We should therefore use the second or third peak to make the measurement.

The variation of the amplitude has the effect of producing peaks and troughs in the same position as the average amplitude. The clipped images will introduce some terms which will be of a much smaller order than the the main terms in equation (7.8)

as long as there are significantly more complete images than incomplete images and so can therefore be ignored.

The summation term will introduce a low frequency term which will raise the zeros of the function, but will not affect the position of the peaks and troughs.

8.2.2 Determination of the streak length from the autocorrelation plane

From equation (7.16) and figure (7–5) we can see that the expected form of the autocorrelation plane was a long thin central peak with two peaks at either end positioned at twice the amplitude of vibration with two copies of this on either side at positions associated with the velocity displacement.

As was noted before this is not generally what we get. We seem to get the peaks at either end appearing as bulges on either side of the thin streak (Figure (8–5) and (7–7)). The Bessel function looks more like its approximation, and the end peaks are not produced.

It is not possible therefore to measure the amplitude of the oscillation from the autocorrelation plane in its present form. The modification of the image plane will be attempted in section (8.5) to see if the autocorrelation plane can still be used to measure the amplitude.

8.2.3 Determination of the velocity from the autocorrelation plane

As well as wanting to measure the velocity amplitude of the oscillations, we are also interested the possibilities of measuring the mean velocity at the same time. Gray et al. [58] measured the streaming velocity at the velocity nodes where the streak length was very small, but had problems where the streak length was longer. The velocity peaks can easily be seen in the Figure (8–5), and it can also be seen that its centre is a much larger peak, which means that the velocity can easily be found by a largest peak search. In this case the largest peaks are at (-11.8,6.0) and (11.8, -6.0) compared with

an expected (-11.6,5.9), so you can see that despite the shape of the peaks it is still possible to find the velocity from the autocorrelation plane in the ordinary manner. These velocity peaks are of the same form as the central peak, but with a smaller low frequency component since we do not have the zero components superimposed.

The broad nature of the velocity peaks could cause problems if the mean velocity was purely in the direction of the oscillation, since this will mean that the central peak and the velocity peaks could overlap, giving rise to false peaks between them. If we consider Figure (8–6) which shows the measured velocity amplitude against the number of pixels across the tube compared to its expected value, we can see that at points close to u_y =0 the u_x value becomes very erratic. This phenomena should be taken into account when considering the area and we should attempt to make either $u_x >> 2A_m$ if u_y is small, or make u_y non-zero by some sort of image shifting.

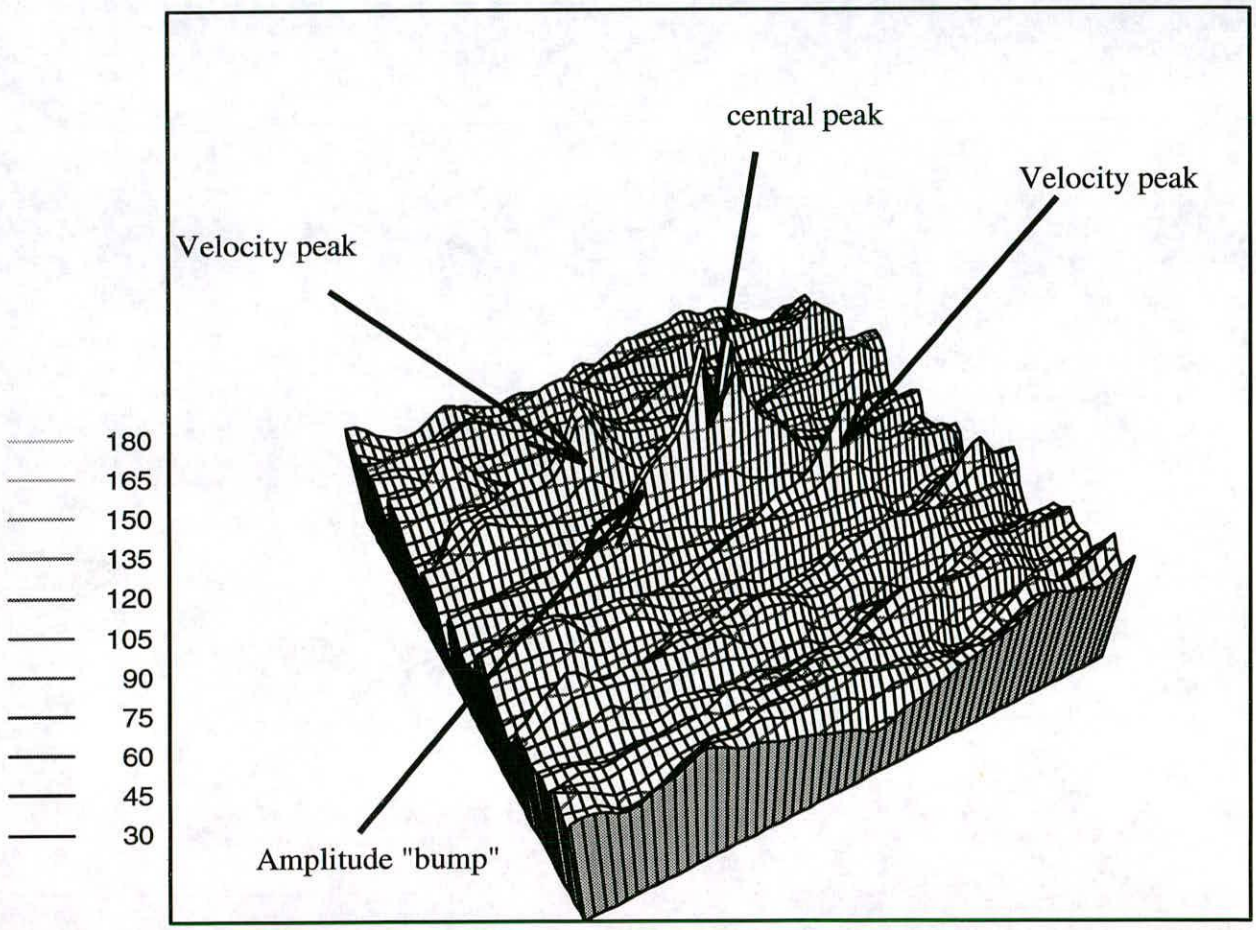

Figure 8–5: Autocorrelation plane of figure (8-1).

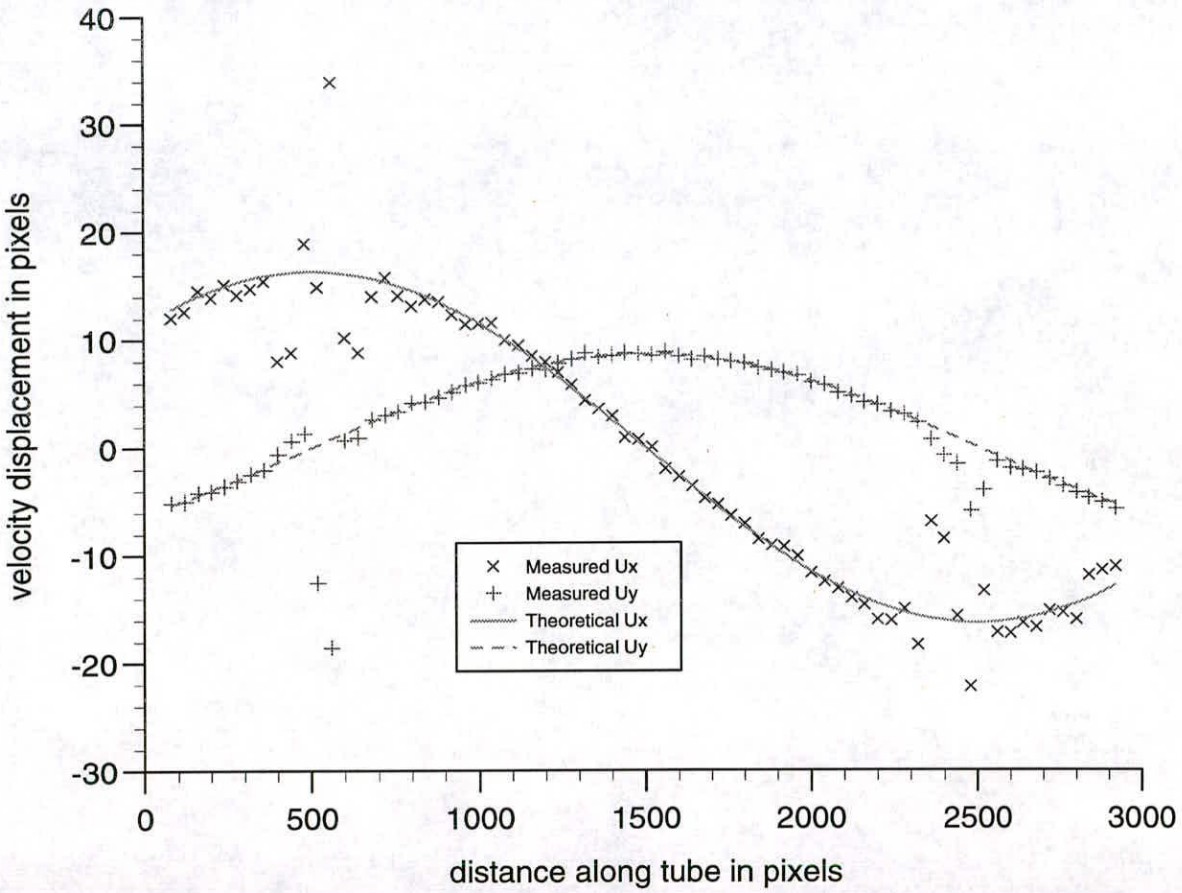

Figure 8–6: Variation of theoretical and measured u_x and u_y velocity displacements in pixels against distance along the photograph in pixels

8.3 The effect of the aperture size on the images.

It can easily be shown that an estimation of the diameter of the image of a seeding particle (d_i) recorded on the photographic film is

$$d_i = \sqrt{M^2 d_p^2 + d_s^2 + d_r^2} \tag{8.8}$$

where d_p is the seeding particle size, M is the magnification of the imaging system, d_s is the diffraction-limited spot diameter of the optical system given by

$$d_s = 2.44(1 + M)f^{\#}\lambda \tag{8.9}$$

and d_r is the resolution of the recording medium [2]. The f-number of the lens is denoted by $f^{\#}$, and λ denotes the wavelength of the light.

Thus the size of the image on the negative will depend on the these parameters only. We are interested in the size of the seeding particle image recorded on the photograph, and so we will note that the image recorded on the negative, SI, will be approximately Gaussian of the form

$$SI \approx e^{-\frac{\pi}{\sigma_n^2}(x^2+y^2)} \tag{8.10}$$

where

$$\sigma_n = \frac{d_i}{2} \tag{8.11}$$

The halo-width on the photograph will be dependent on the magnification between the negative and the photograph (M_1) and this can be defined as

$$\sigma = M_1 \sigma_n \tag{8.12}$$

We will use the measure $\frac{\sigma}{A_m}$ rather than just the measure σ to distinguish between the different types of streaks that can be observed from the convolution in equation (7.2) because the cases of a large halo-width and a large streak length will be the same as for a small halo-width and a small streak length. We shall look at three types of streaks, one in which the streak length is much greater than the seeding image, one in

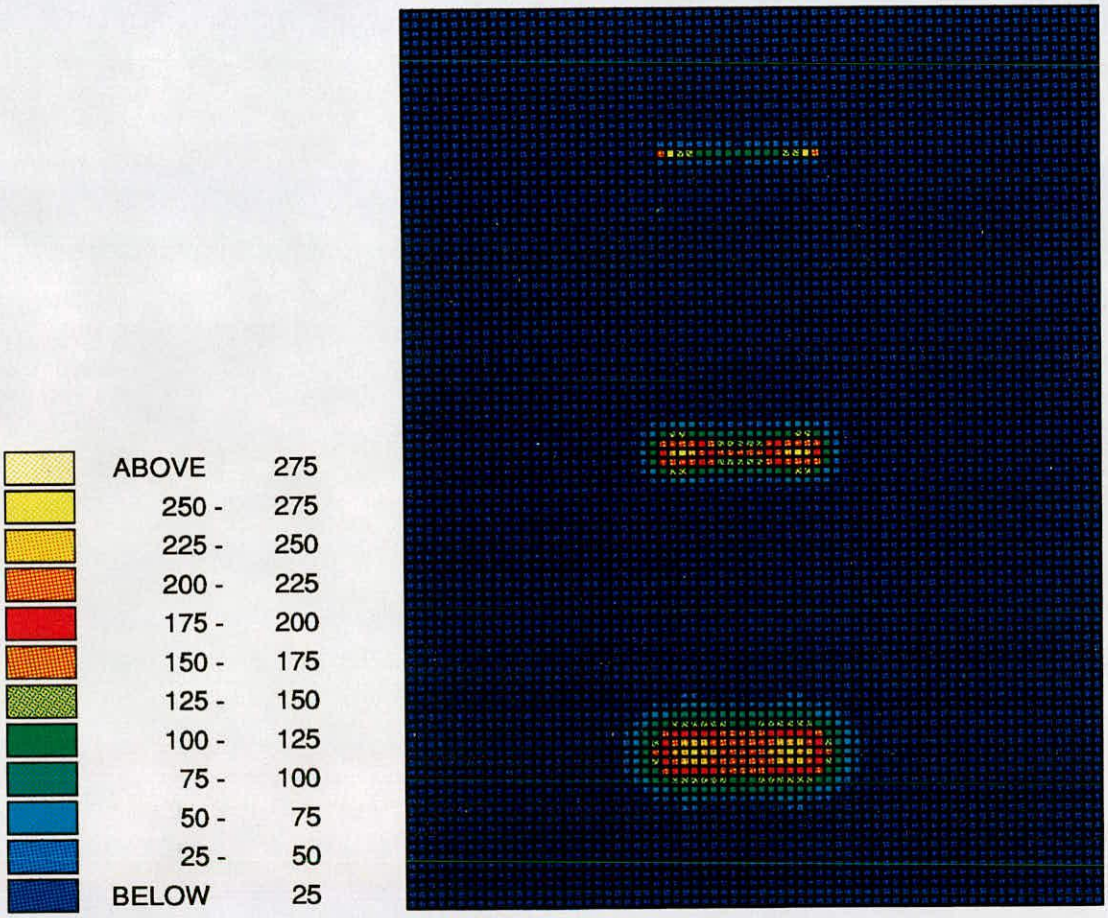

Figure 8–7: Variation of image shape with increase in the width of the image halo for $\frac{\sigma}{A_m} = 0.0177, \frac{\sigma}{A_m} = 0.079, \frac{\sigma}{A_m} = 0.125$ (From top down).

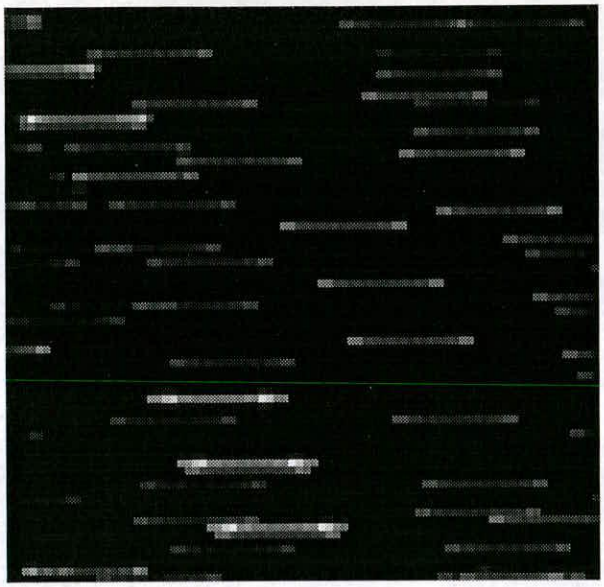

Figure 8–8: Interrogation area for $\frac{\sigma}{A_m} = 0.0177$.

which the seeding image is beginning to affect the results, and one where the seeding image is large enough to affect the results. All three of these cases will be present in a standing wave, since the amplitude of fluctuation is related to the distance along the tube, and so the case of a large amplitude will occur at a velocity anti-node, while a small amplitude of fluctuation will occur at a velocity node.

The images used were $\frac{\sigma}{A_m} = 0.0177$, $\frac{\sigma}{A_m} = 0.0559$ and $\frac{\sigma}{A_m} = 0.079$.(Figure (8–7)) . As you can see from this figure, the increase in the halo-width will shift the position of the highest point of the end-points towards the centre of the image making the streak seem shorter than it is.

We shall construct three separate images with different $\frac{\sigma}{A_m}$ ratios and with an average streak length of approximately 7.92 pixels, and an average velocity displacement of (4.56,8.30) and we shall compare the power spectrums and autocorrelation planes of all three to determine the effect of the image width on the visibility of the amplitude peaks and the velocity peaks. These three images will be identical in every way except that the halo-width to amplitude ratio will be different.

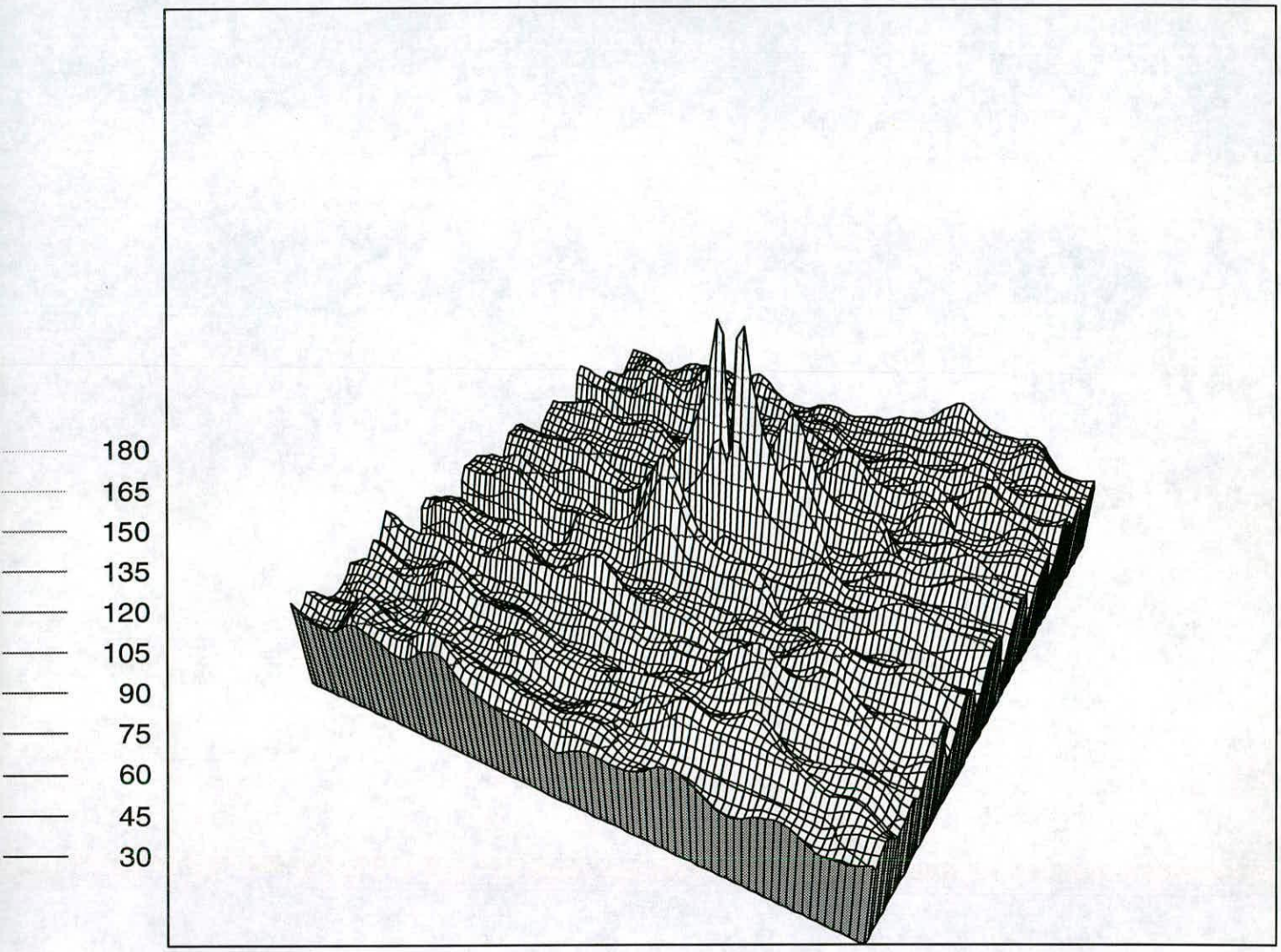

Figure 8–9: Autocorrelation plane for $\frac{\sigma}{A_m} = 0.0177$.

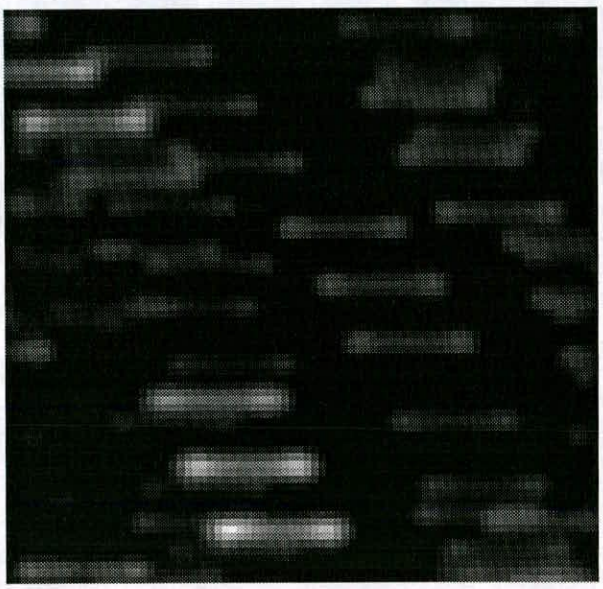

Figure 8–10: Interrogation area for $\frac{\sigma}{A_m} = 0.0559$

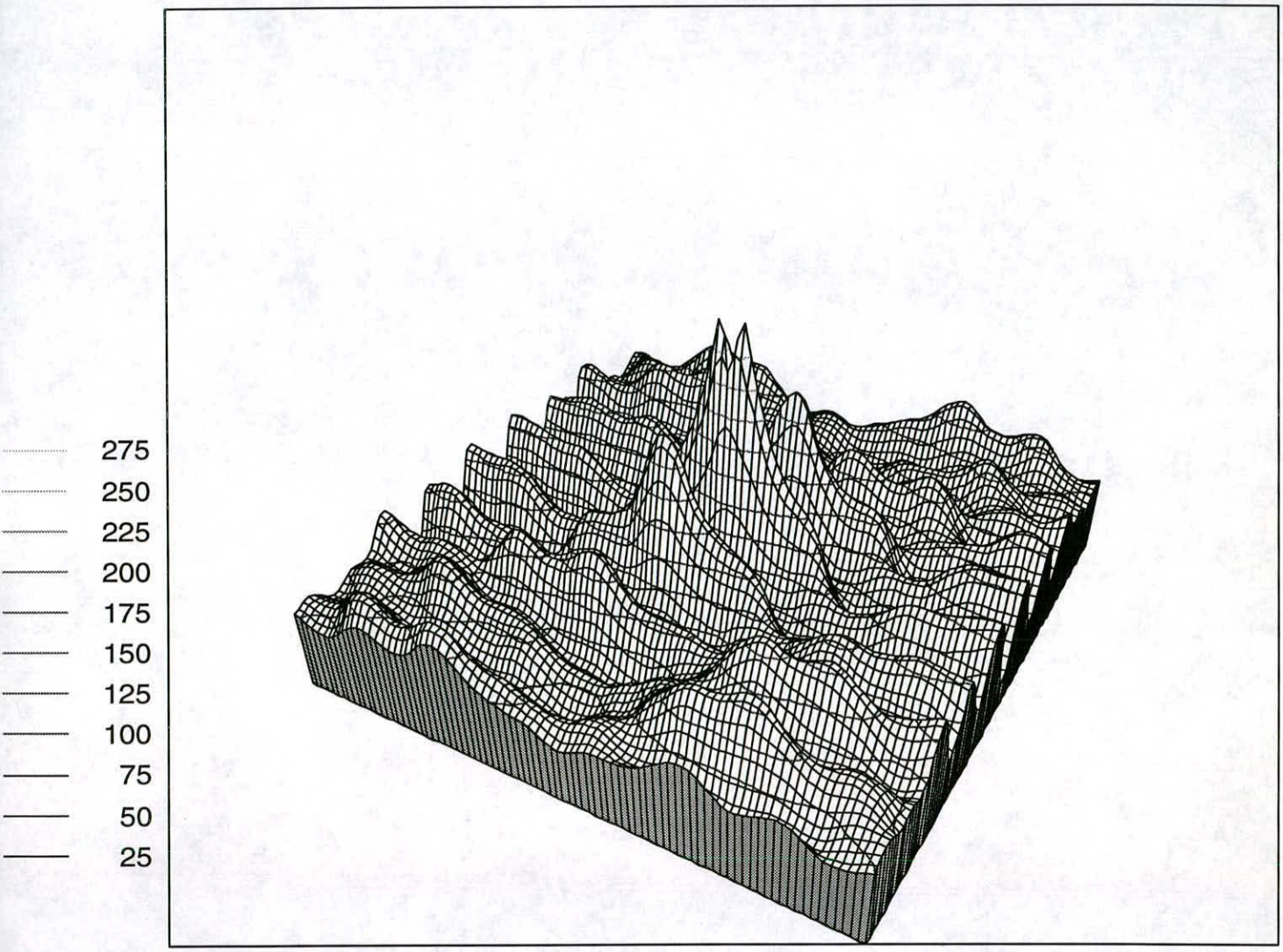

Figure 8–11: Autocorrelation plane for $\frac{\sigma}{A_m} = 0.0559$.

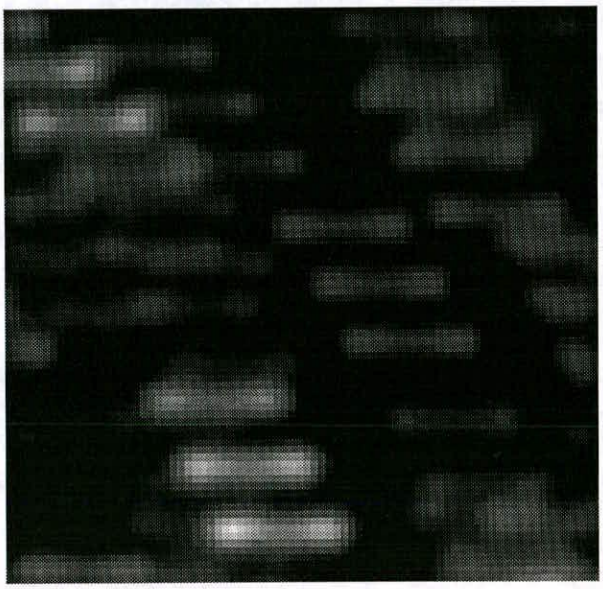

Figure 8–12: Interrogation area for $\frac{\sigma}{A_m} = 0.079$.

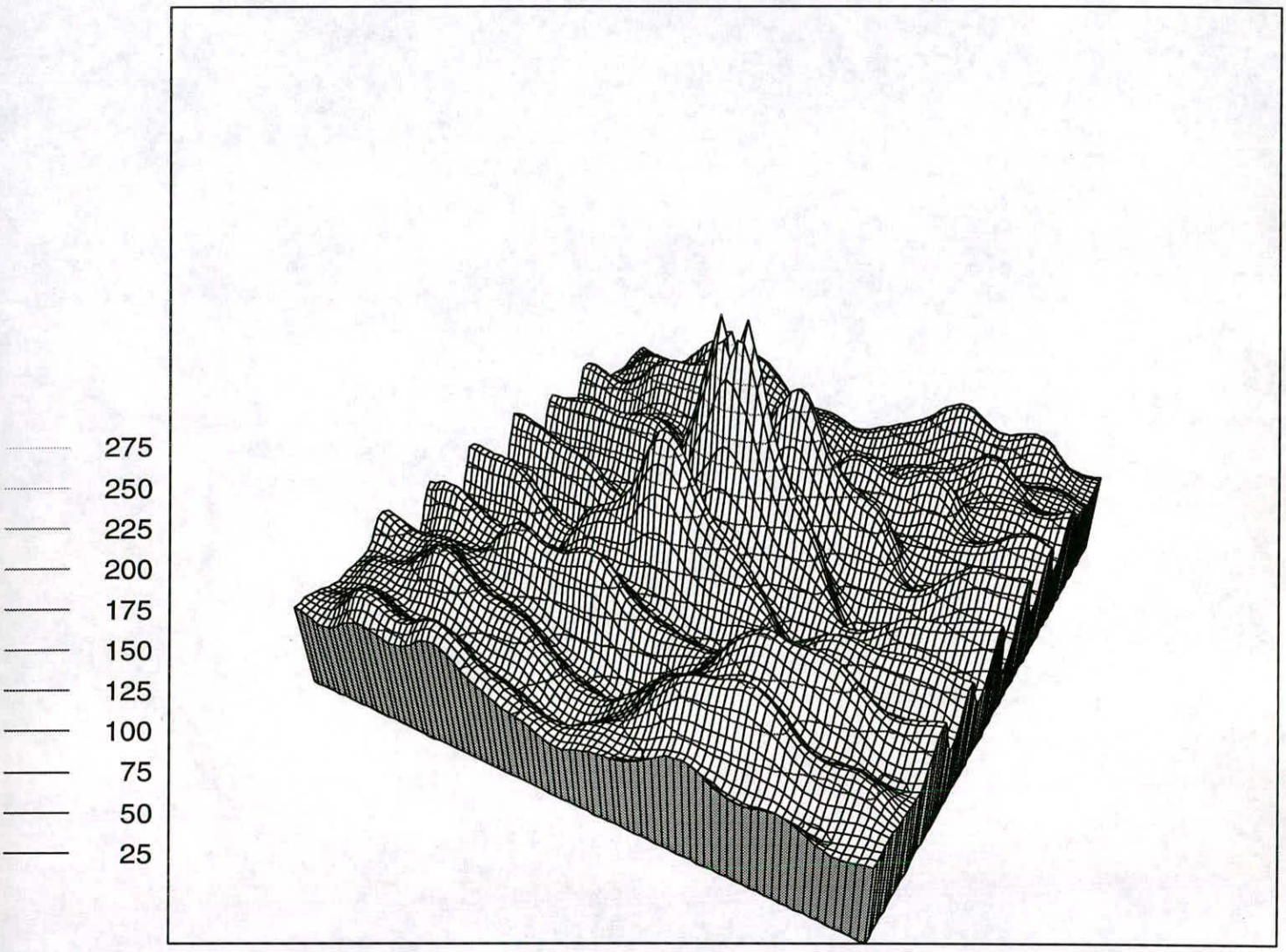

Figure 8–13: Autocorrelation plane for $\frac{\sigma}{A_m} = 0.079$.

Figures (8–8),(8–10) and (8–12) show the chosen interrogation areas of the three cases $\frac{\sigma}{A_m}$=0.0177, $\frac{\sigma}{A_m}$=0.0559 and $\frac{\sigma}{A_m}$=0.079 respectively.

The autocorrelation planes of these images are shown in Figures (8–9), (8–11) and (8–13), while Figure (8–14) shows the profiles of the power spectrum for the three cases and Table (8–2) shows a summary of all results.

$\frac{\sigma}{A_m}$	A_m from 1st peak of PS	A_m from 2nd peak of PS	A_m from 3rd peak of PS	velocity from AP
0.0177	7.92	8.06	7.98	4.09,8.77
0.0559	7.69	8.17	8.10	4.47,8.80
0.079	7.99	8.32	8.24	4.54,8.75

Table 8–2: The amplitude of displacement and the velocity displacement measured for several areas with different image width/amplitude ratios. Expected values were amplitude=7.92 pixels and velocity = (4.56,8.30)

As you can see from the autocorrelation planes, the side peaks are not very prominent at all, but seem to be swamped out more as $\frac{\sigma}{A_m}$ increases showing that it is not easy to find the amplitude from the autocorrelation plane. This means that it is only possible to find the peaks accurately for very small values of $\frac{\sigma}{A_m}$.

Figure (8–14) shows that the increase of the halo-width increases the damping of the profile and there is a small shift of the peaks towards the centre. Figure (8–15) shows that there is a general trend of larger measured values of the amplitude for larger halo-widths although it should be noted that the error in the measurements is of the order of 0.5 pixels. If figure (8–15) is studied closely, we can see that the larger the halo-width, the more each peak is shifted towards the centre. The third peak is shifted less than the second peak and so gives more accurate values in general than the second peak, and we also found that this was true for the second peak giving more accurate values than the first peak, but this is not shown in the example we have chosen here.

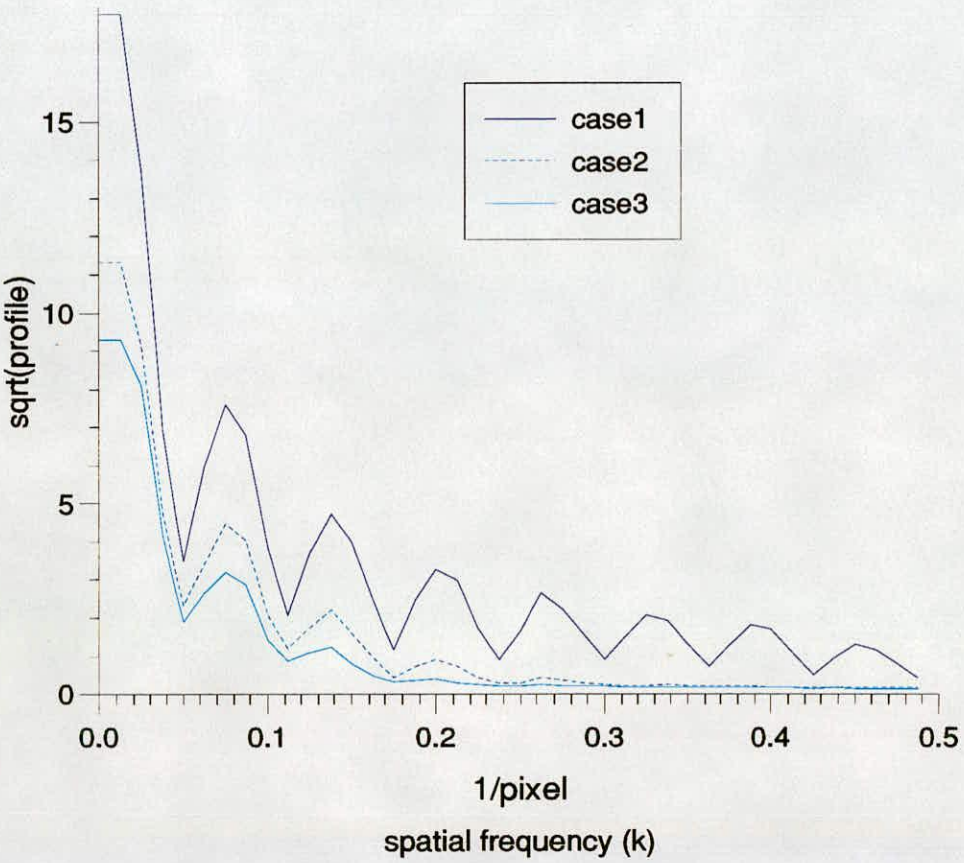

Figure 8–14: Profiles for the three cases being investigated.

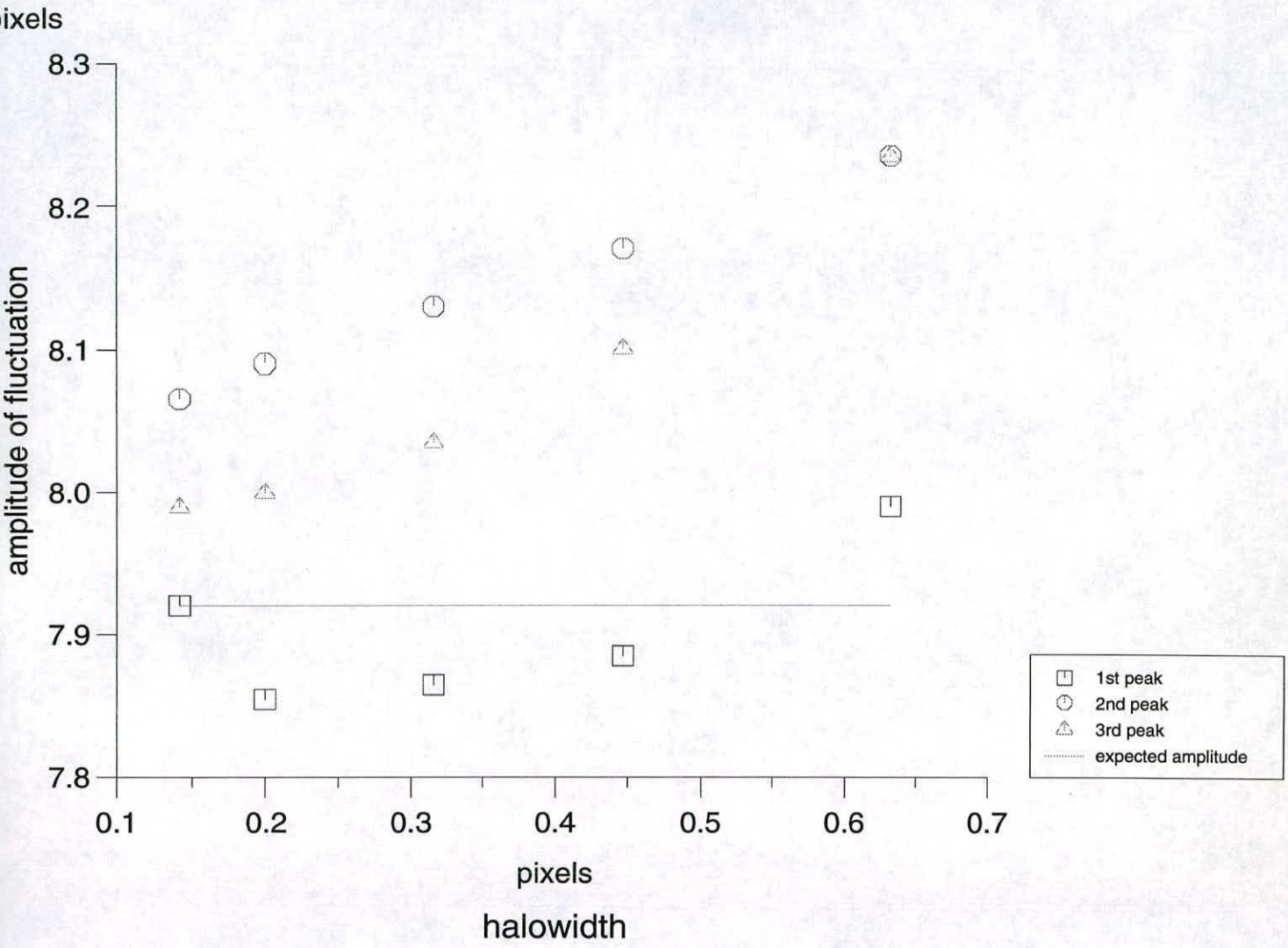

Figure 8–15: Graph showing how expected amplitude and measured amplitude vary with the halowidth.

8.3.1 Discussion of effect of aperture size on images

As we have shown, the increase of the $\frac{\sigma}{A_m}$ ratio will produce autocorrelation planes with amplitude peaks that are swamped by the central peak and so there will not be any amplitude peaks except for at small ratios.

In the measurements of the amplitude from the power spectrum, the increase in $\frac{\sigma}{A_m}$ will cause a general increase in the amplitude. The first peak will be affected more by this than the second or third so it is better to take measurements from the second, or third peak, instead of the first.

We also show that the $\frac{\sigma}{A_m}$ ratio does not affect the velocity measured to a significant amount in these examples. This is true for most $\frac{\sigma}{A_m}$ ratios as long as the velocity displacement is large enough so that the presence of the central peak does not shift the velocity peaks towards the centre. Table (8–2) does have the first velocity smaller than expected by 0.5 pixel, but that can be explained as due to noise in the autocorrelation plane.

8.4 The effect of the size of the interrogation window.

In section (7.1), we discussed the necessary size of the interrogation area and determined that we would like its width to be of the order of 5 or six streak lengths in size for best velocity results. Here we will justify this point and show the effect of the change in the size of the interrogation area on the results obtained from that area.

A simulated photograph was constructed of size 400 pixels x 800 pixels and image width $\sigma = 0.316$ pixels. The images had an amplitude of vibration of approximately 8 pixels long so the streaks were typically of the order of 16 pixels long. Three interrogation areas were taken, centred on the point (210,210), and these were used to investigate how the change in size of the interrogation area affected the results. The average velocity displacement expected for this area was (2.631,-8.790),(2.634,-8.759) and (2.639,-8.713) respectively (the velocity displacements were determined by averag-

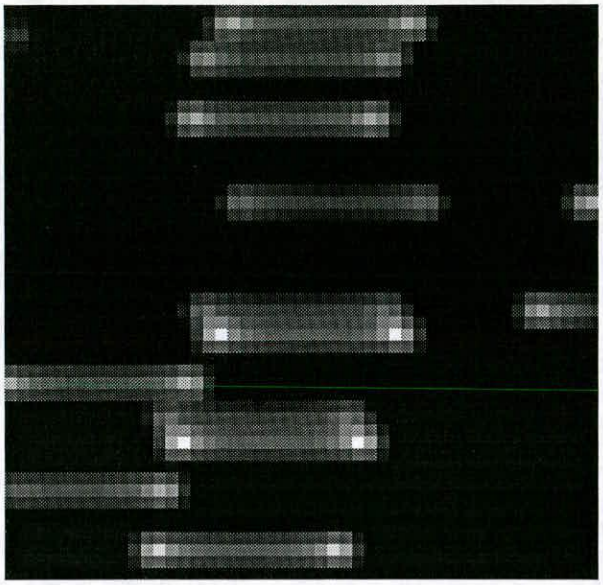

Figure 8–16: An interrogation area of size 48 pixels showing average displacement of (2.631,-8.790) and average amplitude of fluctuation of 7.970 pixels

ing the expected velocity over the whole interrogation area), so the interrogation areas chosen were of the size 3x streak length, 5x streak length and 7x streak length (48 pixels, 80 pixels and 112 pixels). These are shown in Figures (8–16), (8–18) and (8–20) respectively. The centre point is sometimes removed, giving the impression of a double point at the centre, because we wished to scale the heights so that the velocity peaks could be seen and the centre point was sometimes of a much greater order. With the centre point removed, however, the ratio of the highest point to velocity peak height is of a much better order.

Figure (8–22) shows the profiles of these areas and from these we can determine the effect of a larger area. The smallest area of 48 pixels produces a profile which uses only 3-4 points to determine a period of the Bessel function (peak to peak). This means that the profile is not well defined. For the larger area of 80 pixels, the profile is defined with a great deal more accuracy, with there being 6 points defining the period of the Bessel function. For the largest area, the points are again more closely spaced together, allowing the position of the peak to be determined with more accuracy.

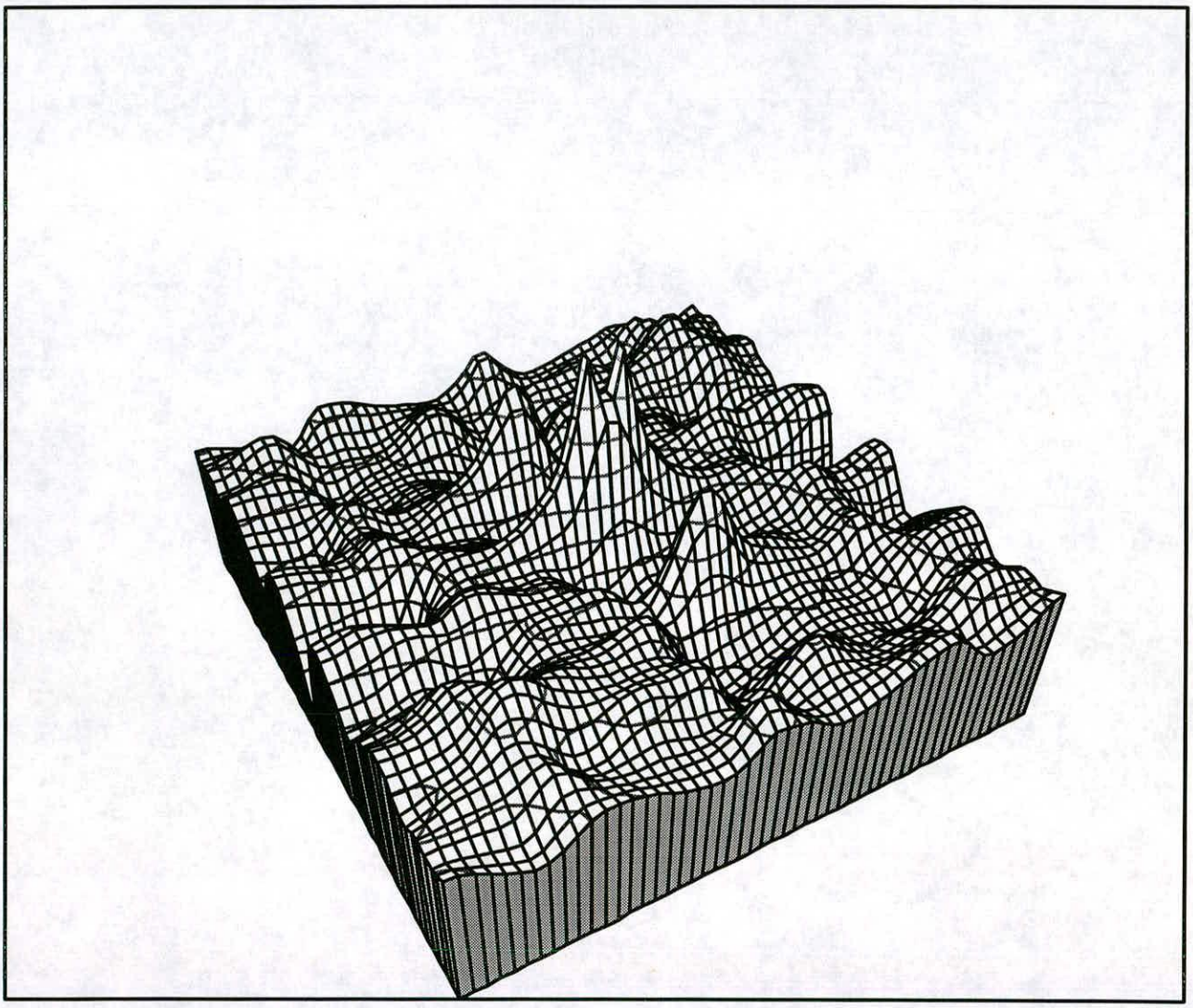

Figure 8–17: Autocorrelation plane with velocity peaks at (2.85,-8.86)

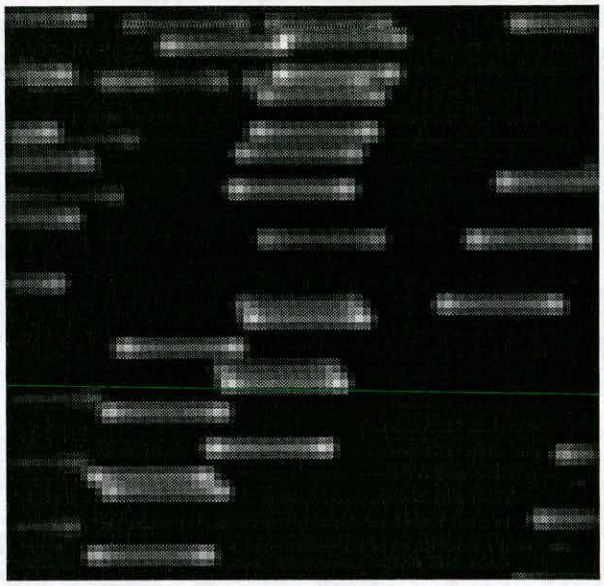

Figure 8–18: An interrogation area of size 80 pixels showing average displacement of (2.634,-8.759) and average amplitude of fluctuation of 7.969 pixels

If we make the assumption that we need a certain number of points in order that the Bessel function can be distinguished, then the determination of optimum size can be discussed mathematically.

The first peak of the Bessel function occurs when

$$(2\pi A_m k_p) = 3.8317 \tag{8.13}$$

where k_p is the wavenumber of the first peak, which can be written as $\frac{s}{2*T}$, where $2*T$ is the size of the interrogation area, and s is the number of pixels to the first peak. This can be rewritten as

$$T = \frac{\pi A_m s}{3.8317} \tag{8.14}$$

If we now assume that we need six points to define the Bessel function to the first peak, then we can replace s by six in equation (8.14) to show that the size of the interrogation area would be of the order $2 * T = 2 * 4.9 * A_m$.

An area smaller than this will not resolve the Bessel function properly, leading to larger errors. An area larger than this will produce errors due to the larger variations

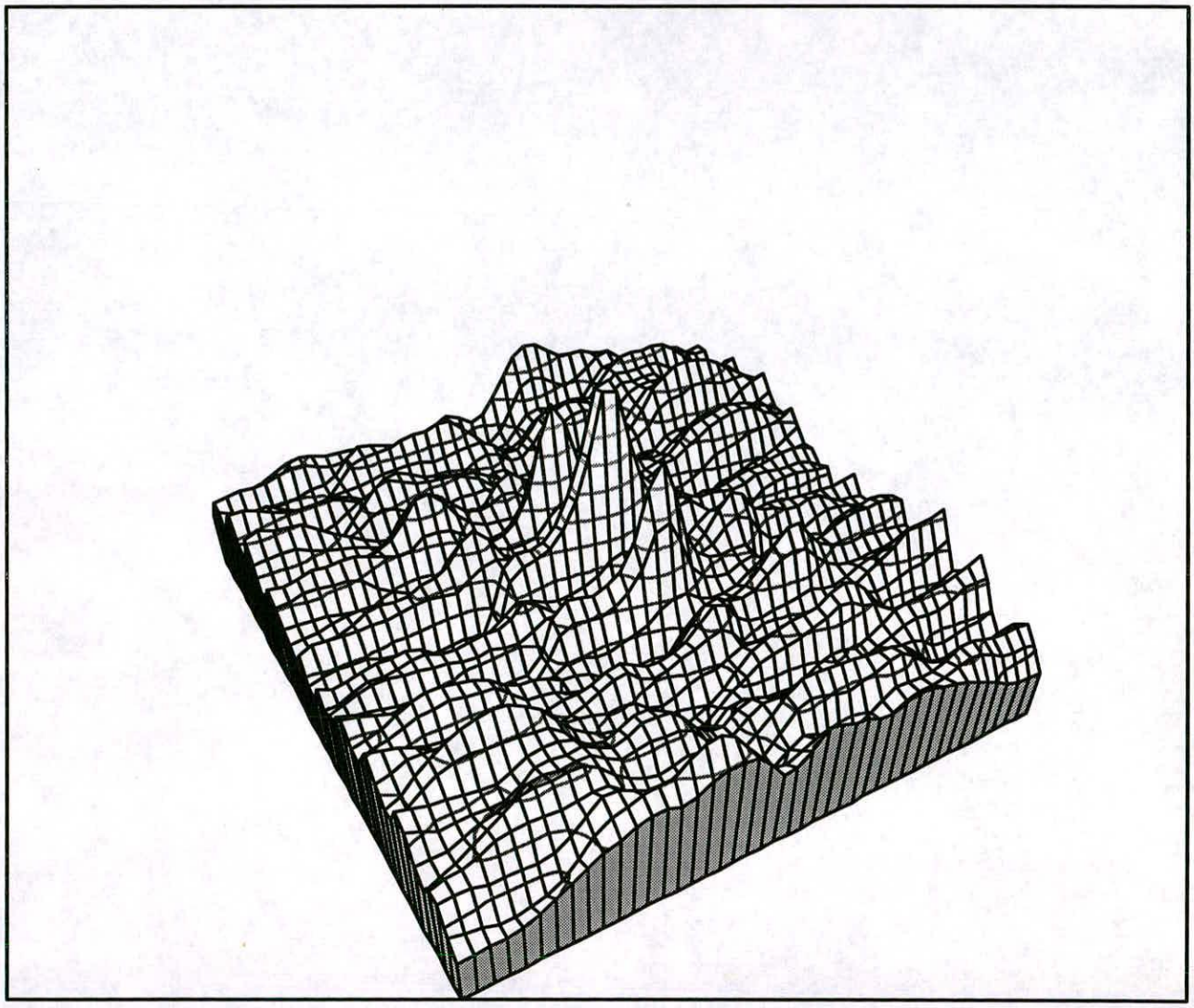

Figure 8–19: Autocorrelation plane with velocity peaks at (2.49,-8.81)

Figure 8–20: An interrogation area of size 112 pixels showing average displacement of (2.639,-8.713) and average amplitude of fluctuation of 7.968 pixels

of the velocity and amplitude which widen and shorten the significant peaks making them harder to detect.

Table(8–3) shows the measured amplitude and the error of measurement from which we can illustrate some points. From the table it can be seen that as the size of the area increases from 48 pixels to 80 pixels, the measured amplitude becomes closer to the expected value and the error associated with the measurement becomes smaller. As the size of the area increases from 80 pixels to 112 pixels, the measured value does not change, but the error decreases.

The autocorrelation planes are shown in Figures (8–17), (8–19) and (8–21) and table (8–3) shows the values obtained for the displacement and the amplitude compared to the average value in the interrogation area. The values for the velocity in these cases correspond quite well with the expected values for all sizes of interrogation areas, since the areas used here were small enough that the velocity peaks were significantly correlated so as to be higher than the random correlations.

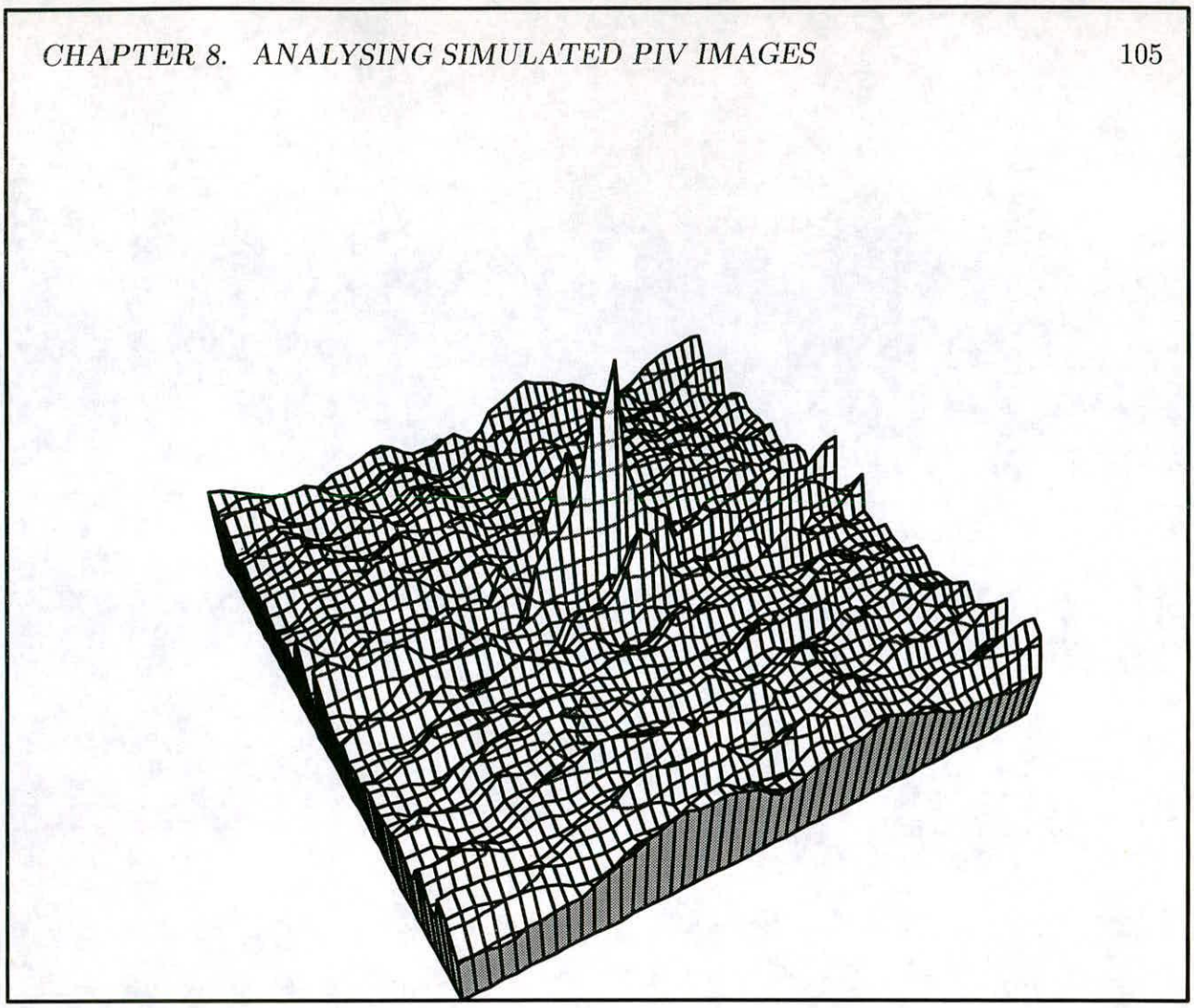

Figure 8–21: Autocorrelation plane with velocity peaks at (2.74,-8.33)

size of area (pixels)	expected A_m (pixels)	A_m from 2nd peak (pixels)	error (pixels)	expected velocity (pixels)	velocity displacement (pixels)
48	7.97	7.77	0.56	(2.63,-8.79)	(2.85,-8.86)
80	7.97	7.97	0.36	(2.63,-8.76)	(2.49,-8.81)
112	7.97	7.98	0.26	(2.64,-8.71)	(2.74,-8.33)

Table 8–3: A table showing how the amplitude of fluctuation measured from the profile and the velocity displacement measured from the autocorrelation plane compare to the known values.

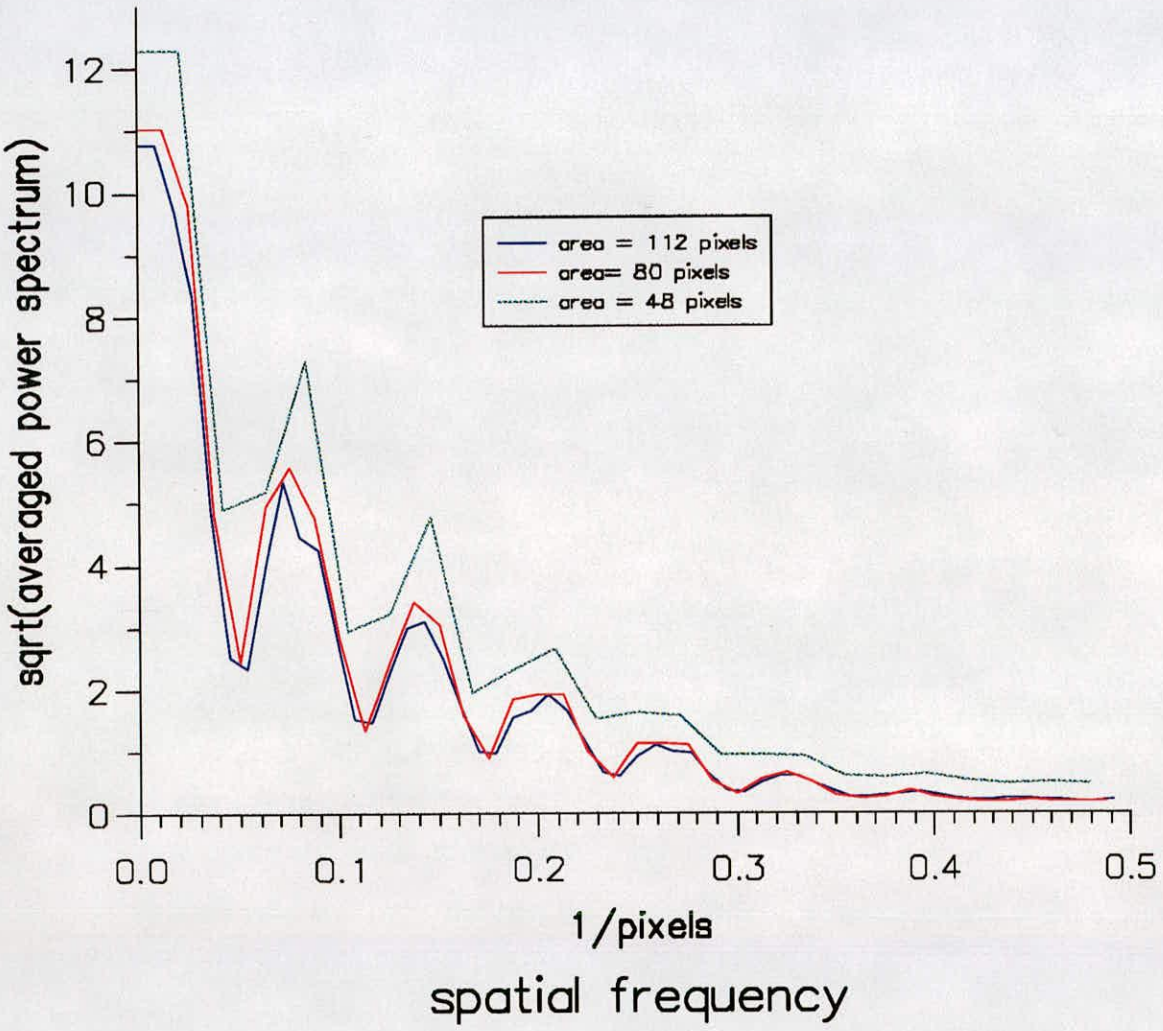

Figure 8–22: Profiles of the three sizes of interrogation area showing increase in resolution that exists for larger areas

8.4.1 Discussion of the ideal interrogation area size.

The two factors which determine the size of the interrogation area are the velocity displacement and the amplitude. As we have shown, the amplitude can be found with acceptable error in an interrogation area which is greater than 5 x streak length. The larger an area is , however, the less significant the results due to the lessening correlation between the images until eventually, for an interrogation area where the velocities change by over 5% over the area, the assumption that the amplitude and velocity do not change by much over the area will be broken, resulting in no significant profile in the Power spectrum and no significant peaks in the autocorrelation plane. The area should be kept as small as possible, therefore, in order that the velocity displacement and amplitude do not vary by a significant amount across the area.

The optimum size of the interrogation area is therefore one which is determined by the size of the amplitude and is of the order of 5*streak length.

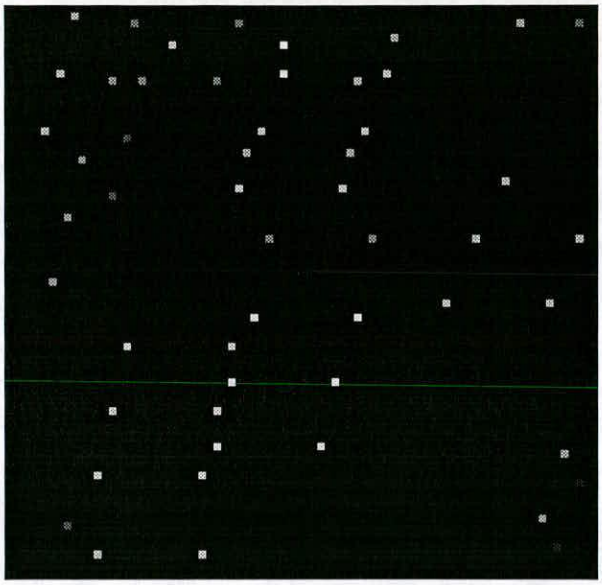

Figure 8–23: Figure 8-18 which has been edited to only show all the local maximums which are the end points of the streaks.

8.5 Modification of the image plane

As can be seen from the discussion of the results from the autocorrelation plane and the power spectrum, the shape of the image causes problems which, although they can be accounted for, are a nuisance. It would be more desirable if the image was simplified in some way, say to make it an image with only two dots at the end of the streaks. This would reduce the problem down to a simple peak finding routine in the autocorrelation plane and this could be carried out quickly and efficiently.

We will do this by finding all the points in the image which are local maximums. These points will be the end points of the streaks and when we calculate the autocorrelation plane of that it will provide four significant peaks, two associated with the amplitude of vibration (the distance between the peaks at either end of the streaks) and two associated with the velocity displacement. If we use Figure (8–18) as an example, we can construct a file which only contains the points which are local maxima (Figure (8–23)) by simply scanning for points which are larger than their neighbours. Comparing this picture with Figure (8–18) will show us that the points which remain

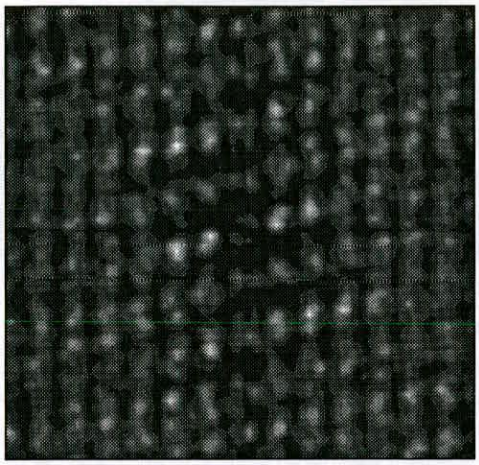

Figure 8–24: Power spectrum of local maximum interrogation area showing two cosine terms superimposed at an angle.

in the area are the ends of the streaks. The power spectrum of this area will be a multiplication of two cosines at different angles (Figure (8–24)) and this will produce the autocorrelation plane Figure (8–25) in which there are four main peaks, one on either side of the centre due to the correlation of the end points, and two positioned below and above the centre caused by the correlation of the images displaced by the velocity displacement. Table (8–4) shows how the displacement values obtained compare to the expected values. The velocity varies by a pixel or more over the interrogation area, so the peak is much smoother allowing the velocity values to be interpolated to greater accuracy. The amplitude does not vary by a significant amount and so the interpolation gives an integer value. If we consider Figure (8–26) which shows the amplitude measured against the distance along the tube, we can see that the measured values go up in integer jumps and are all a constant value smaller than the expected values.

The amplitude peak is always closer than expected to the centre because of the non-continuous nature of the form of the streak. There is a discontinuity at the end of the streak which means that when the halo function is convoluted with it, the peaks

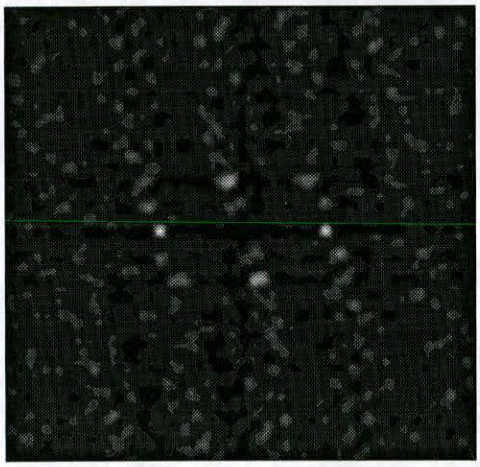

Figure 8–25: Autocorrelation plane of the local maximum interrogation area showing four prominent peaks formed due to end points of streak and velocity displacement between exposures.

	amplitude of fluctuation (pixels)	velocity (pixels)
expected value	7.97	(2.63, -8.76)
measured from original image	7.97 ± 0.36	(2.49,-8.81)
measured from modified image	7.00	(2.15,-8.90)

Table 8–4: A table showing the measured values from the modified image and comparing them to the expected and the measured values from the original

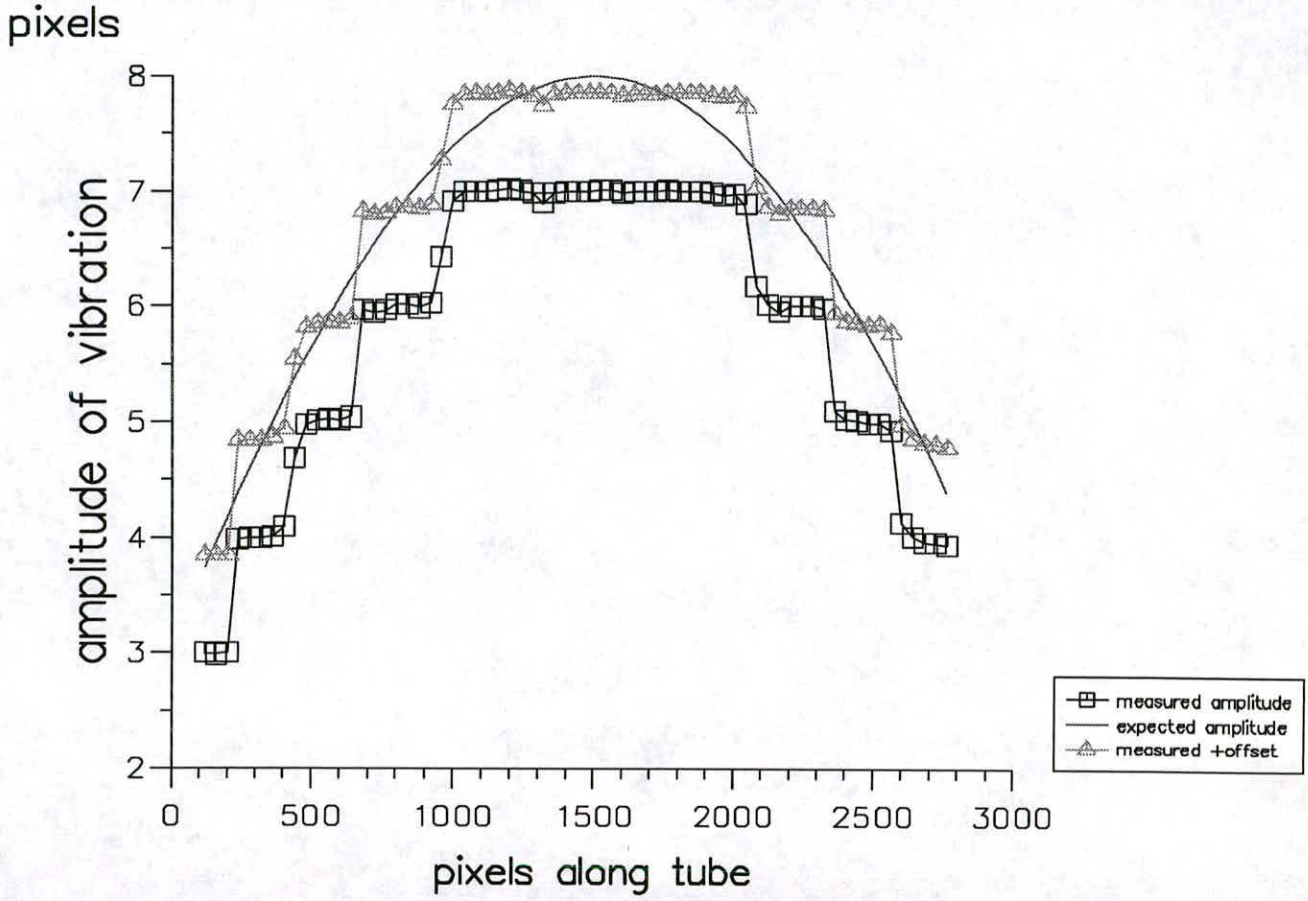

Figure 8–26: Graph showing measured amplitude against expected amplitude and measured amplitude plus an offset of 0.85 pixels.

will be shifted inwards (see Figure (8–7)). The image width which was given to the image in Figure (8–23) was $\sigma = 0.316$ and this will give an amplitude which will be about 0.03 pixels smaller than expected. This is much smaller than the discrepancy.

The factor which can account for some of the discrepancy, however, is associated with the probability density function having a maximum at the far edges of the streak, whereas the pixelated version of it has the peak situated at the centre of the pixel. This will mean that the measured value is at least 0.5 pixels smaller than the expected value. This would account for some of the difference between the expected results and the measured results shown in Figure (8–26).

The rest of the difference can be accounted for if we consider that the pixelation will also cause the end pixel to be of a smaller value than the next to end pixel if the amplitude is slightly more than an integer value due to the shape of the probability density function. If we note that a pixel is defined as

$$HEIGHT\,OF\,PIXEL = \sin^{-1}(\frac{x_n + 0.5}{A_m}) - \sin^{-1}(\frac{x_n - 0.5}{A_m}) \tag{8.15}$$

then the end pixel and the penultimate pixel will be

$$HEIGHT\ OF\ END\ PIXEL = \frac{\pi}{2} - \sin^{-1}(1 - \frac{b}{A_m}) \tag{8.16}$$

$$HEIGHT\ OF\ PENULTIMATE\ PIXEL = \sin^{-1}(1 - \frac{b}{A_m}) - \sin^{-1}(1 - \frac{b+1}{A_m}) \tag{8.17}$$

respectively where $A_m - b$ is the inner edge of the outer pixel. This means that the amplitude is b pixels longer than an integer where $0 < b < 1$. If we compare these two functions (Figure(8–27)) then we can see that they cross at approximately $b = 0.35$. This means that when $b < 0.35$ the end pixel will be smaller than the penultimate pixel and the local peak detection routine will chose the penultimate peak instead of the final peak. This means that the amplitude measured will be at least 0.85 pixels smaller than the expected value if the 0.5 mentioned above is taken into account. This can be seen in Figure (8–26) where the measured value plus the offset of 0.85 fit the expected values much better. The position of the intercept (0.35 in this case) does depend on the amplitude of the oscillation, but does not vary by much. In fact it stays between 0.33–0.38 for $2 < A_m < 100$ pixels.

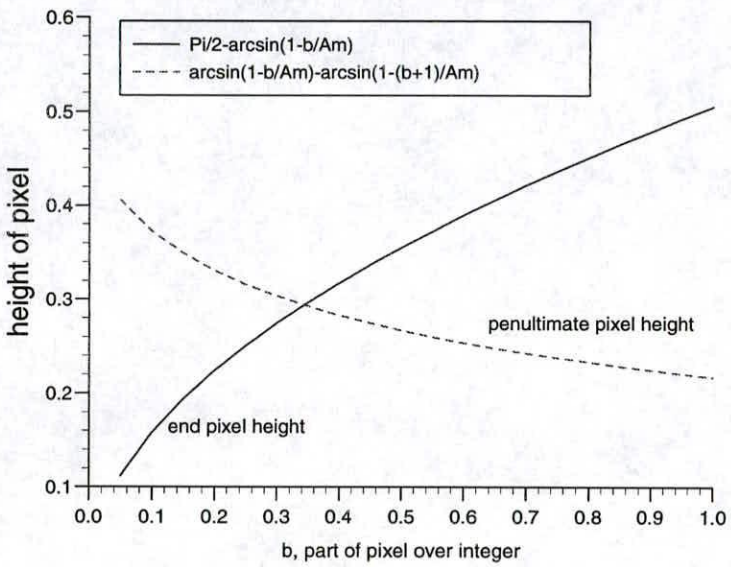

Figure 8–27: Graph showing how the height of the penultimate and ultimate pixels vary against one another when the amplitude is b (a fraction of a pixel) larger than the inner edge of the pixel.

halo-width (pixels)	measured amplitude (pixels)	measured amplitude plus offset (pixels)	velocity displacement (pixels)
0.1414	7.03	7.88	(3.97,9.00)
0.200	7.04	7.89	(3.96,8.99)
0.316	7.00	7.85	(3.97,8.94)
0.447	6.55	7.40	(4.46,8.99)
0.632	6.12	6.97	(4.02,8.96)

Table 8–5: The variation of the measured amplitude against the halo-width for area in which the expected value was 7.92 pixels and the velocity displacement was (4.56,8.3)

8.5.1 Change in halowidth

As we can see from above, the local maximums found are at least 2x0.85 pixels further apart than the expected value due to the pixelation of the image. Another factor which can affect the separation of the images is the halo-width which (as can be seen in figure (8–7)) will affect the position of the highest points of the image.

This correction is small for low values of $\frac{\sigma}{A_m}$ but can be much more noticeable for higher values. Table (8–5) shows how the value obtained varies against the ratio $\frac{\sigma}{A_m}$. From this it can be seen that the measured value decreases compared to the expected value for increasing $\frac{\sigma}{A_m}$. Figure (8–28) shows this in graphical form. This shows that for small halo–widths, we have good agreement, but at larger halo-widths, the measured value drops away very sharply from the expected value.

8.5.2 Discussion of viability of this method

It can be seen from the results that if we use the autocorrelation of the modified image plane to find the amplitude of the oscillation we find that we have to add on a factor of 0.85 pixels due to the pixelation of the image, and also another unknown factor due to the particle image halo-width. This extra factor is very significant at large halo-width, and this means that this technique only gives good measurements at small halo-widths.

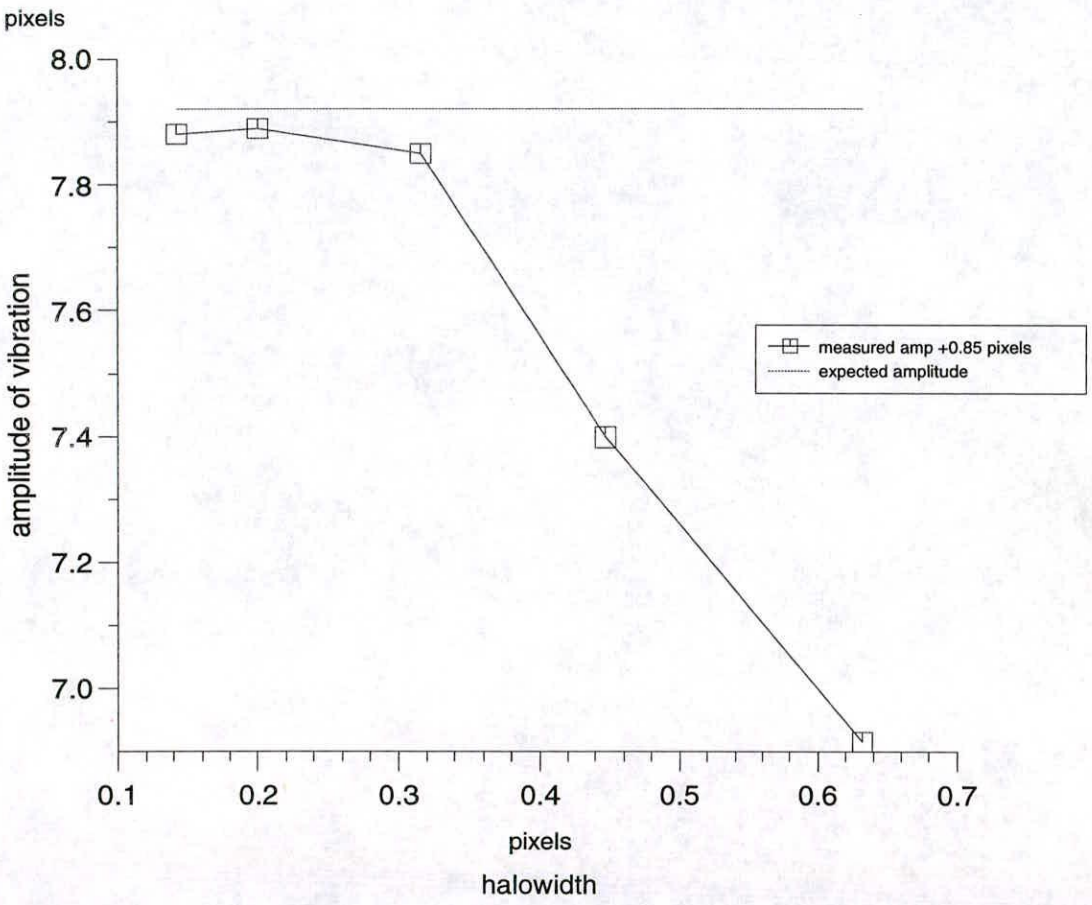

Figure 8–28: Graph showing how measured amplitude plus the offset of 0.85 pixels compares to expected value as the halo-width is varied.

The technique also only measures in pixel steps and therefore is not accurate to more than half of a pixel.

The velocity measurements from the autocorrelation plane are not dependent on the halo-width to as great an extent. In fact a larger halo-width will produce a smoother peak and allow the interpolation routine to identify the peak with sub peak accuracy.

8.6 FT of profile

As we noted in section (7.2) the Bessel function can be approximated by the function

$$J_0(2\pi A_m k) \approx \frac{1}{\sqrt{2\pi A_m k}} \cos(2\pi A_m k - \frac{\pi}{4}) \tag{8.18}$$

and that this will produce an autocorrelation plane which does not have the end peaks expected from the K() function. At the time we just noted that this was true, and in section (8.2.2) it was shown that in general the autocorrelation planes, possibly due to their resolution, did not have these end peaks either. This meant that it was not possible to make a measure of the amplitude from the autocorrelation plane. It was to try to get around this problem that we tried modification of the image plane, but that proved unsatisfactory, so instead we will return to the theory of the autocorrelation plane and consider the possibility of using the approximation of the Bessel function to find the amplitude.

Figures (8–29) and (8–30) show the form of the profile and the Fourier transform of the profile, showing that the Fourier transform has the same form as the approximation of the elliptical integral. The form of this function can be seen to be the box function ending at 15.8 pixels with a $\frac{1}{x}$ type function added to it. We can see that the end of the box function is marked by a steep decline in the function with the centre of that slope being the amplitude. If we consider this in the mathematical terms, the autocorrelation plane can be described as

$$AP(x,y) = \left(FT\left[\frac{1}{4\pi A_m k}\right] + \Pi(2A_m)\right) \otimes e^{-\frac{\Pi}{2\sigma^2}(x^2+y^2)} \tag{8.19}$$

The $FT\left[\frac{1}{4\pi A_m k}\right]$ term will be of the form of a $\frac{1}{x}$ and so if we consider the first derivative of this with respect to x ignoring the $e^{-\frac{\Pi}{2\sigma^2}((y^2)}$ term which is averaged, we

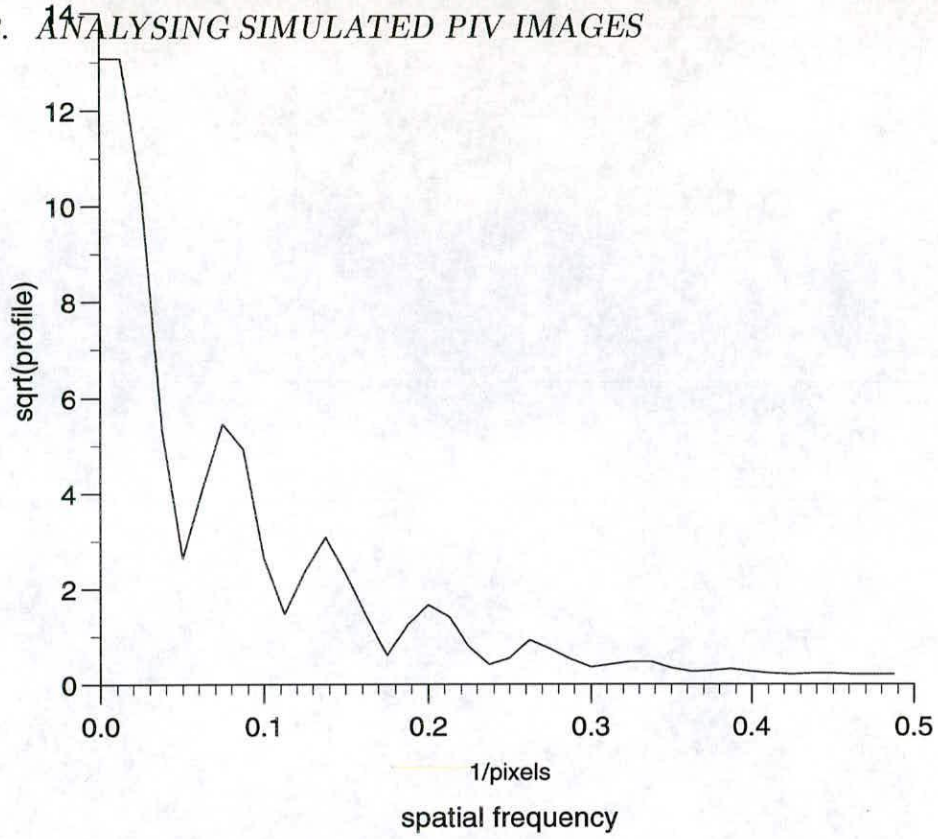

Figure 8–29: Square root of profile of the power spectrum

get

$$\frac{\mathrm{d}AP}{\mathrm{d}x} \approx \left(e^{-\frac{\Pi}{2\sigma^2}((x-2A_m)^2)} + e^{-\frac{\Pi}{2\sigma^2}((x+2A_m)^2)} + e^{-\frac{\Pi}{2\sigma^2}((x)^2)}\right) \tag{8.20}$$

This consists of three peaks, one at the centre and two at either side at a distance $2A_m$ pixels. Two of these peaks can be seen in Figure (8–30), which shows the gradient of the FT of the profile compared to the FT of the profile. The peak at zero is not represented here correctly since there was no value at distance zero where it should have a maximum.

The widths of these peaks will vary with the particle image halo-width as can be seen in figure (8–31) which shows that the change in the shape of the first derivative for varying halo-widths of the seeding particle and, if one considers the $\sigma = 0.200$ pixels and the σ =0.632 pixels first derivative, it also shows that the position of the peak is shifted slightly towards the origin by the central peak. This is also shown in Table (8–6) where we can also see that the amplitude is roughly $\frac{\sigma}{\pi}$ pixels smaller than the

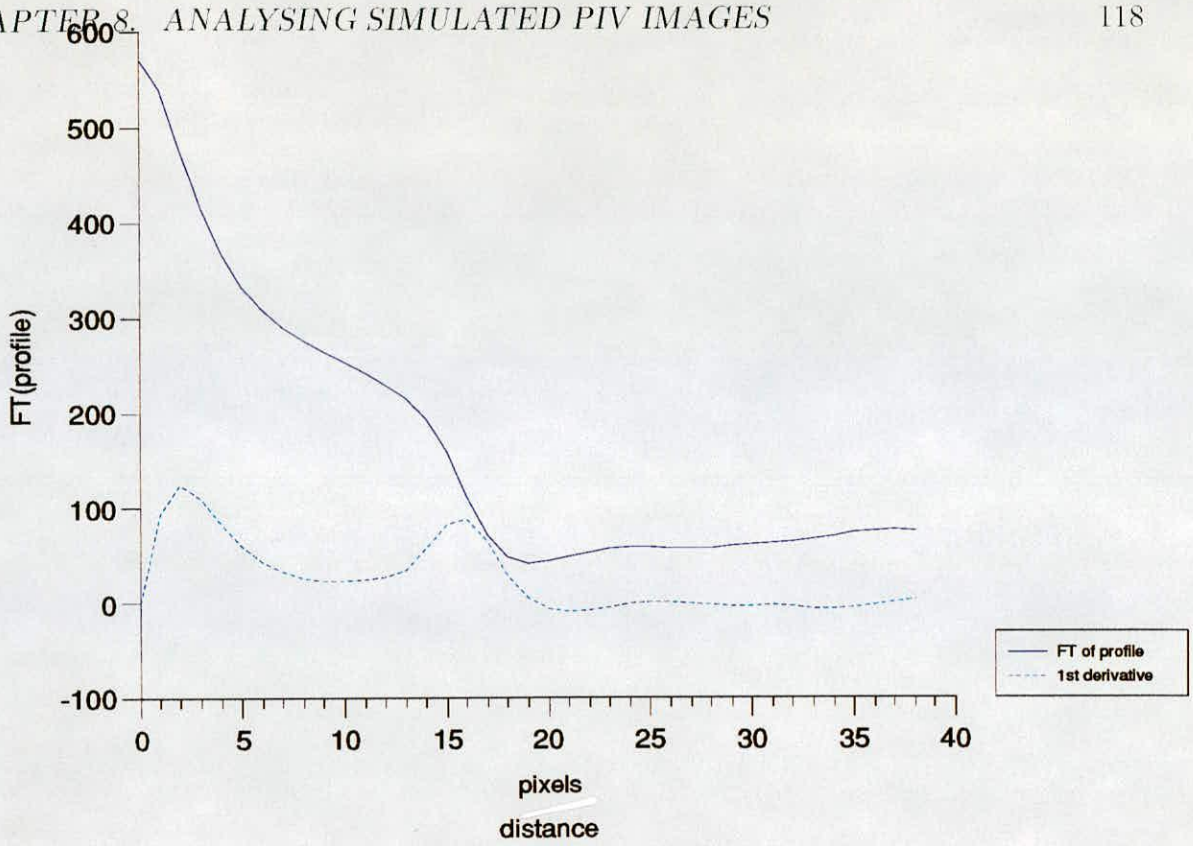

Figure 8–30: Fourier Transform of profile and its calculated gradient.

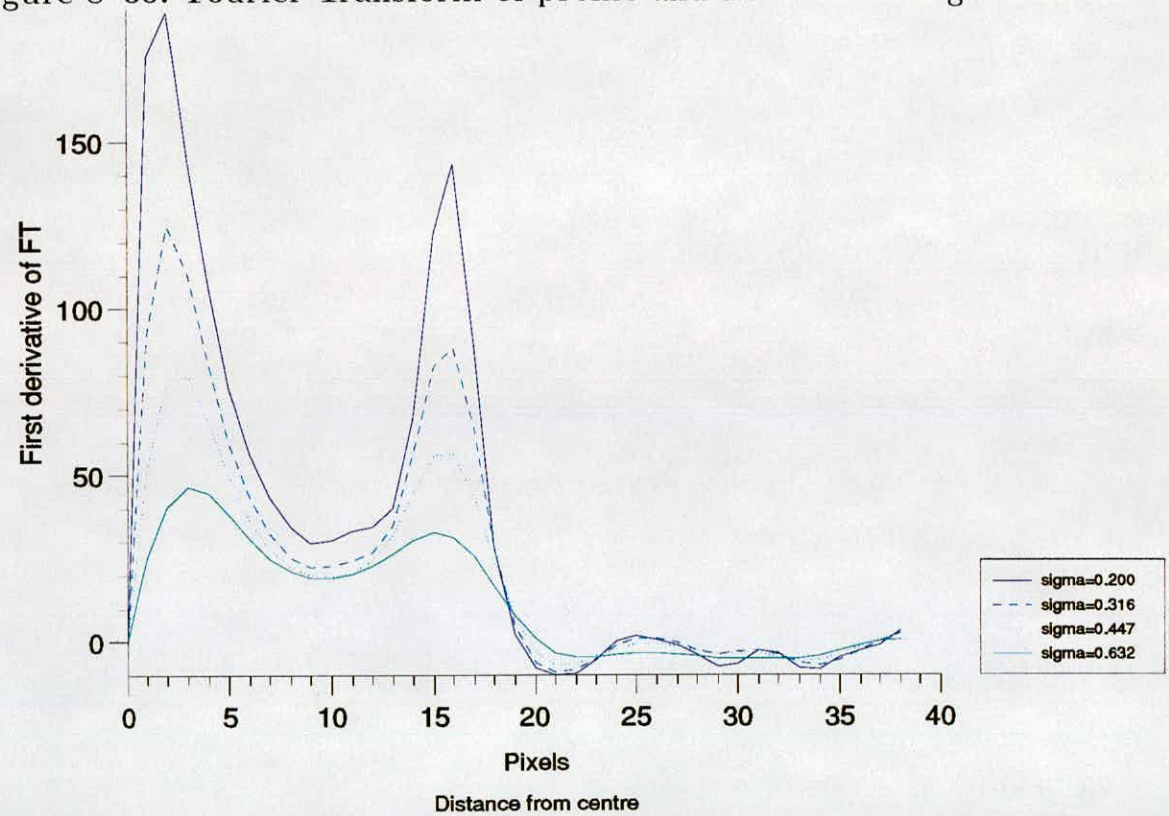

Figure 8–31: Graph showing change in width of peak in gradient of the FT of the Profile for varying halowidths of seeding particles

Halo-width	Measured	amplitude	Width of peak	$\frac{Width}{\pi}$
σ	amplitude	$+\frac{\sigma}{\pi}$		
(pixels)	(pixels)	(pixels)	(pixels)	(pixels)
0.200	7.86	7.92	0.66	0.21
0.316	7.83	7.93	1.04	0.33
0.447	7.77	7.91	1.43	0.45
0.632	7.59	7.79	1.98	0.63

Table 8–6: A table showing how the measured amplitude varies with the halo–width and how the width of the first derivative peak varies with the expected halo-width. Expected amplitude was 7.92 pixels

expected amplitude except at very large σ where some other factors will also become important.

Table (8–6) also shows the width of the first derivative peak which was found by taking the second derivative and finding the peaks present. These peaks will occur at the turning points of the peaks in the first derivative. The width of these peaks divided by π will give the width of the particle image halo (σ) and so can be used to measure this quantity and to determine the shift in the amplitude value imposed by central peak.

Figure (8–32) shows the amplitude measured from the first derivative along the tube compared to the expected amplitude and it can be seen that we get very close correlation between the two lines, with the measured values being slightly smaller than the expected ones due to the the effect of the central peak. This factor is accounted for by adding a correction equal to the width of the peak divided by π^2. Table (8–6) shows the effect of adding this correction to the measured values, and this is also shown in Figure (8–33) and Figure (8–34), where the measured values now fits much closer to the expected values.

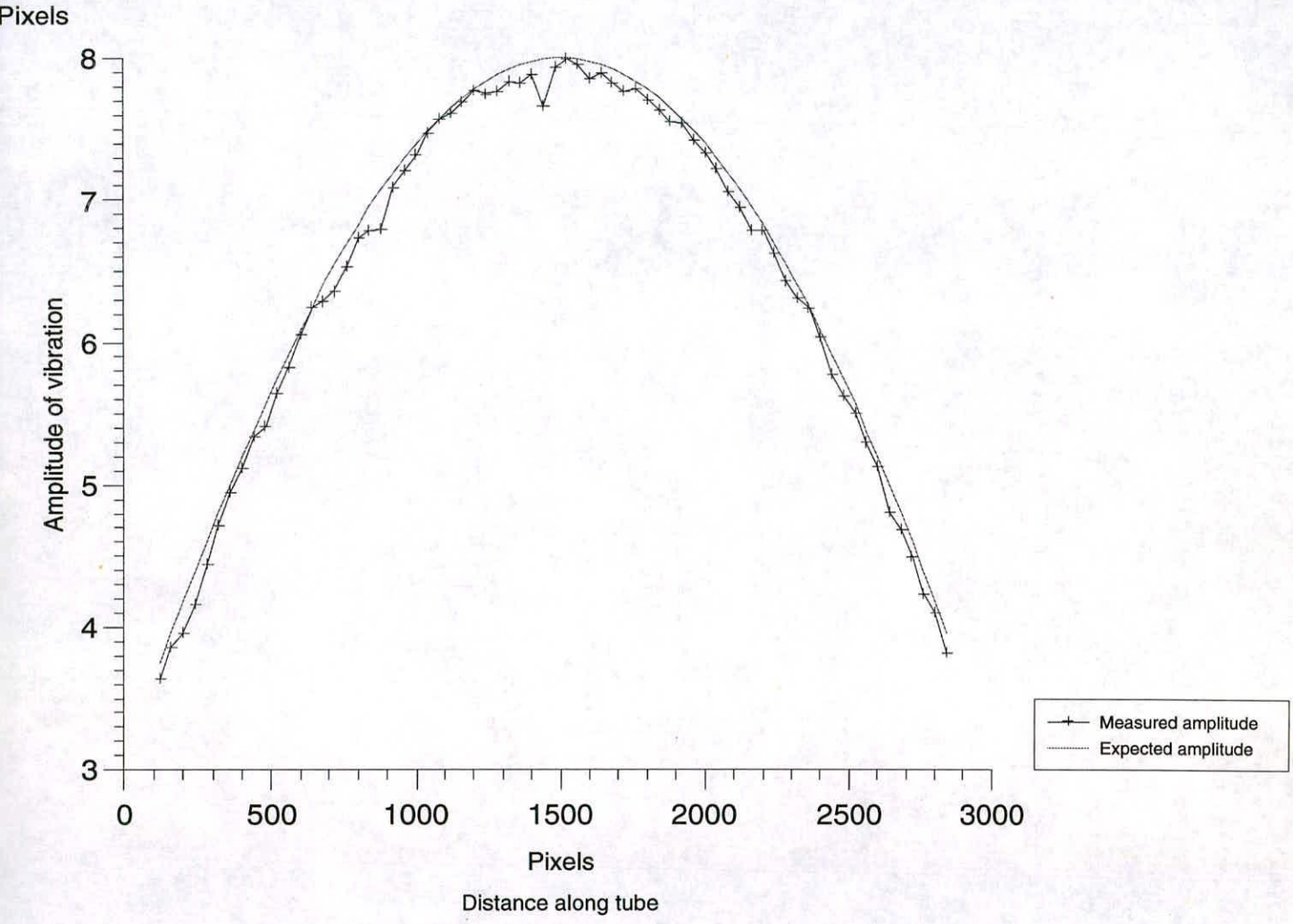

Figure 8–32: Graph showing amplitude measured from the gradient against distance along tube compared to the expected amplitude along the tube.

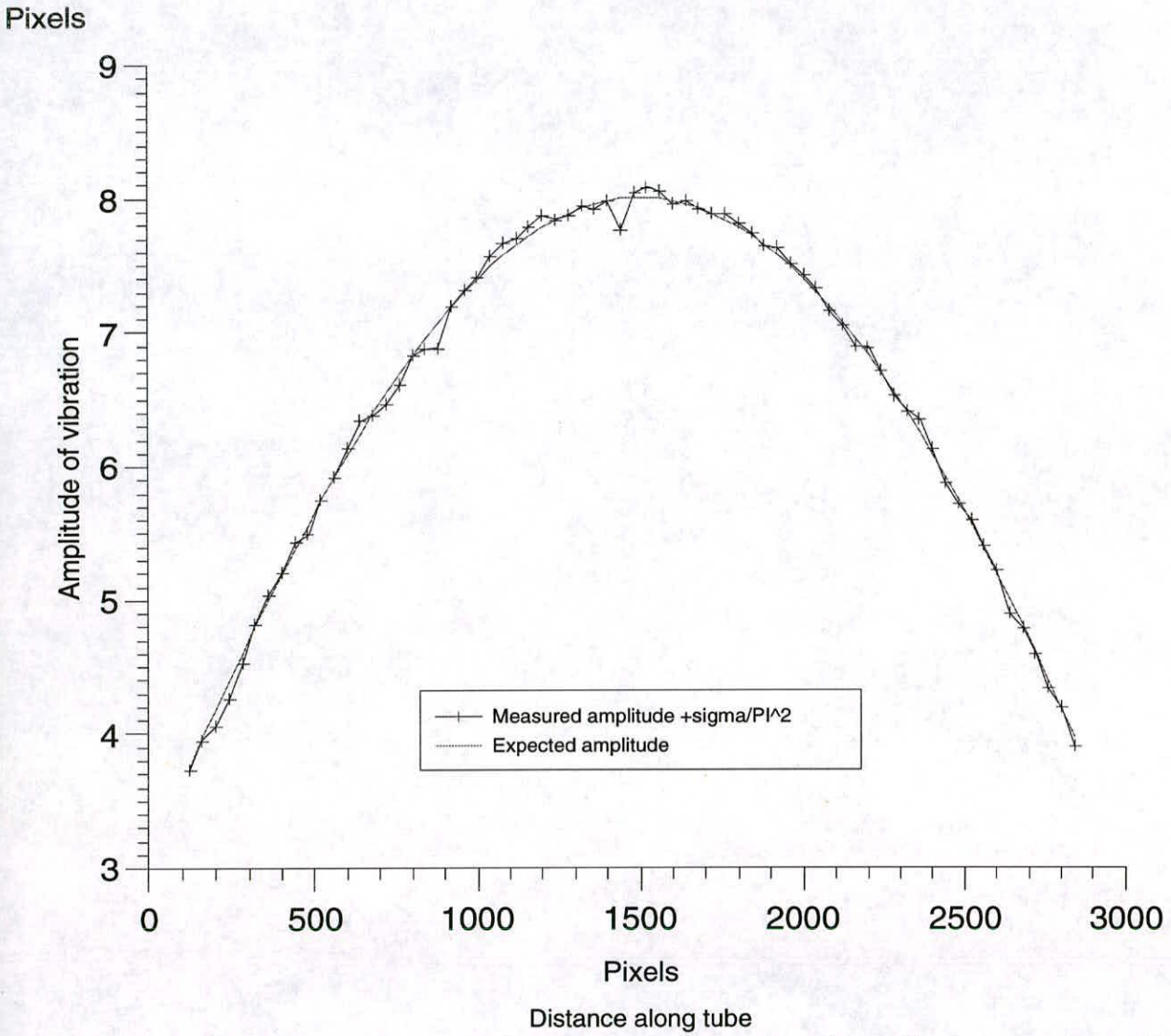

Figure 8–33: Graph showing expected amplitude and measured amplitude plus σ/π^2 against distance along the tube.

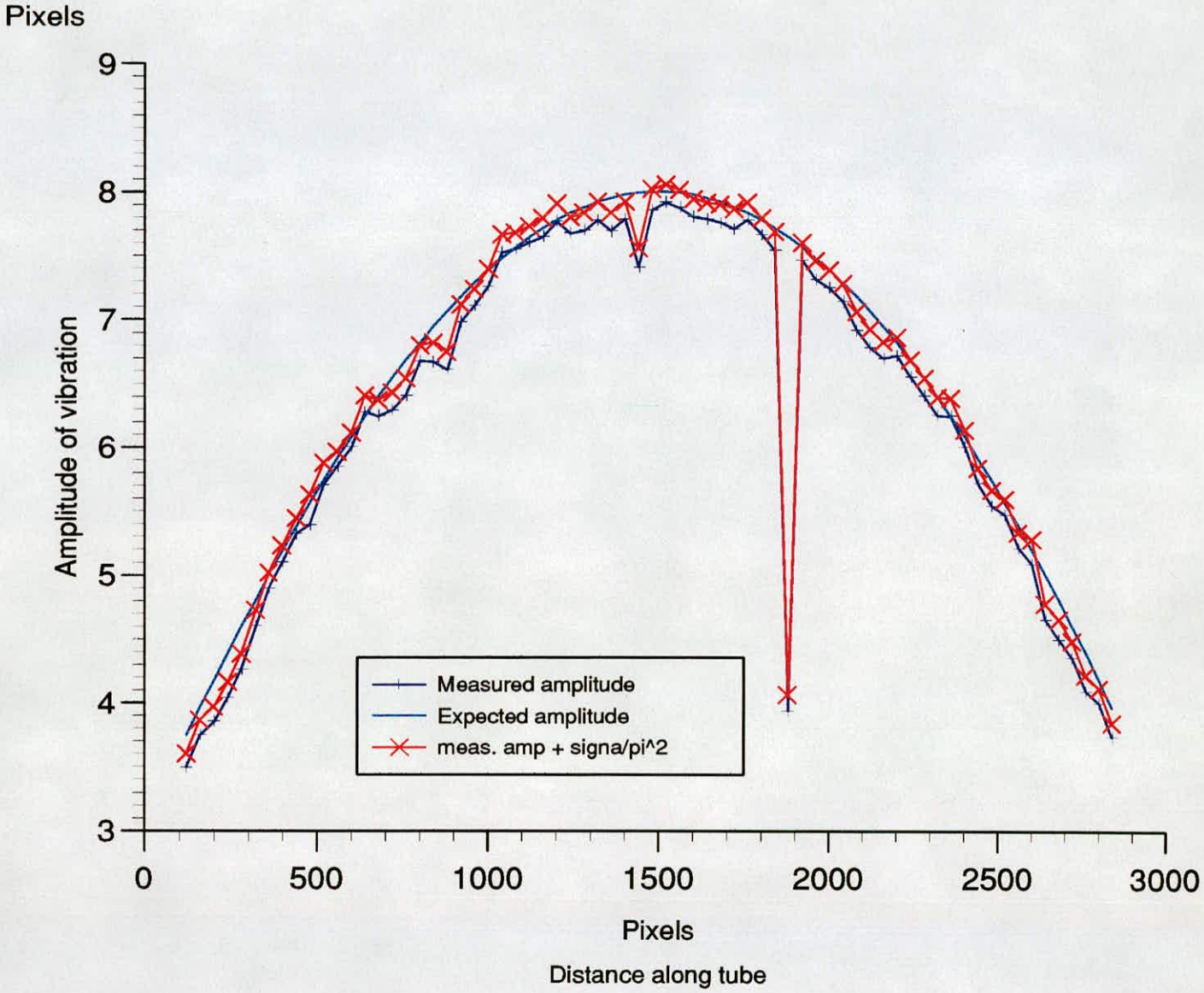

Figure 8–34: Graph showing expected amplitude and measured amplitude plus σ/π^2 against distance along tube for σ =0.447.

8.7 Conclusion

In this chapter we have covered some of the assumptions made at the end of Chapter 7, such as that there are no clipped images and that the amplitude was constant across the interrogation area. We have shown that the effect of clipped images can be neglected in the analysis as long as there are significantly more complete images contained in the area compared to the number of clipped images. The variation of the amplitude was considered, and it was seen that the sum of a number of Bessel functions with varying argument would have the characteristics of the Bessel function with the average argument.

The effect of the seeding particle image halo on the measurement was studied and it was determined that an increase in the image halo increased the measured value of the amplitude. The first peak was shifted by more than the next two peaks and so the second peak was chosen as the best to determine the amplitude from the profile of the Power spectrum.

The minimum size of the interrogation area was shown to be 5 times the streak-length from deliberations of the minimum number of points necessary to describe the Bessel function period. The maximum size of the interrogation area is determined by the variability of the amplitude and the velocity displacement over the area. It is hoped to keep the variation of the amplitude and velocity displacement to a minimum in the area, so the area should be kept as small as possible.

In order to simplify the problem of measuring the amplitude and the velocity from the same negative, it was determined that the complete streak was not necessary, only the position of the end-points of the streaks. A local maximum routine was implemented on a set of pictures to identify all points which were brighter than their immediate neighbours. These points, in general, will be located at the ends of the streaks, and a file containing only these end points will have four definite peaks in the autocorrelation plane, two associated with the amplitude, and two associated with the velocity. A simple peak detection routine can be implemented to find the position of these peaks to measure the amplitude and the velocity displacement.

The discrepancy between the measured values and the expected values was shown to be partly due to the halo-width of the seeding particles, but mainly due to the pixelation of the scanned image. The pixelation would produce values at least 0.85 pixels smaller than expected and the results would also be rounded to the nearest integer.

The technique of analysing the Fourier Transform of the profile was determined to be the best method. The gradient of the FT of the profile has a peak at the position of the amplitude. The width of this peak has the added bonus of giving us a measure of the seeding particle halo-width which can be used to give a correction for the shift of the peak due to the halo-width giving us a more accurate answer.

It is possible to measure the mean flow velocity for the interrogation area in a multiply exposed picture from the largest peaks in the autocorrelation plane in the same manner as in conventional PIV. The streaks produce a long narrow peak instead of the usual circular one, but the centre of the peak is always much higher than the rest. The only problems noted in the measurement of the velocity was when the amplitude and the velocity displacement are in the same direction. The results in this case cannot be relied on and should be edited out. A method of image shifting [37,4], where a fixed velocity displacement is added to the distance between the images could be used to make sure that this situation does not occur, and will also allow a greater range of velocity displacements to be measured.

Chapter 9

An experiment to measure the velocity field and acoustic intensity in a closed square cross-section tube

9.1 Introduction

So far we have shown that it is possible to retrieve the amplitude of the oscillation, and the mean flow velocity, from the simulated images that we artificially constructed, and that the values that we get are very close to the expected values. We will now have to determine whether the simulated images can be compared to the real images.

In order to test the method on real data, an experiment was constructed in which a standing wave was set up in a closed square duct. The standing wave sets up streaming , whose velocity depends on the frequency and maximum intensity of the sound field. The photographs obtained from this experiment will be used to check the validity of the conclusions made using the simulated images, and then the technique will be used to measure firstly, the amplitude of vibration (and hence the acoustic particle velocity) from a single exposure photograph, and then secondly the amplitude of vibration and the mean flow velocity from a multiply exposed photograph. These results are then compared to the expected results.

9.2 Comparison of real images with the simulated images

In order to validate the simulated images that we used we will compare an experimental photograph with a simulated image. We pick an interrogation area from a picture (Figure (9–2)) and generate a simulated image with the same parameters (Figure (9–1)). The power spectrums, autocorrelation planes and FT of the profile of the power spectrum are then compared to see if the results obtained from the simulated images are valid for the experimental images.

Figure (9–2) has an area of 120x120 pixels, and has a measured acoustic particle displacement of 15.99 pixels. The particle image halo is approximately 0.632 pixels in width. Figure (9–1) has been constructed with the same parameters. If we compare the two images, we can see that the real image has more streaks present and with more variation in the intensity of the images. Some of the images in the real picture correspond very well with the images in the simulated image. The bright image in the top right hand corner of the real image is very similar to the simulated images.

If we compare the profiles of the power spectrum (Figure(9–3)) , we can see that both the simulated image and the real image have the same periodicity. The simulated image is more jagged, possibly an artifact of its simulated nature. The graphs have the same peaks and troughs, and decay at the same rate which means that they have the same amplitude and halo-width.

The FT of the profile and its first derivative (Figure(9–4)) give a measure of the amplitude of the fluctuation, and it can be seen that the two pairs of graphs tally very well. The amplitude measured from the peaks of the first derivative is 15.62 pixels for both the real, and simulated image, and, if the shift related to the particle image halo-width is taken into account, then we get 15.99 pixels for both amplitudes. As you can see, the simulated images have a high degree of correlation with the real images with the method working well for both real and simulated images.

Figure 9–1: Computer generated image with σ =0.632 pixels and A_m averaging 15.99 pixels.

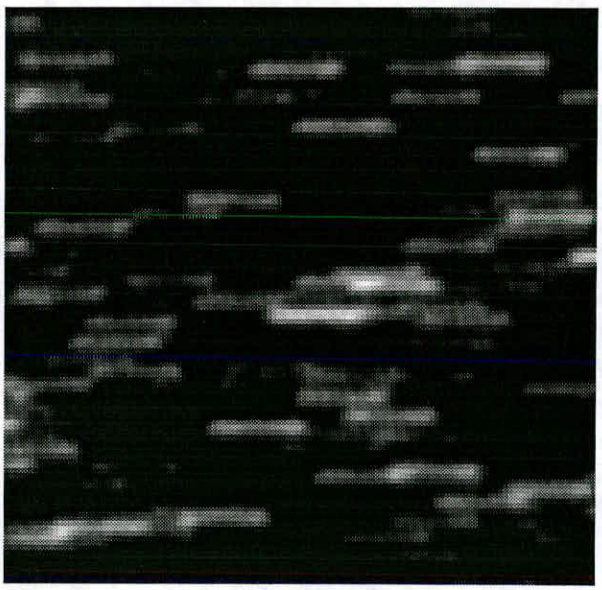

Figure 9–2: Real image with $\sigma \approx 0.632$ pixels and $A_m \approx 15.99$ pixels.

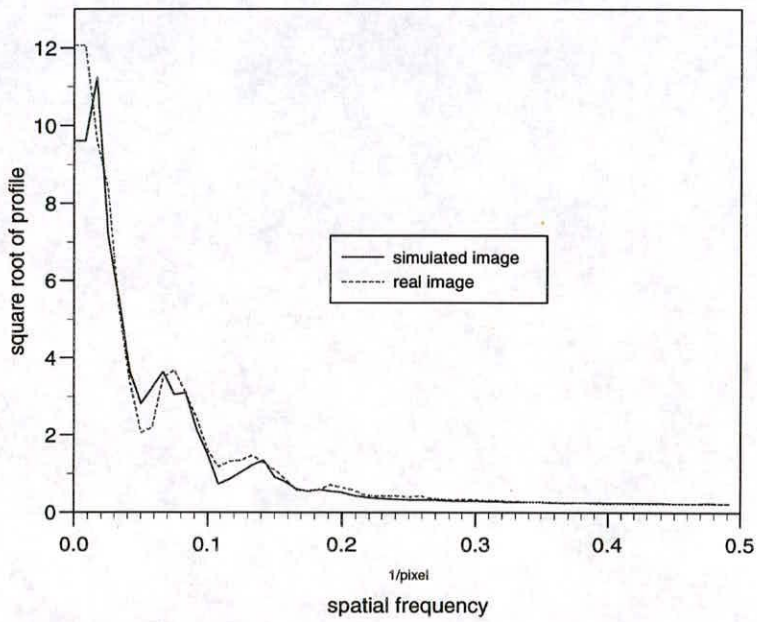

Figure 9–3: Graph showing comparison between simulated image profile and real image profile

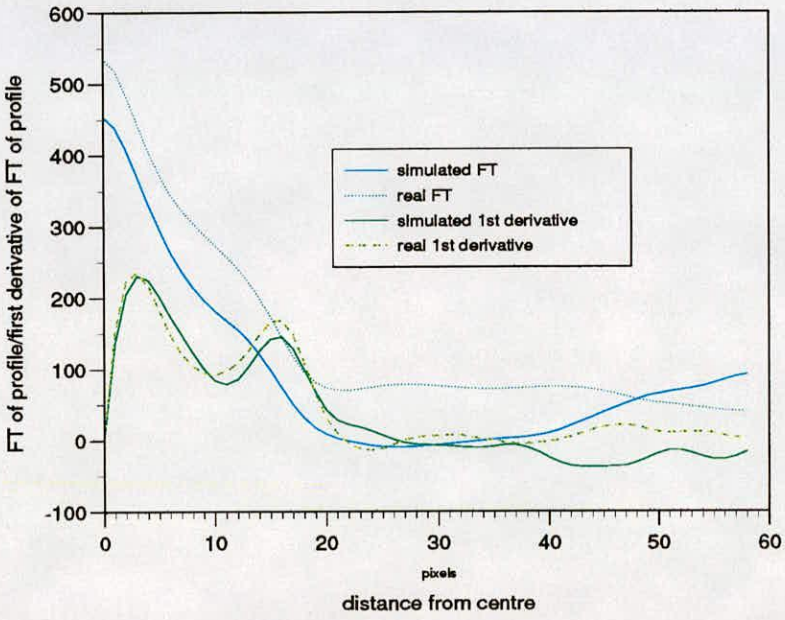

Figure 9–4: Graph showing comparison between simulated image FT and real image FT and their gradients.

9.2.1 Conclusion of comparison

Although the random distribution of the images is different between the pictures, and there are more images in the real case, the profile of the power spectrum and the form of the first derivative of the Fourier transform are very similar. This means that the results derived for the simulated images will be relevant for the real images produced from experiments. So the FT of the profile will be used to measure the amplitude in an experiment.

The shape of the real images themselves are the same as those of the simulated images in the streak direction, but are slightly thinner in the direction perpendicular to the streaks. This could be because the real images were photographed over several periods. If the amplitude of the oscillation varied over several periods, this would produce a streak that was slightly stretched.

9.3 Experiment to measure the acoustic particle velocity from a single exposure photograph

An experiment was set up to measure the amplitude along a square cross section tube in which a standing wave was present. The tube had a 30mm square cross-section and was 700mm long, not including the horn of the loudspeaker. The standing wave had a frequency of 1850Hz and an intensity of 150 $\pm$ 1dB at the pressure anti-nodes as measured with a probe microphone. The tube was illuminated with a thin sheet of light produced by a 2W Argon-ion laser using a cylindrical lens and a spherical lens in series, and the flow was made visible by the introduction of smoke particles into the flow just before the photographs were taken. (Figure(9–5))

The camera was set at an 8 ms exposure in order to capture approximately ten periods of the oscillation. Since the fluid was moving at approximately 1 mm s^{-1}, the image would move 8 μ m, which is approximately half a pixel, so the image will not move by a significant amount in that time. The f# was 4 which allowed a sufficiently wide depth of focus while keeping the seeding particle image as small as possible. The

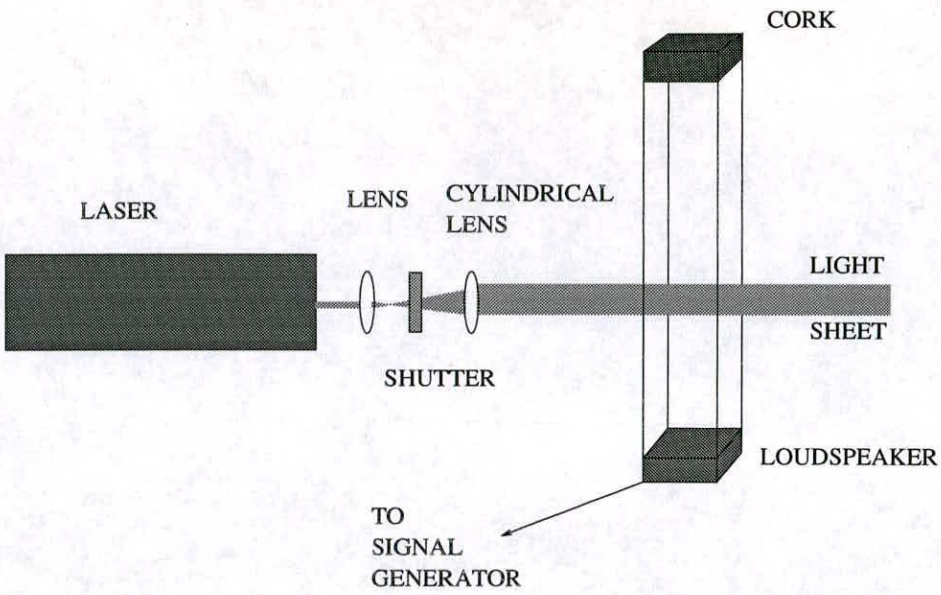

Figure 9–5: Experimental apparatus used to produce photographs of sound field.

wide depth of focus was necessary because, in order that the area under observation was as large as possible on the negative, we put the camera close to the tube. A large aperture would produce too small a depth of field which would mean that there were many out of focus particles in the measuring area.The film was 400 ASA which was push processed to about 800 ASA when it was developed. This was then enlarged to about a4 size and the photograph scanned in to a computer. The scanned image was 1943x 2400 pixels which meant that 1943 pixels was equivalent to 30mm across the tube. This allowed the calculation of the magnification of the scanned picture which was 1pixel equivalent to 0.01544mm.

9.3.1 Technique for getting the best pictures

What we are looking for here is a perfect record of the images seen with the eye. In order to achieve this, there are several criteria which have to be observed. Firstly, we are concerned with only viewing the particles oscillating within a very thin light sheet; secondly, we are concerned that the particles do not blur due to the steady movement over time; and thirdly, we wish the particle to be accurately recorded on the film.

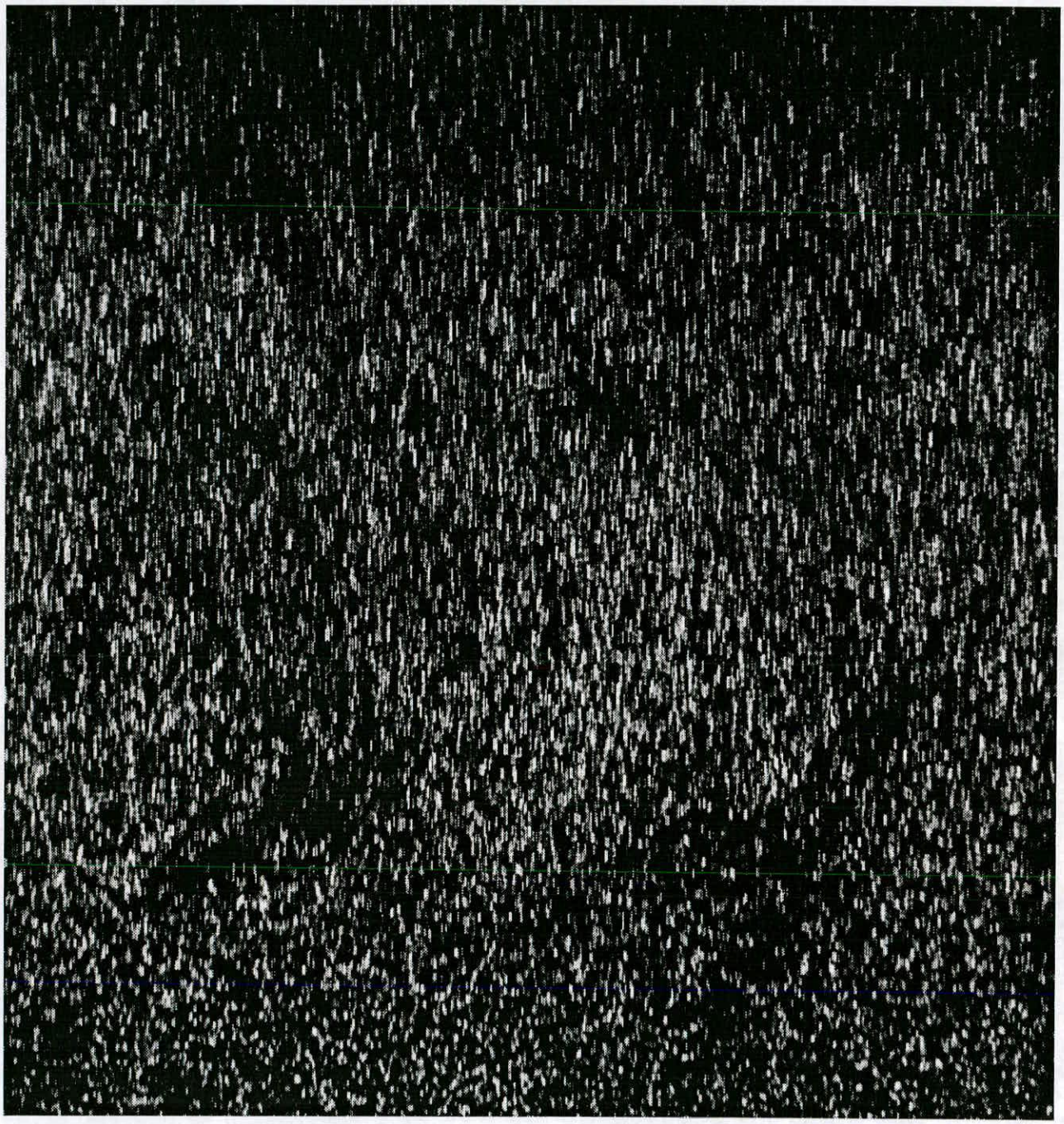

Figure 9–6: Photograph of sound field.

For the first criteria, there are several variables which have to be taken into account, such as the thickness of the light sheet and the depth of focus. The thickness of the light sheet is determined by the configuration of the cylindrical lens and the convex lens and this is usually best set up with the focal point of the lenses being as far away as possible from the laser since this will produce the thinnest, most uniform light sheet. The depth of the focus is determined by the aperture size and the distance between the light sheet and the film. A large aperture has a small depth of focus and the closer the object is, the smaller the depth of focus. We wish all particles within the thin light sheet to be in focus, since out of focus particles will complicate the power spectrum by introducing an extra parameter, and so we have to have a small aperture. But as we showed in Chapter 8, we also wish the aperture size to be as large as possible since that gives the smallest image particle halo and allows the greatest range of measurements. We also have the light sheet close to the camera in order to get the optimum magnification. This means that we have to make a compromise between the size of the image particle halo and the depth of focus. In this experiment the focal number chosen was 4 which provided a depth of focus just deep enough to cover the thickness of the light sheet.

The second criteria is determined by the length of the exposure time and the mean speed of the seeding particles. The oscillating seeding particles will always cover the same ground unless there is a steady flow present. We wish the particles to undergo at least one full oscillation in the exposure time and it is allowable for the particles to oscillate several times as long as the image does not move. In fact the longer that the particle is allowed to oscillate the brighter the images on the film and the greater the resolution of the film since a smaller ASA film can be used. The length of the exposure can, therefore, be up to ten times the period of the oscillation, as long as the particle images move less than a pixel in this time.

The third criteria, the accuracy of recording of the images, is a very important one since there are many factors that can alter the accuracy of the recording. Overlapping images, low resolution, and non-linear recording of images will all affect the accuracy of the recorded image. If the light intensity from the images is not within the linear region of the film, then the image will not be recorded accurately. If images overlap,

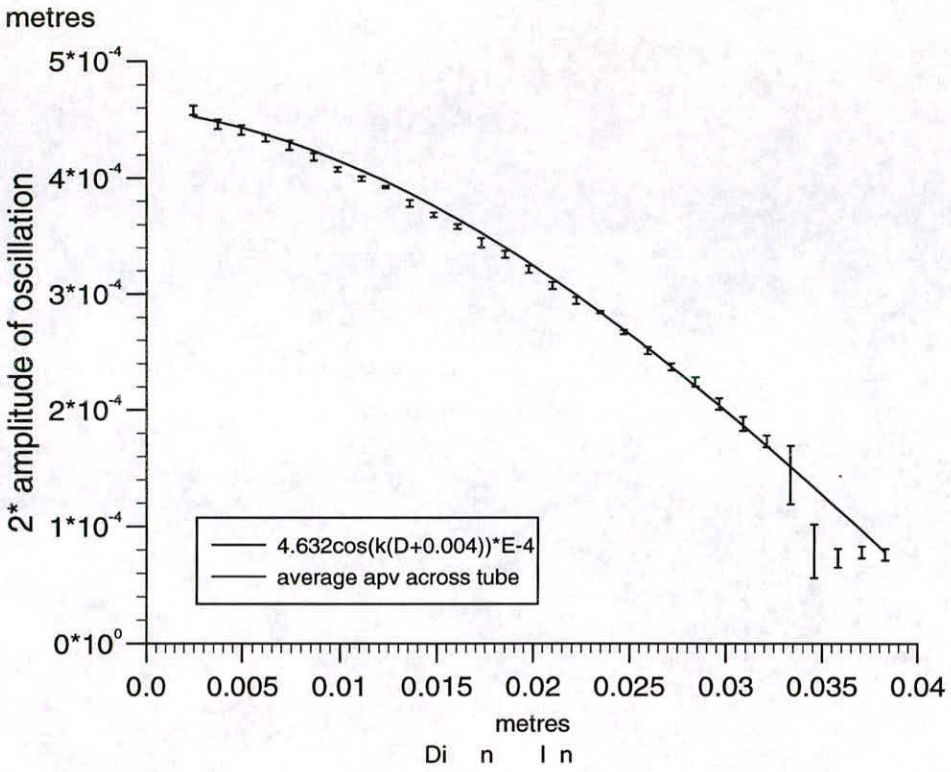

Figure 9–7: Variation of average amplitude of fluctuation against distance along tube compared to expected value. Error bars show variance of value across tube.

the chances of this happening will increase. This means that several pictures have to be taken with different light intensities and concentrations in order to find the most suitable pictures for analysis.

In order to get the best resolution, we placed the camera in the closest position possible to the light sheet. This gives us the greatest magnification and hence the greatest resolution of the images on the film. High resolution is advantageous because it allows greater accuracy in finding the lengths of the streaks.

9.3.2 Analysis of Photographs

One of the photographs taken is shown in Figure (9–6) and if this is studied, it can be seen that the amplitude of the vibration changes along the tube but not across the tube.

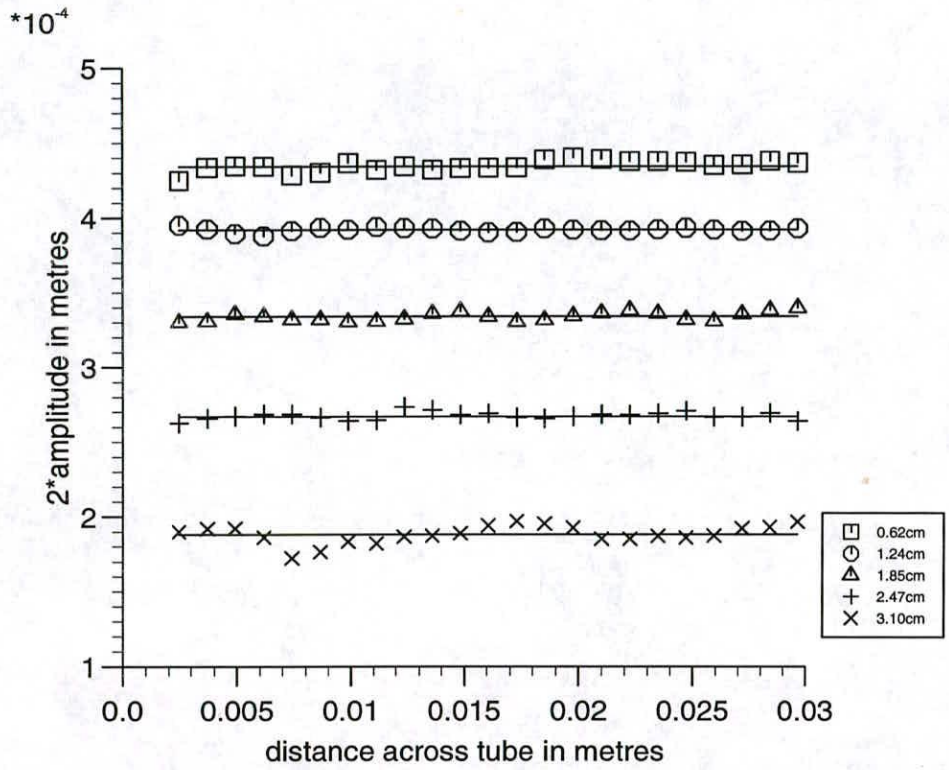

Figure 9–8: Variation of amplitude of fluctuation against distance across tube at five different locations along tube compared to average value.

If we use the method devised for the simulated images, analysing the first derivative of the FT of the profile, to measure the variation of the amplitude along the tube then we get Figure (9–7). The interrogation area was chosen as 160 x 160 pixels and the distance between centre points of the area was 80 pixels. Figure (9–7) shows the variation of the average acoustic particle velocity along the tube and it can be seen that the amplitude along the tube fits the expected cosine with an amplitude of 2.3±0.05 x10^{-4} m and frequency 1850 Hz.

This corresponds to an acoustic particle velocity of 2.7 ± 0.05 ms^{-1} and a sound pressure level of 151.8 ± 0.16dB at the velocity anti-node.

Figure (9–8) shows how the acoustic particle velocity varies across the tube, at five locations along the tube. As we can see the acoustic particle velocity is approximately constant across the tube. There is some variation in the value, but this is within the error of the measurement.

9.3.3 Conclusion

The experimental results and the expected results compare well. The expected intensity was 150 ± 1 dB, measured with a probe microphone, and it is to be expected that this can be a little less than the true value since the positioning of the probe at the position of maximum intensity was difficult. This will increase the the bounds of the error by more than the error associated with the measurement. This means that a measurement of 151.8 dB is well within the expected results error.

The method obviously has some problems at small amplitudes, which is to be expected since the central peak will start to interfere with the position of the amplitude peak at small amplitudes.

9.4 Experiment to find the APV and flow velocity in multiple exposed pictures

A similar experiment to that described in the previous section was set up, but in this case, the shutter was set to open at regular intervals. This would allow the seeding particles to move between exposures with a displacement related to the velocity of the particle at that point. An electronic shutter was used to achieve this which was capable of opening and closing in microseconds. The vector map of the mean flow velocity and the amplitude of the oscillations was measured from the photograph.

9.4.1 Experimental details

The experiment used the same apparatus as in the previous experiment (see Figure (9–5)), but in this case, the camera was set up with the aperture open for 1 second, and the shutter was set up to be open for 4ms with a 125 ms delay between each opening. This meant that in the time the camera shutter was open the electronic shutter opened 7 times. The frequency of the sound in the tube was decreased to 1616Hz which meant that the period of the oscillation was 0.6ms. This means that there were 6 oscillations in the exposure time.

The f# was set at 5.6 to allow a greater depth of field. Several photographs were taken, and the best were enlarged to roughly 240mm x 192mm. This produced a scanned image which was about 3000 pixels x 2400 pixels.

9.4.2 Results

The scanned negative (Figure(9–9)) was analysed in 140x 140pixel section spaced at 70 pixel intervals. The picture was found to be 2001 x 2640 pixels which means that 1 pixel is equivalent to 0.01136 mm.

The average amplitude of oscillation along the tube is shown in Figure (9–10) and this shows that the amplitude varies as a cosine of magnitude 0.247 ± 0.01 x10^{-3}m and

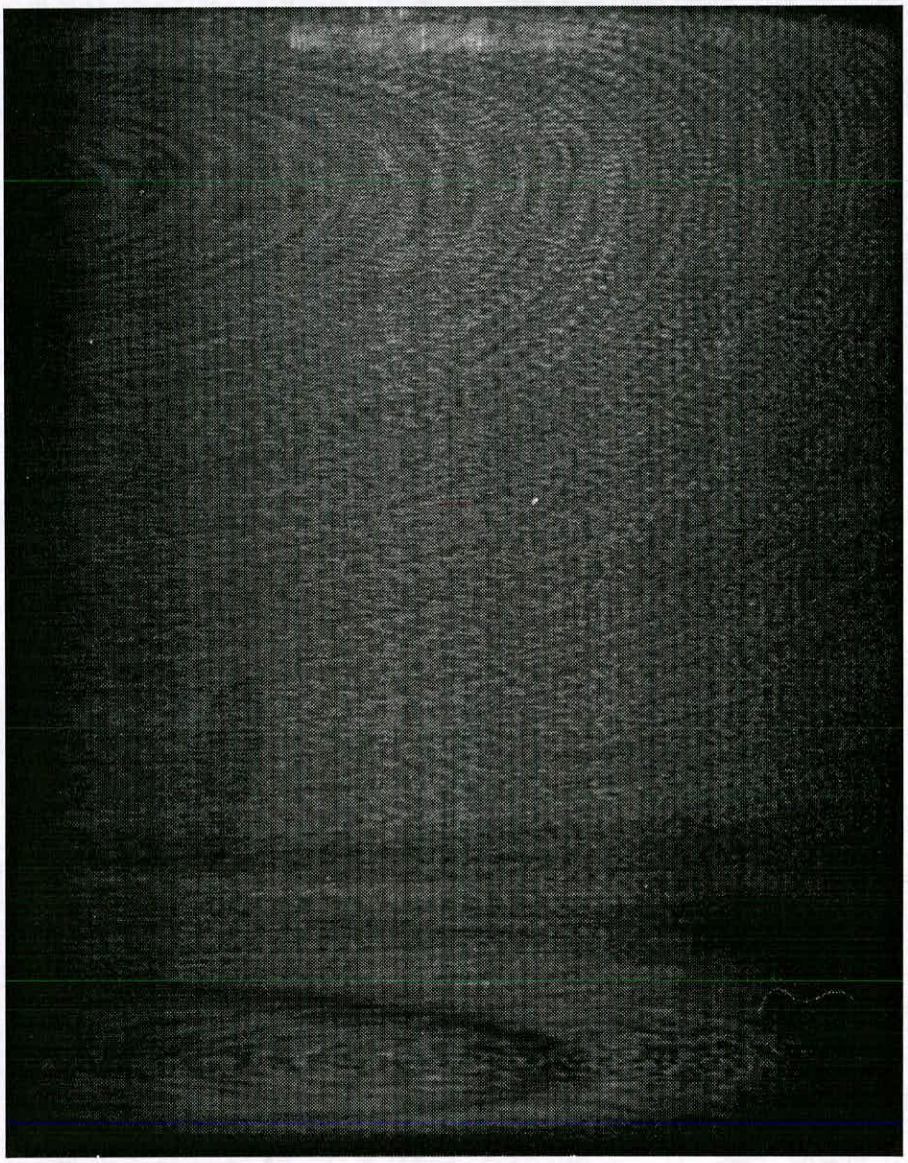

Figure 9–9: Photograph a5-7 showing the multiple images and the vortices formed by the streaming.

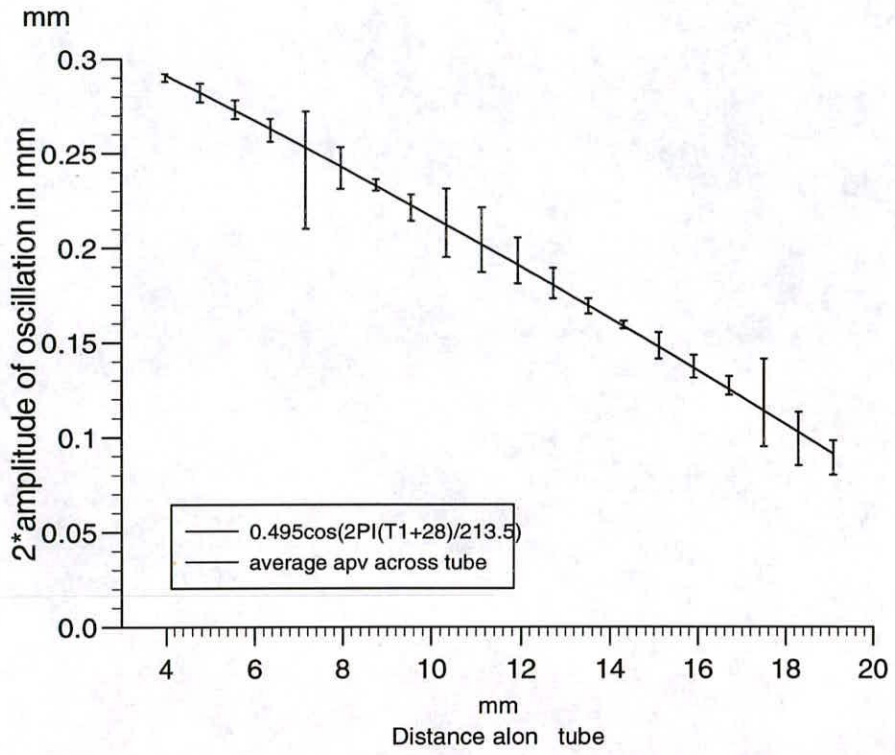

Figure 9–10: Graph of average amplitude against distance along the tube compared to expected amplitude. Error bars area variance of amplitude across tube.

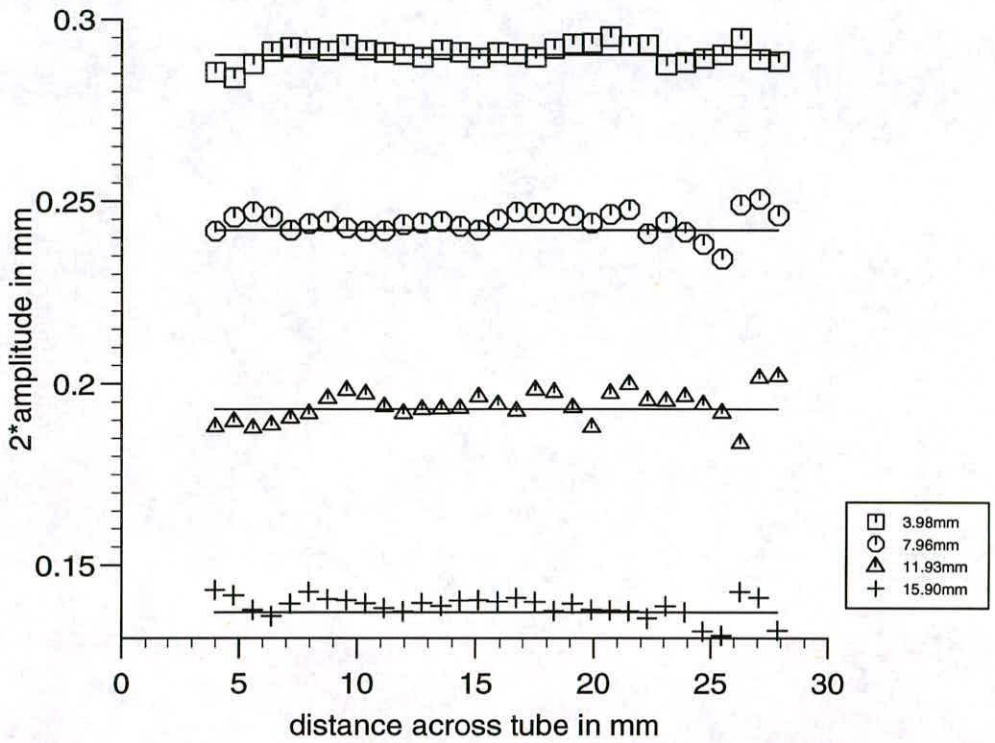

Figure 9–11: Graph of amplitude against distance across the tube at four positions along tube compared to average amplitude at that distance.

wavelength 0.2135 m along the tube. This means that the acoustic particle velocity is $a_m = \frac{A_m \omega}{2}$ =2.51 $\pm$ 0.1 ms^{-1} and the frequency was 1616 Hz (cf with measured frequency of 1616 Hz). This corresponds to an intensity of 151.17 $\pm$ 0.4dB.

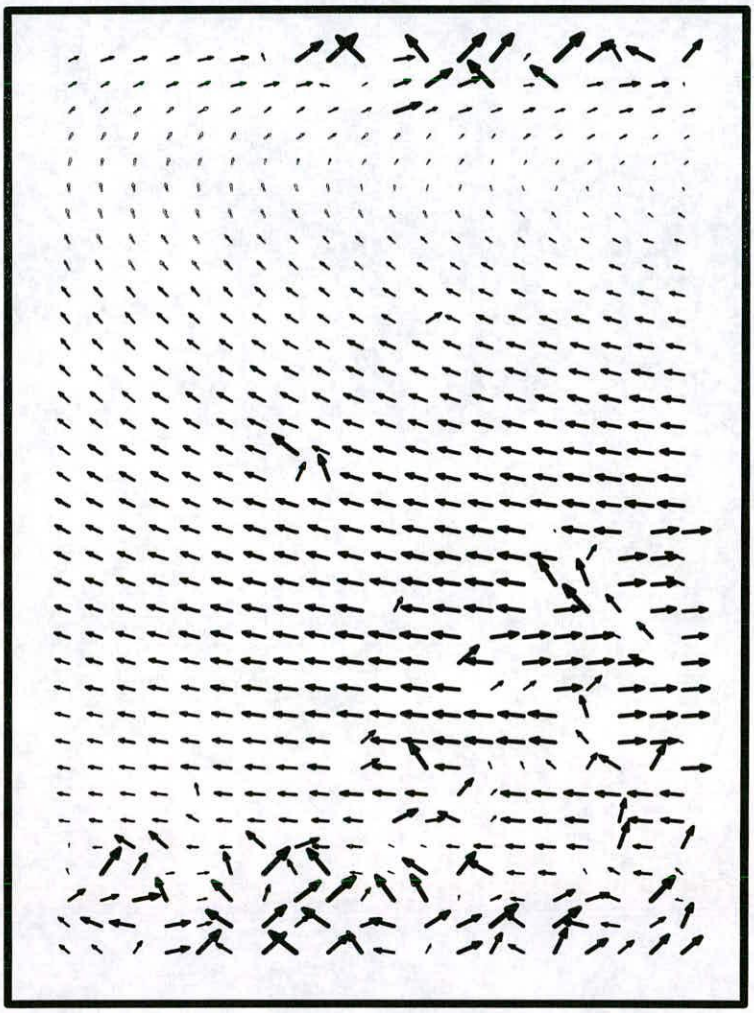

Figure 9–12: Vector map of photograph a5-7

The velocity displacements are shown in Figure (9–12) and it can be seen how closely they match the expected form from the photograph (The vector map is flipped horizontally). The expected form of the velocity should, however, have been symmetrical about the centre of the tube, which it clearly is not. This might be due to several factors, and many attempts were made to correct the streaming pattern. The

adjustment that seemed to be most critical was to seal tightly the edges of the tube, the bungs, and loudspeaker, although this did not completely correct the problem. If the loudspeaker was adjusted slightly, the pattern of streaming would change so it is obviously essential to make the direction of propagation of the exactly sound parallel with the sides of the tube.

The maximum vertical displacement on the velocity map was about 65 pixels which corresponded to a flow velocity of 2.7 mm s^{-1} meaning that the images moved just over a pixel in distance at the position of maximum velocity.

9.5 Discussion

In this chapter we have shown that the results which were found valid for the simulated images is also valid for real images. The method of finding the amplitude of oscillation from the gradient of the FT of the profile, and the flow velocity from the autocorrelation plane seems to work well and consistently gives a high percentage of results with the minimum of post processing editing.

It is also possible to measure a wide range of amplitudes and velocity displacements since we can alter both the exposure time and the delay. In general, it is desirable for the exposure time to be of the order of 3-10 periods (a smaller exposure time is better for obtaining clear images, but we are limited by the laser power and may need a longer exposure if we are to have sufficient light to record the image on the negative) and the delay should be gauged so that the largest displacement is 1/3-1/2 of the interrogation area. The delay however can be adjusted to suit the situation desired.

Chapter 10

General Conclusions

In this thesis, we have described optical methods for the measurement of the acoustic particle velocity and the mean flow velocity in a situation where they were superimposed. The two methods in which we were interested were Laser Doppler Anemometry and Particle Image Velocimetry.

10.1 Laser Doppler Anemometry

Laser Doppler Anemometry has been used to measure the acoustic particle velocity in a sound field and also the mean flow velocity. A general theory was necessary to calculate the form of the photon correlation function for this case. The first set of aims in this Thesis were to:

- develop the theory of Laser Doppler anemometry, using the Photon Correlation method, for the case of a sinusoidal oscillation superimposed on a mean flow to allow the acoustic particle velocity and the mean flow velocity to be retrieved from the experimental information.

- show that the theoretical function agrees with the experimentally measured function.

- use the method to investigate the mean flow and sound field in a situation in which both are linked (e.g. in an organ pipe).

The achievement of the first aim is described in Chapter 4, where we developed the theoretical correlation function when a sinusoidal oscillation and a mean flow velocity is present within the interrogation area. This theoretical expression was shown to be consistent with experimental results not just for when the mean flow velocity is much greater than the acoustic particle velocity, but also when the acoustic particle velocity is larger than the mean flow and negative velocities are therefore present. This has been presented as a paper in the Journal of Physics E: Measuring Science and Technology [26].

The LDA method is known to be a very accurate way of measuring velocities, but its disadvantages are; that it is a one-dimensional measurement, there is a restriction on the ranges of the velocity and intensities which can be measured, that it measures the speed of the seeding particles and not the air itself, and that it is a point measuring technique. However, there are established techniques for finding the other components of velocity, and seeding particle problems can be made negligible. But the fact that we can only measure at a point can be frustrating if we wish to construct a vector map. This means that the method can only be used in steady flow situations, in which the initial conditions do not change as we measure across a duct. The technique is also restricted to situations in which the acoustic particle velocity and the mean flow velocity are of the same order. As is argued by Durrani and Greated [17], that the ratio of the acoustic particle velocity to the mean flow velocity must lie between

$$1/15 < \frac{a_m}{a_0} < 15 \tag{10.1}$$

for both parameters to be measurable in the same correlogram, since we would wish at least one period of the cosine, or one period of the Bessel function to be present in the correlation function, otherwise it will not be possible to analyse. This problem can be corrected, however, by the use of a frequency shifter. This will move the fringe pattern at a known rate and allow us to add or subtract a velocity to bring the two velocities into the same range. The alignment of these devices is very time consuming and so was not done, but frequency shifting does offer the possibility of extending the range of the LDA method quite considerably.

The technique finds two velocities, and the determination of which of these is the mean flow velocity, in a situation where it is not obvious from the knowledge of the flow, can be done by considering the distance of the zeros of the function from one another. If they are at almost regular intervals, then the zeros belong to the Bessel function and hence should be used to determine the acoustic particle velocity. If they are positioned at 1:3, then they are from the cosine term and should be used to determine the mean flow velocity.

In this way the photon correlation function can be analysed to give both the absolute values of the acoustic particle velocity and the mean flow velocity in situations where both are present and possibly linked.

10.2 Particle Image Velocimetry

Particle Image Velocimetry may be used to measure the velocity fields of flows and it offers a quick and fairly accurate method of measuring the two-dimensional velocity vectors in a plane. The advantage of PIV over other methods of velocity measurement is that we can instantaneously measure the velocity over a large area non-intrusively making it a powerful tool in experimental fluid dynamics.

The aims of the second part of the thesis were to:

- develop the theory associated with Particle Image Velocimetry to show the form of the power spectrum and the autocorrelation plane for the case where the particle images were formed by the oscillation of the seeding particles.
- show that this would still allow the measurement of the flow velocity.
- investigate different methods for the measurement of the amplitude of oscillation from the power spectrum or the autocorrelation plane. The method was required to give a high percentage of good results with the minimum of vector editing.
- investigate the effect of different parameters on the measured values using computationally generated simulated images.

- show that the conditions for the measurement of the velocities from the simulated images were also valid for real images.

- use the method in an experiment and compare the results measured with the expected results.

In this Thesis the form of the power spectrum and the autocorrelation plane were determined, and four methods of finding the amplitude of oscillation were considered. The four methods were

- determination of the amplitude of oscillation from the power spectrum.

- determination of the amplitude of oscillation from the autocorrelation plane.

- determination of the amplitude of oscillation from the autocorrelation plane when the image plane has been edited to only include the end points of the streaks.

- determination of the amplitude of oscillation from the gradient of the Fourier transform of the averaged power spectrum.

It was quickly found that it was not generally possible to measure the amplitude from the autocorrelation plane, but it could be used to find the average velocity within the interrogation area. The only consideration for the measurement of the velocity was that the mean velocity displacement should not be in the same direction as the fluctuation velocity, as this produced many spurious peaks which corrupted the measurement.

The attempt to measure the amplitude from the autocorrelation plane if the images were edited to contain only the position of the end points of the streaks was unsuccessful since the positions of these end points was not at the ends of the streaks due to the pixelation of the image and the halo-width of the particle images. The autocorrelation planes were easy to read, but the values obtained usually needed some corrective factor added to them, which increased the error.

The average of the power spectrum had the form of a Bessel function and so we could use the position of the peaks to find the amplitude. This produced good results in particular cases, but tended to produce a high percentage of wrong answers when

the process was automated, due to the process not identifying the second peak. The profile could contain a component from the velocity which would produce a more jagged profile. This would make it harder to identify the second peak for the analysis, giving an answer either twice as big, or half the expected value. A number of peaks were therefore noted and the correct result determined by editing the amplitude data. This was time consuming and it was hoped that this stage could be eliminated using a different method.

The Fourier transform of the average and thence the gradient of this function produced good results more consistently. The gradient was seen to be three exponentials, one located at the zero, and two located at $\pm$ $2A_m$ making it a simple matter of peak detection to determine the fluctuation velocity. It was also discovered that the effect of the halo-width on the results could be accounted for by measuring the spread of the exponential and this meant that we could get more accurate answers. The procedure also produced a good answer consistently, needed less editing time, and was deemed to be the best method. A paper on this method has been written and will be submitted to Acoustica.

The effect of the interrogation area on the results showed that there was a minimum edge size for the area which was found to be about 10 xA_m, since this allowed enough points in the power spectrum to define the Bessel function. Fewer points meant that two or three points were used to describe a period of the Bessel function and this leads to a curve which is too jagged to recognise.

The simulated images were compared to the experimental images and it was shown that the theory worked for both. The amplitude of oscillation was measured along a standing wave in a tube first, and then the amplitude and the velocity were measured from the second picture to show that it is possible to measure both.

10.3 Conclusion

We have demonstrated that it is possible to measure the acoustic particle velocity and flow velocity using the non-intrusive methods of Laser Doppler Anemometry, employing Photon Correlation, and Particle Image Velocimetry.

10.3.1 Comparison of the two methods

The appropriate method to use in a particular situation will be determined by the constraints of the situation being considered.

The PIV system is obviously better in that we can determine two-components of the velocity over a large region instantaneously. This allows us to view flows in which the flow, or acoustic particle velocity changes slowly with time. The LDA only measures the velocities at a point for each measurement, which is measured over a time range of several minutes. The resolution of the sound and flow field can be much finer for LDA, however, since the interrogation area can be smaller so, if the sound or flow field changes quickly across the area under investigation, the LDA system is of more use.The LDA's smaller interrogation area will mean that the velocities are not averaged over as large an area as the PIV.

Seeding is also easier to do for the LDA. The seeding density and size can be much smaller for LDA measurements, since the technique is much more light sensitive. Seeding has even been dispensed with and the natural dust particle of the air used to get good results with LDA. PIV needs the seeding to be denser, possibly causing some interference in the sound field, and the particles are usually slightly larger so that they can reflect more light.

LDA is more useful in the high frequency end of the spectra. The LDA technique can measure acoustic particle velocities even when the amplitude of the vibration is of the same order as the fringe spacing. PIV is constrained by the resolution of the negative. Amplitudes of less than 3 pixels in length are difficult to determine accurately

and so PIV is only useful for relatively large vibrational amplitudes. Thus LDA gives results at higher frequencies and lower intensities of sound than PIV

If we wish to measure over a large area, in which the flow changes slowly, and in which the intensity is large and the frequency in the audible region, the PIV system is obviously better. If we wished to look at a system in which the frequency was large (for example an ultrasonic source) or in which the intensity was low, it would be much more of use to use the LDA system.

10.3.2 Further work

There are a number of ways in which the LDA methods and the PIV methods can be improved. In the LDA method, we can only measure the velocities fully if the velocity components are in one-dimension. This can be extended using some of the standard 2 or 3D methods of measuring LDA. A frequency shifter can be used to improve the range of the LDA technique as well.

In the PIV technique, we are also impeded by the fact that the amplitude is only measured if it is in the x-direction. This problem can easily be overcome if we used a Hough transform and used the brightest line to determine the direction of the fringes in the power spectrum. The power spectrum can then be averaged along this direction to find the profile which can be Fourier transformed to find the amplitude.

A standard technique which was tried briefly was halo subtraction[49]. In this the averaged halo was subtracted from the power spectrum and this removed the centre peak in the autocorrelation plane. This increased the range of the technique for the measurement of the flow velocity and also increased the accuracy by the removal of the influence of the central peak on the velocity peaks. When an acoustic field is present however, the shape of the halo changes across the negative, and this makes this technique difficult to implement.

Image shifting could be introduced to increase the range of the flow velocity measurement and resolve the directional ambiguity. This could also be used to make sure that the flow velocity and acoustic particle velocity are no longer in the same direction, thus removing a source of incorrect results.

Another way of doing this would be the to use a CCD array to record a succession of images and then cross correlate between the two. A fixed amount could be added to the second image to produce the image shift, and there would be the added advantage that the results could be viewed almost instantaneously if the CCD array were connected to a computer, removing the need for a photographic stage altogether. This method also resolves the directional ambiguity since the cross correlation function only has one peak.

Bibliography

[1] J. B. Abbis. Laser anemometry in an unseeded wind tunnel by means of photon correlation spectroscopy of backscattered light. *Journal of Physics. D.*, 5:L100–102, 1972.

[2] R. J. Adrian. Optical methods for measuring vector velocity fields, part ii techniques. Proc. Von Karman Inst. of Fluid Mechanics, 1988. Lecture Series 1988-06.

[3] R. J. Adrian. Particle imaging techniques for experimental fluid mechanics. *Annual Review of Fluid Mechanics*, 23:261–304, 1991.

[4] R.J. Adrian. Image shifting technique to resolve directional ambiguity in double pulsed velocimetry. *Applied Optics*, 25:3853–3855, 1988.

[5] E. N. Da C. Andrade. On the circulations caused by the vibration of air in the tube. *Proceedings of the Royal Society (London) A*, 134:445–469, 1931.

[6] M. P. Arroyo and C. A. Greated. Stereoscopic particle image velocimetry. *Journal of Physics E (Measurement Science and Technology)(2)*, pages 1181–1186, 1991.

[7] F.H. Barnes, Q.I. Daudapota, C.A. Greated, and I. Grant. Applications of photon correlation techniques to the measurement of flow with a sinusoidal perturbation. *Physics of Fluids*, 20:211, 1977.

[8] Yu. Ya. Borisov, A. F. Kiyan, and E. I. Rozenfel'd. Acoustic streaming as one of the factors responsible for the influence of a sound on a laminar flame jet. *Soviet Physics Acoustics (Translated from Russian)*, 19:580–581, 1974.

[9] O. Brandt, H. Fruend, and E. Heidemann. Schwebstoffe in schallfeld. *Zeits. Phys.*, 104:511–533, 1937.

[10] Bruel and Kjaer. Tech. Rev. no4: Sound Intensity (instrumentation and application). Technical report, Bruel and Kjaer, 1982.

[11] J. Y. Chung. Cross-spectral method of measuring acoustic intensity without error caused by instrument phase mismatch. *Journal of the Acoustic Society of America*, 64:1613–1616, 1978.

[12] J. M. Coupland and N. A. Halliwell. Particle image velocimetry: Rapid transparency analysis using optical correlation. *Applied Optics*, 27:1919–21, 1988.

[13] P. E. Doak. A discussion of the first and second viscosities of fluids. vorticity generated by sound. *Proceeding of the Royal Society of London A*, 226:7, 1954.

[14] L.E. Drain. *The Laser Doppler technique.* John Wiley & Sons, New York, 1980.

[15] P.S. Dubbelday and H. C. Schau. Laser doppler anemometry detection of hydroacoustic particle velocity. *Journal of the Acoustical Society of America*, 86:891–894, 1989.

[16] T. D. Dudderar, R. Meynart, and P. G. Simpkins. Full field laser metrology for fluid velocity measurements. *Optics and Lasers in Engineering*, 9:163–200, 1988.

[17] T.S. Durrani and C. A. Greated. *Laser Systems In Flow Measurement.* Plenum:New York, 1977.

[18] F. Durst, A. Melling, and J. H. Whitelaw. *Principles and practise of Laser Doppler anemometry.* Academic Press, New York, 1976.

[19] C. Eckart. Vortices and streams caused by sound waves. *Physical Review*, 73:68–76, 1948.

[20] S. Elliot, J. Bowsher, and P. Watkinson. Input and output transfer response of brass wind instruments. *Journal of the Acoustic Society of America*, 72:1747–1760, 1982.

[21] F. J. Fahy. Measurement of acoustic intensity using the cross-spectral density of two microphone signals. *Journal of the Acoustical Society of America*, 62:1057–1059, 1977.

[22] C. Gray, C. A. Greated, W. J. Easson, and N. E. Fancey. The application of particle image velocimetry to the study of water waves. *Optics and Lasers in Engineering*, 9:265–276, 1988.

[23] C. Gray and C.A. Greated. A processing system for the analysis of particle displacement holograms. *Optical Diagnosis in Fluid and Thermal Flow, SPIE conference San Diego, USA*, 1993.

[24] C. Gray, C.A. Greated, D.R. McCluskey, and W.J. Easson. An analysis of the scanning beam PIV illumination system. *Journal of Physics E (Measurement Science and Technology)*, 2:717–724, 1991.

[25] C. A. Greated. Measurement of acoustic velocity fields. *Strain*, pages 21–24, 1986.

[26] D. B. Hann and C. A. Greated. Acoustic measurements in flows using photon correlation spectroscopy. *Journal of Physics E(Measuring Science and Technology)*, 4:157–164, 1993.

[27] C. Hassa, P. H. Paul, and R. K. Hanson. Laser-induced fluorescence modulation techniques for velocity measurement in gas flows. *Experiments in Fluids*, 5:240–46, 1987.

[28] L. Hesselink. Digital image processing in flow visualization. *Annual Review of Fluid Mechanics*, 20:421–85, 1988.

[29] A. K. Hind and J. R. E. Christy. Digital piv applied to flows around artificial heart valves: analysis by autocorrelation. *Flow visualisation and image analysis, Delft Confrence*, Ed. Nieuwstand, 1993.

[30] J. O. Hinze. *Turbulence: An introduction to its mechanics and theory.* McGraw-Hill, New York, 1959.

[31] I. Hirschberg. New trends in solid state electornic imaging detectors. *Laser Focus*, 21:92–4, 1985.

[32] A. T. Hjelmfelt and L.F. Mockros. Motion of discrete particles in a turbulent fluid. *Applied Science Research.*, 16:149, 1966.

[33] M.L. Jakobsen, W.J. Hossack, C.A. Greated, and W.J. Easson. Piv analysis using an optically–addressed spatial light modulator. *Optics and Lasers in Engineering*, 19:253–260, 1993.

[34] H. H. Jensen and K. Saermark. On the theory of the Rayleigh disk and the sound pressure radiometer. *Acoustica*, 8:79–86, 1958.

[35] C. H. Kieth and J. C. Derrick. Measurement of particle size distribution and concentration of cigarette smoke by the "conifuge". *Journal of Colloidal Science*, 15:340–356, 1960.

[36] L. E. Kinsler, A. R. Frey, A. B. Coppens, and J. V. Sanders. *Fundamental of Acoustics*. John Wiley and Sons, New York, 1982.

[37] C. C. Landreth, R. J. Adrian, and C. S Yao. Double pulsed velocimeter with directional resolution for complex flows. *Experiments in Fluids*, 6:119–128, 1988.

[38] W. Lauterborn and A. Vogel. Modern optical techniques in fluid mechanics. *Annual Review of Fluid Mechanics*, 16:223–44, 1984.

[39] M. M. Lee, T. J. Hanratty, and R. J. Adrian. An axial viewing photographic technique to study turbulence characteristics of particles. *Journal of Multiphase flows*, 15:787–802, 1987.

[40] L. N. Liebermann. The second viscosity of liquids. *Physical Review*, 75:1415, 1949.

[41] J. Lighthill. Acoustic streaming. *Journal of Sound and Vibration*, 61:391–418, 1978.

[42] F. E. Marble and S. M. Candel. Acoustic attenuation in fans and ducts by vaporisation of liquid droplets. *American Institute of Aeronautics and Astronautics*, 11:634–639, 1975.

[43] J. J. Markham. Second order acoustic fields: Streaming due to viscosity and relaxation. *Physical Review*, 86:497, 1952.

[44] H. Medwin. An acoustic streaming experiment in gases. *Journal of the Acoustical Society of America*, 26:332, 1954.

[45] A. Meissenar. . *Zeitschrift fur Techische Physik*, 7:585, 1926.

[46] R.B. Miles, J. J. Connors, E.C. Markovitz, P. J. Howard, and G. J. Roth. Instantaneous profiles and turbulence statistics of supersonic free shear layers by raman excitation plus laser-induced electronic fluorescence (relief) velocity tagging tagging of oxygen. *Experiments in Fluids*, 8:17–24, 1989.

[47] M. Minten, A. Cops, and W. Lauriks. Absorption characteristics of an acoustic material at oblique incidence measured with the two-microphone technique. *Journal of Sound and Vibration*, 120:499–510, 1988.

[48] W. L. Nyborg. Acoustic streaming due to attenuated plane waves. *Journal of the Acoustic Society of America*, 25:68–75, 1952.

[49] C. J. D. Pickering and N. A. Halliwell. Particle Image Velocimetry: fringe visibility and pedestal removal. *Applied Optics*, 24:2474–2476, 1985.

[50] R. L. Pratt, S. J. Elliot, and J. M. Bowsher. The measurement of the acoustic impedance of brass instruments. *Acoustica*, 38:236–246, 1977.

[51] D. C. Pridmore-Brown. Sound propogation in a fluid flowing through an attenuation duct. *Journal of Fluid Mechanics*, 4:393, 1958.

[52] C. G. Rasmussen. An experimental investigation of the diffraction correction for a rayleigh-disk. *Acoustica*, 14:148–156, 1964.

[53] Lord Rayleigh. *The Theory of Sound, article 352*, volume 2. Macmillan, 1983.

[54] H. Schlicting. *Boundary Layer Theory.* McGraw Hill, New York, 6th edition, 1966.

[55] J. P. Sharpe and C. A. Greated. The measurement of periodic acoustic fields using photon correlation spectroscopy. *Journal of Physics D (Applied Physics)*, 20:418–423, 1987.

[56] J. P. Sharpe and C. A. Greated. A stochastic model for photon correlation measurements in sound fields. *Journal of Physics D(Applied Physics)*, 22:1429–1433, 1989.

[57] J. P. Sharpe, C. A. Greated, and D. M. Campbell. The measurement of complex acoustic impedence using photon correlation spectroscopy. *Acoustica*, 66:266–289, 1988.

[58] J. P. Sharpe, C. A. Greated, C. Gray, and D. M. Campbell. The measurement of acoustic streaming using particle image velocimetry. *Acoustica*, 68:168–172, 1989.

[59] A. M. O. Smith. Remarks on transition in a round tube. *Journal of Fluid Mechanics*, 7:565–577, 1960.

[60] J.T. Stuart. *Laminar Boundary Layers, chapter 7, Unsteady Boundary Layers.* (edited by L. Rosenhead) Oxford University Press, London, 1963.

[61] K. J. Taylor. Absolute measurement of acoustic particle velocity. *Journal of the Acoustical Society of America*, 51:691–4, 1976.

[62] K. J. Taylor. Absolute calibration of microphones by a laser doppler technique. *Journal of the Acoustical Society of America*, 70:939–45, 1981.

[63] S. Temkin and R. A. Dobbins. Measurements of attenuation and dispersion of sound by an aerosol. *Journal of the Acoustical Society of America*, 40:1016–1024, 1966.

[64] H. J. Tiziani. Application of speckling for in-plane vibration analysis. *Optica Acta*, 18:891–902, 1971.

[65] C. J. Tranter. *Theory of Bessel Functions.* English University Press., England, 1968.

[66] J. Vignola, Y. H. Berthelot, and J. Jarzynski. Non-intrusive absolute measurement of acoustic particle velocity in fluids. In *13th International conference on Acoustics*, Belgrade, Yugoslavia, 1989.

[67] B.M Watrasiewicz and M.J. Rudd. *Laser Doppler measurements.* Butterworths, London, 1976.

[68] P. J. Westervelt. The theory of steady rotational flow generated by a sound field. *Journal of the Acoustical Society of America*, 25:61–67, 1952.

[69] H. Yeh and H. Z. Cummins. Localised fluid flow measurement with a He-Ne laser spectrometer. *Applied Physics Letters*, 4:176–178, 1964.

Appendix A

Appendix 1

A.1 Mathematical derivation of Autocorrelation function for L.D.A.

This is the actual derivation of the correlation function with explanation of the mathematics and the steps involved. We start with equation (4.10).

We proceed to evaluate by substituting $y = a_0\tau + A_m \sin\alpha$ so that the integral becomes that in equation A.1

$$R(\tau) = \sqrt{\frac{\pi\kappa^4 C_1^2 g_0^2}{8\beta^2}} \int_{-\pi/2}^{\pi/2} \frac{d\alpha}{\pi} \exp\left(\frac{-\beta^2(a_0\tau + A_m \sin\alpha)^2}{2}\right) [M + \cos(Da_0\tau + DA_m \sin\alpha)]. \tag{A.1}$$

The cosine can be expanded to form the autocorrelation function shown in equation A.2

$$R(\tau) = \sqrt{\frac{\pi\kappa^4 C_1^2 g_0^2}{8\beta^2}} \frac{1}{\pi} \exp\left(\frac{\beta^2 a_0^2 \tau^2}{2}\right) \int_{-\pi/2}^{\pi/2} \exp(-\beta^2 a_0 \tau A_m \sin\alpha) \exp\left(-\frac{\beta^2 A_m^2 \sin^2\alpha}{2}\right)$$

$$[M + \cos(Da_0\tau)\cos(DA_m \sin\alpha) - \sin(Da_0\tau)\sin(DA_m \sin\alpha)]d\alpha \tag{A.2}$$

We can now split this into three parts and make the two following substitutions to form equation A.3 - A.6.

$$p = \beta^2 a_0 \tau A_m$$

$$q = \frac{\beta^2 A_m^2}{4}$$

$$R(\tau) = \frac{\kappa^2 C_1 g_0}{2}\sqrt{\frac{\pi}{2\beta^2}}\exp\left(-\frac{\beta^2 a_0^2 \tau^2}{2}\right)(F_1 + F_2 + F_3) \tag{A.3}$$

$$F_1 = \frac{1}{\pi}\cos(Da_0\tau)\int_{-\pi/2}^{\pi/2}\exp(-p\sin\alpha)\exp(-2q\sin^2\alpha)d\alpha \tag{A.4}$$

$$F_2 = \frac{1}{\pi}\cos(Da_0\tau)\int_{-\pi/2}^{\pi/2}\exp(-p\sin\alpha)\exp(-2q\sin^2\alpha)\cos(DA_m\sin\alpha)d\alpha \tag{A.5}$$

$$F_3 = -\frac{1}{\pi}\sin(Da_0\tau)\int_{-\pi/2}^{\pi/2}\exp(-p\sin\alpha)\exp(-2q\sin^2\alpha)\sin(DA_m\sin\alpha)d\alpha. \tag{A.6}$$

Now the integrals F_1,F_2 and F_3 in equations A.4, A.5 and A.6 are evaluated and combined to produce the final autocorrelation function.

First we evaluate F_1 by applying the double angle formula to give equation A.7.

$$F_1 = \frac{1}{\pi}\exp(-q)\int_{-\pi/2}^{\pi/2}\exp(-p\sin\alpha)\exp(q\cos 2\alpha)d\alpha. \tag{A.7}$$

It can be shown from the generating function of the Modified Bessel function [65] that the following equation is true.

$$\exp(x\cos 2\alpha) = I_0(x) + 2\sum_{n=1}^{\infty} I_n(x)\cos 2n\alpha.$$

If this is substituted into equation A.7 and the other exponential split into a cosh and sinh then

$$F_1 = \frac{\exp(-q)}{\pi}\int_{-\pi/2}^{\pi/2}[\cosh(p\sin\alpha) - \sinh(p\sin\alpha)]\left\{I_0(q) + 2\sum_{n=1}^{\infty} I_n(q)\cos 2n\alpha\right\}d\alpha.$$

If we note that the sinh term is odd and disappears, and that equation A.8 is true, then we find that the solution of F_1 is given by equation A.9

$$\int_0^{\pi/2}\cosh(p\sin\alpha)\cos(2n\alpha)d\alpha = (-1)^n\frac{\pi}{2}I_{2n}(p) \tag{A.8}$$

$$F_1 = \exp(-q)\left\{I_0(p)I_0(q) + 2\sum_{n=1}^{\infty}(-1)^n I_n(q)I_{2n}(p)\right\} \tag{A.9}$$

Turning to F_2, we utilise the double angle formula again and also the Bessel function expansion for a cosine with a sinusoidal argument to obtain the following equation for F_2.

$$F_2 = \frac{1}{\pi}\exp(-q)\cos(Da_0\tau)$$

$$\mathrm{x}\int_{-\pi/2}^{\pi/2}\exp(-\mathrm{p}\sin\alpha)\exp(\mathrm{q}\cos 2\alpha)\left\{\mathrm{J_0(DA_m)} + 2\sum_{\mathrm{k=1}}^{\infty}\mathrm{J_{2k}(DA_m)}\cos(2\mathrm{k}\alpha)\right\}\mathrm{d}\alpha$$

$$= \frac{1}{\pi}\exp(-q)\cos(Da_0\tau)\left\{J_0(DA_m)F_1 + 2\sum_{k=1}^{\infty}J_{2k}(DA_m)F_4\right\}, \tag{A.10}$$

Here we have defined F_4 as shown in equation A.11

$$F_4 = \int_{-\pi/2}^{\pi/2}\exp(-p\sin\alpha)\exp(q\cos 2\alpha)\cos(2k\alpha)d\alpha. \tag{A.11}$$

As in the evaluation of F_1 we expand the second exponential in terms of the modified Bessel function and then we expand the first in terms of cosh and sinh. The integrals containing the sinh term is zero when evaluated between these limits so we ignore it. This means that equation A.11 can be rewritten as follows.

$$\begin{aligned} F_4 &= 2\int_0^{\pi/2}\cosh(p\sin\alpha)\cos(2k\alpha)I_0(q)d\alpha \\ &\quad +4\sum_{m=1}^{\infty}I_m(q)\int_0^{\pi/2}\cosh(p\sin\alpha)\cos(2k\alpha)\cos(2m\alpha)d\alpha. \end{aligned}$$

The two cosines in the second term can be made into the sum of two cosines, so the second term can be rewritten.

$$2\sum_{m=1}^{\infty}I_m(q)\int_0^{\pi/2}\cosh(p\sin\alpha)\left[\cos(2[m-k]\alpha) + \cos(2[m+k]\alpha)\right]d\alpha.$$

Using equation A.8 again, we find that F_4 equals

$$\pi I_0(q)(-1)^k I_{2k}(p) + \sum_{m=1}^{\infty}I_m(q)\left[(-1)^{m-k}I_{2(m-k)}(p) + (-1)^{m+k}I_{2(m+k)}(p)\right]. \tag{A.12}$$

To evaluate F_3 we start by expanding the first exponential in terms of cosh and sinh and use the double angle formula on the second exponential and expand it into a series containing modified Bessel functions. The sin term can be expanded as in the following equation.

$$\sin(DA_m \sin\alpha) = 2\sum_{s=0}^{\infty} J_{2s+1}(DA_m)\sin[(2s+1)\alpha]. \tag{A.13}$$

Since the term containing the cosh is odd it is ignored leaving equation A.14.

$$F_3 = -\frac{2}{\pi}\exp(-q)\sin(Da_0\tau)\sum_{s=0}^{\infty} J_{2s+1}(DA_m)$$

$$\int_{-\pi/2}^{\pi/2}\left[I_0(q) + 2\sum_{r=1}^{\infty} I_r(q)\cos(2r\alpha)\right]\sinh(p\sin\alpha)\sin\{(2s+1)\alpha\}d\alpha. \tag{A.14}$$

We then use the addition theorem on the sine-cosine product and then note that equation A.15 is true to get equation A.16.

$$\int_{-\pi/2}^{\pi/2}\sinh(p\sin\alpha)\sin[(2n+1)\alpha]d\alpha = \pi(-1)^n I_{2n+1}(p). \tag{A.15}$$

$$F_3 = -2\exp(-q)\sin(Da_0\tau)\sum_{s=0}^{\infty} J_{2s+1}(DA_m)$$

$$\left[(-1)^s I_0(q)I_{2s+1}(p) + \sum_{r=1}^{\infty} I_r(q)\left[(-1)^{s+r}I_{2s+2r+1}(p) + (-1)^{s-r}I_{2s-2r+1}(p)\right]\right]. \tag{A.16}$$

If we collect this and note equations A.17, A.18 and A.19, we find that the auto-correlation function is given by equation A.20.

$$\sum_{k=1}^{\infty} J_{2k}(DA_m)(-1)^k I_{2k}(\beta^2 A_m a_0\tau) = J_0(A_m\sqrt{D^2 - \beta^4 a_0^2\tau^2}) - J_0(DA_m) \tag{A.17}$$

$$\sum_{s=0}^{\infty} J_{2s+1}(DA_m)(-1)^s I_{2s+1}(\beta^2 a_0 A_m\tau) = 0 \tag{A.18}$$

$$\Gamma = \frac{\kappa^2 C_1 g_0\sqrt{\pi}}{2\sqrt{2\beta^2}} \tag{A.19}$$

$$
\begin{aligned}
R(\tau) &= \frac{\kappa^2 C_1 g_0}{2}\sqrt{\frac{\pi}{2\beta^2}}\exp\left(-\frac{\beta^2 A_m^2}{4}\right)\exp\left(-\frac{\beta^2 a_0^2\tau^2}{2}\right) \\
&\quad [M\left\{I_0\left(\frac{\beta^2 A_m^2}{4}\right)I_0(\beta^2 A_m a_0\tau)+2\sum_{n=1}^{\infty}(-1)^n I_n\left(\frac{\beta^2 A_m^2}{4}\right)I_{2n}(\beta^2 A_m a_0\tau)\right\} \\
&\quad +I_0\left(\frac{\beta^2 A_m^2}{4}\right)\cos(Da_0\tau)J_0\left(A_m\sqrt{D^2-\beta^4 a_0^2\tau^2}\right) \\
&\quad +2\cos(Da_0\tau)\sum_{k=1}^{\infty}J_{2k}(DA_m)\sum_{n=1}^{\infty}I_n\left(\frac{\beta^2 A_m^2}{4}\right)(-1)^{n-k}I_{2(n-k)}(\beta^2 A_m a_0\tau) \\
&\quad +2\cos(Da_0\tau)\sum_{k=1}^{\infty}J_{2k}(DA_m)\sum_{n=1}^{\infty}I_n\left(\frac{\beta^2 A_m^2}{4}\right)(-1)^{n+k}I_{2(n+k)}(\beta^2 A_m a_0\tau) \\
&\quad +2\sin(Da_0\tau)\sum_{k=0}^{\infty}J_{2k+1}(DA_m)\sum_{n=1}^{\infty}I_n\left(\frac{\beta^2 A_m^2}{4}\right)(-1)^{n+k}I_{2n+2k+1}(\beta^2 a_0 A_m\tau) \\
&\quad +2\sin(Da_0\tau)\sum_{k=0}^{\infty}J_{2k+1}(DA_m)\sum_{n=1}^{\infty}I_n\left(\frac{\beta^2 A_m^2}{4}\right)(-1)^{n-k}I_{2n-2k+1}(\beta^2 a_0 A_m\tau)] \quad \text{(A.20)}
\end{aligned}
$$

This is the general stochastic model for a flow with a sinusoidal perturbation superimposed and can be simplified as shown in the main section.

Appendix B

Program listings

```
/* Program to Analyse the power spectrum */

#include "/maps/optics/wjh/include/image.h"
#include "/maps/optics/wjh/include/cio.h"
#include <math.h>

int Analyse(pic,xpos,ypos,T,profile,FTprof,display,orient,APV,APV1,
                                        APVfile,verbose,apvans)
image *pic;
int xpos,ypos,T,display,orient,verbose,apvans;
float *APV, *APV1;
FILE  *profile, *FTprof, *APVfile;
{
/* char *calloc();*/
int i,j,n,m,N1=30,N2=30,N3=30,M=30,N4=0,N5=0;
float sum0=0.0,sum1=0.0, *B,widt,
*A,max1=0.0,max2=0.0,max3=0.0,max4=0.0,max5=0.0,MAX5=0.0,MAX4=0.0,
                MAX3=0.0,MAX1=0.0, MAX2=0.0, Nmax=0.0,
                                    SUM0=0.0, SUM1=0.0,
                               MIN0=10000000000.0,MIN1=10000000000.0;
if (verbose > 2)
printf(" orient = %d \n",orient);
```

```
A=(float *) calloc((unsigned) (T+1), sizeof(float));
B=(float *) calloc((unsigned) (T+1), sizeof(float));
SUM0=0.0;SUM1=0.0;
for( n=0;n<T+1;n++){
  A[n]=0.0;B[n]=0.0;
  sum0 =0.0;sum1=0.0;
  for (m=0;m<2*T;m++){
    sum0 += *F_PIXEL(pic,T-n,m,0)/* + *F_PIXEL(pic,T+n,m,0)*/;
    sum1 += *F_PIXEL(pic,m,T-n,0)/*+ *F_PIXEL(pic,n,T+m,0)*/;
 }
A[n] =sum0;
B[n] =sum1;
SUM0 +=sum0;
SUM1+= sum1;
}
A[0]=A[1];
if (verbose> 2)
printf(" averaged = %f \n",sum1);
for(n=0;n<T;n++){
if (display == 3)
fprintf(profile, " %5f %5f  \n", n /(2.0*T),A[n]);
if (display == 5)
fprintf(profile, " %5f %5f  \n",n/(2.0*T),A[n]);
}

if (verbose > 2)
printf(" saved  = %f \n",sum1);

 MAX1=0.0;MAX2=0.0;MAX3=0.0;MAX4=0.0;N1=0;N2=0;N3=0;N4=0;N5=0;
 for (n=2;n<T;n++){
if ((/*A[n-2] < A[n])&&*/(A[n-1] < A[n]) &&
                        (A[n+1] < A[n] )/*&&(A[n+2] < A[n]*/)){
  if ((A[n] > MAX1) && (n>1)  ){
   MAX5=MAX4;MAX4=MAX3;
```

```
    MAX3=MAX2;
    MAX2=MAX1;
    MAX1= A[n];
    N5=N4;N4=N3;N3=N2;
    N2=N1;
    N1=n;
        }
else  if ( (A[n] > MAX2)){
    MAX5=MAX4;MAX4=MAX3;MAX3=MAX2;
    MAX2=A[n];
    N5=N4;N4=N3;N3=N2;
    N2=n;
    }
else  if ( (A[n] > MAX3)){
  MAX5=MAX4;MAX4=MAX3;MAX3=A[n];
  N5=N4;N4=N3;N3=n;
     }
else  if ( (A[n] > MAX4)){
  MAX5=MAX4;MAX4=A[n];
  N5=N4;N4=n;
     }
else  if ( (A[n] > MAX5)){
  MAX5=A[n];
  N5=n;
     }
}
}


if (verbose > 2)
printf(" calc  = %d \n",orient);

max5 = N5+ (A[N5-1] - A[N5+1])/(2*A[N5-1]-4*A[N5]+2*A[N5+1]);
max4 = N4 + (A[N4-1] - A[N4+1])/(2*A[N4-1]-4*A[N4]+2*A[N4+1]);
```

```
max3 = N3 + (A[N3-1] - A[N3+1])/(2*A[N3-1]-4*A[N3]+2*A[N3+1]);
max2 = N2 + (A[N2-1] - A[N2+1])/(2*A[N2-1]-4*A[N2]+2*A[N2+1]);
max1 = N1 + (A[N1-1] - A[N1+1])/(2*A[N1-1]-4*A[N1]+2*A[N1+1]);



printf(" p1=%5f p2=%5f p3=%5f  p4=%5f p5=%5f \n"
                                    , max1,max2,max3,max4,max5);
if(apvans ==2){
if (max2 >T/2 ){
*APV = (3.8317*T/(3.14159*max1));
*APV1 =  (7.156*T/(3.14159*max1));
}
else{
*APV =  (7.156*T/(3.14159*max2));
*APV1 =  (3.8317*T/(3.14159*max2));
}
printf( "   %5f <  %5f  \n", (2*3.8317*T/(3.14159*max1)),
(2*7.0156*T/(3.14159*max1)) );
printf( " %5f  < %5f <  %5f  \n", (2*3.8317*T/(3.14159*max2)),
(2*7.156*T/(3.14159*max2)),(2*10.0174*T/(3.14159*max2)) );
printf( "  %5f <  %5f< %5f  \n",(2*7.156*T/(3.14159*max3)),
    (2*10.0174*T/(3.14159*max3)),(2*13.324*T/(3.14159*max3)) );
printf( "   %5f< %5f <%5f \n", (2*10.0174*T/(3.14159*max4)),
(2*13.324*T/(3.14159*max4)),(2*16.471*T/(3.14159*max4)));
printf( " %5f <  %5f< %5f  \n",(2*13.324*T/(3.14159*max5)),
(2*16.471*T/(3.14159*max5)),(2*19.616*T/(3.14159*max5)) );
}
autoplane(A,B,T,display,FTprof,(7.0156*T/(3.14159*max2)),MAX1,
                                    APV,&widt,verbose,apvans);
fprintf(APVfile," %5d  %5d    %7f  %5f  %5f  \n",xpos,ypos,
                                        *APV,widt, *APV1);
```

```
if (verbose  >2)
printf("Analysed \n");
return;
}
```

```
\*subroutine which does a 1-d FT on the profile of the power
 spectrum */

autoplane(A,B ,T,display,profile,AM,MAX1,APV,widt,verbose,apvans)

int T,display,verbose,apvans;
float A[] ,B[],AM,MAX1, *APV, *widt;
FILE *profile;
{
int n,k,N=0,N1=0,N2=0;
float *R , *K,max=0.0,max1=0.0,MAX=0.0,MIN=0.0,
aver1=1000000000000.0, aver=10000000000000.0,max2=0.0,MAX2=0.0;
R=(float *) calloc((unsigned)(T+1), sizeof(float));
K=(float *) calloc((unsigned)(T+1), sizeof(float));
/* for (n=5;n<T+1;n++){
   if (aver  >  A[n])
  aver=A[n];
   if (aver1> B[n])
  aver1=B[n];
  }*/
R[0]=0.0;K[0]=0.0;
 for (n=0;n<T+1;n++){
 R[0]+=(1-(n-T/4.0)*(n-T/4.0)/(T*T*1.0))*(A[n]/*-aver*/);
K[0]+=(1-(n-T/4.0)*(n-T/4.0)/(T*T*1.0))*(B[n]/*-aver1*/);
}
for (k=1;k<T;k++){
R[k]=0.0;K[k]=0.0;
  for (n=0;n<T;n++){
 R[k] +=(1-(n-T/4.0)*(n-T/4.0)/(T*T*1.0))* (A[n]/*-aver*/)
                              *cos(2*3.14159*k*n/(2.0*T));
 K[k] += (1-(n-T/4.0)*(n-T/4.0)/(T*T*1.0))*(B[n]/*-aver1*/)
                               * cos(2*3.14159*k*n/(2.0*T));
}
```

```
if (display == 3)
fprintf(profile, " %5d %5f %5f %5f  \n",k-1,R[k-1],R[k-2]-R[k],
                                    (2*R[k-1]-R[k-2]-R[k]));

 if (display == 5)
fprintf(profile, " %5d %5f  \n"
              ,k-1,/*R[k-1],K[k-1],*/(2*R[k-1]-R[k-2]-R[k]));



}
 for (n=4;n<T-2;n++){
if
(((2*R[n-1]-R[n-2]-R[n])<(2*R[n]-R[n-1]-R[n+1]))
&&  ((2*R[n+1]-R[n]-R[n+2])<(2*R[n]-R[n-1]-R[n+1])) ){
  if ((2*R[n]-R[n-1]-R[n+1]) > MAX ){
   MAX= (2*R[n]-R[n-1]-R[n+1]);
   N=n;
       }
}
}
for(n=1;n<10;n++){
if
(((2*R[N+n-1]-R[N+n-2]-R[N+n])>(2*R[N+n]-R[N+n-1]-R[N+n+1]))&&
 ((2*R[N+n+1]-R[N+n]-R[N+n+2])> (2*R[N+n]-R[N+n-1]-R[N+n+1])) ){
  if ((2*R[N+n]-R[N+n-1]-R[N+n+1]) < -MIN ){
 MIN= -(2*R[n]-R[n-1]-R[n+1]);
  N1=N+n;
   }
}
if (verbose >2)
 printf(" peak %5d 1stder %5f 2ndder %5f  \n",n,(R[n-1]-R[n+1])/2.0,
                                        (2*R[n]-R[n-1]-R[n+1]));
}
```

```
 for (n=4;n<T-2;n++){
if(((R[n-1]-R[n])<(R[n]-R[n+1]))&&((R[n+1]-R[n+2])<(R[n]-R[n+1]) )){
  if ((R[n]-R[n+1]) > MAX2 ){
   MAX2= (R[n]-R[n+1]);
   N2=n;
       }
}
}
max = N + ((2.0*R[N-1]-R[N-2]-R[N]) - (2.0*R[N+1]-R[N]-R[N+2]))/
                (2.0*(2.0*R[N-1]-R[N-2]-R[N])-4.0*(2*R[N]-R[N-1]
                                -R[N+1])+2.0*(2*R[N+1]-R[N]-R[N+2]));
max1 = N1+((2.0*R[N1-1]-R[N1-2]-R[N1])-(2.0*R[N1+1]-R[N1]-R[N1+2]))/
(2.0*(2.0*R[N1-1]-R[N1-2]-R[N1])-4.0*(2*R[N1]-R[N1-1]-R[N1+1])
                                    +2.0*(2*R[N1+1]-R[N1]-R[N1+2]));
max2 = N2+0.5 + ((R[N2-1]-R[N2]) - (R[N2+1]-R[N2+2]))/
    (2.0*(R[N2-1]-R[N2])-4.0*(R[N2]-R[N2+1])+2.0*(R[N2+1]-R[N2+2]));
if (verbose >0)
printf(/*" %5d %5f %5d  %5f %5f*/" width %5f pos %5f 1/rt2width  %5f
1/2width %5f 1/4widthsq %5f \n",/*N,max,N1,max1,max+(max1-max)/2.0,*/
(max1-max-1)/2.0, max2,1/(1.4142*(max1-max-1)/2.0),
1/(2*(max1-max-1)/2.0),1/(2*(max1-max-1)/2.0)*1/(2*(max1-max-1)/2.0));

*widt=(max1-max-1)/(3.14159*3.14159);
if (apvans ==1)
 *APV=max2+(max1-max-1)/(3.14159*3.14159);
if (apvans==0)
*APV=max2;
return;
}


\* Program to average halo across picture*/

#include "/maps/optics/wjh/include/image.h"
#include "/maps/optics/wjh/include/cio.h"
```

```
#include <math.h>

int collect_halo(pic,halo,T,radius1)
image *pic, *halo;
int T,radius1;
{
int n,m;
static image pic1;
im_zero(halo);
for (m=0; m<X_SIZE(pic)/(2.0*T);m++){
  for (n=0;n<Y_SIZE(pic)/(2.0*T);n++){
  im_extract(pic,&pic1,2*T,2*T,1.0,1.0,(m*2.0*T),(n*2.0*T),1);
im_stats(&pic1);
im_rscale(&pic1,255.0/R_MAX(&pic1),-R_MIN(&pic1)*255.0/R_MAX(&pic1),0);
im_stats(&pic1);
im_toc('R');
im_convert(&pic1,COMPLEX);
im_fourier(&pic1);
im_fromc('s');
im_convert(&pic1,FLOAT);
im_add(halo,&pic1);
  }
}
im_stats(halo);
for (n = -10;n< 10;n++){
   for (m= -10;m<10;m++){
    if ( (n)*(n)+(m)*(m) < (radius1+1)*(radius1+1) )
      *F_PIXEL(halo,T+n,T+m,0) =R_MIN(&pic1);;
   }
 }
printf("found halo \n");

im_rscale(halo,2.0*T/(1.0*Y_SIZE(pic)),0.0,0.0);
im_stats(halo);
```

```
im_xv(halo,0);
return;
}
```

```
/* Main program for the analysis of PGM files .
Input needs to be of the form
general *.pgm Gsize Size x1 x2 y1 y2 orient PSblank APblank imshift
verbose window offset
Gsize is half the distance between measuring points,
Size is size of interogation area,
x1 x2 y1 y2 are start and finish grid points
orient can be 0 or 1  determined by the direction of the streaks,
PSblank is the no of pixels blanked in the centre of the PS,
APblankis the no of pixels blanked in the centre of the AP,
imshift is the no of pixels in the y direction that the image was
shifted,
verbose can be 0 1 2 3 and each number increases the information
outputed to the screen during running(for debugging),
window determines the guassian window used on the Power spectrum.
offset =redundant.
*/



#include "/maps/optics/wjh/include/image.h"
#include "/maps/optics/wjh/include/cio.h"
#include <math.h>

main(argc,argv)

int argc;
char *argv[];

{
static image pic,pic1,halo,halopict;
int n,m,k,i,j,T=10,G=10,N,N1,M,M1,verbose=0,analyse,display1,screen,
orient =0, radius,radius1,imshift,window1=0.0,x,y, offset,apvans;
```

```
float t=20.0,sumhalo,sumpic,A0,width,APV,APV1,Angle,An=0.0;
FILE *infile1, *autofile, *powerfile, *profile,*FTprof, *peakfile,
*infile2, *APVfile;
if (argc != 15 )
printf("general *.pgm Gsize Size x1 x2 y1 y2 orient PSblank
                    APblank imshift verbose window offset\n");

analyse =intin("0 for general, 1 for findmax, 2 for subhalo",0,0,2);
display1=intin("0=nothing, 1=Autocorrelation, 2= power spectrum,
3=profile and FT of profile, 4=peaks recorded,
 5=Auto,power,profile andFTof profile ",0,0,5);
screen=intin("0 for nothing, 1 xv of interrogation area,2=xv of power
,3=xv of auto,4 of xv and auto  ",0,0,4);
apvans=intin("0for FT, 1for FT+sigma,2for PS, 3for AP",0,0,3);
if ( analyse == 1)
width=intin("width of exp",75,1,100000)/10000.0;
if (display1 == 1)
autofile=openit("autofile","auto.dat","w");
if (display1 == 2)
powerfile=openit("powerfile","power.dat","w");
if (display1 == 5){
autofile=openit("autofile","auto.dat","w");
powerfile=openit("powerfile","power.dat","w");
profile=openit("profile","profile.dat","w");
FTprof=openit("FT of profile","FT.dat","w");
}
if (display1 == 3){
profile=openit("profile","profile.dat","w");
FTprof=openit("FT of profile","FT.dat","w");
}
if (display1 == 4){
APVfile=openit("APVfile","apv.dat","w");
peakfile=openit("peakfile","peak.dat","w");
}
```

```
infile2=openit("filename for analysis",argv[1],"rb");
sscanf(argv[2],"%d",&G);

sscanf(argv[3],"%d",&T);
t=2.0*T;
if ( im_read(&pic,FLOAT,infile2)==NULL)
  printf("failed to read file");
printf(" no x points  %5f no y points %5f \n",
              X_SIZE(&pic)/(2.0*G),Y_SIZE(&pic)/(2.0*G));
sscanf(argv[4],"%d",&N);
sscanf(argv[5],"%d",&N1);
sscanf(argv[6],"%d",&M);
sscanf(argv[7],"%d",&M1);
sscanf(argv[8],"%d",&orient);
sscanf(argv[9],"%d",&radius);
sscanf(argv[10],"%d",&radius1);
sscanf(argv[11],"%d",&imshift);
sscanf(argv[12],"%d",&verbose);
sscanf(argv[13],"%d",&window1);
sscanf(argv[14],"%d",&offset);


for (n=N;n< N1;n++){
    for (m=M;m<M1;m++){

  if (im_alloc(&pic1,2*T,2*T,Z_SIZE(&pic),FORMAT(&pic))
                == NULL)
{
               printf("help");
                }
 for (j = 0; j < Y_SIZE(&pic1); j++)
                {
                y = m*2*G-T +j;
                for (i = 0; i < X_SIZE(&pic1); i++)
```

```
                        {
                        x = n*2*G-T+i ;
/*if(*F_PIXEL(&pic,x,y,0)> offset)*/
if(orient ==0)
  *F_PIXEL(&pic1,i,j,0)=   *F_PIXEL(&pic,x,y,0)/*-1.0*offset*/ ;
if(orient ==1)
*F_PIXEL(&pic1,j,i,0)=   *F_PIXEL(&pic,x,y,0)/*-1.0*offset*/ ;
/* else
*F_PIXEL(&pic1,i,j,0)=0.0;*/
                    }
                }
        SPACE(&pic1) = SPACE(&pic);
        ACCESS(&pic1) = ACCESS(&pic);
        USER(&pic1) = USER(&pic);
        im_title(&pic1,TITLE(&pic));
 /*
 im_extract(&pic,&pic1,2*T,2*T,1.0,1.0,n*2.0*G-T,m*2.0*G-T,1);*/
im_stats(&pic1);
if (verbose > 2 )
im_pstats(&pic1);
printf(" mean = %5f \n",R_MEAN(&pic1));
if (verbose >1)
printf(" offset= %5d \n",offset );

for (i=0;i<X_SIZE(&pic1);i++){
 for (j=0;j<Y_SIZE(&pic1);j++){
*F_PIXEL(&pic1,i,j,0) =
255*(*F_PIXEL(&pic1,i,j,0)-R_MIN(&pic1))/(R_MAX(&pic1)-R_MIN(&pic1));

if (offset >0){
 if ( *F_PIXEL(&pic1,i,j,0)> 4/5.0*R_MEAN(&pic1))
  *F_PIXEL(&pic1,i,j,0) =
(*F_PIXEL(&pic1,i,j,0)-R_MEAN(&pic1)*4/5.0)
*exp(-window1*((i-T)*(i-T)+(j-T)*(j-T))/(T*T*1.0));
```

```
else
*F_PIXEL(&pic1,i,j,0) =0.0;
}
}
}
im_stats(&pic1);
if (verbose>2)
 printf("  T=%d G= %d win1=%d xsize%d ysize %d \n",T,G,window1,
                                        X_SIZE(&pic1),Y_SIZE(&pic1));
if ( screen == 1 )
   im_xv(&pic1,0);
if ( screen == 4 )
   im_xv(&pic1,0);

    im_toc('R');
    im_convert(&pic1,COMPLEX);
    im_fourier(&pic1);
    im_fromc('s');
    im_convert(&pic1,FLOAT);

/*orientation(&pic1, &Angle,T,&An,verbose);*/
An=6.28;
im_stats(&pic1);
im_rscale(&pic1,255.0/R_MAX(&pic1),-R_MIN(&pic1)*255.0/R_MAX(&pic1),0.0);

for (i= -T;i<T;i++){
   for (j= -T;j<T;j++){
if (analyse==1)
 *F_PIXEL(&pic1,T+i,T+j,0) *= exp(-width*(i*i+j*j));
if ((i*i+j*j) < ((radius1+1)*(radius1+1)))
 *F_PIXEL(&pic1,T+i,T+j,0)=0.0;
 *F_PIXEL(&pic1,T+i,T,0)=0.0;
 *F_PIXEL(&pic1,T,T+j,0)=0.0;
  }
```

```
 }

 Analyse(&pic1,n,m,T,profile,FTprof,display1,orient,&APV,&APV1,
                                              APVfile,verbose,apvans);

im_stats(&pic1);
im_rscale(&pic1,255.0/R_MAX(&pic1),0,0);
im_stats(&pic1);
if (display1 == 2 )
im_pgm(&pic1,powerfile,T);
if (display1 == 5 )
im_pgm(&pic1,powerfile,T);
if (screen == 2)
im_xv(&pic1,0);
im_toc('R');
im_convert(&pic1,COMPLEX);
        im_fourier(&pic1);
im_fromc('r');
im_convert(&pic1,FLOAT);


im_stats(&pic1);
im_rscale(&pic1,255.0/R_MAX(&pic1),-R_MIN(&pic1)
                                    *255.0/R_MAX(&pic1),0.0);
findpeak1(&pic1,T,peakfile,n*2*G,m*2*G,display1,APV,APV1,
                                imshift,verbose,radius,apvans);
im_stats(&pic1);
 for (i = 0;i<2*T+1;i++){
 for (j= 0;j<2*T+1;j++){
    if ( (j-T)*(j-T)+(i-T)*(i-T) < (radius+1)*(radius+1) )
       *F_PIXEL(&pic1,i,j,0) = R_MIN(&pic1);;
  }
 }
  *F_PIXEL(&pic1,T,T,0)=R_MIN(&pic1);
```

```
im_stats(&pic1);
if (screen == 3 )
 im_xv(&pic1,0);
if (screen ==4 )
  im_xv(&pic1,0);
if ( display1 == 1 )
 im_pgm(&pic1,autofile,T);
if ( display1 == 5 )
 im_pgm(&pic1,autofile,T);
}
}
printf("%5f is average angle \n", An/(1.0*(N1-N+0.0)*(M1-M+0.0))
                                                    *180/3.14159);
}
```

```
\* subroutine which calculates orientation of fringes*/

int orientation(pic1,Angle1,T,An,verbose)
float *Angle1, *An;
int T,verbose;
image *pic1;
{
int A,B;
float sum,max=0.0,Angle;

for(A=0;A<2*T;A++){
sum=0.0;
Angle= 3*3.14159/4.0 + A*3.14159/(4.0*T);
for (B=0;B<T;B++){
sum+= *F_PIXEL(pic1,T+(int)(B*sin(Angle)),T+(int)(B*cos(Angle)),0)+
 *F_PIXEL(pic1,T-1+(int)(B*sin(Angle)),T+(int)(B*cos(Angle)),0)+
*F_PIXEL(pic1,T+1+(int)(B*sin(Angle)),T+(int)(B*cos(Angle)),0)+
   *F_PIXEL(pic1,T-2+(int)(B*sin(Angle)),T+(int)(B*cos(Angle)),0)
+ *F_PIXEL(pic1,T+2+(int)(B*sin(Angle)),T+(int)(B*cos(Angle)),0);
}
if (sum > max){
max=sum; *Angle1=Angle;
}
if (sum == max){
max= sum;  *Angle1 =( *Angle1+Angle)/2.0;
}
}
for(A=0;A<2*T;A++){
sum=0.0;
Angle= 3.14159/4.0 + A*3.14159/(4.0*T);
for (B=0;B<T;B++){
sum+= *F_PIXEL(pic1,T+(int)(B*sin(Angle)),T+(int)(B*cos(Angle)),0)+
*F_PIXEL(pic1,T+(int)(B*sin(Angle)),T-1+(int)(B*cos(Angle)),0) +
```

```
*F_PIXEL(pic1,T+(int)(B*sin(Angle)),T+1+(int)(B*cos(Angle)),0)  +
*F_PIXEL(pic1,T+(int)(B*sin(Angle)),T-2+(int)(B*cos(Angle)),0) +
*F_PIXEL(pic1,T+(int)(B*sin(Angle)),T+2+(int)(B*cos(Angle)),0);

}
if (sum > max){
max=sum; *Angle1 =Angle;
}
if (sum == max){
max= sum;  *Angle1 =( *Angle1+Angle)/2.0;
}
}
*An = ( *An+  *Angle1);
if (verbose==2)
printf(" %5f  is angle  \n", *Angle1 *180/3.14159);
return;
}
```

```
\* Program which finds the peaks in the autocorrelation plane*/

#include "/maps/optics/wjh/include/image.h"
#include "/maps/optics/wjh/include/cio.h"
#include <math.h>

int findpeak1(pict,T,peakfile,X,Y,display,APV,APV1,imshift,verbose,
radius,apvans)
image *pict;
float APV,APV1;
int T,X,Y,display,imshift,verbose,radius,apvans;
FILE *peakfile;
{
int n,m,i,j,N[4],M[4],pos,pos1,pos2;
float amppos=0.0,amppos1=0.0,amppos2=0.0,amp=0.0,amp1=0.0,amp2=0.0
,max[4],MAX=0.0,MAX1=0.0,MAX2=0.0,Nint=0.0,Mint,Cint,Dint,a1,a2,a3
,b1,b2,b3,c1,c2,c3,d1,d2,d3, e1,e2,e3;
if (verbose >2)
printf("Peaks \n");
for ( i=0;i<4;i++){
 max[i]=0.0;
 N[i]=0;
 M[i]=0;
 }
amp=0.0;amp1=0.0;amp2=0.0;
pos=0;pos1=0;pos2=0;
amppos=0.0;amppos1=0.0;
for (n=radius+2;n<T-2;n++){
 MAX= (*F_PIXEL(pict,T+n,T,0)-*F_PIXEL(pict,T+n+1,T,0));
 MAX1= (*F_PIXEL(pict,T,T+n,0)-*F_PIXEL(pict,T,T+n+1,0));
if (( (*F_PIXEL(pict,T+n-1,T,0) - *F_PIXEL(pict,T+n,T,0))< MAX) &&
  ((*F_PIXEL(pict,T+n+1,T,0) - *F_PIXEL(pict,T+n+2,T,0))<MAX))
   if( MAX > amp){
```

```
    amp=MAX;
    pos=n;
   }

if (( (*F_PIXEL(pict,T,T+n-1,0) - *F_PIXEL(pict,T,T+n,0))< MAX1) &&
  ((*F_PIXEL(pict,T,T+n+1,0) - *F_PIXEL(pict,T,T+n+2,0))<MAX1))
   if( MAX1 > amp1){
    amp1=MAX1;
    pos1=n;
   }

if (( *F_PIXEL(pict,T+n,T,0) >*F_PIXEL(pict,T+n+1,T,0)) &&(
*F_PIXEL(pict,T+n,T,0) >*F_PIXEL(pict,T+n-1,T,0)))
   if (*F_PIXEL(pict,T+n,T,0) > amp2){
    amp2= *F_PIXEL(pict,T+n,T,0);
    pos2=n;
 }

/* printf(" %5d %5f \n",n,MAX);*/
 }

/* for (n=(int)(T/2.0);n<(int)(T+T/2.0)+1 ;n++){
  for (m=(int)(T/10.0);m<(int)(9*T/10.0)+1;m++){ */
   for (n=1;n<2*T;n++){
    for (m=1;m<T;m++){
   MAX = *F_PIXEL(pict,n,m,0);
    if ((n-T)*(n-T)+(m-T)*(m-T) >9 )
      if (( *F_PIXEL(pict,n-1,m,0) < MAX ) && (
*F_PIXEL(pict,n+1,m,0) <  MAX))
       if (( *F_PIXEL(pict,n,m-1,0) < MAX ) && (
*F_PIXEL(pict,n,m+1,0) < MAX ))
        if (( *F_PIXEL(pict,n-1,m-1,0) < MAX ) && (
*F_PIXEL(pict,n+1,m+1,0) < MAX ))
         if (( *F_PIXEL(pict,n-1,m+1,0) < MAX ) && (
```

```
*F_PIXEL(pict,n+1,m-1,0) < MAX )){

 if ( MAX > max[3]){
      max[3]= MAX;
      N[3]=n;
       M[3]=m;
      }
 for (i=2;i> -1 ;i--){
 if ( MAX > max[i]){
      max[i+1]=max[i];
      N[i+1]=N[i];
      M[i+1]=M[i];
      max[i]= MAX;
      N[i]=n;
      M[i]=m;
     }
}

   }
 }
}
if (verbose >2)
printf("N1%5d N2%5d M1%5d M2%5d pos%5d \n", N[0],N[1],M[0],M[1],pos);
a1= *F_PIXEL(pict,N[1]-1,M[1],0);
a2= *F_PIXEL(pict,N[1],M[1],0);
a3= *F_PIXEL(pict,N[1]+1,M[1],0);
b1= *F_PIXEL(pict,N[0]-1,M[0],0);
b2= *F_PIXEL(pict,N[0],M[0],0);
b3= *F_PIXEL(pict,N[0]+1,M[0],0);
c1= *F_PIXEL(pict,N[1],M[1]-1,0);
c2= *F_PIXEL(pict,N[1],M[1],0);
c3= *F_PIXEL(pict,N[1],M[1]+1,0);
d1= *F_PIXEL(pict,N[0],M[0]-1,0);
d2= *F_PIXEL(pict,N[0],M[0],0);
```

```
d3= *F_PIXEL(pict,N[0],M[0]+1,0);
e1= *F_PIXEL(pict,T+pos-1,T,0)- *F_PIXEL(pict,T+pos,T,0);
e2= *F_PIXEL(pict,T+pos,T,0)- *F_PIXEL(pict,T+pos+1,T,0);
e3= *F_PIXEL(pict,T+pos+1,T,0)-  *F_PIXEL(pict,T+pos+2,T,0);

Nint= N[1]+ (a1-a3)/(2*a1-4*a2+2*a3);
Mint= N[0]+ (b1-b3)/(2*b1-4*b2+2*b3);
Cint= M[1]+ (c1-c3)/(2*c1-4*c2+2*c3);
Dint= M[0]+ (d1-d3)/(2*d1-4*d2+2*d3);

amppos=pos+0.5+(e1-e3)/(2.0*e1-4.0*e2+2.0*e3);
e1= *F_PIXEL(pict,T,T+pos1-1,0)- *F_PIXEL(pict,T,T+pos1,0);
e2= *F_PIXEL(pict,T,T+pos1,0)- *F_PIXEL(pict,T,T+pos1+1,0);
e3= *F_PIXEL(pict,T,T+pos1+1,0)-  *F_PIXEL(pict,T,T+pos1+2,0);
amppos1=pos1+0.5+(e1-e3)/(2.0*e1-4.0*e2+2.0*e3);
e1= *F_PIXEL(pict,T+pos2-1,T,0);
e2= *F_PIXEL(pict,T+pos2,T,0);
e3= *F_PIXEL(pict,T+pos2+1,T,0);
amppos2=pos2+(e1-e3)/(2.0*e1-4.0*e2+2.0*e3);

if (verbose >0)
printf("derp1 %7g derp2 %7g peak %7g p1 %5d p2 %5d p3 %5d\n"
                        , amppos, amppos1,amppos2, pos,pos1,pos2);
printf(" %5d %5d peak=( %5g %5g)  PS= %7g  inline peak=%5g
                                                  inlineder=%5f\n"
,X,Y, Mint-T,Dint-T+imshift,APV,amppos2,amppos1);
if (verbose >1)
 printf(" %5g %5g %7g \n", Nint-T,Cint-T, max[1]);

 if (display == 4){
if(apvans==3)
 fprintf(peakfile,"  %5f %5f     %7f  %7f %7f \n", (1.0*X),
1.0*Y, 1.0*Mint-1.0*T,Dint-1.0*T+imshift,amppos2) ;
else
```

```
fprintf(peakfile,"  %5f %5f      %7f  %7f %7f \n", (1.0*X),
1.0*Y, 1.0*Mint-1.0*T,Dint-1.0*T+imshift,APV) ;
}
return;
}
```

```
\*program which outputs image in a style recognisable by unigraph*/

#include "/maps/optics/wjh/include/image.h"
#include "/maps/optics/wjh/include/cio.h"
#include <math.h>

int im_pgm(pict,optr,T)
image *pict;
FILE *optr;
int T;
{
int n,m;
 for (n=0;n<X_SIZE(pict);n++){
 for (m=0;m<Y_SIZE(pict);m++){
  fprintf(optr," %d %d %f\n",n,m,( *F_PIXEL(pict,n,m,0)));
 }
}

return;
}
```

```
\* Program to generate the simulated images *?

#include "/maps/optics/wjh/include/image.h"
#include "/maps/optics/wjh/include/cio.h"
#include <math.h>

#define M1 259200
#define IA1 7141
#define IC1 54773
#define RM1 (1.0/M1)
#define M2 134456
#define IA2 8121
#define IC2 28411
#define RM2 (1.0/M2)
#define M3 243000
#define IA3 4561
#define IC3 51349

#define MBIG 1000000000
#define MSEED 161803398
#define MZ 0
#define FAC (1.0/MBIG)

main()

{
float ran1(),ran3();
static image bigpic,imagepic;
int i,j,n,m,N,x,y,Noimages,Xsize,Ysize,X1,halowidth;
float Y1,vis,tempran, halow;
FILE *outfile, *infile, *Fillfile;
halowidth=intin("halowidth*1000",1000,0,100000);
halow= halowidth/1000.0;
```

```
Xsize=intin("xsize of pic",100,90,2000);
Ysize=intin("Ysize of pic",100,90,2000);
X1=intin("Start position of cosine",200,0,1000);
im_alloc(&bigpic,Xsize,Ysize,1,FLOAT);
im_zero(&bigpic);
Noimages=intin("No of images",1,0,4);
N=intin("no of points",1000,0,100000);
outfile=openit("filename of output","Art.pgm","wb");
im_alloc(&imagepic,50,50,1,FLOAT);
im_zero(&imagepic);
/* printf("filled image \n"); */
Y1=901.0;/* Y1=451.0;*/
for (n=0;n<N;n++){
x=50;
y=30;
x=(int)(80+(Xsize-160.0)*ran1(y)+0.5);
y=(int)(80+(Ysize-160.0)*ran3(x)+0.5);
tempran=ran1(x);
vis=tempran*20;
/*printf("filled image \n");*/
fillpoints(&bigpic,&imagepic,x,y,Noimages,Y1,vis,X1,halow);
}
 for (n=0;n<X_SIZE(&bigpic);n++){
   for (m=0;m<Y_SIZE(&bigpic);m++){
*F_PIXEL(&bigpic,n,m,0)= *F_PIXEL(&bigpic,n,m,0)+(0.25*ran3(x));
   }
  }
printf("found maxima \n");
im_stats(&bigpic);
im_wpgm(&bigpic,0,outfile);
}
```

```
\*Subroutine to create images */


int fillpoints(picture,imagepic,x,y,Noimages,Y1,vis,X1,halow)
image *picture, *imagepic;
int x, y,Noimages,X1 ;
float Y1,vis,halow;
{

int n,m,i,j,k,X,Y,N,M;
float am,AN,U,V,AM1,AM2,B=0.02831,lambda=8000.0;
X= x+X1;
Y= y;
for (M=0;M<Noimages;M++){

am= 8.0*cos(6.2832*X/lambda)/*(1-(Y1-Y)*(Y1-Y)/(2.0*Y1*Y1))*/;
/* printf("N= %5d \n",N);*/
printf("filled image %5d %5f \n",M,am);

for (i=0;i<X_SIZE(imagepic);i++){
  for (j=0;j<Y_SIZE(imagepic);j++){
/* printf("filled image %5d %5d \n",i,j);*/
if ((i-25)<0)
    *F_PIXEL(imagepic,i,j,0) = 255 *j0(3.14159*((1*am)*(25-i)/25.0))
 *exp(-3.14159*((i-25)*(i-25)+(j-25)*(j-25))/(2500.0*halow))  ;
else
   *F_PIXEL(imagepic,i,j,0) = 255 *j0(3.14159*((1*am)*(i-25)/25.0))
 *exp(-3.14159*((i-25)*(i-25)+(j-25)*(j-25))/(2500.0*halow))  ;
   }
}
/* printf("filled image \n");*/
im_stats(imagepic);/*
im_xv(imagepic,0);*/
```

```
im_toc('R');
im_convert(imagepic,COMPLEX);
im_fourier(imagepic);
im_fromc('r');
im_convert(imagepic,FLOAT);
im_stats(imagepic);
/*im_xv(imagepic,0);*/
/*printf("filled image \n");*/

  for (n=0;n<X_SIZE(imagepic);n++){
    for (m=0;m<Y_SIZE(imagepic);m++){
    *F_PIXEL(picture,X-X1+n-25,Y+m-25,0) +=
            ( *F_PIXEL(imagepic,n,m,0)*2*vis/((am+1)*1.0));
}
}
/*printf("filled image \n");*/
U=20*(1-3*(Y1-Y)*(Y1-Y)/(Y1*Y1))*sin(2*6.2832/lambda *X);
V=40.0/lambda *6.2832 *(Y1-Y)*(1-(Y1-Y)*(Y1-Y)/(Y1*Y1))
                                *cos(2*6.2832/lambda *X);
if (U<0)
   X= X+(int)(U-0.5);
else
   X= X+(int)(U+0.5);
if (V<0)
   Y=Y+(int)(V-0.5);
else
   Y=Y+(int)(V+0.5);

}
return;
}
```

```
\*Random number generator 1*/

float ran1(idum)
int idum;

{
static long ix1,ix2,ix3;
static float r[98];
float temp;
static int iff=0;
int j;

if (idum < 0 || iff == 0) {
iff=1;
ix1=(IC1-(idum)) % M1;
ix1=(IA1*ix1+IC1) % M1;
ix2=ix1 % M2;
ix1=(IA1*ix1+IC1) % M1;
ix3=ix1 % M3;
for (j=1;j<=97;j++) {
ix1=(IA1*ix1+IC1) % M1;
ix2=(IA2*ix2+IC2) % M2;
r[j]=(ix1+ix2*RM2)*RM1;
}
idum = 1;
}
ix1=(IA1*ix1+IC1) % M1;
ix2=(IA2*ix2+IC2) % M2;
ix3=(IA3*ix3+IC3) % M3;
j=1 + ((97*ix3)/M3);
if (j > 97 || j < 1)
fprintf(stderr,"RAN1: This cannot happen.");
temp=r[j];
```

```
r[j]=(ix1+ix2*RM2)*RM1;
return temp;
}
```

```
\*Random number generator 2*/

float ran3(idum)
int idum;

{
static int inext,inextp;
static long ma[56];
static int iff=0;
float test;
long mj,mk;
int i,ii,k;

if (idum <0 || iff == 0)
{
iff=1;
mj=MSEED-(idum < 0 ? -idum : idum);
mj %= MBIG;
ma[55]=mj;
mk=1;
for (i=1;i<=54;i++)
{
ii=(21*i) % 55;
ma[ii]=mk;
mk=mj-mk;
if (mk < MZ) mk += MBIG;
mj=ma[ii];
}
for (k=1;k <= 4;k++)
for (i=1;i<=55;i++)
{
ma[i] -= ma[1+(i+30) % 55];
if (ma[i] < MZ) ma[i] +=MBIG;
```

```
}
inext=0;
inextp=31;
idum=1;
}

if (++inext == 56) inext=1;
if (++inextp == 56) inextp=1;
mj=ma[inext] - ma[inextp];

if (mj < MZ) mj += MBIG;
ma[inext]=mj;
return mj*FAC;
}
/* printf("%ld\n",mj); */
/* printf("place, end: %f\n",mj*FAC); */
/* printf ("ran3 %f\n",test); */
```

Meas. Sci. Technol. 4 (1993) 157–164. Printed in the UK

Acoustic measurements in flows using photon correlation spectroscopy

D Hann and C A Greated

The Department of Physics, The University of Edinburgh, James Clerk Maxwell Building, The King's Buildings, Edinburgh EH9 3JZ, UK

Received 22 May 1993, in final form 16 September 1993, accepted for publication 18 October 1993

Abstract. Laser doppler anemometry using the photon correlation method of signal processing has been used to measure a velocity field in which sinusoidal fluctuations generated acoustically are superimposed on a steady flow. A stochastic model has been developed for the form of the correlation function, and it is shown to be consistent with previous models for a steady flow and for sinusoidal fluctuations in an acoustic field. Measurements have been made of the velocity field associated with steady flow in a tube with a superimposed acoustic field, the results were shown to be consistent with the theoretical predictions.

1. Introduction

The standard method of measuring acoustic fields in pipes is by using pressure gradient microphones and Rayleigh discs. Both of these methods require calibrations [12], due to the fact that they will affect the flow by their introduction, which are difficult and the behaviour of the Rayleigh disc especially requires a number of assumptions [1, 2]. These methods are unacceptable when we have a flow present as well. Hot wire anemometers have been used to measure the flow velocity in this case, but these too require calibration, and will affect the flow by their introduction. Since there are many cases in which a mean flow field and an acoustic field are present, and it is known that a flow will interact with an acoustic field [14], a non-intrusive method of measuring the flow and acoustic field would be very advantageous. Laser doppler anemometry has been used successfully to measure the absolute acoustic particle velocity in a sinusoidal acoustic field [3, 5, 8, 11, 15] using both frequency analysis and the photon correlation method. There is also an approximation for the form of the correlation function for a steady flow with a sinusoidal component superimposed, but the theory makes the assumption that the sinusoidal component is of a much smaller magnitude than the steady flow [6].

Here we will develop a more general stochastic model for the form of the correlation function when there is a sinusoidal vibration superimposed on a steady flow which does not make the assumption that the flow velocity is larger than the absolute acoustic particle velocity. This model is a more general case of the stochastic model for a sinusoidal acoustic field developed by Sharpe and Greated [8] and contains this as a special case.

The theory was tested by comparing the results with that of a simple experiment to show that the experimental results fitted the theoretical curve for the cases of flow velocity greater than acoustic particle velocity, and for flow velocity smaller than acoustic particle velocity. The experiment also compared the acoustic particle velocity in the tube before and after the flow was introduced, and it is shown that the flow does change the acoustic particle velocity.

2. Theory of the method

The notation used throughout this paper is similar to that used by Durrani and Greated [16, section 3.3] and Sharpe and Greated [9]. It will be assumed that the differential Doppler set-up with Gaussian crossed beams forming the observation volume is used. The results presented here apply equally well if a coherent detection arrangement is used, as described in [16], provided that the intensity profiles of both illuminating and reference beams are Gaussian. It was also assumed that the seeding particles (either smoke particles or dust particles naturally present in air) faithfully follow the flow; this is valid for frequencies up to 1 kHz if the particles are smaller than 1 μm [13]. The fringe spacing in the observation volume is given by

$$d = \frac{\lambda}{2 \sin \theta}. \tag{1}$$

λ is the laser light wavelength and θ is the half-angle between the beams. Then the output from the detector

0957-0233/93/020157+08$07.50

associated with any pth particle in the observation volume is given by

$$x_p(t) = \kappa K_p W(\beta\xi_p(t))(M + \cos D\xi_p(t)). \quad (2)$$

κ is a constant associated with the optical power and detector sensitivity, K_p characterizes the particle scattering cross section, M is a constant introduced if the beams are not of equal strength and $\xi_p(t)$ is the particle position at time t.

The total output is then given by equation (3) where D is the so-called frequency-to-velocity conversion factor, which relates the Doppler frequency to the particle speed and beam intersection angle, which is defined in equation (4) and $W(\beta\xi_p(t))$ is the spatial weighting function, which represents the envelope on the fringes due to the Gaussian cross section of the laser beams (equation (5)):

$$x(t) = \kappa \sum_p K_p W(\beta\xi_p(t))(M + \cos D\xi_p(t)) \quad (3)$$

$$D = \omega_0 U = \frac{4\pi \sin\theta}{\lambda} \quad (4)$$

$$W(\beta\xi_p(t)) = \exp(-\beta^2\xi_p^2(t)) \quad (5)$$

where

$$\beta = \frac{\cos\theta}{r_0}.$$

Here r_0 is the radius at the e^{-2} intensity points of the beam waist. This is of the order of 0.1 mm, and can be compared to the fringe spacing used, which is of the order of 4 μm . For the 675 Hz standing wave at 129.77 dB as in the experimental set-up, the amplitude of the oscillation is of the order of 20 μm, so the oscillating particle passes through many fringes in one cycle.

In equation (3) the low-frequency term has been retained; this can be filtered out since it is not necessary, but for this derivation shall retain it.

To determine the autocorrelation function for $x(t)$ we write ξ_p as the initial particle position (at time $t = 0$) and ζ_p as its position at time τ later

$$\zeta_p = \xi_p + \int_0^\tau v_p(z)\,dz = \xi_p + \eta_p(\tau). \quad (6)$$

Here $v_p(z)$ is the instantaneous velocity of the pth particle, which in this case is

$$v_p(z) = a_0 + a_m \sin(\omega_m z + \psi). \quad (7)$$

Here a_0 is the mean flow velocity, a_m is the particle velocity amplitude of the sound field, ω_m is the sound frequency and ψ is a random phase. We are interested in recovering the velocity amplitude a_m and the mean flow velocity a_0.

The velocity amplitude (or acoustic particle velocity) is an important parameter in the sound field since it is possible to define the sound pressure level solely in terms of the velocity amplitude for sound fields in which the acoustic impedence is known. The sound pressure level is defined in equation (8) where pressure and velocity amplitude are related by the characteristic impedance Z_a, which is generally complex:

$$\mathrm{SPL} = 10 \log \frac{p_{\mathrm{rms}} u_{\mathrm{rms}}}{p_0 u_0} \quad (8)$$

$$\frac{p_{\mathrm{rms}}}{u_{\mathrm{rms}}} = Z_a.$$

For standing waves, which is the case here, the pressure and velocity fluctuations are $\pi/2$ out of phase so $Z_a = iz_a$ is purely imaginary. To be properly defined, we would need to know all three components of the flow and sound field, but in the case we are using here, the flow and sound field are along the axis of the tube and do not have any other components. This means that only the component in the direction of the axis of the tube needs to be measured so it is not necessary to have a two component system to find the intensity vector.

It can be seen from the above arguments that p_{rms} can be expressed in terms of the velocity fluctuations and the characteristic impedance. If we note that $p_0 u_0 = 10^{-12}$ W, which is the threshold of hearing for the ear, then the SPL is

$$\mathrm{SPL} = 10 \log \frac{a_m^2 z_a}{2} \times 10^{12}$$

$$= 20 \log \frac{a_m \sqrt{z_a}}{\sqrt{2}} + 120. \quad (9)$$

In cases where the phase of the characteristic impedance is not known, it is possible to use a combination of measurement of the acoustic particle velocity using LDA and measurement of the pressure using a miniature or probe microphone to determine its phase [10].

Following the derivation of Durrani and Greated [16, section 3.3] in which it was assumed that ζ and ξ are independent random variables, since the position of a particle depends only on its own previous position and its instantaneous velocity (we assume that there are no collisions in the measuring volume) we find that the autocorrelation function of the output voltage of the photomultiplier is

$$R(\tau) = E[x(t)x(t+\tau)]$$
$$= \left[\kappa C_0 g_0 \int_{-\infty}^{\infty} W(\beta y)(M + \cos Dy)\,dy\right]^2$$
$$+ \frac{\kappa^2 C_1 g_0}{2} \int_{-\infty}^{\infty} p_\eta(y;\tau) R_w(\beta y)(M + \cos Dy)\,dy \quad (10)$$

where $E[\,]$ is the expectation operator, $C_0 = E[K_p]$, $C_1 = E[K_p^2]$, g_0 is the average number of particles per unit length of the measuring volume and $R_w(\beta y)$ is the autocorrelation of the spatial weighting function of a Gaussian beam system, given by

$$R_w(\beta y) = \left(\frac{\pi}{2\beta^2}\right)^{1/2} \exp\left(-\frac{\beta^2 y^2}{2}\right).$$

Here $p_\eta(y;t)$ is the probability density function of the variable $\eta(t)$ which must be determined in order to evaluate the autocorrelation function. This is done below, but first we note that the first term in equation (10) is the square of the mean value of the Doppler signal. This will be ignored since it is time-independent and so will only contribute a constant or pedestal to the correlation function.

From equations (6) and (7) we have

$$\eta_p(\tau) = a_0\tau + a_m \int_0^\tau \sin(\omega_m z + \psi)\,dz$$
$$= a_0\tau + \frac{2a_m}{\omega_m}\left[\sin\left(\frac{\omega_m\tau}{2}\right)\sin\left(\frac{\omega_m\tau}{2} + \psi\right)\right] \qquad (11)$$

where ψ is a random variable uniformly distributed over the interval 0–2π:

$$p(\psi) = \frac{1}{2\pi} \qquad 0 < \psi < \frac{1}{2\pi}.$$

We can use the relationship for a function of random variables to obtain

$$p_\eta(y;\tau) = \frac{1}{\pi[A_m^2 - (y - a_0\tau)^2]^{1/2}}$$
$$-y + a_0\tau \leqslant A_m \leqslant y - a_0\tau$$

$$A_m = \frac{2a_m}{\omega_m}\sin\left(\frac{\omega_m\tau}{2}\right).$$

If we ignore the constant term then equation (10) takes the form

$$R(\tau) = \left(\frac{\pi\kappa^4 C_1^2 g_0^2}{8\beta^2}\right)^{1/2} \int_{a_0\tau - A_m}^{a_0\tau + A_m} \frac{dy}{\pi[A_m^2 - (y - a_0\tau)^2]^{1/2}}$$
$$\times \exp\left(\frac{-\beta^2 y^2}{2}\right)(M + \cos Dy).$$

If we proceed to evaluate by substitution of $y = a_0\tau + A_m$ and solve (see appendix), we get

$$R(\tau) = \frac{\kappa^2 c_1 g_0}{2}\left(\frac{\pi}{2\beta^2}\right)^{1/2}\exp\left(-\frac{\beta^2 A_m^2}{4}\right)$$
$$\times \exp\left(-\frac{\beta^2 a_0^2\tau^2}{2}\right)$$

$$M * \left\{ I_0\left(\frac{\beta^2 A_m^2}{4}\right) I_0(\beta^2 A_m a_0\tau) \right.$$
$$\left. + 2\sum_{n=1}^{\infty}(-1)^n I_n\left(\frac{\beta^2 A_m^2}{4}\right) I_{2n}(\beta^2 A_m a_0\tau)\right\}$$
$$+ I_0\left(\frac{\beta^2 A_m^2}{4}\right)\cos(Da_0\tau) J_0[A_m(D^2 - \beta^4 a_0^2\tau^2)^{1/2}]$$
$$+ 2\cos(Da_0\tau)\sum_{k=1}^{\infty} J_{2k}(DA_m)$$
$$\times \sum_{n=1}^{\infty} I_n\left(\frac{\beta^2 A_m^2}{4}\right)(-1)^{n-k} I_{2(n-k)}(\beta^2 A_m a_0\tau)$$
$$+ 2\cos(Da_0\tau)\sum_{k=1}^{\infty} J_{2k}(DA_m)$$
$$\times \sum_{n=1}^{\infty} I_n\left(\frac{\beta^2 A_m^2}{4}\right)(-1)^{n+k} I_{2(n+k)}(\beta^2 A_m a_0\tau)$$
$$- 2\sin(Da_0\tau)\sum_{k=0}^{\infty} J_{2k+1}(DA_m)$$
$$\times \sum_{n=1}^{\infty} I_n\left(\frac{\beta^2 A_m^2}{4}\right) I_{2n+2k+1}(\beta^2 a_0 A_m\tau)$$
$$- 2\sin(Da_0\tau)\sum_{k=0}^{\infty} J_{2k+1}(DA_m)$$
$$\times \sum_{n=1}^{\infty} I_n\left(\frac{\beta^2 A_m^2}{4}\right) I_{2n-2k+1}(\beta^2 a_0 A_m\tau). \qquad (13)$$

This is the full expression for the time-dependent part of the autocorrelation function. From this three important limiting cases can be seen.

If we consider a situation with zero mean flow, that is $a_0 = 0$, then the expression becomes

$$R(\tau) = \frac{\kappa^2 c_1 g_0}{2}\left(\frac{\pi}{2\beta^2}\right)^{1/2}\exp\left(-\frac{\beta^2 A_m^2}{4}\right)$$
$$\times\left[I_0\left(\frac{\beta^2 A_m^2}{4}\right)[M + J_0(DA_m)]\right.$$
$$\left. + 2\sum_{k=1}^{\infty} I_k\left(\frac{\beta^2 A_m^2}{4}\right) J_{2k}(DA_m)\right]. \qquad (14)$$

This is exactly the expression calculated by Sharpe and Greated [9] for a periodic acoustic field. The equation can be simplified by taking typical values of β and a_m . For example, for a laser beam of unfocused e^{-1} width 0.5 mm focused from 2 cm separation using a 20 cm focal length lens, β takes the value 25 000. If this is put into equation (14) and we consider the behaviour of $e^{-x} I_n(x)$ [4] for small values of x, this approximates to

$$R(\tau) \propto J_0(DA_m).$$

This can further be simplified to

$$R(\tau) \propto J_0(Da_m\tau). \qquad (15)$$

Since we generally are concerned with cases where $\omega_m\tau$ is small we can approximate

$$A_m = \frac{2a_m}{\omega_m}\sin\left(\frac{\omega_m\tau}{2}\right) \approx a_m\tau.$$

If there is no acoustic field present, that is $a_m = 0$,then the equation (12) becomes

$$R(\tau) = \frac{\kappa^2 C_1 g_0}{2}\left(\frac{\pi}{2\beta^2}\right)^{1/2}\exp\left(-\frac{\beta^2 a_0^2\tau^2}{2}\right)$$
$$\times [M + \cos(Da_0\tau)]. \qquad (16)$$

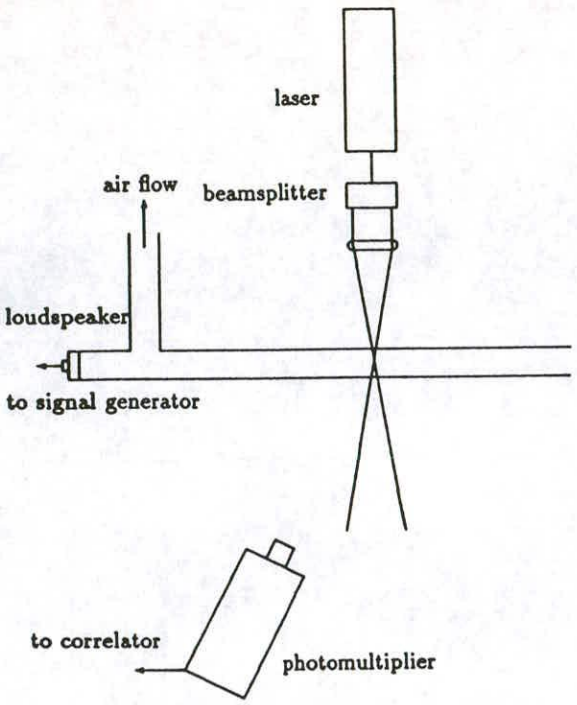

Figure 1. A schematic diagram of the laser Doppler anemometry arrangement.

This is an expression for non-turbulent flow [7, 16].

If we now consider a combined flow with typical magnitudes for β, a_m and a_0 then again the expression can be simplified. If we consider the behaviour of $e^{-x}I_n(x)$ for small values of x [4] and note the $\omega_m\tau$ is also small we can show that the correlation function $R(\tau)$ approximates to

$$\frac{\kappa^2 C_1 g_0}{2}\left(\frac{\pi}{2\beta^2}\right)^{1/2}\exp\left(-\frac{\beta^2\tau^2(a_0^2+a_m^2/2)}{2}\right)\times\{M+\cos(Da_0\tau)J_0(a_m\tau(D^2-\beta^4a_0^2\tau^2)^{1/2}]\}. \tag{17}$$

Interaction of the $J_0()$ term and the cosine will produce beats in the correlation function and it is from these beats that the measurements are taken.

3. Experimental apparatus

The validity of equation (17) was tested in a series of experiments in which a flow and sound field could be introduced into a glass tube both separately and at the same time. The correlation functions for the cases of flow field only, sound field only and combined fields were measured and compared. A schematic diagram of the apparatus is shown in figure 1. The working area was a glass tube of length 70 cm, diameter 2.5 cm, which had a loudspeaker fitted at one end. The tube had a side branch close to the loudspeaker, to which a fan was connected. A standing wave of frequency 675 Hz was set up in the tube and the fan was used to produce a flow simultaneously.

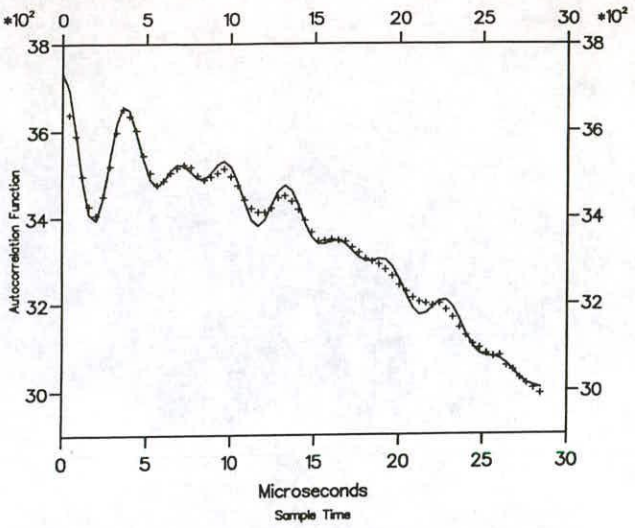

Figure 2. Theoretical and experimental autocorrelation functions for combined flow. Flow velocity 0.9684 m s^{-1}, amplitude of fluctuations 0.190 m s^{-1}.

For the optical measuring system, a 15 mW He–Ne laser was used as the light source, its beam being split into two parallel components 26 mm apart, which were then focused into the tube by a lens of focal length 153 mm. The positioning of the crossover point of the beams was important since the amplitude of the velocity fluctuations was larger at a velocity antinode and zero at a velocity node. So the crossover point of the beams was positioned at the centre of the tube at a velocity antinode, which was detected using a probe microphone. The photomultiplier was aligned at an angle of approximately 25° to the optical axis and focused on the crossover point. The digital signal was then processed to give the photon correlation function. Two cases were looked at, one where the acoustic particle velocity was smaller than the flow velocity and one where it was larger than the flow velocity. In the first case the flow velocity and acoustic particle velocity were measured separately and these values compared with values obtained when the flow and sound field were combined.

4. Results and discussion

The values of the velocities were ascertained from the positions of the peaks and zeros of the correlograms and these values were used in the theoretical equation to generate a correlogram, which was then compared with the experimental correlogram.

The flow velocities of figures 2 and 4 were found by measuring the time τ between peaks and using equation (16). We can see that $a_0 = 2n\pi/(D\tau)$ where n is the number of the peak from the centre. The acoustic particle velocity can be worked out in a similar way; from equation (14) $a_m = 7.0157/(D\tau)$ where the time τ measured here is the time to the first peak of the correlation function.

In the case of the combined flow and sound field, it is necessary to know which of the two velocities are

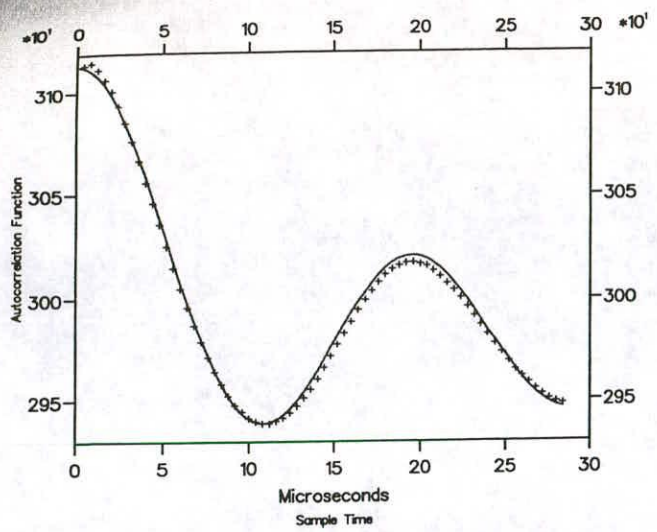

Figure 3. Theoretical and experimental autocorrelation functions for sound field only. Amplitude of fluctuations 0.210 m s^{-1}.

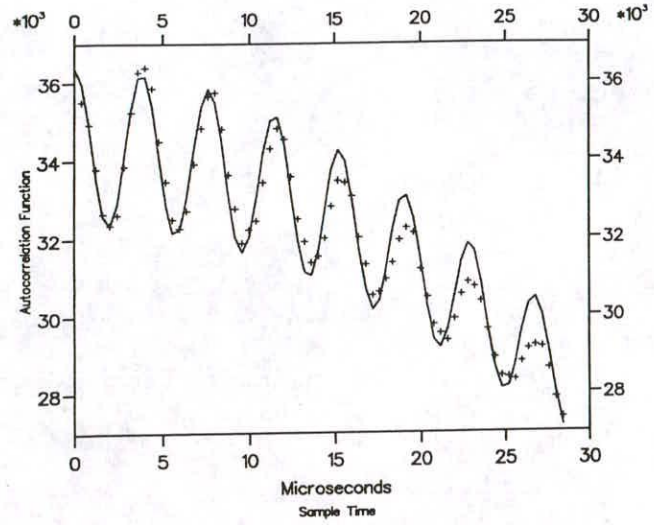

Figure 4. Theoretical and experimental autocorrelation functions for flow field only. Flow velocity 0.9684 m s^{-1}.

larger. In figure 2 the flow velocity is the larger and the time to the nth peak can be used to calculate the flow velocity as before and time to the first zero is used to find the acoustic particle velocity. In figure 5, the acoustic particle velocity is larger, and so the time to the first zero is used to find the flow velocity and the time to the first peak for the acoustic particle velocity.

These results are shown in figures 2–5. The acoustic particle velocity was then used in equation (9) to calculate the intensity of the sound field. If we note that the characteristic impedance of air at room temperature is 430 kg m^{-2} s^{-1}, then the SPL for each case is 128.90 dB in the combined field, 129.77 dB in the sound field only and 135.45 dB in the second combined field.

Figures 2–4 show respectively the combined fields, the sound field without the flow in the pipe and the flow without the sound field. Figure 5 shows a case in which the flow velocity is of a much smaller magnitude than the acoustic particle velocity so that the instantaneous velocity is sometimes negative. Three things can be

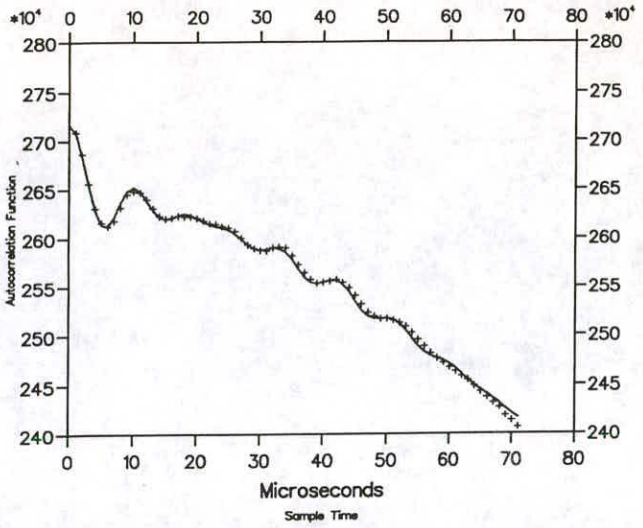

Figure 5. Theoretical and experimental autocorrelation functions for combined field. Flow velocity 0.0421 m s^{-1}, amplitude of fluctuations 0.4039 m s^{-1}.

seen from these figures.

Firstly, the theoretical results fit well with the experimental results. However, in figures 2 and 4 the measured damping of the curve is somewhat greater than that predicted by theory. This is no doubt due to the presence of turbulence, which would have the effect of introducing an extra exponential damping term. This is verified in the case of figure 5, where the flow velocity was of a smaller magnitude than for that of figure 2 and there was less turbulence in the tube, and the theoretical results fit the experimental results much better. Introducing such a term for turbulence into the theoretical expression would produce an even closer fit, but the effect of such a damping term will not significantly alter the position of the peaks and zeros of the function, which are the measures being used.

Secondly, the agreement between theory and experiment is equally good in two extreme cases. The first graph is for a larger flow velocity than acoustic particle velocity. Figure 5 is for a much smaller flow velocity than acoustic particle velocity. Thus the theory is not constrained to the case where the flow velocity is larger than the acoustic particle velocity and indeed the instantaneous velocity can be negative.

Thirdly, the values obtained for the acoustic particle velocity for the combined fields and for the case where the sound field was measured separately are not the same. In the combined field the acoustic particle velocity is less than in the sound field only case. This could be because the acoustic particle velocity in the sound field only case was measured at the velocity antinode (or pressure node), which was found using a probe microphone. When the flow was introduced into the tube it would cause a low-pressure area where it sucked the air out moving the standing wave along the tube. This would mean that we were no longer measuring at the point of highest acoustic particle velocity, but slightly along from it, where the amplitude is less.

5. Conclusions

These results show that the laser Doppler photon correlation technique can indeed be used to measure absolute flow velocities and acoustic particle velocities simultaneously over a wide range of flow velocities and acoustic particle velocities. The results presented do not show the limits of the technique and further work will have to be done to investigate the range of reliable operation.

Appendix

We proceed to evaluate by substituting $y = a_0\tau + A_m \sin\alpha$ so that the integral becomes that in equation (18),

$$R(\tau) = \int_{-\pi/2}^{\pi/2} \frac{d\alpha}{\pi} \exp\left(\frac{-\beta^2(a_0\tau + A_m \sin\alpha)^2}{2}\right) \times [M + \cos(Da_0\tau + DA_m \sin\alpha)]. \quad (18)$$

The cosine can be expanded to form the autocorrelation function shown in equation (19),

$$R(\tau) = \frac{1}{\pi} \exp\left(\frac{\beta^2 a_0^2 \tau^2}{2}\right) \int_{-\pi/2}^{\pi/2} \exp(-\beta^2 a_0 \tau A_m \sin\alpha) \times \exp\left(-\frac{\beta^2 A_m^2 \sin^2\alpha}{2}\right) [M + \cos(Da_0\tau) \times \cos(DA_m \sin\alpha) - \sin(Da_0\tau)\sin(DA_m \sin\alpha)]\, d\alpha. \quad (19)$$

We can now split this into three parts and make the two following substitutions to form equation (20)–(23):

$$p = \beta^2 a_0 \tau A_m$$

$$q = \beta^2 A_m^2/4$$

$$R(\tau) = \frac{\kappa^2 C_1 g_0}{2}\left(\frac{\pi}{2\beta^2}\right)^{1/2} \times \exp\left(-\frac{\beta^2 a_0^2 \tau^2}{2}\right)(F_1 + F_2 + F_3) \quad (20)$$

$$F_1 = \frac{1}{\pi}\cos(Da_0\tau) \int_{-\pi/2}^{\pi/2} \times \exp(-p\sin\alpha)\exp(-2q\sin^2\alpha)\, d\alpha \quad (21)$$

$$F_2 = \frac{1}{\pi}\cos(Da_0\tau) \int_{-\pi/2}^{\pi/2} \exp(-p\sin\alpha) \times \exp(-2q\sin^2\alpha)\cos(DA_m\sin\alpha)\, d\alpha \quad (22)$$

$$F_3 = -\frac{1}{\pi}\sin(Da_0\tau) \int_{-\pi/2}^{\pi/2} \exp(-p\sin\alpha) \times \exp(-2q\sin^2\alpha)\sin(DA_m\sin\alpha)\, d\alpha. \quad (23)$$

Now the integrals F_1,F_2 and F_3 in equations (21)–(23) are evaluated and combined to produce the final autocorrelation function.

First we evaluate F_1 by applying the double angle formula to give equation (24):

$$F_1 = \frac{1}{\pi}\exp(-q) \int_{-\pi/2}^{\pi/2} \exp(-p\sin\alpha)\exp(q\cos 2\alpha)\, d\alpha. \quad (24)$$

It can be shown from the generating function of the modified Bessel function [4] that the following equation is true.

$$\exp(x\cos 2\alpha) = I_0(x) + 2\sum_{n=1}^{\infty} I_n(x)\cos 2n\alpha.$$

If this is substituted into equation (24) and the other exponential split into a cosh and sinh then

$$F_1 = \frac{1}{\pi}\exp(-q)x \int_{-\pi/2}^{\pi/2} [\cosh(p\sin\alpha) - \sinh(p\sin\alpha)] \times \left(I_0(q) + 2\sum_{n=1}^{\infty} I_n(q)\cos 2n\alpha\right) d\alpha.$$

If we note that the sinh term is odd and disappears, and that equation (25) is true, then we find that the solution of F_1 is given by equation (26):

$$\int_0^{\pi/2} \cosh(p\sin\alpha)\cos(2n\alpha)\, d\alpha = (-1)^n \frac{\pi}{2} I_{2n}(p) \quad (25)$$

$$F_1 = \exp(-q)\left(I_0(p)I_0(q) + 2\sum_{n=1}^{\infty}(-1)^n I_n(q) I_{2n}(p)\right). \quad (26)$$

Turning to F_2, we utilize the double-angle formula again and also the Bessel function expansion for a cosine with a sinusoidal argument to obtain the following equation for F_1.

$$F_2 = \frac{1}{\pi}\exp(-q)\cos(Da_0\tau) \times \int_{-\pi/2}^{\pi/2} \exp(-p\sin\alpha)\exp(q\cos 2\alpha) \times \left(J_0(DA_m) + 2\sum_{k=1}^{\infty} J_{2k}(DA_m)\cos(2k\alpha)\right) d\alpha$$

$$= \frac{1}{\pi}\exp(-q)\cos(Da_0\tau) \times \left(J_0(DA_m)F_1 + 2\sum_{k=1}^{\infty} J_{2k}(DA_m)F_4\right) \quad (27)$$

Here we have defined F_4 as shown in equation (28):

$$F_4 = \int_{-\pi/2}^{\pi/2} \exp(-p\sin\alpha)\exp(q\cos 2\alpha)\cos(2k\alpha)\, d\alpha. \quad (28)$$

As in the evaluation of F_1 we expand the second exponential in terms of the modified Bessel function and then we expand the first in terms of cosh and sinh. The integral containing the sinh term is zero when evaluated between these limits so we ignore it. This means that equation (28) can be rewritten as follows:

$$F_4 = 2\int_0^{\pi/2} \cosh(p\sin\alpha)\cos(2k\alpha)I_0(q)\,d\alpha + 4\sum_{m=1}^{\infty} I_m(q)\int_0^{\pi/2} \cosh(p\sin\alpha) \times \cos(2k\alpha)\cos(2m\alpha)\,d\alpha.$$

The two cosines in the second term can be made into the sum of two cosines, so the second term can be rewritten.

$$2\sum_{m=1}^{\infty} I_m(q)\int_0^{\pi/2} \cosh(p\sin\alpha)\{\cos[2(m-k)] + \cos[2(m+k)]\}\,d\alpha.$$

Using equation (25) again, we find that F_4 equals

$$\pi I_0(q)(-1)^k I_{2k}(p) + \sum_{m=1}^{\infty} I_m(q) \times [(-1)^{m-k} I_{2(m-k)}(p) + (-1)^{m+k} I_{2(m+k)}(p)]. \quad (29)$$

To evaluate F_3 we start by expanding the first exponential in terms of cosh and sinh and use the double angle formula on the second exponential and expand it into a series containing modified Bessel functions. The sin term can be expanded as in the following equation:

$$\sin(DA_m\sin\alpha) = 2\sum_{s=0}^{\infty} J_{2s+1}(DA_m)\sin[(2s+1)\alpha]. \quad (30)$$

Since the term containing cosh is odd, it is ignored, leaving equation (31):

$$F_3 = -\frac{2}{\pi}\exp(-q)\sin(Da_0\tau)\sum_{s=0}^{\infty} J_{2s+1}(DA_m) \times \int_{-\pi/2}^{\pi/2}\left(I_0(q) + 2\sum_{r=1}^{\infty} I_r(q)\cos(2r\alpha)\right) \times \sinh(p\sin\alpha)\sin[(2s+1)\alpha]\,d\alpha. \quad (31)$$

We then use the addition theorem on the sine–cosine product and then note that equation (32) is true, to get equation (33):

$$\int_{-\pi/2}^{\pi/2} \sinh(p\sin\alpha)\sin[(2n+1)\alpha]\,d\alpha = \pi(-1)^n I_{2n+1}(p) \quad (32)$$

$$F_3 = -2\exp(-q)\sin(Da_0\tau)\sum_{s=0}^{\infty} J_{2s+1}(DA_m) \times \left((-1)^s I_0(q) I_{2s+1}(p) + \sum_{r=1}^{\infty} I_r(q)[(-1)^{s+r} \times I_{2s+2r+1}(p) + (-1)^{s-r} I_{2s-2r+1}(p)]\right). \quad (33)$$

If we collect this and note equations (34) and (35), we find that the autocorrelation function is given by equation (36):

$$\sum_{k=1}^{\infty} J_{2k}(DA_m)(-1)^k I_{2k}(\beta^2 A_m a_0\tau) = J_0[A_m(D^2 - \beta^4 a_0^2\tau^2)^{1/2}] - J_0(DA_m) \quad (34)$$

$$\sum_{s=0}^{\infty} J_{2s+1}(DA_m)(-1)^s I_{2s+1}(\beta^2 a_0 A_m\tau) = 0 \quad (35)$$

$$\begin{aligned} R(\tau) = {} & \frac{\kappa^2 C_1 g_0}{2}\left(\frac{\pi}{2\beta^2}\right)^{1/2}\exp\left(-\frac{\beta^2 A_m^2}{4}\right) \\ & \times \exp\left(-\frac{\beta^2 a_0^2\tau^2}{2}\right) \\ & \times \{M + \cos(Da_0\tau)J_0[A_m(D^2 - \beta^4 a_0^2\tau^2)^{1/2}]\} \\ & \times \left\{\left[I_0\left(\frac{\beta^2 A_m^2}{4}\right)I_0(\beta^2 A_m a_0\tau) + 2\sum_{n=1}^{\infty}(-1)^n I_n\left(\frac{\beta^2 A_m^2}{4}\right)I_{2n}(\beta^2 A_m a_0\tau)\right]\right. \\ & + 2\cos(Da_0\tau)\sum_{k=1}^{\infty} J_{2k}(DA_m) \times \sum_{n=1}^{\infty} I_n\left(\frac{\beta^2 A_m^2}{4}\right)(-1)^{n-k} I_{2(n-k)}(\beta^2 A_m a_0\tau) \\ & + 2\cos(Da_0\tau)\sum_{k=1}^{\infty} J_{2k}(DA_m) \times \sum_{n=1}^{\infty} I_n\left(\frac{\beta^2 A_m^2}{4}\right)(-1)^{n+k} I_{2(n+k)}(\beta^2 A_m a_0\tau) \\ & - 2\sin(Da_0\tau)\sum_{s=0}^{\infty} J_{2s+1}(DA_m) \times \sum_{r=1}^{\infty} I_r\left(\frac{\beta^2 A_m^2}{4}\right)(-1)^{s+r} I_{2s+2r+1}(\beta^2 a_0 A_m\tau) \\ & - 2\sin(Da_0\tau)\sum_{s=0}^{\infty} J_{2s+1}(DA_m) \times \left.\sum_{r=1}^{\infty} I_r\left(\frac{\beta^2 A_m^2}{4}\right)(-1)^{s-r} I_{2s-2r+1}(\beta^2 A_m a_0\tau)\right\}. \end{aligned} \quad (36)$$

This is the general stochastic model for a flow with a sinusoidal perturbation superimposed and can be simplified as shown in the main text.

References

[1] Bruel and Kjaer 1982 *Bruel and Kjaer Technical Review 3: Sound Intensity (Theory)*

[2] Bruel and Kjaer 1982 *Bruel and Kjaer Technical Review 4: Sound Intensity (Instrumentation)*

[3] Greated C A 1986 Measurement of acoustic velocity fields *Strain* pp 21–4

[4] Tranter C J 1968 *Theory of Bessel Functions* (English University Press)
[5] Dubbelday P S and Schau H C 1989 Laser doppler anemometry detection of hydroacoustic particle velocity *J. Acoust. Am.* **86** 891–4
[6] Barnes F H, Daudapota Q I, Greated C A and Grant I 1977 Applications of photon correlation techniques to the measurement of flow with a sinusoidal perturbation *Phys. Fluids* **20** 211
[7] Abbis J B 1972 Laser anemometry in an unseeded wind tunnel by means of photon correlation spectroscopy *J. Phys. D: Appl. Phys.* **5** L100–2
[8] Sharpe J P and Greated C A 1987 The measurement of periodic acoustic fields using photon correlation spectroscopy *J. Phys. D: Appl. Phys.* **20** 418–23
[9] Sharpe J P and Greated C A 1989 A stochastic model for photon correlation measurements in sound fields *J. Phys. D: Appl. Phys.* **22** 1429–33
[10] Sharpe J P, Greated C A and Campbell D M 1988 The measurement of complex acoustic impedence using photon correlation spectroscopy *Acoustic* **66** 266–89
[11] Taylor K J 1976 Absolute measurement of acoustic particle velocity *J. Acoust. Soc. Am.* **51** 691–4
[12] Taylor K J 1981 Absolute calibration of microphones by a laser doppler technique *J. Acoust. Soc. Am.* **70** 939–45
[13] brandt O, Fruend H and Heidemann E 1937 Schwebstoffe in Schallfeld *Z. Phys.* **104** 511–33
[14] Pridnore-Brown 1958 Sound propogation in a fluid flowing through an attenuation duct *J. Fluid Mech.* **4** 393
[15] Hanish S 1983 *A Treatise on Acoustic Radiation* vol 2 (Washington, DC: Naval Research Laboratory) ch 6
[16] Durrani T S and Greated C A 1977 *Laser Systems In Flow Measurements* (New York: Plenum)

Measurement of Acoustic Particle Velocity using Particle Image Velocimetry Techniques.

D. B. Hann and C. A. Greated,
Department of Physics and Astronomy,
James Clerk Maxwell Building,
The University of Edinburgh,
Kings Buildings,
West Mains Rd,
Edinburgh.

1 Abstract

It is shown that the technique of Particle Image Velocimetry can be used to measure the acoustic particle velocity in a monotonic sound field. The mathematical forms for the power spectrum and autocorrelation functions of the image formed on film by a sinusoidally oscillating seeding particle are derived.

An experiment using a standing wave is used to show that the expected results agree with those obtained experimentally. The acoustic particle velocity along the tube is compared to values predicted by theory.

2 Introduction

There are many situations in which it is of interest to measure the acoustic particle velocity over a large area. Particle Image Velocimetry (PIV), in its conventional form, gives the velocity vectors of a flow field over large areas [1], but does not predict the sound field. We will show here that it is possible to measure the acoustic particle velocity over an area using PIV techniques.

Laser Doppler Anemometry (LDA)has been used to measure the acoustic particle velocity [6, 3, 5, 8] but has the disadvantage that it is a point measuring device and so the sound field has to be held stable for a long period if many measurements are desired, say to measure the acoustic particle velocity across a tube.

PIV is also non-intrusive, and gives the absolute acoustic particle velocity so there is no interference due to the measuring device, and no calibration is necessary. PIV has the advantage over LDA in that we can measure a complete velocity field virtually instantaneously with the size of the field determined by the resolution and size of our camera. It has been used successfully to measure the flow velocity in a standing wave tube near the velocity node when acoustic streaming has been set up [7].

If the image of a sinusoidally oscillating seeding particle is captured on film, it will form dumbbell shaped streaks. The length of these streaks ($2A_m$)will be related to the acoustic particle velocity (a_m) by the relationship

$$A_m = 2\frac{a_m}{\omega} \tag{1}$$

Here ω is the angular frequency of the oscillation. The length of the streaks was measured by Brandt et al. [2] using a traveling microscope, but this can be

excessively time consuming. We shall use image processing techniques to automate this process in order that a vector map of the acoustic particle velocity can be constructed with the minimum of human intervention.

The main problems with PIV are that optical access is required and the flow needs to be seeded. Since one is actually measuring the movement of seeding particles it is important to ensure that they are faithfully following the movement of the surrounding air. It is known that smoke particles are submicron and will follow the motion of air for frequencies up to 10kHz [2].

We shall first discuss the theoretical forms of the power spectrum and autocorrelation for an image which is formed by an oscillating particle showing how an example matches the theory, before using the results to measure the acoustic particle velocity along and across a standing wave in a tube.

3 Theory of measuring the Acoustic Particle Velocity using PIV

In order that we can properly analyze our measurements in the power spectrum and autocorrelation plane we need to have a theoretical model giving the shape of these functions in terms of the velocity parameters. We shall therefore try to construct a model to show their approximate forms.

For a monotonic sound field, the image is formed by sinusoidally oscillating particles and the probability that the particle will be at any distance x from the centre of oscillation is

$$P(x) = \frac{\Pi(A_m)}{\pi\sqrt{(A_m^2 - x^2)}} \tag{2}$$

where A_m is the amplitude of the vibration and $\Pi(A_m)$ is the box function which is one for all values of x smaller than A_m.

We will make two assumptions about the image thus formed. Firstly we will assume that the image will be a convolution of the probability density function of a sine wave (shown in Equation (2)) and the image which would have been formed by the seeding particle if it had been at rest[9]. The image formed by this convolution will be the form of a streak with magnified discs at either end, with the distance between the ends equal to $2A_m$.

Our second assumption is that the image will be recorded linearly and accurately with sufficient resolution. This is important since if the image is not linearly recorded, or has inadequate resolution, then it will no longer be of the shape envisaged. For the moment we shall assume that the image is recorded accurately.

For ease of calculation, we will assume that the oscillation is in the x direction. This means that the image of a single particle recorded on the film using a camera whose aperture is open for the period of the oscillation will have an intensity distribution of the form

$$\mathrm{I_i(x,y)} = \frac{B_i \Pi(A_{im})\delta(y)}{\pi\sqrt{A_{im}^2 - x^2}} \otimes \Psi(x,y). \tag{3}$$

where A_{im} is the amplitude of the i^{th}particle and B_i is related to the intensity of the i^{th} paticle. The image of a seeding particle $\Psi(x,y)$ will be of the form of an Airy disc with a width of σ say and this can further be approximated by a Gaussian of width $\frac{\sigma}{\pi}$ in order to simplify the mathematics slightly (Figure (1)).

The intensity of the interrogation area can be considered to be a summation of these images randomly placed. This can be expressed mathematically by the expression in equation (4).

$$\begin{aligned} \mathrm{I(x,y)} &= \sum_i B_i \mathrm{I_i(x,y)} \\ &= \sum_i \frac{B_i \Pi(A_{im})\delta(y-y_n)}{\pi A_{im}\sqrt{A_{im}^2-(x-x_i)^2}} \otimes e^{-\pi\sigma(x^2+y^2)} \end{aligned} \tag{4}$$

This is only an approximate expression for Intensity over the interrogation area since we are neglecting any noise and also making three assumptions.

Firstly we are assuming that all the seeding particle images are the same size and shape; for smoke particles this is usually a good approximation for fresh smoke. Brandt et al.[2] discusses the coagulation of smoke particles in a strong acoustic field and shows that after 10 minutes the smoke has formed ropes of particles of indeterminate length and shape. Since we are taking measurements in the regime where the smoke is still relatively fresh, this criteria will not significantly affect our results.

Secondly, we are assuming that all particles are in focus. Since the depth of focus of the camera is very small, the particles which are out of focus in the interrogation area will generally cause a constant background illumination across the negative and this will not significantly alter the expression.

Thirdly, we are assuming that all the images are contained by the window. The images have a length which is sometimes of the order of 1/5th of the size of the interrogation area and so there is a large number of images which are clipped by the edges of the window. The large number of incomplete particle images will produce a low frequency component in the power spectrum which will translate into a larger central peak in the autocorrelation plane.

Using the Wiener-Kinchine method of producing the autocorrelation plane means that the power spectrum is defined as;

$$\mathrm{PS(k,l)} = FT[\mathrm{I(x,y)}]FT[\mathrm{I(x,y)}]^* \tag{5}$$

where FT denotes the Fourier Transform. The Autocorrelation plane is defined as

$$\mathrm{R(x,y)} = FT[\mathrm{PS(k,l)}]. \tag{6}$$

The Fourier transform of the image can be shown to be,

$$\begin{aligned} FT[\mathrm{I(x,y)}] &= \sum_i \frac{C_i}{A_{im}} J_0(2\pi A_{im}k) e^{-\frac{\pi}{\sigma^2}(k^2+l^2)} \\ &\quad (\cos[2\pi(kx_i+ly_i)] + \mathbf{i}\sin[2\pi(kx_i+ly_i)]) \end{aligned} \tag{7}$$

where C_i is a constant realted to B_i and $J_0()$ denotes the zero order Bessel function. Therefore the power spectrum is

$$\begin{aligned} \mathrm{PS(k,l)} &= \sum_i \sum_j \frac{C_i C_j}{A_{im}A_{jm}} J_0(2\pi A_{im}k) J_0(2\pi A_{jm}k) e^{-\frac{2\pi}{\sigma^2}(k^2+l^2)} \\ &\quad \cos[2\pi(k(x_i-x_j)+l(y_i-y_j))] \end{aligned} \tag{8}$$

If we assume that the streak length is fairly constant over the area under investigation, say $2A_m$, then the expression can be simplified to

$$\begin{aligned} \mathrm{PS(k,l)} &= \frac{1}{A_m^2} J_0^2(2\pi A_m k) e^{-\frac{2\pi}{\sigma^2}(k^2+l^2)} \\ &\quad \sum_i \sum_j C_i C_j \cos[2\pi(k(x_i-x_j)+l(y_i-y_j))] \end{aligned} \tag{9}$$

Looking at Figure (6), the power spectrum of a section of the experimental photograph (Figure (5)), we can see that there are two parts to the equation of significance, the $J_0^2()e^{-\frac{2\pi}{\sigma^2}(k^2+l^2)}$ term and the summation.

The summation term causes the speckle and is a low frequency effect which can be ignored at the moment. The $J_0^2()e^{-\frac{2\pi}{\sigma^2}(k^2+l^2)}$ term determines the shape of the halo. The Bessel function produces fringes which are perpendicular to the direction of the streak. We can approximate the Bessel function term in the power spectrum to make the mathematics simpler. If we note that for $2\pi A_m k >> 2.5$ (see Figure (2) then

$$J_0(2\pi A_m k) \approx \frac{1}{\sqrt{2\pi A_m k}} \cos(2\pi A_m k - \frac{\pi}{4}) \tag{10}$$

and equation (9) can, if we consider the summation term as being roughly constant, be approximated as

$$\mathrm{PS(k,l)} = \frac{1}{4\pi A_m^2 k} e^{-\frac{2\pi}{\sigma^2}(k^2+l^2)} (1 + \sin(4\pi A_m k)) \tag{11}$$

Averaging the Power spectrum along the fringes will give us a the profile of the Power Spectrum (Figure (7)) which will be proportional to

$$\frac{1}{4\pi A_m^2 k} e^{-\frac{2\pi}{\sigma^2}k^2} (1 + \sin(4\pi A_m k)) \tag{12}$$

The Fourier Transform of this will be of the form shown in Figure(8) which has a steep slope at the expected amplitude. The gradient of the Fourier Transform can be calculated using the relationship

$$FT[\mathbf{i}2\pi k f(k)] = \frac{\mathrm{d}F(x)}{\mathrm{d}x} \tag{13}$$

where $F(x)$ is the Fourier transform of $f(k)$.

This means that the gradient of the Fourier Transform can be written as

$$\begin{aligned} \frac{\mathrm{d}R(x)}{\mathrm{d}x} &= FT\left[\mathbf{i}2\pi k \frac{1}{4\pi A_m^2 k} e^{-\frac{2\pi}{\sigma^2}k^2} (1 + \sin(4\pi A_m k))\right] \\ &= FT\left[\frac{\mathbf{i}}{2A_m^2} (1 + \sin(4\pi A_m k))\, e^{-\frac{2\pi}{\sigma}k^2}\right] \\ &= \frac{1}{2A_m^2}\left(e^{-\frac{\pi\sigma^2}{2}x^2} + e^{-\frac{\pi\sigma^2}{2}(k-2A_m)^2} + e^{-\frac{\pi\sigma^2}{2}(k+2A_m)^2}\right) \end{aligned} \tag{14}$$

It is seen that there is a peak at the centre, and two peaks at $\pm 2A_m$ which should be easy to detect.

A computer program was therefore written using equation (14) to find the peaks in the gradient of the Fourier Transform and this was used for analyzing the photographs in the experiment discussed below.

4 Experimental Method

An experiment was set up to measure the acoustic amplitude along a square cross section tube in which a standing wave was present. The tube had a 30mm square cross-section and was 700mm long not including the horn of the loudspeaker (Figure(3)). The standing wave had a frequency of 1850Hz and was about 150dB at the pressure antinodes, measured with a probe microphone. The tube was illuminated with a

thin sheet of light produced by a 2W Argon-ion laser using a cylindrical lens and a spherical lens in series, and the flow was made visible by the introduction of smoke particles into the flow just before the photographs were taken.

The camera was set at an 8ms exposure in order to capture a practically stationary image which would not move with the streaming and would be roughly ten periods of the oscillation. The camera lens aperture was set to f# 4 which allowed a sufficiently wide depth of focus whilst keeping the diffraction broadening effects of the seeding particle image as small as possible. This was necessary because of the closeness of the camera to the tube in order that the area under observation was as large as possible on the negative. A large aperture would produce too small a depth of field which would mean that there were many out of focus particles in the measuring area.The film was 400ASA and was push processed to about 800ASA when it was developed. An A4 size print of the negative was made and scanned onto a computer[4]. The scanned image had a resolution of 1943x 2400 pixels which meant that 1943 pixels was equivalent to 30mm across the tube. This allowed us to get a resolution of 1 pixel equivalent to 0.01544mm in the object plane.

One of the photographs taken is shown in Figure (4); if this is studied, it can be seen that the amplitude of the vibration changes along the length of the tube (vertical in the picture), but not across the tube (horizontal in the picture). A section of the photograph is magnified and shown in Figure(5) and its power spectrum, profile and FT of profile are shown in Figures (6), (7) and (8) respectively.

In order to analyse the sound field from the photographs, we use the technique just described, of computing the first derivative of the FT of the profile of the power spectrum, to measure the variation of the amplitude across the tube.

This gives us Figure (9) in which we have superimposed all the points across the tube. The interrogation area was chosen as 160 x 160 pixels and the distance between centre points of the area was 80 pixels. It can easily be seen that the amplitude is nearly constant across the tube which is what is expected for a plane wave. The amplitude along the tube also fits the expected cosine with an amplitude of $2.3 \pm 0.05 \times 10^{-4}$ m. This corresponds to an acoustic particle velocity of 2.7 ± 0.05 ms^{-1} and a sound pressure level of 151.8 ± 0.16dB at the velocity antinode.

4.1 Conclusion

The experimental results fit well with the theoretical predictions, consistent with the acoustic particle velocity propagating along the tube sinusoidally in a planar wave with a maximum intensity of 151.8 dB. The amplitude across the tube is fairly constant and there are few measurements which do not fit the curve. The results at the extreme edge of the tube are not included since the analysis system could not deal with the high velocity gradients within the boundary layer.

A difficulty arises in the areas where the acoustic particle velocity is small and it is generally in these areas that we have to consider the effect of the central peak on the amplitude peak. The presence of the central peak in the graph of the gradient of the Fourier Transform will shift the amplitude peak towards the centre by a small amount which is dependent on the value of σ the width of the image of the seeding particle if it was at rest. For small σ this will only become apparent at small amplitudes, but as σ increases, the error will also increase. This puts a lower limit on the amplitude of oscillation which can be measured by the technique. There is no upper limit to the amplitude.

One of the main limitations of the technique at the moment is that the particle oscillations need all to be in the same direction. This can be overcome if we have sufficient resolution of the images. If we rotated the power spectrum so that the fringes were aligned with the x-axis, then the procedure for finding the amplitude

would be the same. This would allow the measurement of more complicated acoustic fields in which the oscillations are not aligned in a single direction.

References

[1] R. J. Adrian. Optical methods for measuring vector velocity fields, part ii techniques. *Proc. Von Karman Inst. of Fluid Mechanics*, pages Lecture Series 1988–06, 1988.

[2] H. Brandt, O.and Fruend and E. Heidemann. Schwebstoffe in schallfeld. *Zeits. Phys.*, 104:511–533, 1937.

[3] D. B. Hann and C. A. Greated. Acoustic measurements in flows using photon correlation spectroscopy. *Journal of Physics E(Measuring Science and Technology)*, 4:157–164, 1993.

[4] A. K. Hind and J. R. E. Christy. Digital piv applied to flows around artificial heart valves: analysis by autocorrelation. *Flow visualisation and image analysis, Delft Confrence*, Ed. Nieuwstand, 1993.

[5] J. P. Sharpe and C. A. Greated. The measurement of periodic acoustic fields using photon correlation spectroscopy. *J.Phys.D (Applied Physics)*, 20:418–423, 1987.

[6] J. P. Sharpe and C. A. Greated. A stochastic model for photon correlation measurements in sound fields. *J. Phys. D(Applied Physics)*, 22:1429–1433, 1989.

[7] J. P. Sharpe, C. A. Greated, C. Gray, and D. M. Campbell. The measurement of acoustic streaming using particle image velocimetry. *Acoustica*, 68:168–172, 1989.

[8] K. J. Taylor. Absolute measurement of acoustic particle velocity. *J.Acoust.Soc.Am*, 51:691–4, 1976.

[9] H. J. Tiziani. Application of speckling for in-plane vibration analysis. *Optica Acta*, 18:891–902, 1971.

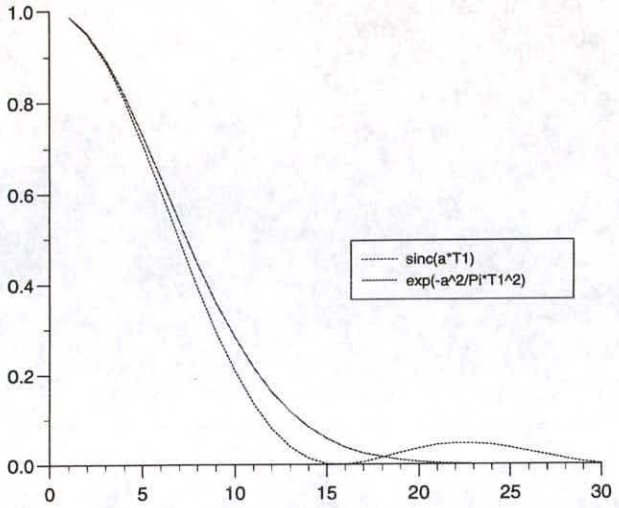

Figure 1: The comparison of an airy function of width σ with an exponential of similar argument

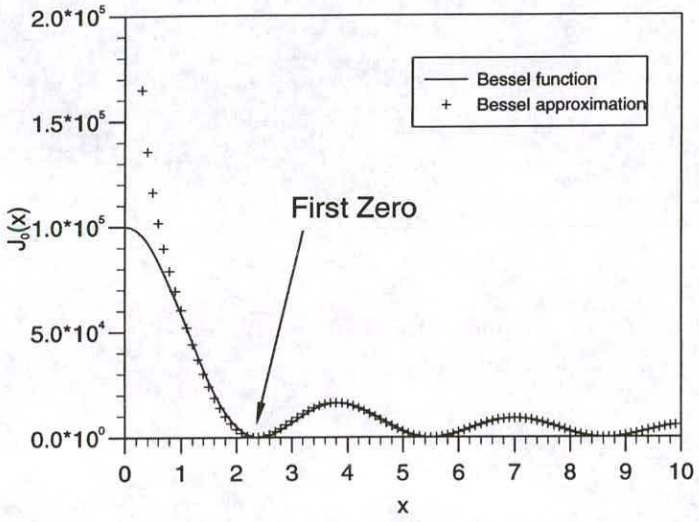

Figure 2: A graph showing a bessel function and its approximation showing that past the first zero they coincide.

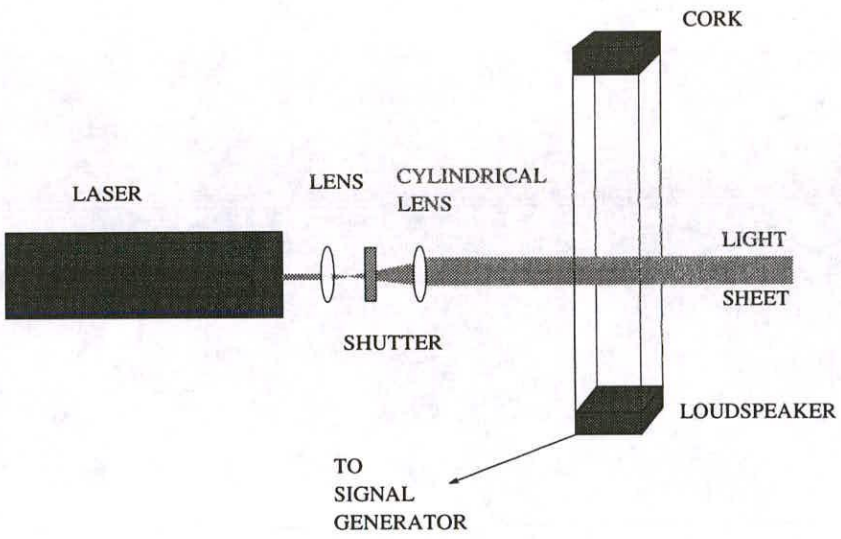

Figure 3: The experimental apparatus used to produce photographs of the sound field.

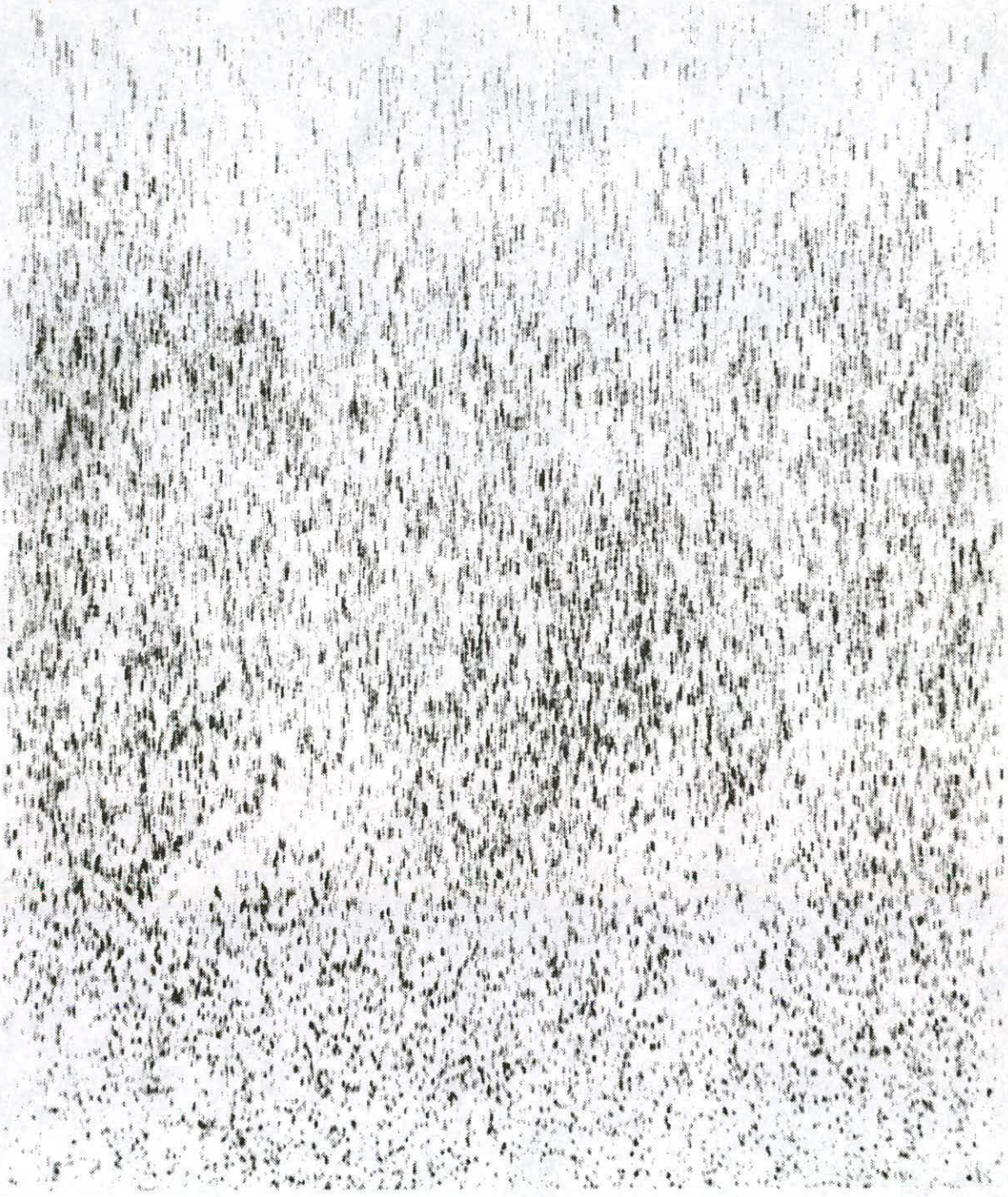

Figure 4: The photograph of the sound field.

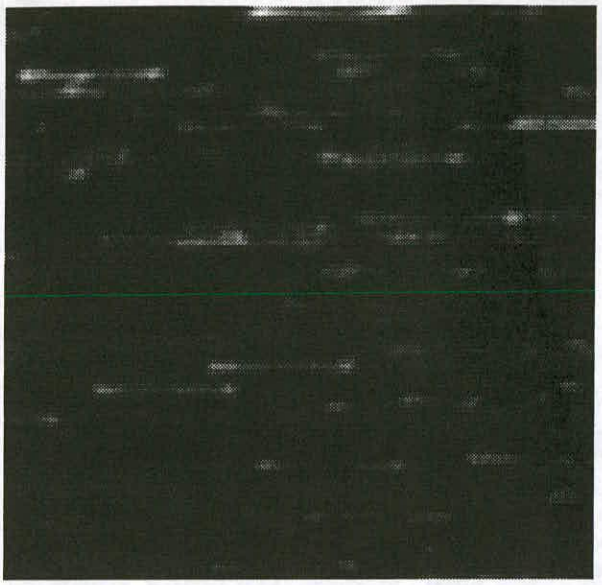

Figure 5: An interrogation area showing the form of the images formed in a flow which is oscillating

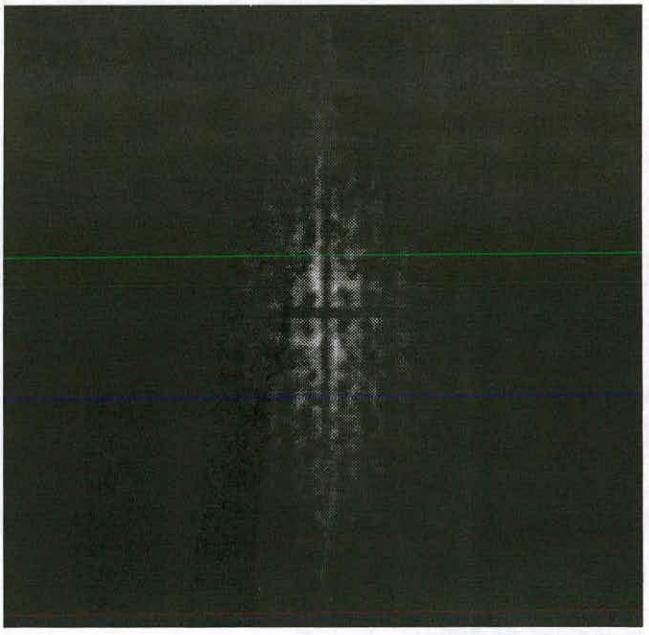

Figure 6: The power spectrum showing the vertical fringes formed by the shape of the image.

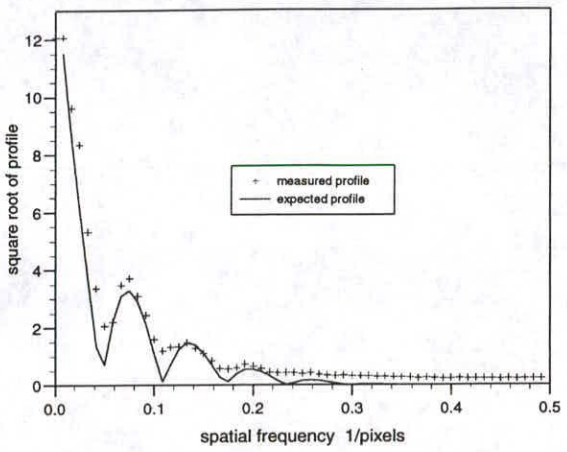

Figure 7: The square root of the measured profile compared to the expected profile

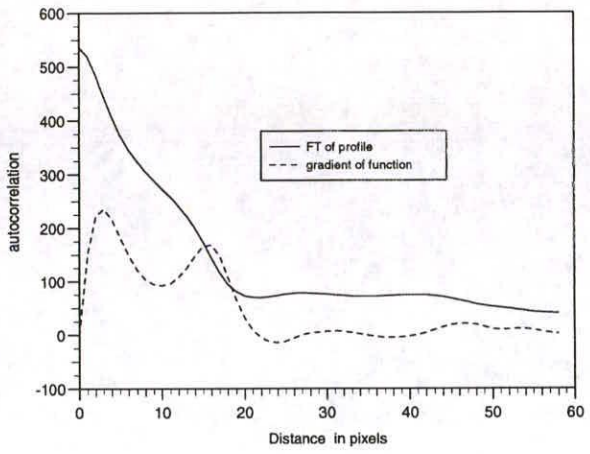

Figure 8: The Fourier Transform of the profile and its gradient

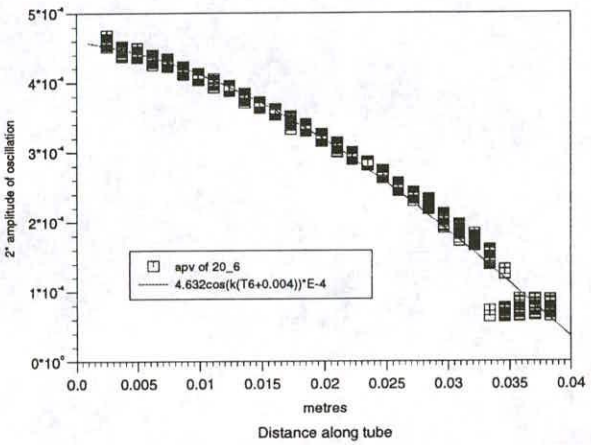

Figure 9: The variation of the amplitude of fluctuation with the distance along the tube compared to the expected value.